

POLITECNICO DI TORINO

SCUOLA DI DOTTORATO
Dottorato in Elettronica e delle Comunicazioni – XX ciclo

Tesi di Dottorato

A Statistical Theory for GNSS Signal Acquisition



Daniele Borio

Tutore

prof. Letizia Lo Presti
prof. Gérard Lachapelle

Coordinatore del corso di dottorato

prof. Ivo Montrosset

Marzo 2008

Contents

1	Introduction	3
1.1	Objectives and Motivations	3
1.2	Thesis Outline	3
1.3	Thesis Contributions	13
I	GNSS Acquisition in the absence of interference	15
2	Direct Sequence Spread Spectrum (DSSS) and GNSS signals	17
3	GNSS signal acquisition	23
3.1	Basic concepts	23
3.2	CAF evaluation	25
3.2.1	CAF evaluation methods	28
3.2.2	Method 1: Serial scheme	28
3.2.3	Method 2: parallel acquisition in the time domain	28
3.2.4	Method 3: FFT in the Doppler domain	29
3.3	Envelope and Average	30
3.4	Detection and Decision	31
3.5	Multi-trial and Verification	32
3.6	Receiver Operating Characteristics	32
3.7	Coherent output SNR	37
4	Cell and decision probabilities	39
4.1	Statistical model	40
4.1.1	Searching strategies	42
4.2	Detection probability	42
4.2.1	Maximum search strategy	42
4.2.2	Serial search technique	43
4.2.3	Hybrid search	44
4.3	Miss-detection probability	45

4.4	False alarm probabilities	45
4.5	Simulation analysis	46
4.5.1	Probability curves	48
4.6	Enhanced model	53
4.7	Network assisted GPS	56
5	Increasing the acquisition performance	59
5.1	Non-coherent signal combining	60
5.2	Differentially coherent combining	62
5.3	Equivalent Coherent SNR	66
5.3.1	Empirical formula	67
5.3.2	Generalized SNR	68
5.3.3	Equivalent area criterion	69
5.4	Formulas validation	74
5.4.1	Test for fixed false alarm probability	74
5.4.2	ROC distance	76
6	Acquisition losses	81
6.1	Frontend filtering	81
6.1.1	Equivalent representation of the acquisition block	82
6.1.2	Coherent output SNR	84
6.2	Quantization loss	88
6.2.1	One-bit quantization	89
6.2.2	Two-bit quantization	93
6.2.3	B-bit quantization	97
6.2.4	Analysis and Simulation	100
6.3	Doppler and delay residual errors	103
7	Acquisition of composite GNSS signals	107
7.1	Signal model	109
7.2	Single period acquisition	109
7.2.1	Non-coherent channel combining	110
7.2.2	Coherent channel combining with sign recovery	112
7.2.3	Differentially coherent channel combining	115
7.2.4	Simulation analysis and comparison	117
7.2.5	Simulation results	118
7.2.6	ROC comparison	119
7.3	Multiple code period integration	122
7.3.1	Signal integration without sign recovery	123
7.3.2	Non-coherent integration	124

7.3.3	Semi-coherent integration	124
7.3.4	Differentially coherent integration	127
7.3.5	Signal integration with sign recovery	128
7.3.6	Exhaustive bit search	128
7.3.7	Secondary code partial correlation	131
7.3.8	Number of bit combinations with secondary code constraints	131
7.3.9	Simulation results	133
8	Conclusions	141
II	GNSS Acquisition in the presence of interference	143
9	Interference source classification	145
9.1	Interference from FM, VHF and UHF emitters	147
9.1.1	Interference from TV emitters	148
9.2	Personal Electronic Devices	149
9.2.1	Ultra Wide-Band (UWB) interference	150
9.3	Satellite-based Services	151
9.3.1	Intersystem and Intrasystem Interference	152
9.4	Radar and Navigation systems	152
9.5	Other sources	153
10	Gaussian narrow-band interference	155
10.1	Digital SCCs	156
10.2	ROC analysis and SSCs interpretation	160
10.3	Simulation results	160
11	Continuous Wave Interference (CWI)	163
11.1	Detection and false alarm probabilities	164
11.1.1	Useful signal contribution	165
11.1.2	Interference contribution	165
11.1.3	Noise contribution	166
11.1.4	Detection probability	167
11.1.5	False Alarm probability	169
11.2	Impact of the acquisition parameters	171
11.3	Simulations	175
12	CWI mitigation	179
12.1	General Overview	179
12.2	One-pole notch filter	182

12.2.1	The adaptive criterion	183
12.2.2	Wiener solution	186
12.2.3	Bandwidth and attenuation	190
12.2.4	Performance analysis and test on real data	194
12.3	Two-pole notch filter	201
12.3.1	The detection unit	202
12.4	Multi-pole notch filter	206
12.4.1	Multi-pole notch filter performance	206
13	Time-frequency analysis for interference detection and mitigation	211
13.1	General Overview	211
13.1.1	Time-Frequency representations	213
13.2	Reconfigurable GNSS Acquisition Scheme for Time-Frequency Applications	214
13.2.1	Modified acquisition block	215
13.2.2	Real data and simulation tests	218
13.3	A Time-Frequency Excision Algorithm	224
14	Conclusions	235
III	Appendices and Bibliography	237
A	Acquisition analysis for Galileo BOC modulated Signals: theory and simulation	239
A.1	Abstract	239
A.2	Introduction	240
A.3	Acquisition schemes	241
A.3.1	Serial search scheme	242
A.3.2	Parallel acquisition in time delay domain	243
A.3.3	Parallel acquisition in Doppler frequency domain	244
A.4	Detection criteria	245
A.4.1	Acquisition losses	247
A.4.2	Detection probability in presence of losses	250
A.5	Acquisition Model Validation	253
A.6	Coherent and non-Coherent Integration Comparison	255
A.7	Conclusions	261
A.8	References	261
B	Independence of search space cells	263
C	Exact computation of the polynomial $P_{K-1}(\rho_c)$	267

D	$P_{K-1}(\rho_c)$ approximations	269
D.1	Constant term	270
D.2	First power coefficient	271
E	Independence of the random variables at the output of the data and pilot correlators	273
F	Computation of the coefficients $\{a_{K,i}\}_{i=1}^K$ and $\{b_{K,i}\}_{i=1}^K$	275
G	Equivalent probability distribution of φ_1 and φ_2	279
H	Proof of (11.20)	281
	Bibliography	283

List of Tables

4.1	Simulation parameters	50
5.1	Equivalent coherent SNR when K non-coherent integrations are employed.	72
5.2	Conversion formulas for determining the equivalent SNR and the number of non-coherent integrations.	75
6.1	Optimal AGC gain.	101
6.2	Simulation Parameters	101
7.1	False alarm and detection probabilities for different acquisition schemes. The symbol “■” denotes the original contributions of this chapter.	118
7.2	Simulation parameters.	118
7.3	Comparison of the number of possible bit combinations to be tested with and without the constrains imposed by the secondary codes. In order to have a fair comparison with the other two cases the integration time for the data channel alone has been doubled.	133
7.4	Simulation parameters.	133
9.1	Interference type and source classification.	147
9.2	Harmonics from FM, VHF and UHF emitters, from [22].	148
10.1	Simulation parameters.	161
10.2	SSCs values, pure number.	161
11.1	Simulation parameters	175
13.1	NordNav-R30 characteristics.	218
13.2	Simulation parameters.	227
A.1	Coherent and non-Coherent C/N_0 gain comparison	256

List of Figures

1.1	Structure of the first part of the thesis, "Acquisition in the absence of interference", and interdependence of the different chapters.	5
1.2	Structure of the second part of the thesis, "Acquisition in the presence of interference", and interdependence of the different chapters.	10
2.1	Basic principles of DS/CDMA GNSSs: the signals broadcast by the different satellites are identified by means of different PRNs. The transit time is estimated by exploiting the correlation properties of the spreading sequences.	18
2.2	Examples of basic pulses generating the subcarrier signals.	19
3.1	Conceptual representation of the acquisition process. GNSS acquisition is composed of different steps that, starting from the input signal, lead to the final decision and to a rough estimation of the Doppler frequency and code delay.	24
3.2	Conceptual scheme for the evaluation of the Cross Ambiguity Function (CAF). The received signal is multiplied by two orthogonal sinusoids and a local signal replica. The resulting signals are then integrated, generating the real and imaginary parts of the CAF.	27
3.3	Time parallel acquisition scheme: the CAF is determined by using a circular convolution employing efficient FFT's.	29
3.4	Frequency parallel acquisition scheme: the CAF is evaluated by using efficient FFT.	30
3.5	Scheme of the basic acquisition block. Only coherent integrations are used.	31
3.6	General detection scheme: the input signal is processed in order to produce a decision variable used for establishing the presence of a desired signal. $\{C\}$ is the set of parameters describing the channel impact on the desired signal whereas $\{P\}$ refers to the processing parameters. β is the decision threshold, while P_d and P_{fa} are the detection and the false alarm probabilities, respectively.	32
3.7	ROC curves for different values of C/N_0 . Basic acquisition scheme, 1 ms coherent integration time.	37

4.1	Decision detection probability vs decision false alarm probability in the absence of signal, Gaussian model.	49
4.2	Decision false alarm probability in the presence of signal vs decision false alarm probability in the absence of signal, Gaussian model.	49
4.3	Decision detection probability vs decision false alarm probability in the absence of signal, simulated acquisition system.	51
4.4	Decision false alarm probability in the presence of signal vs decision false alarm probability in the absence of signal, simulated acquisition system.	51
4.5	Decision miss-detection probability vs decision false alarm probability in the absence of signal, simulated acquisition system.	52
4.6	Decision detection probability vs decision false alarm probability in the absence of signal, mean adjusted model.	54
4.7	Part of a noiseless search space obtained with a GPS CA code with 2 samples/chip and a Doppler step of 666 Hz.	55
4.8	Decision detection probability vs decision false alarm probability in the absence of signal, enhanced model.	56
4.9	Principle of network assisted GPS (AGPS): mobile telephone network provides additional information to the GNSS receiver in order to reduce the size of the acquisition search space.	57
4.10	Reduction of the acquisition search space due to network assistance.	57
5.1	Acquisition scheme with non-coherent integrations.	61
5.2	Acquisition scheme with differentially coherent integrations.	62
5.3	Squaring loss vs coherent SNR obtained from Eq.(5.24). The dashed line represents the loss evaluated according to Eq. (5.29) whereas the continuous curves refer to the loss obtained by using the equivalent coherent SNR evaluated according to the equivalent area criterion. In the latter case the loss depends on the number of non-coherent integrations.	69
5.4	Comparisons between ROCs obtained with K non-coherent integrations (continuous curves) and the ones obtained by using only coherent integration and the corresponding equivalent coherent SNR (dashed curves). Parameter ρ_c is the coherent SNR.	73
5.5	Comparisons of ROCs obtained by using different criteria for evaluating the equivalent coherent SNR. Continuous curves represent the original ROCs obtained by using K non-coherent integrations. The other curves are obtained by using only coherent integrations and the equivalent SNR evaluated according to different criteria. In the title, ρ_c is the coherent SNR, while the number of non-coherent integrations is $K = 5$ in both subplots.	74
5.6	Comparison between different detection probabilities achieved with $P_{fa} = 10^{-3}$ and target equivalent SNR = 5 dB.	76

5.7	Comparison between different detection probabilities achieved with $P_{fa} = 10^{-3}$ and target equivalent SNR = 10 dB	77
5.8	Number of non-coherent integrations vs coherent SNR for a target equivalent SNR = 5 dB.	78
5.9	ROC distance with $P_{max} = 0.1$ vs coherent SNR for a target equivalent SNR = 5 dB.	79
5.10	Number of non-coherent integrations vs coherent SNR for a target equivalent SNR = 10 dB.	79
5.11	ROC distance with $P_{max} = 0.1$ vs coherent SNR for a target equivalent SNR = 10 dB.	80
6.1	The first stages of a GNSS receiver are the antenna and the frontend, used to recover the GNSS signal. The frontend downconverts, filters and amplifies the received signal.	82
6.2	The signal at the input of the acquisition block is composed of the useful GNSS signal and a noise component. In general the noise component is a colored sequence and the useful signal is a filtered version of the transmitted GNSS signal. These effects can be accounted by an equivalent filter $h_f[n]$ that models the frontend filtering.	83
6.3	Equivalent representations of the basic acquisition scheme. a) the code multiplication and the subsequent integration can be interpreted as an equivalent filtering. b) Equivalent complex representation of the acquisition block.	84
6.4	Effect of the different acquisition stage blocks on the noise PSD. a) Input signal PSD. b) Effect of the complex modulation. c) Effect of the equivalent code filtering.	86
6.5	One-bit quantization for GNSS signal.	89
6.6	a) Representation of the probabilities characterizing the process $r_B[n]$ with respect to the noise probability density function. b) Representation of the expected value of $r_B[n]$ with respect to the noise probability density function.	91
6.7	Two-bit quantization for GNSS signal.	93
6.8	Pictorial representation of the integrals that lead to the expected value of the quantized signal $r_B[n]$	95
6.9	Signal quantization over B bits.	97
6.10	Quantization loss as a function of the normalized AGC gain ($A_g \sigma_{IF}$).	100
6.11	Quantization loss: comparison between theoretical and Monte Carlo results. ($C/N_0 = 35$) dB.	102
6.12	Quantization loss: comparison between theoretical and Monte Carlo results. ($C/N_0 = 45$) dB.	103

7.1	Acquisition scheme for non-coherent channel combining: the data and the pilot are acquired separately and the correlator outputs are non-coherently combined.	110
7.2	Acquisition scheme for coherent channel combining with sign recovery: data and pilot spreading sequences are combined to generate two equivalent codes. The maximum of the correlations with the two equivalent codes is used as decision variable.	112
7.3	Acquisition scheme for differentially coherent channel combining with bit recovery: the correlations with the data and pilot local codes are performed separately and differentially coherent combined. Some modifications have been introduced to the traditional differentially coherent combining scheme in order to account for the phase difference between data and pilot channels.	115
7.4	Theoretical and simulated ROCs for the different acquisition methods.	119
7.5	ROC comparison among the different acquisition strategies. $C/N_0 = 40$ dB-Hz.	120
7.6	ROC comparison among the different acquisition strategies. $C/N_0 = 35$ and $C/N_0 = 30$ dB-Hz	121
7.7	Detection probability vs. C/N_0 for a fixed false alarm rate, $P_{fa} = 10^{-3}$	122
7.8	Principle of signal integration without sign recovery. A phase/sign independent random variable $S_k(\tau, F_D)$ is produced for each primary code period. These random variables are then directly summed producing the final decision statistic $S(\tau, F_D)$	123
7.9	Possible positions of the input signal block with respect to the data and pilot secondary code.	132
7.10	ROC comparison among different acquisition strategies. $C/N_0 = 30$ dB-Hz, $K = 3$	134
7.11	ROC comparison among different acquisition strategies. $C/N_0 = 35$ dB-Hz, $K = 3$	135
7.12	ROC comparison among different acquisition strategies. $C/N_0 = 30$ dB-Hz, $K = 5$	136
7.13	ROC comparison among different acquisition strategies. $C/N_0 = 35$ dB-Hz, $K = 5$	137
7.14	ROC comparison among different acquisition strategies. $C/N_0 = 25$ dB-Hz, $K = 10$	138
7.15	ROC comparison among different acquisition strategies. $C/N_0 = 30$ dB-Hz, $K = 10$	139
7.16	ROC comparison among different acquisition strategies. $C/N_0 = 35$ dB-Hz, $K = 10$	140
9.1	Interference source frequency bands.	147
9.2	Potential interference from TV emitters (from [22]).	149

9.3	UWB spectral mask for indoor communication systems.	150
10.1	ROC curves for the BOC(1,1) Galileo signal.	161
10.2	ROC curves for the GPS signal.	162
11.1	Probability density function of the decision cell amplitude α under the hypothesis of useful signal presence. $A_{INT} = 2$, $C = 1$, $k_1 = 0.5$ and $k_2 = 0.2$.	170
11.2	Probability density function of the decision cell amplitude α under the hypothesis of useful signal absence. $A_{INT} = 2$, $k_1 = 0.5$ and $k_2 = 0.2$.	171
11.3	Pictorial representation of the convolution of the spreading sequence $c_{code}[n]$ with the subcarrier signal $s_c[n]$.	173
11.4	a) Modulus of the DFTs of the GNSS code and of the subcarrier. b) Spectrum of the equivalent filter $h_c[n]$	174
11.5	a) Zoom of the DFT of the $h_L[n]$ with $L = 4$. As $L \rightarrow +\infty$, $H_L(f)$ tends to an impulse train and spectral lines clearly appear. b) Zoom of the DFT of the equivalent filter $h_c[n]$.	174
11.6	Probability distribution of the decision cell under detection hypothesis, i.e., in the presence of useful signal. The theoretical model fits Monte Carlo simulations.	176
11.7	Probability distribution of the decision cell under the false alarm hypothesis, i.e., in the absence of useful signal. The theoretical model fits Monte Carlo simulations.	177
11.8	Comparison between theoretical ROCs and Monte Carlo simulations. The ROC in the absence of interference is reported as reference. $\Delta f \cdot f_s = 500$ Hz.	178
12.1	High-level scheme of a GNSS receiver equipped with interfering detection/mitigation units. In this context digital detection/mitigation units are considered and additional devices are added between the frontend and the traditional receiver units.	180
12.2	Notch filter structure: $r[n]$ is the digital input signal, $x_i[n]$ is the signal after the AR block and $x_f[n]$ is the final filtered signal.	183
12.3	Transfer function of the notch filter, $k_\alpha = 0.9$ and $k_\alpha = 0.7$.	185
12.4	Normalized spectrum of the input signal [dB]. The signal power has been normalized to unity.	185
12.5	Normalized spectrum of the filtered signal [dB]. The signal power has been normalized to unity.	186
12.6	Wiener solution according to [95].	188
12.7	Notch filter Wiener solution: the absolute value of the notch filter zero z_0 that minimizes the output power is reported as function of J/N for different values of k_α . The label "calmettes" refers to the solution reported in [95] that is independent from k_α .	190
12.8	$ H_n(z) $ minimum vs k_α , $\rho = 0.985$.	192

12.9	$ H_n(z) $ maximum vs $k_\alpha, \rho = 0.985$	192
12.10	Normalized 3 dB bandwidth vs k_α , for different values of ρ . The 3 dB bandwidth is normalized with respect to the sampling frequency.	194
12.11	Transfer function of the notch filter, $k_\alpha = 0.9$ and $\delta = 0.07$	195
12.12	Convergence of modulus of the zero z_0 , $k_\alpha = 0.9$ and $\delta = 0.07$	195
12.13	LMS and Wiener solution for different values of k_α and comparison between theoretical and simulation results.	196
12.14	Scheme of experimental setup used for collecting and processing the GPS data corrupted by CWI.	197
12.15	Procedure adopted for processing the GPS samples. An Hilbert transform was used in order to produce a complex signal that can be processed by the one-pole notch filter.	198
12.16	PSD of the input and output signals.	199
12.17	CAF obtained by processing the GPS signal corrupted by the CWI. Without mitigation unit is not possible to detect the signal peak. The search space has been evaluated by using a coherent integration time of 1 ms and $K = 3$ non-coherent integrations.	199
12.18	CAF obtained by processing the GPS signal corrupted by the CWI after interference mitigation. The one-pole notch filter effectively removes the CWI and the signal peak emerges from the search space. The search space has been evaluated by using a coherent integration time of 1 ms and $K = 3$ non-coherent integrations.	200
12.19	Magnitude of the adjusted parameter z_0 through the LMS convergence process.	202
12.20	Transfer function of the notch filter, $k_\alpha = 0.9$, steady state conditions.	203
12.21	Convergence characteristics of the amplitude of the notch filter zero for different J/N . $k_\alpha = 0.9$	204
12.22	Mean magnitude of the adjusted parameter z_0 : threshold setting.	204
12.23	Scheme of the adaptive notch filter coupled with the detection unit. The notch filter is always active but the detection unit decides if it is better to use the original or the filtered signal.	205
12.24	Detection algorithm based on the convergence characteristics of the zero of the two-pole notch filter.	205
12.25	Scheme of the multi-pole notch filter.	207
12.26	Experimental setup used for testing the multi-pole notch filter.	208
12.27	Resulting power spectral density of the input signal of the multi-pole notch filter.	208
12.28	Resulting power spectral densities of the output signals of the three two-pole notch filters activated by the detection units.	209

12.29	Resulting transfer functions of the three notch filters activated by the detection units.	209
13.1	Spectrogram and Wigner-Ville distribution of a signal with sinusoidal frequency modulation. The spectrogram has been evaluated by using a Hamming window of length $L = 127$ samples.	214
13.2	Modified serial search acquisition. The traditional serial search acquisition scheme has been modified in order to explore a wider range of Doppler frequencies and to allow the use of specific analysis windows for TF applications.	216
13.3	Modified parallel acquisition in the frequency domain. The parallel acquisition scheme has been modified allowing the use of specific analysis windows for TF applications.	217
13.4	Modified parallel acquisition scheme in the time domain. The parallel acquisition scheme has been modified in order to explore a wider range of Doppler frequencies and to allow the use of specific analysis windows for TF applications.	217
13.5	Spectrogram of a swept interference. The input signal has been collected by using the NordNav R30 frontend in the proximity of TV repeaters. The spectrogram has been evaluated by using the modified parallel acquisition scheme in the time domain.	219
13.6	Power Spectral density estimates of the input signal used for the evaluation of the spectrogram in Figure 13.5. a) PSD of the original signal, sampling frequency $f_s = 16.3676$ MHz. b) PSD of the downsampled signal, sampling frequency $f_s = 4.0919$ MHz.	220
13.7	Spectrogram of a CWI. The input signal has been collected by using the NordNav R30 frontend. The spectrogram has been evaluated by using the modified parallel acquisition scheme in the time domain.	221
13.8	Power Spectral density estimates of the input signal used for the evaluation of the spectrogram in Figure 13.7. a) PSD of the original signal, sampling frequency $f_s = 16.3676$ MHz. b) PSD of the downsampled signal, sampling frequency $f_s = 4.0919$ MHz.	222
13.9	Spectrogram and time domain representation of a simulated GPS signal corrupted by pulsed interference. The spectrogram has been evaluated by using the modified parallel acquisition scheme in the time domain.	223
13.10	Functional scheme of the TF excision algorithm consisting of three blocks: TF representation, instantaneous frequency estimation unit and notch filter.	224
13.11	Transfer functions of the different excision filters.	226

13.12 Correlations of a BOC(1,1) signal in the presence of interference only. A linearly frequency modulated signal has been added to the GNSS signal and processed with the excision algorithm. The notch filter clearly outperforms the FIR filter proposed in [111].	227
13.13 Spectrogram of simulated GPS signal in zero mean Gaussian noise and chirp interference. $C/N_0 = 36$ dB-Hz, $J/N = 10$ dB.	228
13.14 Wigner-Ville distribution of simulated GPS signal in zero mean Gaussian noise and chirp interference. $C/N_0 = 36$ dB-Hz, $J/N = 10$ dB.	229
13.15 Peaks-interpolation performances in terms of RMSE vs the number of samples used for the TFR.	230
13.16 Mean squared error of the interference frequency estimation provided by the peaks-interpolation algorithm vs the J/N	231
13.17 ROC curves for different pole contraction factors with an ideal IF estimation. $C/N_0 = 36$ dB-Hz, $J/N = 10$ dB.	231
13.18 ROC curves for different IF estimation techniques. $C/N_0 = 36$ dB-Hz, $J/N = 10$ dB, $k_\alpha = 0.95$	232
13.19 Search space of a GPS signal under interference: chirp, $J/N = 10$ dB, $C/N_0 = 45$ dB-Hz.	232
13.20 Search space of a GPS signal uner interference after TF-excision: chirp, $J/N = 10$ dB, $C/N_0 = 45$ dB-Hz.	233
A.1 Serial Search Acquisition scheme.	242
A.2 Parallel Acquisition in time domain scheme.	244
A.3 Parallel Acquisition in Doppler frequency domain	245
A.4 Autocorrelation function of Galileo BOC(1,1) code for two different code phase alignments.	248
A.5 Performance loss as a function of the code phase offset.	249
A.6 Logarithmic Doppler loss.	251
A.7 Loss contribution comparison, ROC curve for the Galileo BOC(1,1) signal and $C/N_0 = 30$ dB-Hz	252
A.8 Loss contribution comparison, SNR curve for the Galileo BOC(1,1) signal and desired $P_{fa} = 10^{-3}$	253
A.9 ROC Comparison for the Analytic and Simulated Results for the Galileo BOC(1,1) signal for a C/N_0 of 30 dB-Hz and from one up to five non-coherent integration times.	254
A.10 SNR Comparison for the Analytic and Simulated Results for the Galileo BOC(1,1) signal for a desired $P_{fa} = 10^{-3}$ and from one up to five non-coherent integration times.	254
A.11 Coherent and non-Coherent Integration Comparison for two Galileo BOC(1,1) Code periods, ROC curve calculated for a $C/N_0 = 30$ dB-Hz	256

A.12	Coherent and non-Coherent Integration Comparison for two Galileo BOC(1,1) Code periods, SNR curve for a desired P_{fa} of 10^{-3}	257
A.13	Coherent and non-Coherent Integration Comparison for three Galileo BOC(1,1) Code periods, ROC curve calculated for a $C/N_0 = 30$ dB-Hz	257
A.14	Coherent and non-Coherent Integration Comparison for three Galileo BOC(1,1) Code periods, SNR curve for a desired P_{fa} of 10^{-3}	258
A.15	Coherent and non-Coherent Integration Comparison for four Galileo BOC(1,1) Code periods, ROC curve calculated for a $C/N_0 = 30$ dB-Hz	258
A.16	Coherent and non-Coherent Integration Comparison for four Galileo BOC(1,1) Code periods, SNR curve for a desired P_{fa} of 10^{-3}	259
A.17	Coherent and non-Coherent Integration Comparison for five Galileo BOC(1,1) Code periods, ROC curve calculated for a $C/N_0 = 30$ dB-Hz	259
A.18	Coherent and non-Coherent Integration Comparison for five Galileo BOC(1,1) Code periods, SNR curve for a desired P_{fa} of 10^{-3}	260
B.1	Portion of the matrix $\mathbf{C}\mathbf{C}^T$ obtained with a GPS code of 1023 chips and 2 samples per chip	265
G.1	Transformation from θ_{int} and ϕ_0 to φ_1 and φ_2 . Since the cosine is 2π -periodic the values of φ_1 and φ_2 outside $[-\pi; \pi)$ are folded into this range leading to two independent random variables uniformly distributed.	280

Acronym

AD	Analog to Digital
ADC	Analog to Digital Converter
AGC	Automatic Gain Control
AR	Auto-Regressive
ARMA	Auto-Regressive Moving Average
AWGN	Additive White Gaussian Noise
BPSK	Binary Phase Shifting Key
BOC	Binary Offset Carrier
C/A	Coarse Acquisition
CAF	Cross Ambiguity Function
CCF	Cross Correlation Function
CDMA	Code Division Multiple Access
chf	characteristic function
CWI	Continuous Wave Interference
DME	Distance Measuring Equipment
DoD	Department of the Defense
DS	Direct Sequence
DSSS	Direct Sequence Spread Spectrum
DFT	Discrete Fourier Transform
DTFT	Discrete Time Fourier Transform
FDMA	Frequency Division Multiple Access
FFT	Fast Fourier Transform
FIR	Finite Impulse Response
GLONASS	GLObal NAVigation Satellite System
IDFT	Inverse Discrete Fourier Transform
IF	Intermediate Frequency
IIR	Infinite Impulse Response
ILS	Instrument Landing System
ITU	International Telecommunication Union
J/N	Jammer to Noise ratio

JTIDS	Joint Tactical Information Distribution System
LNA	Low Noise Amplifier
LMS	Least Mean Square
MA	Moving Average
MES	Mobile Earth Station
MGF	Moment Generating Function
MIDS	Multifunction Information Distribution System
MSS	Mobile Satellite Service
pdf	probability density function
PSD	Power Spectral Density
RMSE	Root Mean Squared Error
ROC	Receiver Operating Characteristic
SIS	Signal-in-Space
SNR	Signal to Noise Ratio
SNIR	Signal to Noise and Interference Ratio
SSC	Spectral Separation Coefficient
SSR	Secondary Surveillance Radar
TACAN	TACTical Air Navigation
TF	Time-Frequency
TFR	Time-Frequency Representation
VOR	VHF Omnidirectional Radio-range
WPAN	Wireless Personal Area Network
WSS	Wide Sense Stationary

Chapter 1

Introduction

1.1 Objectives and Motivations

The main objective of this thesis is to provide a complete and cohesive analysis of the acquisition process clarifying different aspects that are often neglected in the current literature. In particular the thesis provides the statistical tools required for the characterization of the acquisition process. A general methodology is developed and applied to

- the acquisition of new composite GNSS signals,
- the acquisition in the presence of interference.

The theoretical results obtained in the thesis have been verified by Monte Carlo simulations and, where possible, by means of real data. In particular the NordNav R30 front-end [1] has been used for collecting real GPS signals that have been used for testing different algorithms considered in the thesis. Of particular interest are the data collected at two different sites: the so called "colle della Maddalena" and the hill of the "Basilica di Superga". These sites are located on two different hills around Torino (Italy). The first one is characterized by the presence of several antennas for the transmission of analog and digital TV signals, whereas the second one is in direct view of the colle della Maddalena antennas. Two different kinds of interference have been observed. In the proximity of the colle della Maddalena, the GPS signal was corrupted by a swept interference, whereas a strong Continuous Wave Interference (CWI) has been observed on the hill of Superga. Those data are analyzed in Chapters 11, 12 and 13.

1.2 Thesis Outline

This thesis is organized in two parts that respectively deal with the acquisition process in the presence and absence of interfering signals.

Part I deals with the development of a unified approach for the characterization of the acquisition process from a functional and a statistical point of view. In particular the acquisition process is analyzed in the presence of Additive White Gaussian Noise (AWGN) only. The presence of AWGN only represents the normal operating conditions in which a GNSS receiver is supposed to work and thus is considered in Part I.

The structure of the first part of this thesis and the logical dependencies between the different chapters is depicted in Figure 1.1. In Figure 1.1 rounded rectangles represent chapters whereas square boxes are used to highlight topics that have been specifically developed in the thesis or arguments that link two different chapters. Although most of the results presented in the first chapters of this part, essentially Chapters 2, 3 and part of Chapter 5, are available in the literature, they are scattered in different textbooks [2–4] and research papers. However, by presenting them in a cohesive and structured manner, those chapters can serve as introductory material with key references for those who would like to study the subject further. Moreover the theory developed in those chapters will be extensively used in the second part of the thesis.

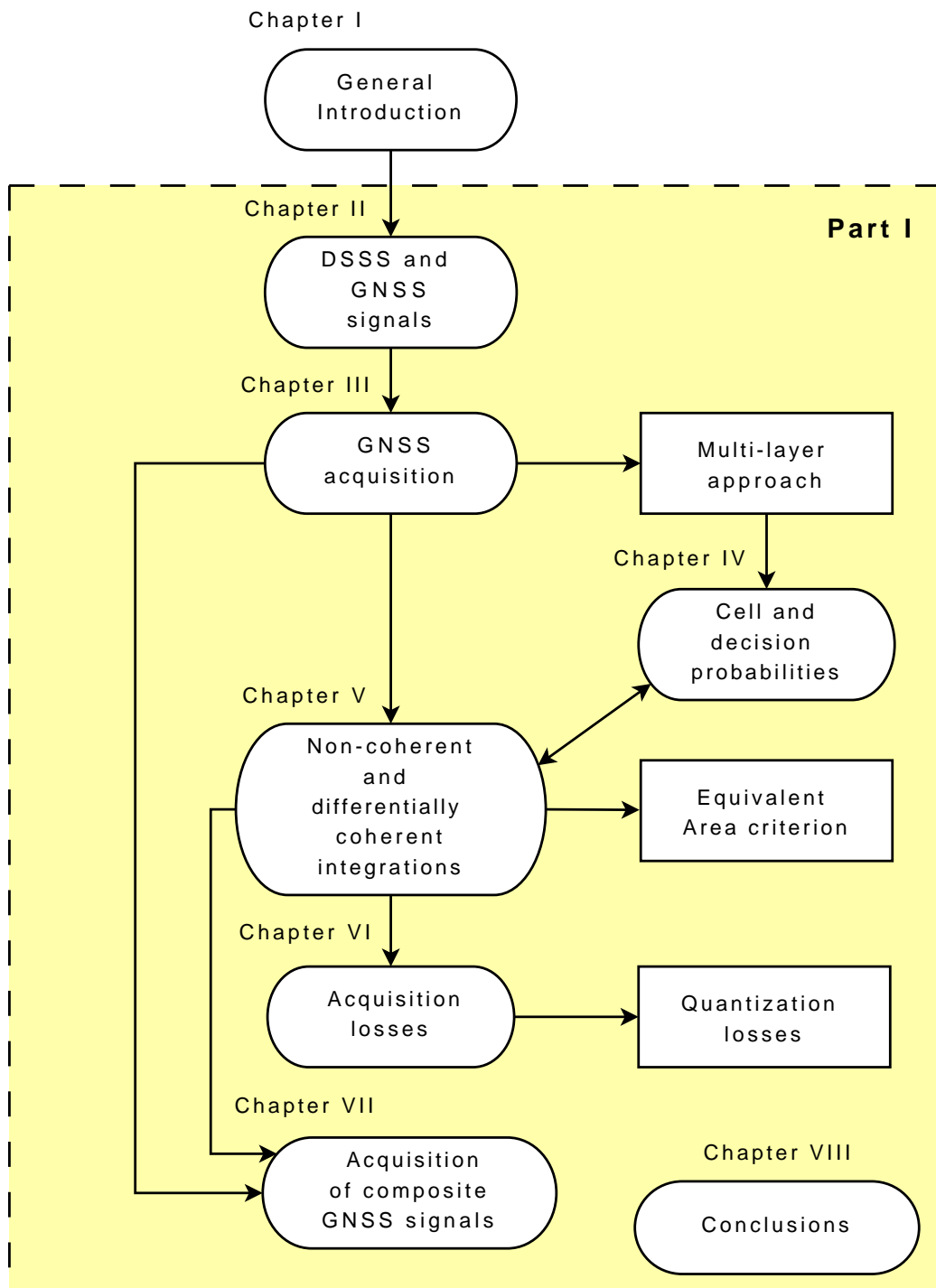


Figure 1.1. Structure of the first part of the thesis, "Acquisition in the absence of interference", and interdependence of the different chapters.

Part I is organized as follows:

- In **Chapter 2**, a short review of Direct Sequence Spread Spectrum (DSSS) modulations is provided and basic models for Global Navigation Satellite System (GNSS) signals are introduced.
- **Chapter 3** deals with the basic principles of the acquisition process. In particular a **multi-layer approach** for characterizing the acquisition process is introduced. This approach represents one of the innovative contributions of this thesis and it is essentially aimed at providing a structured view of the different stages or layers that form the acquisition process. In particular it is recognized that an acquisition system implements some well-known results of detection and estimation theory and that different logical and functional blocks take part in the process. In the GNSS literature the exact role of these disciplines and of these functional blocks is sometimes unclear. In this chapter a general acquisition system is described as the interaction of four functional blocks that perform four different logical operations. The framework developed by using these four elements allows to describe the majority of the acquisition systems, providing an effective tool for comparative analysis. It is further recognized that at each acquisition stage corresponds a different metric that should be considered for the characterization of an acquisition algorithm.
- In **Chapter 4** the concept of **cell** and **decision probabilities** is introduced. In particular, based on the multi-layer approach developed in chapter 3, it is recognized that an acquisition scheme is essentially characterized by two different sets of probabilities. The first set is relative to the search space cells that are random variables characterized by their probability density function (pdf). The cell pdfs depend on the techniques employed for evaluating the single cell and on the considered channel model. For instance the type of integrations used for reducing the noise impact [2,5] and the presence or absence of fading [6,7], strongly impact the single cell probabilities. The second probability set refers to the decision statistic provided by the decision unit. In the rest of the thesis the first set of probabilities is called cell probabilities whereas the second one is called decision probabilities.
These two sets are strongly dependent but they do not generally coincide. In the literature the role of cell probabilities is well assessed and different contributions analyze these probabilities [8–10]. Instead the decision probabilities are only marginally considered. The major texts in the GNSS literature [2–4] usually analyze the cell probabilities only, whereas the decision ones are completely ignored. The decision probabilities allow to completely quantify the acquisition performance, since they do not only depend on the statistical properties of the search space but also on the strategy adopted for the signal detection.

The innovative contribution of this chapter consists in explicitly defining the concept of decision probabilities and providing a general methodology for their analysis. Three acquisition algorithms are considered: the typical serial scheme, the maximum search technique and a hybrid strategy, formed by the combination of the two other methods. To the best of the author's knowledge, the analysis of the hybrid strategy, from the decision probabilities point of view, was still lacking in the current literature and therefore it represents one of the innovative contributions of this thesis. The first part of the chapter establishes a theoretical model describing the relationship between cell and decision probabilities in the three acquisition strategies considered. In this context the cell probabilities are not specified and general formulas, independent from the search space computation method, are derived. In the second part, the theoretical model is tested by simulations.

Surprisingly, it is proved that secondary phenomena, such as the imperfect code orthogonality and the presence of secondary correlation peaks, strongly impact the decision probabilities. These secondary phenomena are generally neglected in the literature [2, 4], since their impact is not clearly observable at the cell probabilities level: the reported simulations allow a better understanding of their role in the acquisition performance. An enhanced model accounting for these secondary phenomena has been proposed herein, finally finding a good agreement with the theoretical formulas.

- In **Chapter 5** different integration techniques, i.e. coherent, non-coherent and differentially coherent integration, are considered and analyzed. For each technique the cell probabilities are provided.

Although those techniques are well known in the literature [8–12] various issues remain. Of particular interest is the characterization of the decision variable by means of a single parameter, the post-correlation or output SNR. However the integration techniques, described in the first part of the chapter, nonlinearly combine the input signal samples, mixing the useful signal and noise components. This process leads to a decision variable whose quality cannot be easily determined. All those issues are discussed in this chapter and, in particular the problem of the so called **squaring loss** is analyzed. Although the expression “squaring loss” is used throughout the literature when referring to the change in output SNR by going from coherent to non-coherent integration, a clear and unique mathematical definition cannot be found and, as highlighted in [13], some paradoxes arise. In this chapter a new definition of the output SNR is provided and used for evaluating the squaring loss. An analytical formulation of the problem is provided, and a new criterion, called **equivalent area criterion**, is proposed. Closed-form formulas, relating the input

SNR and the number of non-coherent integrations to the output SNR are then derived. To the best of the author's knowledge, this criterion has never been previously adopted in the literature for quantifying the impact of non-coherent integration, and thus it represents the innovative contribution of this chapter. Results from radar and signal detection theory are adapted to the GNSS acquisition case and compared with formulas developed in the chapter. A methodology for testing the quality of the conversion formulas is developed and it is proved that the criterion provided gives better results than the ones already present in the literature. The problem of evaluating the number of non-coherent integrations from the desired output SNR is also addressed. The comparison of the various criteria for non-coherent summations is a further contribution of this chapter and shows that there are significant differences in the number of non-coherent integrations predicted according to the different criteria.

- **Chapter 6** deals with the different losses that are introduced in the acquisition process by several factors such as front-end filtering, quantization, code delay and Doppler frequency residual errors.

Particular attention has been given to the analysis of the quantization loss and to the Automatic Gain Control (AGC) threshold setting. Although the quantization loss in the context of DSSS signals has been extensively studied in the past [3, 14, 15], a renewed interest on the subject has been spurred by the introduction of new GNSS signals with power spectral densities (PSDs) different from that of the classical BPSK modulation. An example of this renewed interest is a recent work [16] that assesses the combined effect of GNSS interference, bandlimiting, sampling, and quantizing. For this reason the quantization loss and AGC setting are analyzed in this chapter.

- **Chapter 7** deals with the analysis of strategies for acquiring composite GNSS signals. In the first part of the chapter the analysis focuses on three different algorithms for data and pilot combining on a single primary code period. The first technique, non-coherent channel combining, is from the literature [17, 18] and is used for comparison. The second strategy, coherent channel combining with relative sign recovery, corresponds to the sub-optimal detector described in [19] whereas the last one, differentially coherent channel combining, is, to the best of the author's knowledge, new. Differentially coherent channel combining is obtained by modifying the traditional differentially coherent acquisition technique [12] that exploits the correlation properties between two consecutive GNSS signal periods. In this case data and pilot components are used instead of the two consecutive signal periods. Some modifications have also been introduced to deal with the phase difference between the two components. For each acquisition strategy the probabilities of detection

and false alarm are provided. In particular, closed-form expressions for the probabilities of coherent channel combining and of the differentially coherent integration strategy are derived. To the best of the author’s knowledge, these expressions are new. Monte Carlo techniques have been used to support the theoretical analysis and simulations and analytical expressions agree well, proving the effectiveness of the proposed theory.

In the second part of the chapter acquisition algorithms able to deal with the problem of bit transitions are analyzed. Two classes of acquisition algorithms have been identified, depending whether the bit information is recovered or not. Among the first class three acquisition strategies, pure non-coherent, semi-coherent and the differentially coherent combining, have been considered. Secondary code partial correlation and the exhaustive bit search are the two techniques analyzed in the context of the second class. For each acquisition algorithm the detection and false alarm probabilities have been analyzed and different architectural aspects have been discussed.

- Finally in [Chapter 8](#), conclusions for the first part of the thesis are drawn.

The widespread diffusion of precise positioning services and the growing demand for GNSS receivers able to correctly operate in adverse conditions have motivated the study of the different sources of interference that can possibly degrade acquisition. Due to its weakness the GNSS signal is extremely vulnerable to different kinds of electromagnetic emissions and for this reason appropriate countermeasures are required. The detection and mitigation techniques considered in this thesis are placed before the acquisition block and are aimed to clean the received signal from the interference. Thus the acquisition performance has been used for characterizing the algorithms proposed in the thesis.

Part II deals with the analysis of the different sources of interfering signals. Appropriate models are provided for each interference. The interference impact on the acquisition process is characterized and different countermeasure are proposed.

The structure of the second part of this thesis and the logical dependencies between the different chapters are depicted in [Figure 1.2](#), where the same conventions used in [Figure 1.1](#) have been used.

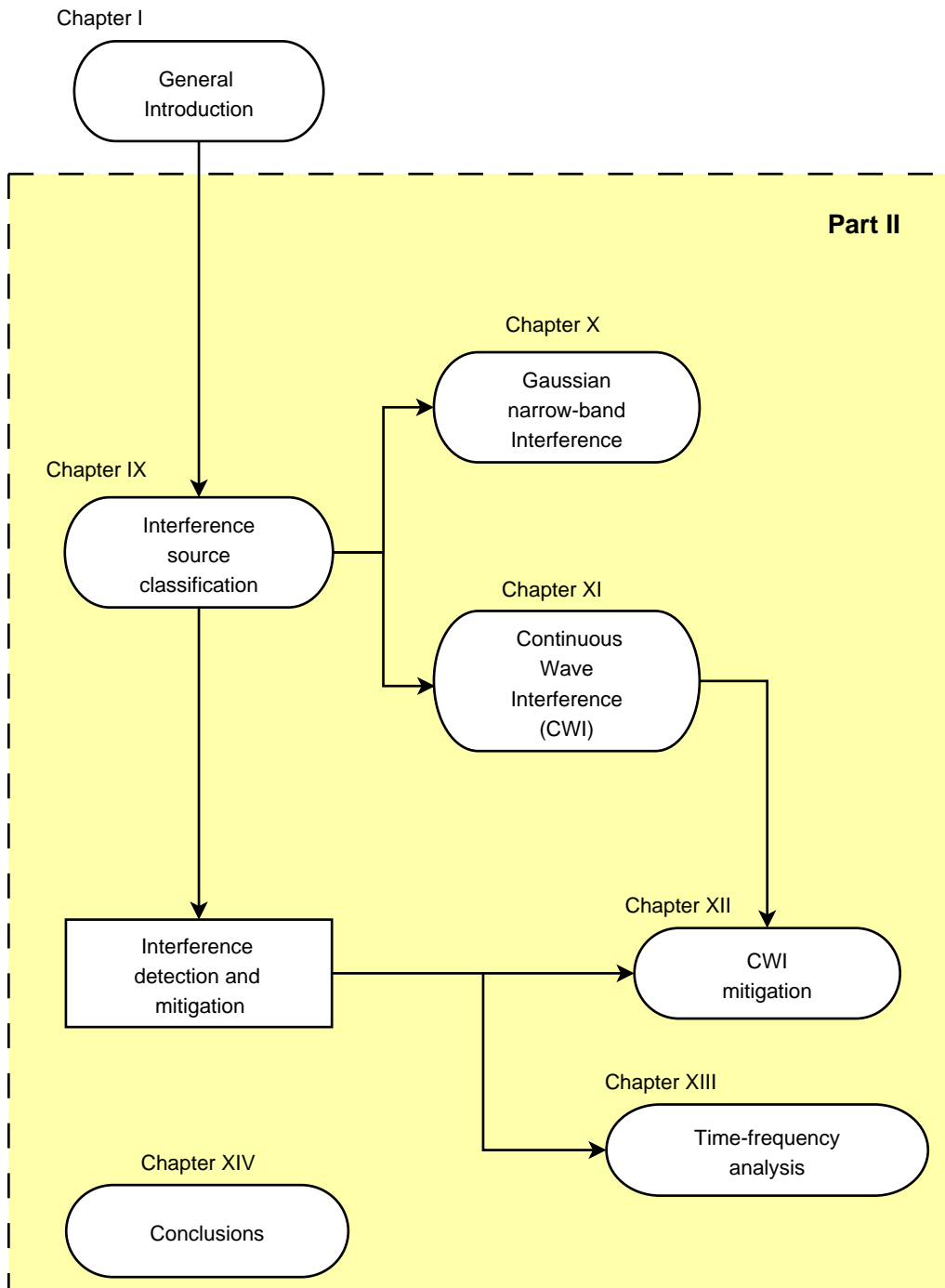


Figure 1.2. Structure of the second part of the thesis, "Acquisition in the presence of interference", and interdependence of the different chapters.

Part II is organized as follows:

- **Chapter 9** reviews the different classes of interference, analyzing the different sources that can generate electromagnetic emission potentially dangerous for GNSS signals. The chapter provides a review of literature results relative to interference in the GNSS context.
- In **Chapter 10** a first class of interference is analyzed. This class is denoted as **narrow-band Gaussian interference** and refers to all those disturbing signals that can be modeled as Gaussian processes. In particular the adjective "narrow-band" refers to the fact that the spectrum of these signals occupies only a relatively small portion of the receiver band.

In the literature, different parameters have been investigated in order to quantify the effect of Gaussian interference on the signal quality, and in particular a quantity called "effective C/N_0 " was introduced to reflect the effect of interference at the input of the receiver, avoiding receiver-specific details such as integration time and the use of coherent or non-coherent processing. Furthermore a parameter called **spectral separation coefficient (SSC)** was introduced in [20, 21] to distinguish the effects of the interference spectral shape from the effects due to the interfering power.

In this chapter the concepts of effective C/N_0 and SSC are extended to digital devices and related to the Receiver Operating Characteristics (ROC) as indicators of system performance. The analysis is supported by simulations.

- **Chapter 11** is devoted to the development of a consistent model to evaluate the performance of GNSS signal acquisition in the presence of CWI. The class of CWIs includes all those narrow-band signals that can be reasonably represented as pure sinusoids with respect to the GNSS bands. This kind of interfering signals can be generated by UHF and VHF TV, VHF Omnidirectional Radio-range (VOR) and Instrument Landing System (ILS) harmonics, by spurious signals caused by power amplifiers working in non-linearity regions or by oscillators present in many electronic devices [22]. The problem of CWI detection and mitigation has been extensively considered in the recent literature [23–25]. However a model focusing on the detection and false alarm probabilities at the acquisition level has never been previously proposed and it thus represents an innovative contribution.

The proposed model is general and accounts for the impact of the CWI frequency and of the GNSS code. In particular it is shown that the acquisition performance strongly depends on two parameters that can be interpreted as the generalization of the SSC developed for quantifying the impact of Gaussian narrow-band interference.

The chapter also investigates the evolution of the CWI through the acquisition chain

along with the impact of the coherent integration time. The analogy with models for radar detection in clutter environments [26] and the role of the GNSS signal phase are finally described.

- In **Chapter 12** the problem of CWI mitigation is addressed. After a review of the different techniques currently available in the literature, the chapter focuses on the design of **multi-pole notch filters**. The chapter deals in detail with the problem of determining the number of disturbing CWIs that affect the received signals and of activating an appropriate number of notch filters for their removal. This problem has rarely been treated in the literature and represents the innovative contribution of the chapter. The proposed detection algorithm is based on the removal of the constraint on the location of the filter zeros whose amplitude is adjusted by an adaptive unit. The zeros amplitude is adjusted on the basis of the Jammer to Noise ratio (J/N) and thus it can be used as metric for the detection of the disturbing signals.

A multi-pole notch filter is obtained by cascading two or more two-pole notch filters. When more than one CWI is present, the first two-pole notch filter in the chain mitigates the most powerful disturbing signal, whereas the other filters remove the other interferers with progressively decreasing power. The detection units coupled with each notch filter in the chain allow to activate only a number of filters equal to the number of interferences, thus minimizing the loss on the useful GNSS signal.

- **Chapter 13** deals with the use of **Time-Frequency (TF)** analysis for interference detection and mitigation. The chapter is organized in three different sections. In the first one, a short review of TF techniques for signal analysis is provided and in particular the spectrogram and the Wigner-Ville distributions are discussed. In the second section the problem of implementing TF techniques in a GNSS receiver is addressed. In particular an efficient solution for implementing the spectrogram on GNSS receivers is proposed. This solution is based on the key observation that the acquisition stage implicitly performs a sort of TF analysis. In the acquisition stage the delay and the Doppler frequency of the GNSS signal are estimated exploiting the correlation properties of the Pseudo-Random Noise (PRN) sequences used for spreading the transmitted signal. In this section it is shown that the evaluation of the search space for the delay and the Doppler frequency corresponds to the evaluation of a spectrogram, whose analysis window is adapted to the received signal. Thus the adoption of a different analysis window allows the detection/estimation of disturbing signals. Based on this principle the method described in the chapter proposes a slight modification of the basic acquisition scheme that allows a fast and efficient TF analysis for interference detection. The method reuses the resources already available for the acquisition stage and the analysis can be performed when the normal acquisition operations shut down or stand temporally idle.

In the last section of the chapter a TF excision technique is proposed and analyzed.

- Finally **Chapter 14** concludes the part and the thesis.

1.3 Thesis Contributions

The main contributions of this thesis are summarized in the following:

- Introduction of a multi-layer model for describing the acquisition process and the resulting distinction between cell and decision probabilities. Some results reported in this thesis have been published by the author in [27, 28] and have been used in [29, 30] as basic parameters for assessing the impact of network assistance on GPS positioning. The information broadcasted by cellular network is used to reduce the size of the search space since it can provide a rough estimation of the code delay and of the Doppler frequency of the different signals. In this way the GNSS receiver has to test a reduced number of cells during the acquisition process. In this case cell probabilities cannot be used to measure the improvement of the acquisition performance since the statistic of the single cell remains unchanged. Only the decision probabilities are able to completely characterize the acquisition performance and the impact of network assistance.
- Analysis of the output SNR and the squaring loss in the context of coherent and non-coherent integrations and the formulation of a new criterion, namely the Equivalent Area criterion for determining the impact of non-coherent accumulations.
- Design of new acquisition algorithms suitable for the new composite GNSS signals. Each acquisition algorithm has been characterized from a statistical point of view and the false alarm and detection probabilities have been determined.
- Characterization of the different classes of interference and their impact on the acquisition block. The thesis presents in a cohesive and structured manner results from the literature and introduces new models for the characterization of interference.
- A detection/mitigation algorithm for CWIs. A multi-pole notch filter able to deal with multiple CWI has been designed. The algorithm is currently under patenting process.
- A TF detection algorithm that exploits the acquisition structure for efficiently computing the spectrogram of the received signal. The algorithm is currently under patenting process.

Part I

GNSS Acquisition in the absence of interference

Chapter 2

Direct Sequence Spread Spectrum (DSSS) and GNSS signals

Global Navigation Satellite Systems (GNSSs) are, in general, Direct Sequence Spread Spectrum (DSSS) systems: spreading codes with good correlation/cross-correlation properties are used to spread the navigation message and serve as the basic tool for measuring the transmission time from satellites to receiver. The signals broadcast by the different satellites are generally identified by different spreading sequences that are quasi-orthogonal. Quasi-orthogonality means that the cross-correlation between two different spreading sequences is almost zero. In this optic, GNSSs are Direct Sequence Code Division Multiple Access (DS/CDMA) systems. Examples of such systems are the GPS, the future European Galileo and the Chinese Compass. The Russian GLONASS adopts a Frequency Division Multiple Access (FDMA) system to differentiate the signals broadcast by the different satellites.

In Figure 2.1 the basic principles of DS/CDMA GNSSs can be summarized as follows: the signals broadcast by the different satellites are identified by means of different pseudo-random noises (PRN). The PRNs are the sequences used to spread the transmitted signals. The time needed by the transmitted signal to reach the receiver is estimated by exploiting the correlation properties of the spreading sequences. An overview on DSSS and CDMA can be found in [31] and the analysis of these techniques in the context of GNSS is better reviewed in [2–4, 32].

In this chapter the signal model for DS/CDMA GNSSs is introduced. This model is simplified in different ways allowing a first analysis of the acquisition performance and a characterization of the acquisition process. Some simplifications adopted in this chapter will be progressively removed in the next chapters and in particular in Chapter 6.

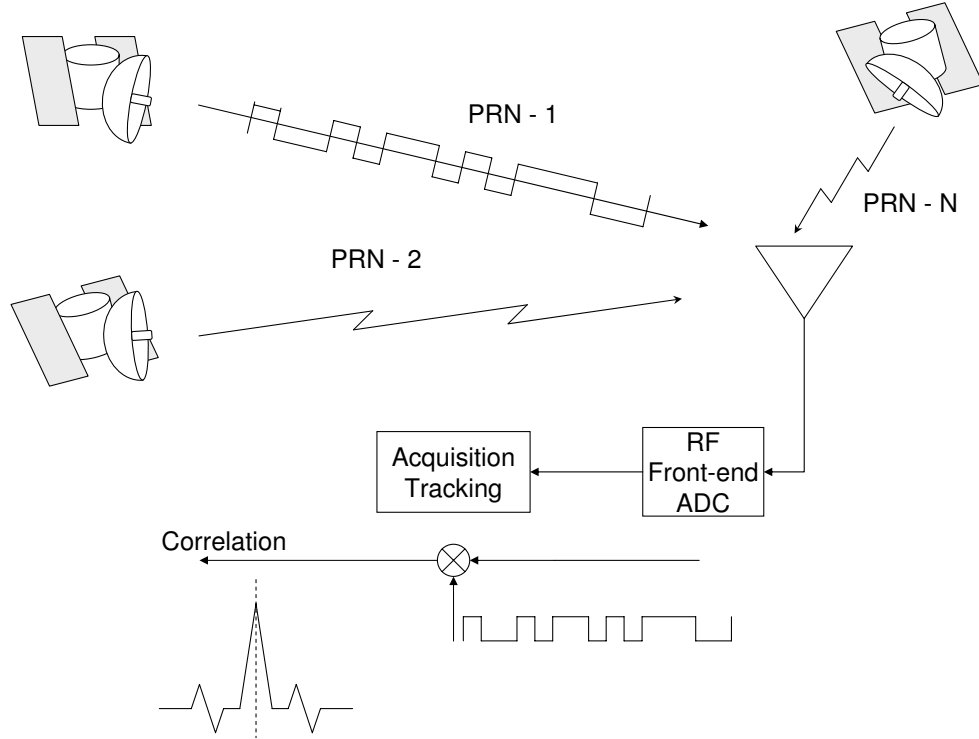


Figure 2.1. Basic principles of DS/CDMA GNSSs: the signals broadcast by the different satellites are identified by means of different PRNs. The transit time is estimated by exploiting the correlation properties of the spreading sequences.

The signal at the input of a GNSS receiver, in a one-path additive Gaussian noise environment, can be written as

$$r_{RF}(t) = \sum_{i=1}^L y_{RF,i}(t) + \eta_{RF}(t), \quad (2.1)$$

that is the sum of L useful signals, broadcast by L different satellites, and a noise term $\eta_{RF}(t)$. The useful signals $y_{RF,i}(t)$ usually assume the following structure:

$$y_{RF,i}(t) = A_i c_i (t - \tau_{i,0}^a) d_i (t - \tau_{i,0}^a) \cos [2\pi (f_{RF} + f_{d,0}^i) t + \phi_{i,0}] \quad (2.2)$$

where

- A_i is the amplitude of the i -th useful signal,
- $\tau_{i,0}^a$ is the delay introduced by the communication channel,
- $f_{d,0}^i$ is the Doppler frequency affecting the i -th useful signal and $\phi_{i,0}$ is a random phase,

- f_{RF} is the carrier frequency and depends on the GNSS and on the band under analysis. For GPS L1 band $f_{RF} = 1575.42$ MHz,
- $c_i(t)$ is the spreading sequence and can be given by the product of different terms. $c_i(t)$ is assumed to take value in the set $\{-1, 1\}$,
- $d_i(t)$ is the navigation message.

The spreading sequence $c_i(t)$ can be expressed as

$$c_i(t) = c_{1,i}(t) c_{2,i}(t) s_{b,i}(t) \quad (2.3)$$

where $c_{1,i}(t)$ is the periodic repetition of the primary spreading code, $c_{2,i}(t)$ is the secondary code and $s_{b,i}(t)$ is the subcarrier signal. The subcarrier $s_{b,i}(t)$ is the periodic repetition of a basic wave that determines the spectral characteristics of $y_{RF,i}(t)$. Two examples of subcarrier signals are the Binary Phase Shifting Key (BPSK) and the Binary Offset Carrier BOC(1,1). The basic waves that generate those subcarriers are shown in Figure 2.2. The BPSK is adopted by the GPS Coarse Acquisition (C/A) and consists in a constant pulse of duration T_h . The periodic repetition of the BPSK basic wave leads to $s_{b,i}(t) = 1$. With the advent of new GNSSs, such as the European Galileo, the Chinese

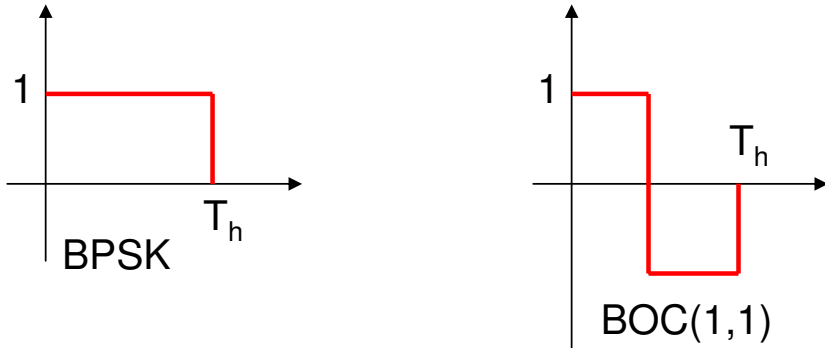


Figure 2.2. Examples of basic pulses generating the subcarrier signals.

Compass and the modernized GPS, more complex modulations than the one described by Eq. (2.2) have been adopted. Some of those modulations will be discussed in Chapter 7.

The term $\eta_{RF}(t)$ is assumed to be Additive White Gaussian Noise (AWGN) with power spectral density (PSD) $\frac{N_0}{2}$. Each useful signal $y_{RF,i}(t)$ is characterized by power

$$C_i = \frac{A_i^2}{2} \quad (2.4)$$

and the overall signal quality is quantified by the carrier power-to-noise-density ratio C_i/N_0 .

The input signal (2.1) is recovered by the receiver antenna, downconverted and filtered by the receiver front-end. In this way the received signal, before the Analog to Digital (AD) conversion, is given by

$$\begin{aligned} r(t) &= \sum_{i=1}^L y_i(t) + \eta(t) \\ &= \sum_{i=1}^L A_i \tilde{c}_i (t - \tau_{i,0}^a) d_i (t - \tau_{i,0}^a) \cos [2\pi (f_{IF} + f_{d,0}^i) t + \phi_{i,0}] + \eta(t) \end{aligned} \quad (2.5)$$

where f_{IF} is the receiver intermediate frequency. The term $\tilde{c}_i (t - \tau_{i,0}^a)$ represents the spreading sequence filtered by the frontend. At this point the simplifying condition

$$\tilde{c}_i(t) \approx c_i(t) \quad (2.6)$$

is assumed and the impact of the frontend filter is neglected. $\eta(t)$ is the down-converted and filtered noise component.

Finally Eq. (2.5) is sampled and digitalized. Neglecting the quantization impact, the following signal model is obtained:

$$\begin{aligned} r(nT_s) &= \sum_{i=1}^L y_i(nT_s) + \eta(nT_s) \\ &= \sum_{i=1}^L A_i \tilde{c}_i (nT_s - \tau_{i,0}^a) d_i (nT_s - \tau_{i,0}^a) \cos [2\pi (f_{IF} + f_{d,0}^i) nT_s + \phi_{i,0}] + \eta(nT_s) \end{aligned} \quad (2.7)$$

In the following, the notation $x[n] = x(nT_s)$ will indicate a discrete-time sequence $x[n]$, obtained by sampling a continuous-time signal $x(t)$ with a sampling frequency $f_s = 1/T_s$. For this reason Eq. (2.7) can be rewritten as

$$\begin{aligned} r[n] &= \sum_{i=1}^L y_i[n] + \eta[n] \\ &= \sum_{i=1}^L A_i \tilde{c}_i [n - \tau_{i,0}^a/T_s] d_i [n - \tau_{i,0}^a/T_s] \cos [2\pi (f_{IF} + f_{d,0}^i) nT_s + \phi_{i,0}] + \eta[n] \\ &= \sum_{i=1}^L A_i \tilde{c}_i [n - \tau_{i,0}] d_i [n - \tau_{i,0}] \cos [2\pi F_{D,0}^i n + \phi_{i,0}] + \eta[n] \end{aligned} \quad (2.8)$$

where $F_{D,0}^i = (f_{IF} + f_{d,0}^i) T_s$ and $\tau_{i,0} = \tau_{i,0}^a/T_s$.

The spectral characteristics of $\eta[n]$ depend on the type of filtering along with the sampling

and decimation strategy adopted in the front-end. A convenient choice is to sample the IF signal with a sampling frequency $f_s = 2B_{IF}$, where B_{IF} is the front-end bandwidth. In this case, it is easily shown that the noise variance becomes

$$\sigma_{IF}^2 = \text{E}\{\eta^2(t)\} = \text{E}\{\eta^2(nT_s)\} = N_0 f_s / 2 = N_0 B_{IF} \quad (2.9)$$

The autocorrelation function

$$R_{IF}[m] = \text{E}\{\eta[n]\eta[n+m]\} = \sigma_{IF}^2 \delta[m]$$

implies that the discrete-time random process $\eta[n]$ is a classical independent and identically distributed (iid) wide sense stationary (WSS) random process, or a white sequence. $\delta[m]$ is the Kronecker delta.

As a result of code orthogonality, the different useful GNSS signals are analyzed separately by the receiver, and thus the case of a single satellite is considered and the index i is dropped. The resulting signal is

$$r[n] = y[n] + \eta[n] = A\tilde{c}[n - \tau_0] d[n - \tau_0] \cos[2\pi F_{D,0}n + \phi_0] + \eta[n] \quad (2.10)$$

Chapter 3

GNSS signal acquisition

3.1 Basic concepts

The first operation performed by a GNSS receiver is the signal acquisition that decides either the presence or the absence of the signal under test and provides a rough estimation of the code delay and of the Doppler frequency of the incoming signal. The acquisition system implements some well-known results of the detection and estimation theory and different logical and functional blocks take part in the process. In the GNSS literature the exact role of these disciplines and of these functional blocks is sometimes unclear. In this chapter a general acquisition system is described as the interaction of four functional blocks that perform four different logical operations. The framework developed by using these four elements allows one to describe the majority of the acquisition systems, providing an effective tool for comparative analysis. All the acquisition systems for GNSS applications described in literature [2,4,32,33] are based on the evaluation and processing of the Cross Ambiguity Function (CAF) that, in the discrete time domain, can be defined as

$$Y(\tau, F_D) = \frac{1}{N} \sum_{n=0}^{N-1} r[n] c[n - \tau] \exp \{-j2\pi F_D n\} \quad (3.1)$$

where $r[n]$ is the received signal, $c[n - \tau]$ the local replica reproducing the PRN code, the subcarrier and potentially the secondary code. τ and F_D are the code delay and the Doppler frequency tested by the receiver. Eq. (3.1) will be further discussed in following sections.

Ideally the CAF should present a sharp peak that corresponds to the values of τ and F_D matching the delay and the Doppler frequency of the SIS. However the phase of the incoming signal, the noise and other impairments can degrade the readability of the CAF in which case further processing is needed. For instance, in a non-coherent acquisition block only the envelope of the CAF is considered, avoiding the phase dependence. Moreover

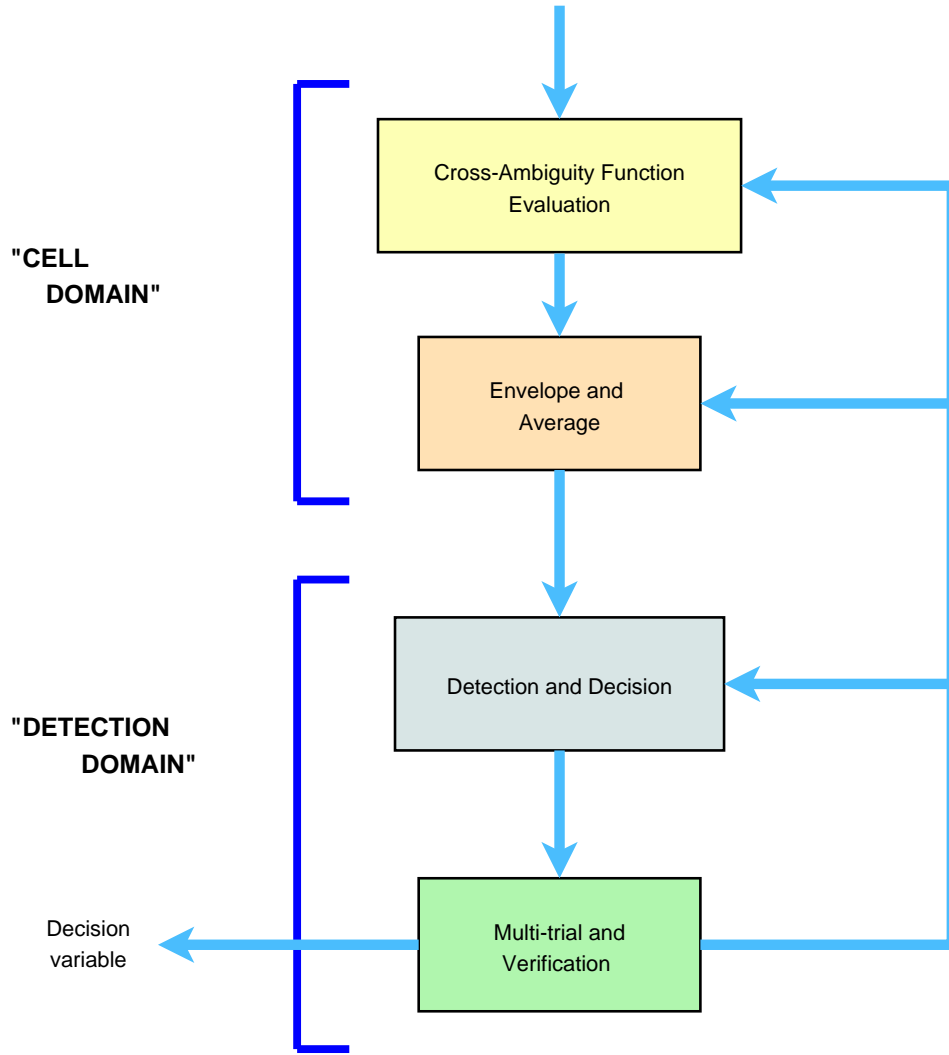


Figure 3.1. Conceptual representation of the acquisition process. GNSS acquisition is composed of different steps that, starting from the input signal, lead to the final decision and to a rough estimation of the Doppler frequency and code delay.

coherent and non-coherent integrations can be employed in order to reduce the noise impact.

When the envelope of the averaged CAF is evaluated, the system can make a decision on the presence of the satellite. Different detection strategies can be employed. Some strategies are only based on the partial knowledge of the CAF and interactions among the different acquisition steps may be required. The detection can be further enhanced

by using multi-trial techniques that require the use of CAFs evaluated on subsequent portions of the incoming signal.

In Figure 3.1 the general scheme of an acquisition system is depicted, highlighting the presence of the four functional blocks:

- **CAF evaluation,**
- **Envelope and Average,**
- **Detection and Decision,**
- **Multitrial and Verification.**

The first two stages are devoted to the evaluation of the CAF (3.1) and to improve its readability. The last two determine the signal presence and verify if the decision that has been taken is correct. The different stages are strictly interconnected and each layer can require further processing from the previous levels. These interactions are depicted in Figure 3.1. The four blocks are discussed below.

3.2 CAF evaluation

The first stage of the acquisition block consists in the evaluation of the CAF of Eq. (3.1). More in details the received signal $r[n]$ is multiplied by two orthogonal sinusoids at the frequency $F_D = (f_{IF} + f_d) T_s$. In this way two new signals are generated:

$$\begin{aligned} Y_c(n, F_D) &= r[n] \cos(2\pi F_D n) \\ Y_s(n, F_D) &= -r[n] \sin(2\pi F_D n). \end{aligned} \quad (3.2)$$

The multiplication by these two orthogonal sinusoids is aimed at translating in baseband the received signal, removing the effect of the Doppler shift. These multiplications correspond to the complex modulation of Eq. (3.1) that is implemented in GNSS receivers by splitting the incoming signal in two branches and separately multiplying them by cosine and sine. The normalized frequency

$$F_D = (f_{IF} + f_d) T_s = \frac{f_{IF} + f_d}{f_s}$$

is given by two terms:

- the intermediate frequency, f_{IF} ,
- the local Doppler frequency f_d .

The intermediate frequency f_{IF} is known and depends on the receiver architecture [32, 33], whereas f_d is chosen from a finite set of the type:

$$f_d = f_{d,\min} + l\Delta f \quad \text{for } l = 0, 1, \dots, L - 1. \quad (3.3)$$

Different Doppler frequencies are tested in order to determine the Doppler shift of the incoming signal. For low dynamic applications, $-5 \text{ KHz} \leq f_d \leq 5 \text{ KHz}$ [2]. The Doppler step Δf and its normalized counterpart $\Delta F = \Delta f / f_s$ are chosen in order not to exceed a maximum loss due to Doppler residual errors, as discussed in Section 6.3.

The signals $Y_c(n, F_D)$ and $Y_s(n, F_D)$ are then multiplied by a local signal replica that reproduces the primary PRN code $c_1[n]$, the subcarrier $s_b[n]$ and potentially the secondary code $c_2[n]$. The local signal replica is delayed by τ and the signals

$$\begin{aligned} Y'_c(n, \tau, F_D) &= r[n] \cos(2\pi F_D n) c[n - \tau] \\ Y'_s(n, \tau, F_D) &= -r[n] \sin(2\pi F_D n) c[n - \tau] \end{aligned} \quad (3.4)$$

are obtained. The delay τ is taken from a set

$$\tau = \tau_{\min} + h\Delta\tau \quad \text{for } h = 0, 1, \dots, H - 1. \quad (3.5)$$

By testing the different delays, the acquisition block is able to estimate the delay of the received signal $r[n]$.

The signals $Y'_c(n, \tau, F_D)$ and $Y'_s(n, \tau, F_D)$ are then integrated, leading to the in-phase and quadrature components $Y_I(\tau, F_D)$ and $Y_Q(\tau, F_D)$:

$$\begin{aligned} Y_I(\tau, F_D) &= \frac{1}{N} \sum_{n=0}^{N-1} Y'_c(n, \tau, F_D) \\ Y_Q(\tau, F_D) &= \frac{1}{N} \sum_{n=0}^{N-1} Y'_s(n, \tau, F_D). \end{aligned} \quad (3.6)$$

In Eq. (3.6), N represents the number of samples used for evaluating the in-phase and quadrature components and is used to define the **coherent integration time**:

$$T_c = NT_s \quad (3.7)$$

that is usually chosen as a multiple of the primary PRN code period. In general, H can be different from N since only a subset of all possible delays can be tested.

The two components of Eq. (3.6) represent the real and the imaginary parts of the CAF that is finally given by

$$Y(\tau, F_D) = Y_I(\tau, F_D) + jY_Q(\tau, F_D) \quad (3.8)$$

and that corresponds to Eq. (3.1).

In Figure 3.2, the operations previously described are highlighted. The CAF is a bi-

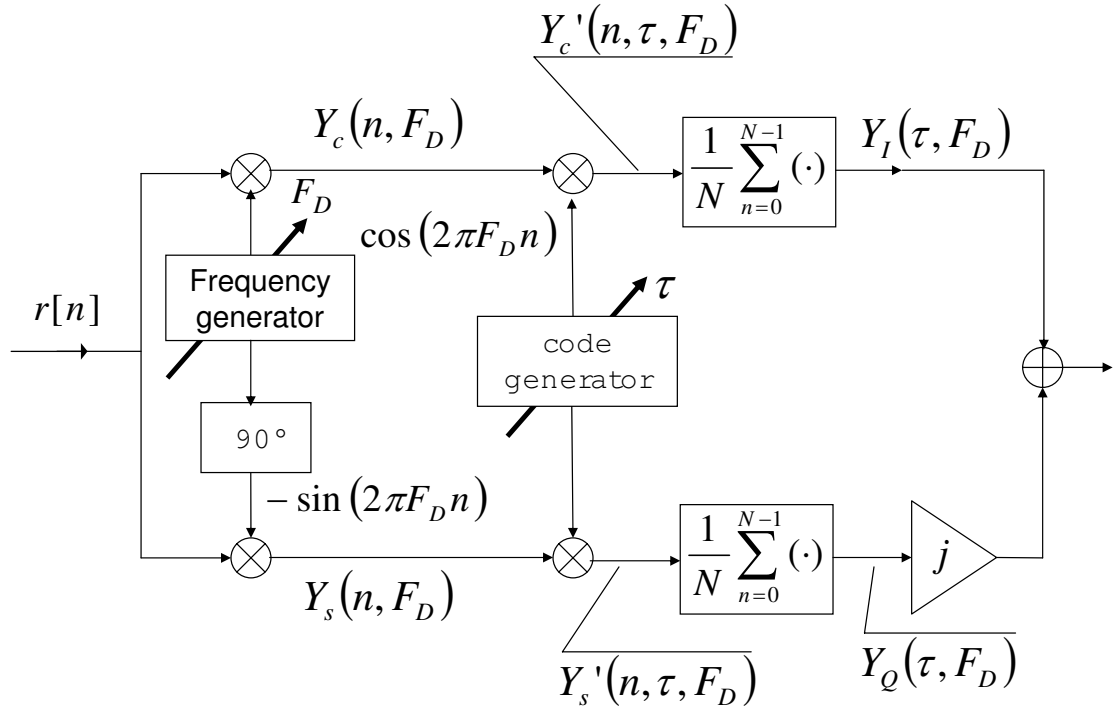


Figure 3.2. Conceptual scheme for the evaluation of the Cross Ambiguity Function (CAF). The received signal is multiplied by two orthogonal sinusoids and a local signal replica. The resulting signals are then integrated, generating the real and imaginary parts of the CAF.

dimensional function that depends on the Doppler frequency F_D and on the delay τ . Since both F_D and τ are evaluated on the discrete sets represented by Eqs. (3.3) and (3.5), the CAF results defined over a bi-dimensional grid that is usually referred to as the **search space**. Each value of F_D and τ defines a **cell** of the search space, that is in general, a random variable to be used for deciding the presence of the useful signal.

Since at the “CAF evaluation” and “Envelope and Average” stages the cells of the search space are processed separately, those two blocks are said to work in the **cell domain**, in contrast with the last two blocks of Figure 3.1 that operate in the **decision domain**. In the decision domain a function of possibly all the search space cells is used to determine the final acquisition decision.

3.2.1 CAF evaluation methods

In the acquisition systems described in the literature different methods of evaluating the CAF are presented. They give the same (or approximately the same) results and the choice of the method mainly depends on the hardware and software tools available for the receiver implementation. In the following a macro classification of classical acquisition methods is described.

3.2.2 Method 1: Serial scheme

In this scheme a new CAF is evaluated at each instant n . The input vector $\mathbf{r} = [r[0], r[1], \dots, r[N - 1]]$ can be updated instant by instant by adding a new input value and by discarding the former one. To avoid ambiguity in this case, the notation $\mathbf{r}_n = [r[n] r[n - 1] \cdots r[n - N + 1]]$ will be adopted. With this approach the delay τ moves throughout the vector \mathbf{r}_n at each new instant. Therefore the local code $c[n]$ is always the same and the CAF is given by the expression

$$Y(\tau, F_D) = \frac{1}{N} \sum_{m=0}^{N-1} r[\tau - N + m + 1] c[m] \exp\{-j2\pi F_D m\} \quad (3.9)$$

It is quite easy to verify that this approach is equivalent to moving the delay of $c[n]$ as the mutual delay between $c[n]$ and the received code is the unknown quantity of interest.

3.2.3 Method 2: parallel acquisition in the time domain

In this scheme the vector \mathbf{r} is extracted by the incoming SIS and multiplied by $\exp\{-j2\pi F_D n\}$, obtaining the sequence

$$q_l[n] = r[n] \exp\{-j2\pi F_D n\} \quad (3.10)$$

for each frequency bin. At this point the term

$$Y(\tau, F_D) = \frac{1}{N} \sum_{n=0}^{N-1} q_l[n] c[n - \tau] \quad (3.11)$$

assumes the form of a Cross-Correlation Function (CCF), which can be evaluated by means of a circular cross-correlation defined by

$$\tilde{Y}(\tau, F_D) = \frac{1}{N} \text{IDFT}\{\text{DFT}[q_l[n]] \text{DFT}[c[n]]^*\} \quad (3.12)$$

where DFT and IDFT stand for the well-known Discrete Fourier Transform and Inverse Discrete Fourier Transform. It is easy to show that the CCF and the circular CCF coincide only in presence of periodic sequences. This is the case when $F_D = F_{D,0}$, except for the noise contribution and a residual term due to a double frequency $2F_D$ component contained in the term $q_l[n]$. In the other frequency bins, the presence of a sinusoidal component could alter the periodicity of the sequence.

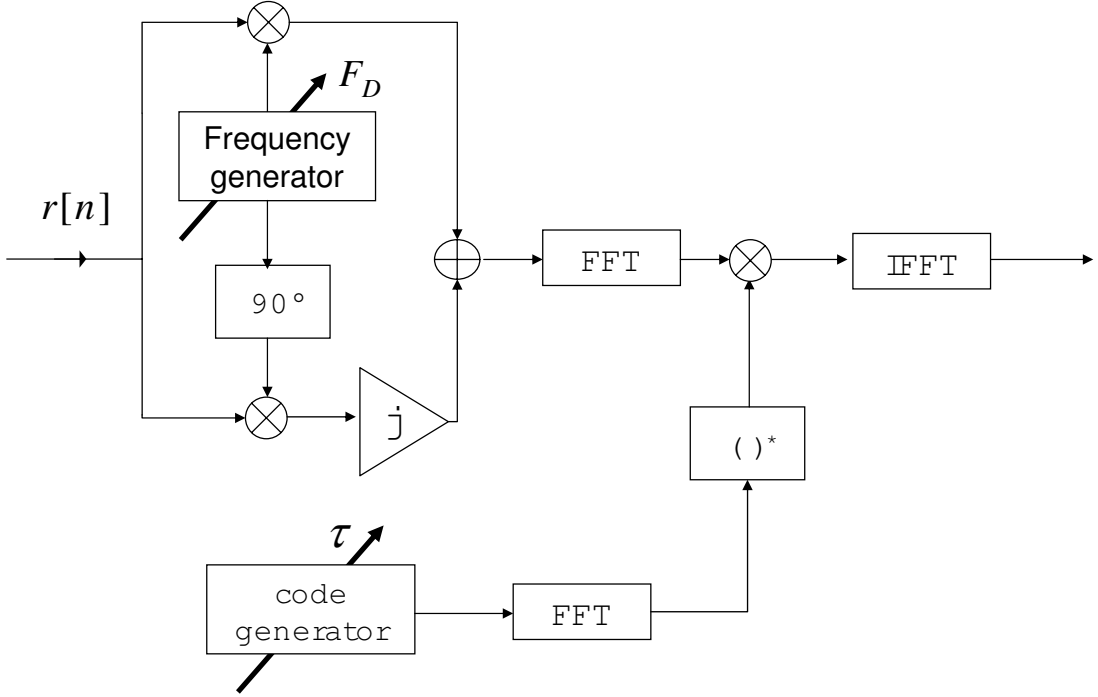


Figure 3.3. Time parallel acquisition scheme: the CAF is determined by using a circular convolution employing efficient FFT's.

3.2.4 Method 3: FFT in the Doppler domain

In this scheme the vector \mathbf{r} can be extracted by the incoming SIS instant by instant, as in the method 1, and multiplied by $c[n]$, obtaining the sequence

$$q_i[m] = r[\tau - N + 1 + m]c[m] \quad (3.13)$$

for each delay bin. A similar result can be obtained by extracting an input vector \mathbf{r} every N samples, and multiplying it by a delayed version of the local code $c[n]$. As mentioned before, this delay is obtained by applying a circular shift to the samples of $c[n]$. At this point the term

$$Y(\tau, F_D) = \frac{1}{N} \sum_{m=0}^{N-1} q_i[m] \exp \{-j2\pi F_D m\} \quad (3.14)$$

assumes the form of a Discrete-Time Fourier Transform (DTFT). It is well known that a DTFT can be evaluated by using a Fast Fourier Transform (FFT) if the normalized frequency F_D is discretized with a frequency interval

$$\Delta F = \frac{1}{N}$$

in the frequency range $(0,1)$, which corresponds to the analog frequency range $(0, f_s)$. The evaluated frequency points become

$$f_d T_s = \frac{l}{N} - f_{IF} T_s$$

and the CAF can be written as

$$S(\tau, F_D) = \frac{1}{N} \sum_{m=0}^{N-1} q_i[m] \exp \left\{ -j \frac{2\pi}{N} l m \right\} \quad (3.15)$$

With this method the search space along the frequency axis and the frequency bin size depend on the sampling frequency f_s and on the integration time N . If the same support and bin size used in methods 1 and 2 are used, the integration time has to be changed, and some decimation (with pre-filtering) has to be adopted before applying the FFT. This modifies the input signal, degrading its quality and introducing some losses [34]. In Fig-

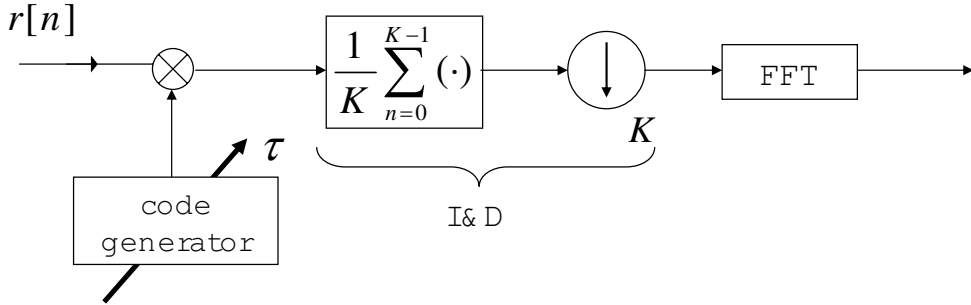


Figure 3.4. Frequency parallel acquisition scheme: the CAF is evaluated by using efficient FFT.

ure 3.4 the frequency domain acquisition block is reported. An “integrate and dump” block followed by a decimation unit is inserted in order to reduce the number of samples on which the FFT is evaluated. This operation reduces the computational load but introduces a loss in the CAF quality [34].

3.3 Envelope and Average

After having evaluated the CAF, the acquisition system has to remove the dependence on the input signal phase and apply noise reduction techniques. The simplest way of removing the dependence of the input signal phase is to consider the square absolute value of the CAF (3.1). In this case the cells of the search space assume the following

expression:

$$S(\tau, F_D) = \left| \frac{1}{N} \sum_{n=0}^{N-1} r[n] c[n - \tau] \exp \{-j2\pi F_D n\} \right|^2 \quad (3.16)$$

The noise reduction is performed by the integration blocks $\frac{1}{N} \sum_{n=0}^{N-1} (\cdot)$ before the envelope operation. This operation corresponds to averaging different CAFs before evaluating the envelope and this kind of averaging is called **coherent integration**. This kind of integration provides the best performance in terms of noise variance reduction. In fact before the envelope the noise terms are zero mean Gaussian random variables and the coherent integrations average elements that can be either positive or negative. In Figure

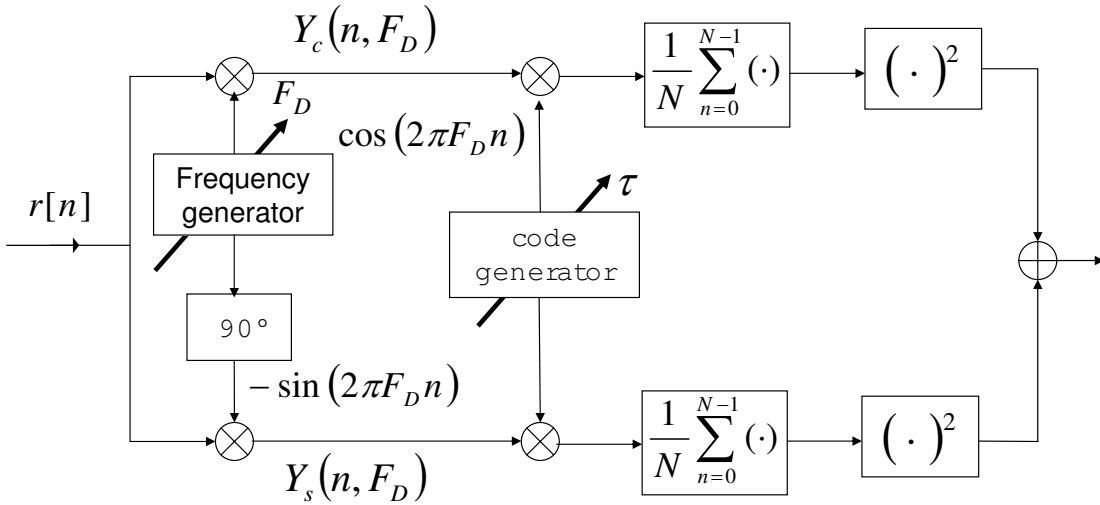


Figure 3.5. Scheme of the basic acquisition block. Only coherent integrations are used.

[3.5](#) the basic acquisition scheme, corresponding to the use of coherent integration only, is reported. The envelope is obtained by squaring and summing the in-phase and quadrature components. In this way $S(\tau, F_D)$ assumes the following expression:

$$S(\tau, F_D) = Y_I^2(\tau, F_D) + Y_Q^2(\tau, F_D) \quad (3.17)$$

Other integration techniques can be used to improve the quality of the search space and reduce the impact of input noise. Examples of these techniques are **non-coherent integration** and **differentially integration** that will be better discussed in Chapter [5](#).

3.4 Detection and Decision

Once $S(\tau, F_D)$ is evaluated, the system can make a decision regarding the presence of the satellite. Different strategies can be employed. The detection strategies can control the

previous blocks, for example, by requiring the computation of $S(\tau, F_D)$ only on a subset of the values of τ and F_D .

In Chapter 4, three different strategies are analyzed and compared in terms of system performance.

The introduction of the Galileo SIS does not essentially change the role of this block and the considerations described in Chapter 4 still apply.

3.5 Multi-trial and Verification

When a first decision about the satellite presence and a first estimation of the code delay and of the Doppler frequency are available, the system can refine the results. Thus multi-trial techniques, based on the use of different $S(\tau, F_D)$ and evaluated over subsequent portions of the input signal, can be employed. Two examples of these techniques are the M on N [2] and the Tong [2, 35] methods.

Multi-trial techniques generally do not require the computation of more than one complete $S(\tau, F_D)$, since they interact with the other blocks changing the requirements for the subsequent iterations occurring in the process.

3.6 Receiver Operating Characteristics

A general detection process consists in determining the presence of a desired signal from a set of noisy data [36]. A general detection process is depicted in Figure 3.6: the noisy input signal is processed and a decision variable derived. The decision variable is then used for establishing the presence of the desired signal. The input signal is characterized by an *input SNR*, that is the ratio between the desired signal and noise powers. The desired signal can be further degraded by the presence of additional impairments, such

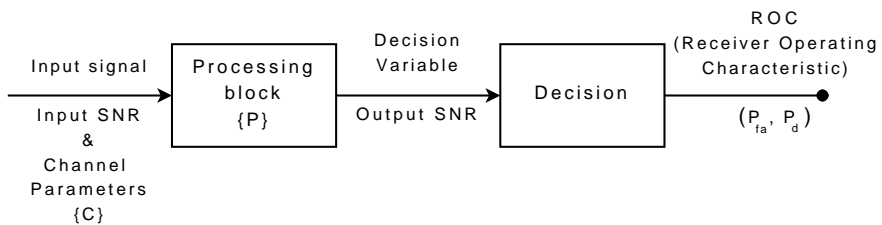


Figure 3.6. General detection scheme: the input signal is processed in order to produce a decision variable used for establishing the presence of a desired signal. $\{C\}$ is the set of parameters describing the channel impact on the desired signal whereas $\{P\}$ refers to the processing parameters. β is the decision threshold, while P_d and P_{fa} are the detection and the false alarm probabilities, respectively.

as clutter, fading and interference. All these impairments are accounted for by specific models [26, 37–39] and characterized by a set of parameters, $\{\mathbf{C}\}$, describing the channel responsible for the degradation of the useful signal.

The processing block is aimed at enhancing the desired signal by combining its samples and by exploiting a priori information available at the detector.

The acquisition block is at first a detection process aimed to determine the presence or absence of the signal transmitted by a specific satellite. In this sense an acquisition block can be characterized by the same parameters adopted to characterize a general detector. The aim of this and of the next section is the introduction of the basic tools for characterizing a detection process and thus the acquisition block. Different processing techniques can be adopted, such as coherent, non-coherent [40–42] and differentially non-coherent integrations [9, 10]. The processing block is characterized by the set of parameters $\{P\}$ that, for instance, may include the coherent integration time and the number of non-coherent integrations. The output of the processing block is a random variable, namely the decision variable, characterized by two probability density functions (pdf) referring to the presence or absence of the desired signal. These pdfs and, in particular, the corresponding complementary cumulative distributions, completely determine the detector performance. The probability that the decision variable passes a threshold β is called the detection probability if the desired signal is present, and false alarm probability if it is absent. The plot of the detection probability versus the false alarm probability is called the Receiver Operating Characteristic (ROC) [36, 43].

In the GNSS case the two conditions of signal presence and absence correspond to the two hypotheses:

- *the null hypothesis*, H_0 : the signal is not present or not correctly aligned with the local replica;
- *the alternative hypothesis*, H_1 : the signal is present and correctly aligned.

In particular the detection and the false alarm probabilities are defined as

$$P_{fa}(\beta) = P(X > \beta | H_0) = P(X > \beta | \tau \neq \tau_0 \cup F_D \neq F_{D,0}) \quad (3.18)$$

$$P_d(\beta) = P(X > \beta | H_1) = P(X > \beta | \tau = \tau_0 \cap F_D = F_{D,0}) \quad (3.19)$$

In Eqs. (3.18) and (3.19) a generic random variable X has been used. In Chapter 4 it is shown that two different sets of probabilities can be defined. The first one is related to the cell domain, whereas the second one is relative to the decision domain. In particular

$$X = \begin{cases} S(\tau, F_D) & \text{cell domain} \\ D & \text{decision domain} \end{cases} \quad (3.20)$$

The distinction between cell and decision probabilities and their relative role will be investigated in Chapter 4. In this section only cell probabilities are considered and thus

$$X = S(\tau, F_D).$$

When only coherent integration is used, as in the scheme depicted in Figure 3.5, each cell of the search space is given by Eq. (3.16):

$$S(\tau, F_D) = \left| \frac{1}{N} \sum_{n=0}^{N-1} r[n] c[n - \tau] \exp \{-j2\pi F_D n\} \right|^2$$

$S(\tau, F_D)$ is obtained as the square absolute value of a complex Gaussian random variable with independent real and imaginary parts. Moreover

$$\begin{aligned} \text{Var}[Y_I(\tau, F_D)] &= \text{Var} \left[\Re \left\{ \frac{1}{N} \sum_{n=0}^{N-1} r[n] c[n - \tau] \exp \{-j2\pi F_D n\} \right\} \right] \\ &= \text{Var} \left[\frac{1}{N} \sum_{n=0}^{N-1} r[n] c[n - \tau] \cos(2\pi F_D n) \right] \\ &= \frac{1}{N^2} \sum_{n=0}^{N-1} \text{Var}[r[n] c[n - \tau] \cos(2\pi F_D n)] \\ &= \frac{1}{N^2} \sum_{n=0}^{N-1} \frac{\sigma_{IF}^2}{2} = \frac{\sigma_{IF}^2}{2N} \end{aligned} \quad (3.21)$$

Similarly

$$\begin{aligned} \text{Var}[Y_Q(\tau, F_D)] &= \text{Var} \left[\Im \left\{ \frac{1}{N} \sum_{n=0}^{N-1} r[n] c[n - \tau] \exp \{-j2\pi F_D n\} \right\} \right] \\ &= \text{Var} \left[\frac{1}{N} \sum_{n=0}^{N-1} r[n] c[n - \tau] \sin(2\pi F_D n) \right] \\ &= \frac{1}{N^2} \sum_{n=0}^{N-1} \text{Var}[r[n] c[n - \tau] \sin(2\pi F_D n)] \\ &= \frac{1}{N^2} \sum_{n=0}^{N-1} \frac{\sigma_{IF}^2}{2} = \frac{\sigma_{IF}^2}{2N} \end{aligned} \quad (3.22)$$

thus

$$\text{Var}[Y_I(\tau, F_D)] = \text{Var}[Y_Q(\tau, F_D)] = \sigma_n^2 \quad (3.23)$$

Under the null hypothesis H_0 , $\mathbb{E}[S(\tau, F_D)] = 0$ and thus

$$S(\tau, F_D) | H_0 = Y_I^2(\tau, F_D) + Y_Q^2(\tau, F_D) | H_0 \sim \text{Exp} \left(\frac{1}{2\sigma_n^2} \right) \quad (3.24)$$

i.e. $S(\tau, F_D) | H_0$ is exponentially distributed with parameter $\frac{1}{2\sigma_n^2}$. Eq. (3.24) can be proved by using basic properties of Gaussian random variables and of transformation of random

variables [44]. The pdf of $S(\tau, F_D) | H_0$ is given by

$$f_0(s) = \frac{1}{2\sigma_n^2} \exp \left\{ -\frac{s}{2\sigma_n^2} \right\} \quad (3.25)$$

and the probability of false alarm is

$$P_{fa}(\beta) = \int_{-\infty}^{+\infty} f_0(s) ds = \exp \left\{ -\frac{\beta}{2\sigma_n^2} \right\} \quad (3.26)$$

Under the alternative hypothesis H_1 , $Y_I(\tau, F_D)$ and $Y_Q(\tau, F_D)$ are no longer zero mean, and in particular:

$$\begin{aligned} \mathbb{E}[Y_I(\tau, F_D)] &= \mathbb{E} \left[\frac{1}{N} \sum_{n=0}^{N-1} r[n] c[n - \tau] \cos(2\pi F_D n) \right] \\ &= \frac{1}{N} \sum_{n=0}^{N-1} \mathbb{E}[y[n] + \eta[n]] c[n - \tau] \cos(2\pi F_D n) \\ &= \frac{1}{N} \sum_{n=0}^{N-1} y[n] c[n - \tau] \cos(2\pi F_D n) \end{aligned} \quad (3.27)$$

By using the signal model (2.10) and by assuming that $F_D = F_{D,0}$ and $\tau = \tau_0$, Eq. (3.27) becomes

$$\begin{aligned} \mathbb{E}[Y_I(\tau, F_D)] &= \frac{A}{N} \sum_{n=0}^{N-1} c^2[n - \tau_0] \cos(2\pi F_{D,0} n + \phi_0) \cos(2\pi F_{D,0} n) \\ &= \frac{A}{2N} \sum_{n=0}^{N-1} [\cos \phi_0 + \cos(4\pi F_{D,0} n + \phi_0)] \\ &= \frac{A}{2} \cos \phi_0 \end{aligned} \quad (3.28)$$

Eq. (3.28) has been evaluated by neglecting the quantization effect, the impact of the front-end filter and delay and frequency residual errors. The impact of these factors will be analyzed in Chapter 6.

Similarly $\mathbb{E}[Y_Q(\tau, F_D)]$ is given by

$$\mathbb{E}[Y_Q(\tau, F_D)] = \frac{A}{2} \sin \phi_0 \quad (3.29)$$

The variance of $Y_I(\tau, F_D)$ and $Y_Q(\tau, F_D)$ is not influenced by the presence of the useful signal that is considered as a deterministic component. Thus

$$\begin{aligned} Y_I(\tau, F_D) | H_1 &\sim \mathcal{N} \left(\frac{A}{2} \cos \phi_0, \frac{\sigma_{IF}^2}{2N} \right) \\ Y_Q(\tau, F_D) | H_1 &\sim \mathcal{N} \left(\frac{A}{2} \sin \phi_0, \frac{\sigma_{IF}^2}{2N} \right) \end{aligned} \quad (3.30)$$

The sum of the square of two non-zero mean independent Gaussian random variables leads to a non-central χ^2 random variable with two degrees of freedom [44]

$$S(\tau, F_D) | H_1 = Y_I^2(\tau, F_D) + Y_Q^2(\tau, F_D) | H_1 \sim \chi_{nc,2}^2(\lambda, \sigma_n^2) \quad (3.31)$$

where

$$\lambda = E^2[Y_I(\tau, F_D)] + E^2[Y_Q(\tau, F_D)] = \frac{A^2}{4} \quad (3.32)$$

is the non-centrality parameter.

The pdf of $S(\tau, F_D)$ under H_1 is given by

$$f_1(s) = \frac{1}{2\sigma_n^2} \exp\left\{-\frac{s+\lambda}{2\sigma^2}\right\} I_0\left(\frac{\sqrt{s\lambda}}{\sigma_n^2}\right) \quad (3.33)$$

where $I_0(\cdot)$ is the modified Bessel function of the first kind and zero order [45]. The detection probability is thus given by

$$P_d(\beta) = Q_1\left(\sqrt{\frac{\lambda}{\sigma_n^2}}, \sqrt{\frac{\beta}{\sigma_n^2}}\right) \quad (3.34)$$

where $Q_K(a,b)$ is the generalized Marcum Q-function [37, 46] defined as

$$Q_K(a,b) = \frac{1}{a^{K-1}} \int_b^{+\infty} x^K \exp\left\{-\frac{a^2+x^2}{2}\right\} I_{K-1}(ax) dx \quad (3.35)$$

In Figure 3.7, ROC curves for different values of C/N_0 are shown. The coherent integration time is limited to 1 ms.

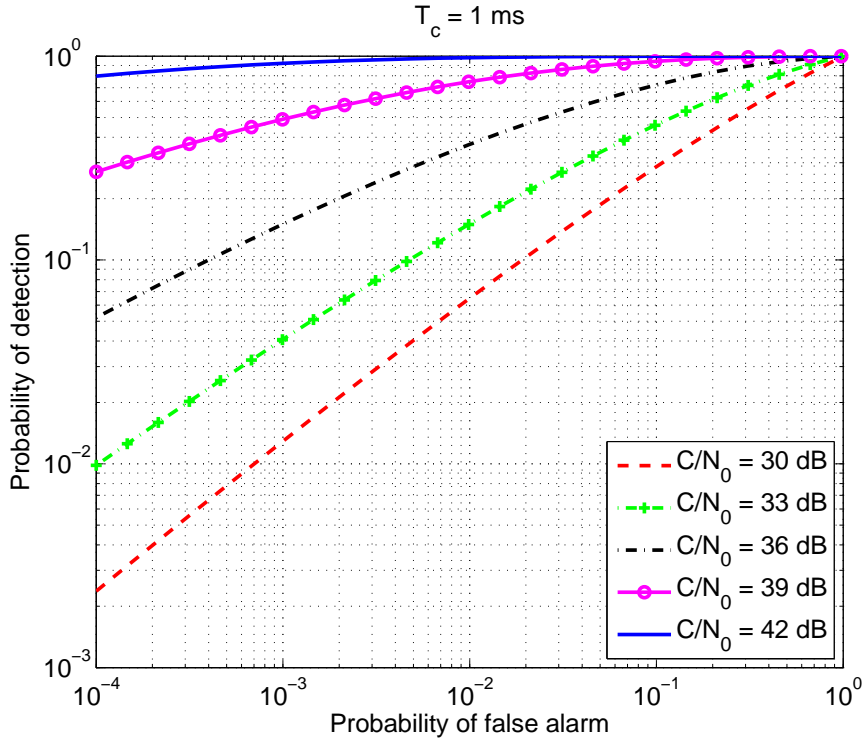


Figure 3.7. ROC curves for different values of C/N_0 . Basic acquisition scheme, 1 ms coherent integration time.

3.7 Coherent output SNR

Although the ROC completely characterizes the detector performance [43], it is often useful to have a single metric, *the output or equivalent coherent SNR*, which encapsulates as much information about the detector performance as possible. This parameter characterizes the quality of the cell random variable and, in some sense, summarizes the information carried by the ROC.

In general, determining the equivalent coherent SNR is a difficult problem, since a general acquisition block employs non-linear operations for increasing the quality of the decision variables and reducing the impact of phase and frequency errors and other signal impairments. Nonlinear operations mix the useful signal and noise components leading to cell and decision variables whose quality cannot be easily determined. The problem of quantifying the equivalent coherent SNR when non-coherent integrations are used has been thoroughly investigated in the literature and will be considered in Chapter 5.

When considering the basic acquisition scheme reported in Figure 3.5, one notices that all the operations before the squaring blocks are linear and thus the variables $Y_I(\tau, F_D)$ and $Y_Q(\tau, F_D)$ are Gaussian under the hypothesis that the input signal is also normally

distributed. The quality of the GNSS signal is usually measured at this stage [20, 21] by the so called *coherent output SNR*, defined as

$$\rho_c = \max_{\phi_0} \frac{\text{E}^2 [Y_I(\tau, F_D)]}{\text{Var}[Y_I(\tau, F_D)]} \quad (3.36)$$

By using Eqs. (3.28) and (3.21), the coherent output SNR, under ideal conditions, assumes the following expression

$$\begin{aligned} \rho_c &= \max_{\phi_0} \frac{A^2}{4} \frac{2N}{\sigma_{IF}^2} \cos^2 \phi_0 = \frac{A^2}{2} \frac{N}{\sigma_{IF}^2} = \frac{\lambda}{\sigma_n^2} \\ &= \frac{NC}{N_0 f_s / 2} = 2 \frac{C}{N_0} N T_s = 2 \frac{C}{N_0} T_c \end{aligned} \quad (3.37)$$

The ROC defined by Eqs. (3.26) and (3.34) is a parametric curve where the decision threshold β is only an intermediate parameter. Thus it is possible to operate the following change of variable

$$\beta' = \frac{\beta}{\sigma_n^2} \quad (3.38)$$

In this way the ROC can be parameterized with respect to β' , leading to the following expression:

$$\begin{cases} P_{fa}(\beta') = \exp \left\{ -\frac{\beta'}{2} \right\} \\ P_d(\beta') = Q_1 \left(\sqrt{\rho_c}, \sqrt{\beta'} \right) \end{cases} \quad (3.39)$$

From Eq. (3.39) it clearly emerges that, when only coherent integrations are used, the ROC only depends on ρ_c , the coherent output SNR. In this case the coherent output SNR completely characterizes the acquisition performance and corresponds to the equivalent coherent SNR.

The coherent output SNR represents a fundamental metric for characterizing the acquisition performance. In other words, the degradations due to quantization, front-end filtering and frequency and delay errors can be directly expressed in terms of losses affecting ρ_c . These degradations will be discussed in Chapter 6.

In Chapter 5 different integration strategies are considered. Also in these cases the coherent output SNR represents a fundamental parameter for quantifying the acquisition performance, however it is no longer sufficient for completely characterizing the acquisition block and additional parameters have to be introduced.

Chapter 4

Cell and decision probabilities

In Chapter 3 it was shown that acquisition is a complex process that requires several steps in order to provide a reliable decision variable that can be used for deciding the presence of the signal and providing a rough estimation of its Doppler frequency and code delay. Moreover, it has been recognized that GNSS acquisition is carried out in two different domains, the *cell domain* and the *decision domain*. Thus two different sets of probabilities, respectively related to the cell domain and to the decision domain, characterize the acquisition performance. The first set is relative to the search space cells that are random variables characterized by their pdfs. The cell pdfs depend on the techniques employed for evaluating the single cell and on the channel model considered. For instance the type of integration used for reducing the noise impact, coherent [2,5], non-coherent [40,42] and differentially non-coherent [9], and the presence or absence of fading [6,7], strongly impact the single cell probabilities. The second probability set refers to the decision statistic provided by the decision unit. In the rest of the thesis the first set of probabilities is called **cell probabilities** whereas the second one is called **decision probabilities**. These two sets are strongly dependent but they do not generally coincide. In the literature the role of cell probabilities is well assessed and different works analyze these probabilities [47,48]. Instead the decision probabilities are only marginally considered. The major texts in the GNSS literature [2,4,32] usually analyze only the cell probabilities, whereas the decision cells are completely ignored. The decision probabilities allow one to completely quantify the acquisition performance, since they do not only depend on the statistical properties of the CAF but also on the strategy adopted for the signal detection. Indeed two acquisition systems can have the same cell probabilities and one can have better performance than the other due to characterization by better decision probabilities. This chapter provides a complete framework for the analysis of decision probabilities, deriving their relationship with cell probabilities. The concept of decision probabilities is not new, for instance in [48,49], the correlation maximum-based strategy is thoroughly analyzed and

in [50, 51] the serial search technique is considered. However no explicit comparison between strategies is made and often the proposed models are not supported by simulation results. In [47] the serial search with double dwell decision and the maximum search technique are analyzed from the decision probabilities point of view. However only the case of Doppler absence is considered and miss-detection and false alarm probabilities are not studied.

Three acquisition algorithms are considered: the typical serial scheme, the maximum search technique and a hybrid strategy [34, 52], formed by the combination of the two other methods. The spread of GNSS receivers employing hybrid structures for signal acquisition is self-imposing because, with the advent of longer spreading codes, a full serial search would be too slow, while a full parallel search would be prohibitively expensive [53]. Furthermore the availability of digital techniques based on the FFT algorithm [54] allows a faster computation of the search space so that the development of hybrid algorithms is the natural consequence of the row-by-row structure of these techniques. The first part of the chapter establishes a theoretical model describing the relationship between cell and decision probabilities with the three considered acquisition strategies. In this context the cell probabilities are not specified and general formulas, independent from the search space computation method, are derived. In the second part, the theoretical model is tested by simulations. Surprisingly, it is shown that secondary phenomena, such as the imperfect code orthogonality and the presence of secondary correlation peaks, strongly impact the decision probabilities. These secondary phenomena are generally neglected in the literature [2, 4, 32], since their impact is not clearly observable at the cell probabilities level: the reported simulations allow a better understanding of their role in the acquisition performance. An enhanced model accounting these secondary phenomena has been proposed, finally establishing a good agreement with the theoretical formulas. The simulation tests have been also performed under unrealistic conditions in order to have a complete validation of the theoretical results and in order to clearly observe possible secondary effects.

4.1 Statistical model

Since the search space $S(\tau, F_D)$ is evaluated over a finite and discrete set of code delays and Doppler frequencies, $\tau = \tau_{\min} + h\Delta\tau$ and $f_d = f_{d,\min} + l\Delta f$, it can be represented as a matrix of random cells X_n with $n = 1, 2, \dots, M = HL$. Therefore, the basic elements of the system performance evaluation are the detection and false alarm probabilities of a single cell, hereinafter indicated respectively as P_d and P_{fa} , and also known as single-trial [2] probabilities. The cells X_n are distributed according to

$$X_n | H_0 \sim f_{X_n}(x) \quad (4.1)$$

under the null hypothesis H_0 that is verified when the local code delay or the local Doppler shift do not match the input signal ones. The false alarm probability on a *single cell* is given by

$$P_{fa}(\beta) = \int_{\beta}^{+\infty} f_{X_n}(x)dx \quad (4.2)$$

where β is a preassigned threshold. The alternative hypothesis H_1 implies perfect code and Doppler shift alignment and the corresponding random variable is distributed according to

$$X_n|H_1 \sim f_A(x) \quad (4.3)$$

thus the cell detection probability is given by

$$P_d(\beta) = \int_{\beta}^{+\infty} f_A(x)dx \quad (4.4)$$

Even if single cell statistics play a fundamental role in determining the overall performance, the acquisition decision is taken on the basis of the whole search space. In particular a decision strategy is usually adopted and a decision statistic is derived from the whole search space. Thus the acquisition performances are strongly dependent on the decision statistic and the *overall detection* and the *overall false alarm probabilities*, denoted P_D (detection) and P_{FA} (false alarm) should be evaluated.

In the next sections, the expression of P_D and P_{FA} are derived for the main searching strategies described in literature, adopting the following assumptions:

- The alternative hypothesis H_1 is verified only in one single cell. This means that if the Doppler shift and the code delay are rightly compensated on the n -th cell, only the n -th random variable is affected by this condition, being distributed according to $f_A(x)$, whereas the adjacent cells still remain distributed according to $f_{X_n}(x)$. This condition corresponds to the assumption that the principal lobe of the correlation function is tight enough to influence one cell only. The random cell verifying H_1 will be denoted by X_A .
- Only one random variable X_A is present in the search space.
- The variable X_A can be in any cell with a uniform probability $\frac{1}{M} = \frac{1}{LH}$.
- All the random cells of the search space are assumed to be statistically independent. This condition is justified in Appendix B.

Note that the probabilistic model of the searching process does not depend on the specific expressions for $f_{X_n}(x)$ and $f_A(x)$: these distributions depend on how the ambiguity function is evaluated over the search space, on the integration time and on the type of averaging.

4.1.1 Searching strategies

In the acquisition process different strategies can be adopted in order to explore the search space more or less quickly and with a minor or greater accuracy. In this section three strategies are considered.

- 1) **Maximum:** the CAF is evaluated all over the search space, for each value of Doppler shift and code delay. Then the decision is taken only on the maximum of the ambiguity function. If the maximum's value is greater than the imposed threshold β , the satellite is considered acquired and the estimated Doppler shift and code delay are those corresponding to the maximum position.
- 2) **Serial:** this strategy consists in serially evaluating the ambiguity function cell by cell. Once a value is obtained, it is immediately compared with the threshold and the acquisition process stops at the first threshold crossing. The estimated Doppler shift and code delay are those corresponding to the position of the cell under test. In this way, on average, only half of the search space cells is evaluated.
- 3) **Hybrid:** the ambiguity function is evaluated row-by-row (or column-by-column), exploiting, for example, FFT-based algorithms, and the decision is taken on the maximum of each row (column). The acquisition process terminates as soon as the maximum in the current row (column) exceeds the threshold.

4.2 Detection probability

This section is devoted to the evaluation of the decision detection probability P_D for the three strategies described in previous section.

4.2.1 Maximum search strategy

When the maximum search strategy is employed, a right detection is obtained when X_A assumes the maximum value of the search space and it passes the threshold β ; then $P_D(\beta)$ can be written as

$$P_D(\beta) = P \left(X_A = \max_n \{X_n\}, X_A > \beta \right) \quad (4.5)$$

By definition X_A is maximum only if it is greater than or equal to all the other random variables. The equality condition is verified only when the X_n under test coincides with X_A (in this case X_n is another “name” of X_A), then

$$P(X_A = X_n) = \begin{cases} 1 & \text{when } X_A \equiv X_n \\ 0 & \text{otherwise} \end{cases} \quad (4.6)$$

and thus P_D can be written as

$$P_D(\beta) = P(X_A \geq X_1, X_A \geq X_2, \dots, X_A \geq X_{M-1}, X_A \geq X_M, X_A > \beta)$$

By using the theorem of the total probability in the case of continuous random variables, P_D can be expressed as

$$\begin{aligned} P_D(\beta) &= \int_{\beta}^{+\infty} P(X_A \geq X_1, X_A \geq X_2, \dots, X_A \geq X_{M-1}, X_A \geq X_M | X_A = x) f_A(x) dx \\ &= \int_{\beta}^{+\infty} P(X_A \geq X_1 | X_A = x) \cdots P(X_A \geq X_M | X_A = \beta) f_A(x) dx \\ &= \int_{\beta}^{+\infty} \prod_{n=1}^M P(X_A \geq X_n | X_A = x) f_A(x) dx \end{aligned} \quad (4.7)$$

In the last product all the terms are equal, except the one corresponding to the case $X_A \equiv X_n$. So there are $M - 1$ terms of the type

$$P(X_A \geq X_n | X_A = x) = P(X_n < x | H_0) = 1 - P(X_n > x | H_0) = 1 - P_{fa}(x) \quad (4.8)$$

and one equal to

$$P(X_A \geq X_n | X_A = x) = P(x \geq x | X_A = x) = 1 \quad (4.9)$$

The detection probability becomes

$$P_D(\beta) = \int_{\beta}^{+\infty} [1 - P_{fa}(x)]^{M-1} f_A(x) dx \quad (4.10)$$

Notice that if $P_{fa}(\beta)$ is small enough, Eq. (4.10) reduces to

$$P_D(\beta) \approx \int_{\beta}^{+\infty} f_A(x) dx \quad (4.11)$$

4.2.2 Serial search technique

In the serial strategy the detection probability is given by

$$\begin{aligned} P_D(\beta) &= P(X_A \text{ in cell 1}, X_1 > \beta) + \\ &\quad P(X_A \text{ in cell 2}, X_2 > \beta, X_1 < \beta) + \\ &\quad P(X_A \text{ in cell 3}, X_3 > \beta, X_1 < \beta, X_2 < \beta) + \\ &\quad \dots \\ &\quad P(X_A \text{ in cell M}, X_M > \beta, X_1 < \beta, X_2 < \beta, \dots, X_{M-1} < \beta) \end{aligned} \quad (4.12)$$

Analyzing the different terms in Eq. (4.12) it follows that

- $P(X_A \text{ in cell 1}, X_1 > \beta) = P(X_A \text{ in cell 1})P(X_A > \beta) = \frac{1}{M} \int_{\beta}^{+\infty} f_A(x)dx$
- $$\begin{aligned} P(X_A \text{ in cell 2}, X_2 > B, X_1 < \beta) &= P(X_A \text{ in cell 2})P(X_A > \beta)P(X_1 < \beta) \\ &= \frac{1}{M} \int_{\beta}^{+\infty} f_A(x)dx [1 - P_{fa}(\beta)] \end{aligned}$$
- $$\begin{aligned} P(X_A \text{ in cell 3}, X_3 > \beta, X_1 < \beta, X_2 < \beta) &= P(X_A \text{ in cell 3})P(X_A > \beta)P(X_1 < \beta)P(X_2 < \beta) \\ &= \frac{1}{M} \int_{\beta}^{+\infty} f_A(x)dx [1 - P_{fa}(\beta)]^2 \end{aligned}$$

The other terms in the summation are obtained in the same way, and Eq. (4.12) becomes

$$P_D(\beta) = \frac{1}{M} \int_{\beta}^{+\infty} f_A(x)dx \sum_{n=0}^{M-1} [1 - P_{fa}(\beta)]^n \quad (4.13)$$

and, after manipulations,

$$P_D(\beta) = \frac{1}{M} \frac{1 - [1 - P_{fa}(\beta)]^M}{P_{fa}(\beta)} \int_{\beta}^{+\infty} f_A(x)dx \quad (4.14)$$

Also in this case, for $P_{fa}(\beta) \ll 1$ Eq. (4.14) becomes

$$P_D(\beta) \approx \frac{1 - [1 - MP_{fa}(\beta)]}{MP_{fa}(\beta)} \int_{\beta}^{+\infty} f_A(x)dx = \int_{\beta}^{+\infty} f_A(x)dx \quad (4.15)$$

4.2.3 Hybrid search

By proceeding in the same way as the two previous cases the overall detection probability results in

$$P_D(\beta) = \frac{1}{L} \frac{1 - [1 - P_{fa}(\beta)]^M}{1 - [1 - P_{fa}(\beta)]^H} \int_{\beta}^{+\infty} [1 - P_{fa}(x)]^{H-1} f_A(x)dx \quad (4.16)$$

where H is the number of code bins.

Also in this case, for small values of $P_{fa}(\beta)$ the approximation

$$P_D(\beta) \approx \int_{\beta}^{+\infty} f_A(x)dx \quad (4.17)$$

holds.

4.3 Miss-detection probability

A miss-detection occurs when the satellite is present but it is not detected. This happens when no cell value exceeds the threshold, corresponding to the event that all the random variables X_n are lower than the threshold β . Since the threshold is never reached, the ambiguity function is evaluated in all cells. Therefore, the miss-detection probability is the same for the three cases and is given by

$$P_{MD}(\beta) = \prod_{n=1}^M P(X_n < \beta) \quad (4.18)$$

where

$$P(X_n < \beta) = \begin{cases} 1 - P_d(\beta) & \text{when } X_A \equiv X_n \\ 1 - P_{fa}(\beta) & \text{when } X_A \neq X_n \end{cases} \quad (4.19)$$

and $P_d(\beta) = \int_{\beta}^{+\infty} f_A(x)dx$ is the single cell detection probability. The miss-detection probability becomes

$$P_{MD}(\beta) = [1 - P_d(\beta)] \prod_{n=1}^{M-1} [1 - P_{fa}(\beta)] = [1 - P_{fa}(\beta)]^{M-1} [1 - P_d(\beta)] \quad (4.20)$$

and therefore

$$P_{MD}(\beta) = [1 - P_{fa}(\beta)]^{M-1} \int_0^{\beta} f_A(x)dx \quad (4.21)$$

4.4 False alarm probabilities

A false alarm occurs when the detection output is wrong (wrong satellite or wrong delay or Doppler shift), corresponding to the event that a noise cell exceeds the threshold. While the cell false alarm probability is by definition an absence of signal, the decision false alarm probability changes depending whether the signal is present or not. In order to avoid confusion, the decision false alarm probabilities will be designed hereinafter as P_{FA}^a (absence) and P_{FA}^p (presence). The case of signal absence is analyzed first.

- **Maximum.** With this strategy, a wrong detection happens when the maximum exceeds B ; then the system false alarm probability P_{FA}^a becomes

$$\begin{aligned} P_{FA}^a(\beta) &= P\left(\max_n(X_n) > \beta\right) = 1 - P\left(\max_n(X_n) < \beta\right) \\ &= 1 - \prod_{n=1}^M (1 - P(X_n > \beta)) = 1 - (1 - P_{fa}(\beta))^M \end{aligned} \quad (4.22)$$

- **Serial.** In the serial strategy the system false alarm probability is given by

$$\begin{aligned}
 P_{FA}^a(\beta) &= P(X_1 > \beta) + P(X_2 > \beta)P(X_1 < \beta) + \\
 &\quad P(X_3 > \beta)P(X_2 < \beta)P(X_1 < \beta) + \dots \\
 &= P_{fa}(\beta) + P_{fa}(\beta)(1 - P_{fa}(\beta)) + P_{fa}(\beta)(1 - P_{fa}(\beta))^2 + \dots \\
 &= \sum_{n=0}^{M-1} P_{fa}(\beta)(1 - P_{fa}(\beta))^n = P_{fa}(\beta) \frac{1 - (1 - P_{fa}(\beta))^M}{1 - (1 - P_{fa}(\beta))} \\
 &= 1 - (1 - P_{fa}(\beta))^M
 \end{aligned} \tag{4.23}$$

- **Hybrid.** By proceeding as in the two previous cases it can be found that

$$P_{FA}^a(\beta) = 1 - (1 - P_{fa}(\beta))^M \tag{4.24}$$

Eqs. (4.22), (4.23) and (4.24) show that the three searching strategies have the same performance in terms of decision false alarm probability when the SIS is absent. However, when the signal is present, the decision false alarm probabilities differ according to the adopted algorithm, and they can be easily obtained by difference, that is

$$P_{FA}^p(\beta) = 1 - P_D(\beta) - P_{MD}(\beta) \tag{4.25}$$

as the three cases (detection, miss-detection and false alarm in presence of signal) represent all the possible events.

4.5 Simulation analysis

In order to validate the results of Sections 4.2, 4.3 and 4.4, a simplified scenario has been adopted using simplified expressions for the single cell probabilities. In particular, the simulated code delay and Doppler shift have been selected exactly on the grid of the search space, the received SIS has been coherently integrated over a single code period, and no non-coherent averages have been performed. Under these hypotheses and as reported in Section 3.6, the cell probabilities assume the following expressions:

$$P_{fa}(\beta) = \exp\left(-\frac{\beta}{2\sigma_n^2}\right) \tag{4.26}$$

$$f_A(x) = \frac{1}{2\sigma_n^2} \exp\left(-\frac{x + \lambda}{2\sigma_n^2}\right) I_0\left(\frac{\sqrt{x\lambda}}{\sigma_n^2}\right) \tag{4.27}$$

$$P_d(\beta) = Q_1\left(\sqrt{\frac{\lambda}{\sigma_n^2}}; \sqrt{\frac{\beta}{\sigma_n^2}}\right) \tag{4.28}$$

where $I_0(\cdot)$ is the modified Bessel function of the first kind of zero order [45] and $Q_1(\cdot, \cdot)$ is the Marcum's Q -function [37]. λ and σ_n^2 have been defined in Section 3.6 and are respectively given by:

$$\begin{aligned}\lambda &= \frac{A^2}{4} = \frac{C}{2} \\ \sigma_n^2 &= \frac{\sigma_{IF}^2}{2N} = \frac{N_0 B_{IF}}{2N}\end{aligned}$$

It is worthwhile to notice that the false alarm probability in Eq. (4.26) has been derived by supposing that the outputs of the in-phase and quadrature branches of the acquisition block are zero-mean Gaussian random variables before squaring. This corresponds to the hypothesis that the ambiguity function is null, in absence of noise, for $\tau \neq \tau_0$ and $f_d \neq f_{d,0}$. Eq. (4.26) is exact only when the signal is absent.

By substituting Eqs. (4.26), (4.27) and (4.28) into the expressions derived in Sections 4.2, 4.3 and 4.4, the decision detection probabilities take the following forms:

-

$$P_D(\beta) = \sum_{i=0}^{M-1} \binom{M-1}{i} \frac{(-1)^i}{i+1} \exp\left\{-\frac{i\lambda}{2(i+1)\sigma_n^2}\right\} Q_1\left(\frac{\sqrt{\lambda}}{\sigma_n\sqrt{i+1}}; \frac{\sqrt{(i+1)\beta}}{\sigma_n}\right) \quad (4.29)$$

for the maximum search strategy;

-

$$\begin{aligned}P_D(\beta) &= \frac{1}{L} \frac{1 - [1 - \exp\{-\frac{\beta}{2\sigma_n^2}\}]^M}{1 - [1 - \exp\{-\frac{\beta}{2\sigma_n^2}\}]^H} \\ &\quad \sum_{i=0}^{H-1} \binom{H-1}{i} \frac{(-1)^i}{i+1} \exp\left\{-\frac{i\lambda}{2(i+1)\sigma_n^2}\right\} Q_1\left(\frac{\sqrt{\lambda}}{\sigma_n\sqrt{i+1}}; \frac{\sqrt{(i+1)\beta}}{\sigma_n}\right)\end{aligned} \quad (4.30)$$

for the hybrid search strategy;

- and

$$P_D(\beta) = \frac{1}{M} \frac{1 - [1 - \exp\{-\frac{\beta}{2\sigma_n^2}\}]^M}{\exp\{-\frac{\beta}{2\sigma_n^2}\}} Q_1\left(\frac{\sqrt{\lambda}}{\sigma_n}; \frac{\sqrt{\beta}}{\sigma_n}\right) \quad (4.31)$$

for the serial search strategy.

Expressions (4.29) and (4.30) have been obtained by expanding binomials in Eqs. (4.10) and (4.16) and manipulating the terms under the integrals in order to obtain the Marcum Q -function definition. The main advantage of introducing the Q -function lies in the formula implementation: the Q -function eliminates the necessity of computing the numerical integrals that appear in the previous expressions of the probabilities, thus avoiding

problems linked to the correct setting of the involved parameters. The summations in Eq. (4.29) and Eq. (4.30) involve a high number of elements that, however, are rapidly decreasing thus allowing a truncation over the first few terms.

In the same way, the miss-detection probability can be written as

$$P_{MD}(\beta) = \left[1 - \exp \left\{ -\frac{\beta}{2\sigma_n^2} \right\} \right]^{M-1} \left[1 - Q_1 \left(\frac{\sqrt{\lambda}}{\sigma_n}; \frac{\sqrt{\beta}}{\sigma_n} \right) \right] \quad (4.32)$$

4.5.1 Probability curves

The expressions of detection, false alarm, and miss-detection probabilities given in the previous sections have been validated in two steps. In the first step an artificial search space has been created generating M random variables with the statistical characteristics leading to the cell probabilities reported before. This means that the searching strategies described in Section 4.1.1 have been implemented in software and applied to a grid of values obtained as the squared absolute value of a complex zero-mean Gaussian matrix generated by simulation. Only one cell, representing the aligned case, presented a mean equal to $\sqrt{\lambda}$.

The system performances have been evaluated in terms of ROC. In Figures 4.1 and 4.2 the ROC curves show the decision detection and false alarm probabilities in the presence of signal versus the decision false alarm probability in its absence. The decision false alarm probability in the absence of signal has been chosen as a parameter for the threshold setting, since it represents a more critical system performance indicator. In fact, it is easy to show that the condition

$$P_{FA}^a(\beta) \geq P_{FA}^p(\beta) \quad \forall \beta \quad (4.33)$$

is true for all strategies considered in this chapter. For this reason, the threshold is derived by fixing a decision false alarm probability in the absence of signal: by inverting Eq. (4.22), (4.23) or (4.24), a cell false alarm probability is evaluated and thus the threshold β is fixed by means of Eq. (4.26). This procedure allows one to fix the P_{FA}^a and thus to control the decision false alarm probability P_{FA}^p thanks to Eq. (4.33). Furthermore, determining the threshold from $P_{FA}^p(\beta)$ would require prior information about the signal, i.e. its presence and its power level. These parameters are generally not available since they should be estimated by the acquisition block. In the rest of the chapter, all ROCs will be a function of the decision false alarm probability in the absence of signal.

The curves are reported by using a linear scale and the ROCs are evaluated for values of the decision false alarm probability in the absence of signal on the entire range [0,1]. Even if in practice the decision false alarm probability should be set to a value close to zero, the aim of these simulations was to validate the theoretical model provided in previous sections for every decision false alarm probability, and thus the entire range [0,1] has been

4.5 – Simulation analysis

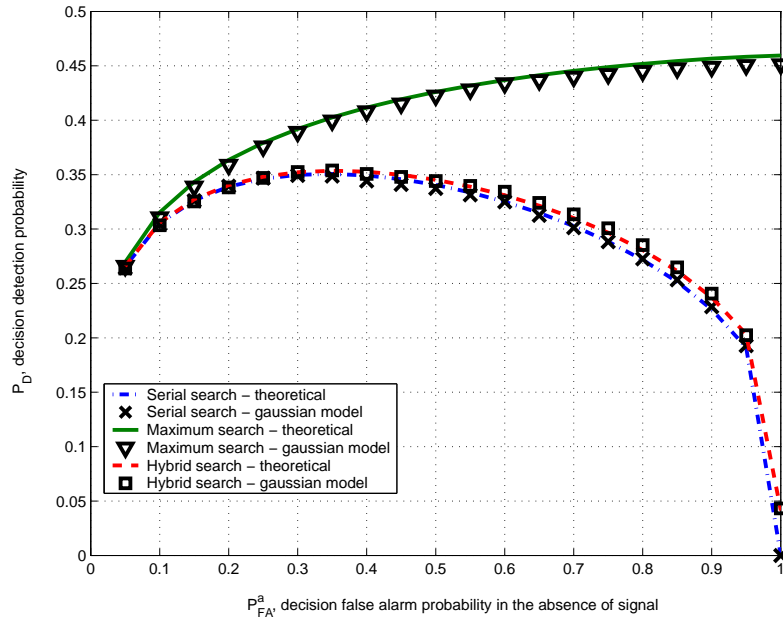


Figure 4.1. Decision detection probability vs decision false alarm probability in the absence of signal, Gaussian model.

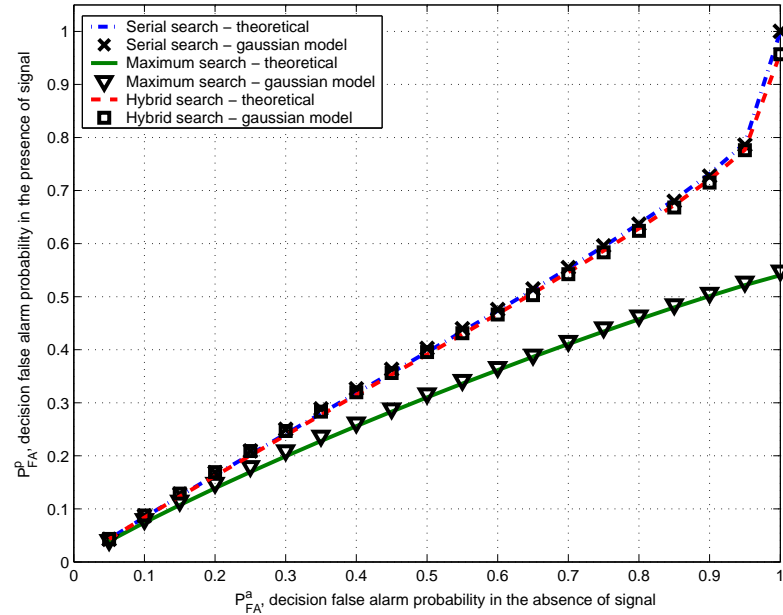


Figure 4.2. Decision false alarm probability in the presence of signal vs decision false alarm probability in the absence of signal, Gaussian model.

investigated. The linear scale has been adopted since no appreciable representation enhancement was found by using the logarithmic scale.

The curves of Figures 4.1 and 4.2 have been evaluated with the parameters reported in Table 4.1; the performance obtained with the artificial search space (indicated with “Gaussian”) and the theoretical ones (indicated with “theoretical”) coincide, thus validating the formulas. In the second step, the acquisition system of Figure 3.5 has been

Table 4.1. Simulation parameters.

Parameter	Value
C/N_0	40 dB-Hz
Sampling frequency	2.046 MHz
Receiver bandwidth	1.023 MHz
No. of Doppler bins, L	17
No. of code samples, H	2046
$M = LH$	34782

implemented in software for the GPS SIS in the L1 band, and the decision probabilities have been estimated by means of Monte Carlo simulation experiments. In this case, a realistic search space is generated, since the acquisition system is fed by a source able to simulate an Intermediate Frequency (IF) GPS signal affected by the AWGN and Doppler shift. The simulation parameters are the ones in Table 4.1 and an intermediate frequency, $f_{IF} = 38500$ Hz, has been employed by applying the acquisition scheme proposed in [33].

In Figures 4.3, 4.4 and 4.5, the ROC decision probability curves of decision probabilities are drawn as a function of the decision false alarm probability in the absence of signal. Note that the curves obtained with the acquisition simulator and the theoretical ones have the same shape but do not coincide, except for the case of the miss-detection. The misalignment is due to the adopted simplified probabilistic model, as better explained in Section 4.6. Both the simulated and theoretical curves give the same coarse information on the system characteristics and therefore, they can be properly used to draw some preliminary considerations. As expected, the searching strategy based on the maximum gives the best performances. In this case, the ROC curve of Figure 4.3 tends to the point $(1, p_{\max})$, where p_{\max} is the probability that the cell X_A assumes the maximum value over the whole search space. In fact, from Eq. (4.10) it follows that

$$\begin{aligned}
 p_{\max} &= \lim_{P_{FA}^a \rightarrow 1} \int_{\beta}^{+\infty} [1 - P_{FA}(x)]^{M-1} f_A(x) dx = \lim_{\beta \rightarrow 0} \int_{\beta}^{+\infty} [1 - P_{FA}(x)]^{M-1} f_A(x) dx \\
 &= \int_0^{+\infty} [1 - P_{FA}(x)]^{M-1} f_A(x) dx = P \left(X_A = \max_n \{X_n\} \right).
 \end{aligned} \tag{4.34}$$

4.5 – Simulation analysis

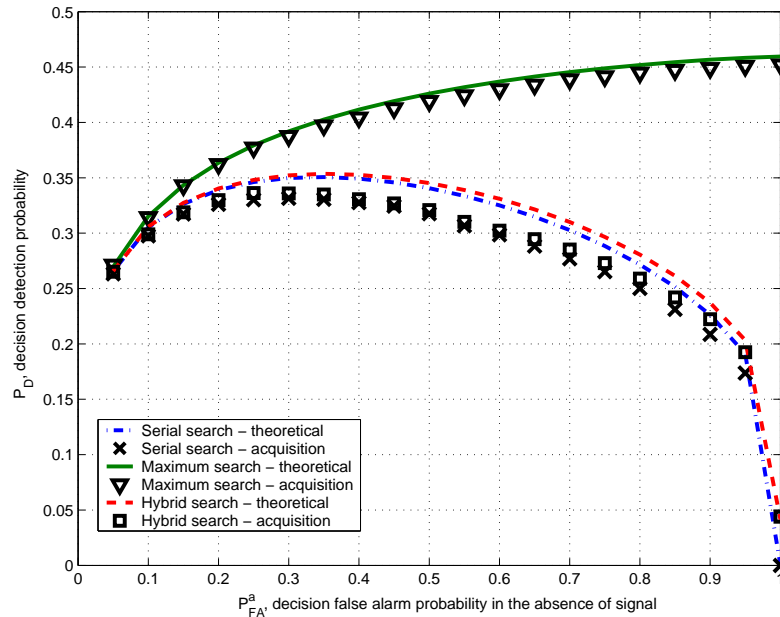


Figure 4.3. Decision detection probability vs decision false alarm probability in the absence of signal, simulated acquisition system.

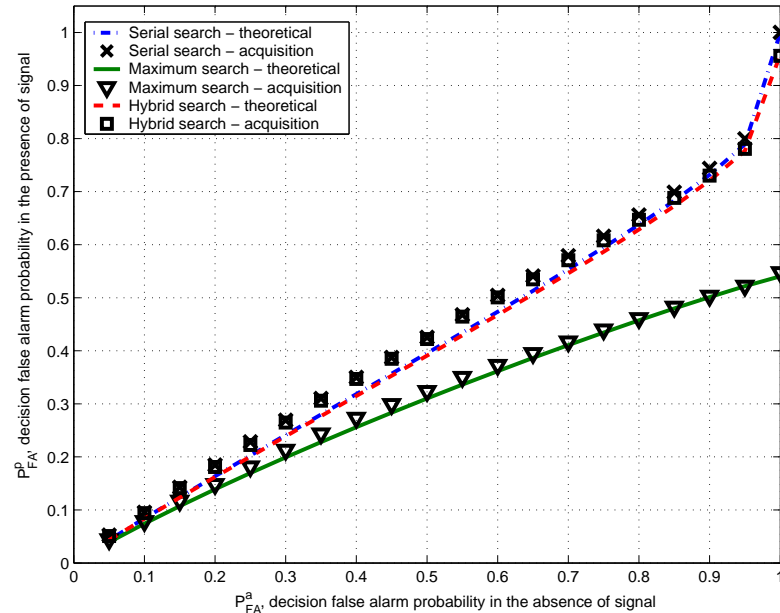


Figure 4.4. Decision false alarm probability in the presence of signal vs decision false alarm probability in the absence of signal, simulated acquisition system.

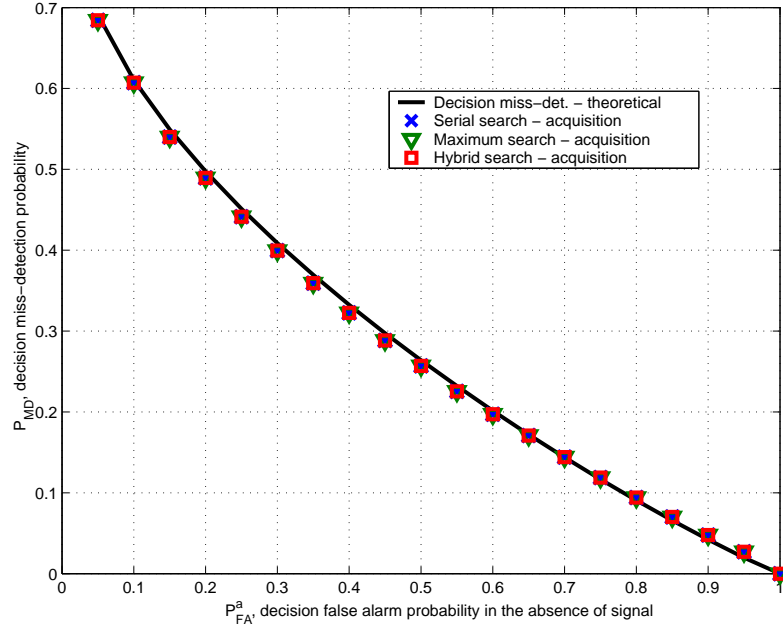


Figure 4.5. Decision miss-detection probability vs decision false alarm probability in the absence of signal, simulated acquisition system.

The limit change of Eq. (4.34) is justified by the fact that a false alarm probability tending to unity implies a null threshold. By using Eq. (4.29) and considering the case of Figure 4.3 results in

$$p_{\max} = \sum_{i=0}^{M-1} \binom{M-1}{i} \frac{(-1)^i}{i+1} \exp \left\{ -\frac{i\lambda}{2(i+1)\sigma_n^2} \right\} = 0.4584. \quad (4.35)$$

The serial and hybrid systems exhibit similar performance, much worse than the one based on the maximum. When the decision false alarm probability tends to unity, the detection probability for the serial search equals the probability that the first cell corresponds to the aligned case X_A , i.e.

$$p_{ser} = \lim_{\beta \rightarrow 0} = \frac{1}{M} \frac{1 - [1 - P_{fa}(\beta)]^M}{P_{fa}(\beta)} \int_{\beta}^{+\infty} f_A(x) dx = \frac{1}{M} = 1.6912 \cdot 10^{-6}. \quad (4.36)$$

In the hybrid case the limit detection probability becomes

$$p_{hyb} = \frac{1}{L} \int_0^{\infty} [1 - P_{fa}(x)]^{H-1} f_A(x) dx = 0.0446 \quad (4.37)$$

i.e. the probability that X_A is the maximum of the first Doppler row.

4.6 Enhanced model

Since acquisition curves do not exactly coincide with the theoretical ones, a more thorough analysis has been performed and simplifying hypotheses have been progressively removed in order to provide more accurate models.

First of all, the cell false alarm probability of Eq. (4.26) has been evaluated supposing that the ambiguity function, in absence of noise, is null when the code delay and the Doppler frequency are not exactly matched, however secondary peaks are present, because of correlation side values. In the simplified model each random variable X_n , except in the cell where $X_n \equiv X_A$, can be written as

$$X_n = \nu_{I,n}^2 + Y_{Q,n}^2 \quad (4.38)$$

where $Y_{I,n}$ and $Y_{Q,n}$ are Gaussian zero-mean random variables, while in the actual search space each cell is given by

$$\begin{aligned} X_n &= (a_{I,n} + Y_{I,n})^2 + (a_{Q,n} + Y_{Q,n})^2 \\ &= (a_{I,n}^2 + a_{Q,n}^2) + (Y_{I,n}^2 + Y_{Q,n}^2) + \zeta_n \end{aligned} \quad (4.39)$$

where $a_{I,n}$ and $a_{Q,n}$ depend on the secondary correlation peaks and ζ_n is a zero-mean random variable.

In order to account for the effect of secondary correlation peaks, a constant mean factor μ has been introduced into the theoretical model. In particular, the search space cells have been modeled as

$$\begin{aligned} X_n &= (\mu + Y_{I,n})^2 + (\mu + Y_{Q,n})^2 \\ &= 2\mu^2 + (Y_{I,n}^2 + Y_{Q,n}^2) + \xi_n \end{aligned} \quad (4.40)$$

where the value of μ has been set to

$$\mu = \frac{1}{\sqrt{2}} \sqrt{\mathbb{E} [a_{I,n}^2 + a_{Q,n}^2]} \quad (4.41)$$

$\mathbb{E} [\cdot]$ is the expected value that can be easily estimated by averaging the secondary peaks of a search space obtained in absence of noise. By applying this correction the cell false alarm probability becomes

$$P_{fa,C}(\beta, \mu) = Q \left(\frac{\mu}{\sigma_n}, \frac{\sqrt{\beta}}{\sigma_n} \right). \quad (4.42)$$

Eq. (4.42) allows one to obtain new expressions for the decision probabilities, providing a more accurate model. Notice that a more conservative estimation of μ could be used instead of Eq. (4.41). In particular the maximum of the secondary lobes of a noiseless search space could be adopted instead of their mean. In this case the false alarm probability on

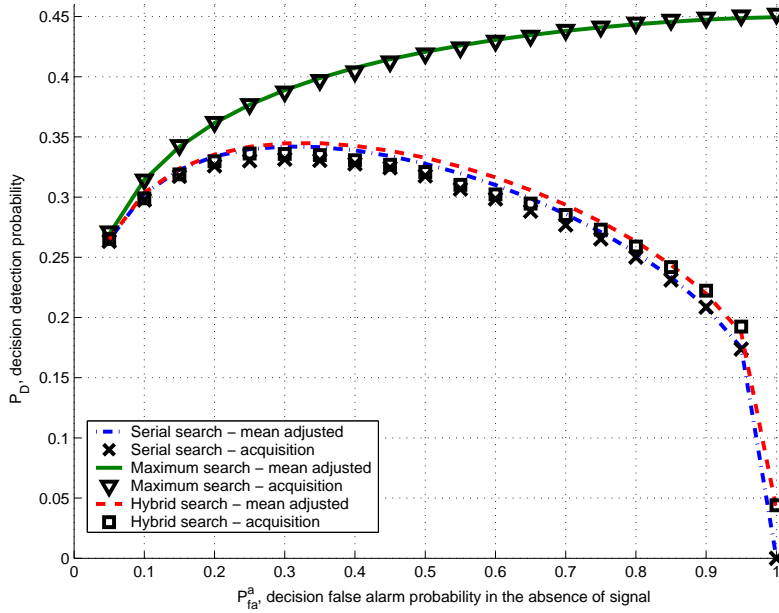


Figure 4.6. Decision detection probability vs decision false alarm probability in the absence of signal, mean adjusted model.

the single cell would be overestimated, providing a bound for the decision probabilities. In Figure 4.6 the curves obtained with the simulated acquisition block have been compared with the new theoretical model accounting for the secondary peaks impact. In this case, the theoretical values are closer to the simulated ones and the maximum search performance exactly matches the one expected theoretically. However residual model imperfections are still present in the hybrid and serial search cases. This residual effect can be explained by the initial hypothesis that the main correlation peak affects only a single cell. In Figure 4.7 the square root of the main lobe of a noiseless search space is reported. The square root has been considered since it is directly connected with the mean of the Gaussian random variables generating the search space. In particular the square root of the aligned cell X_A of a noiseless search space equals $\sqrt{\lambda}$, the amplitude parameter of Eq. (4.27) and Eq. (4.28). From this figure it is clear that the cells in proximity of the X_A are significantly affected by the signal presence: the two adjacent cells along the code direction value $\sqrt{\lambda}/2$ and similar values are assumed by the two adjacent cells along the Doppler shift direction. The presence of these random variables with a significant mean can cause additional false alarm for the serial and hybrid strategies, since side cells can easily pass the fixed threshold. The maximum strategy is less affected since the probability that a side cell passes X_A is low.

In order to test the impact of adjacent cells with significant means on the decision probabilities, an enhanced Gaussian model has been tested: all the simulated Gaussian random

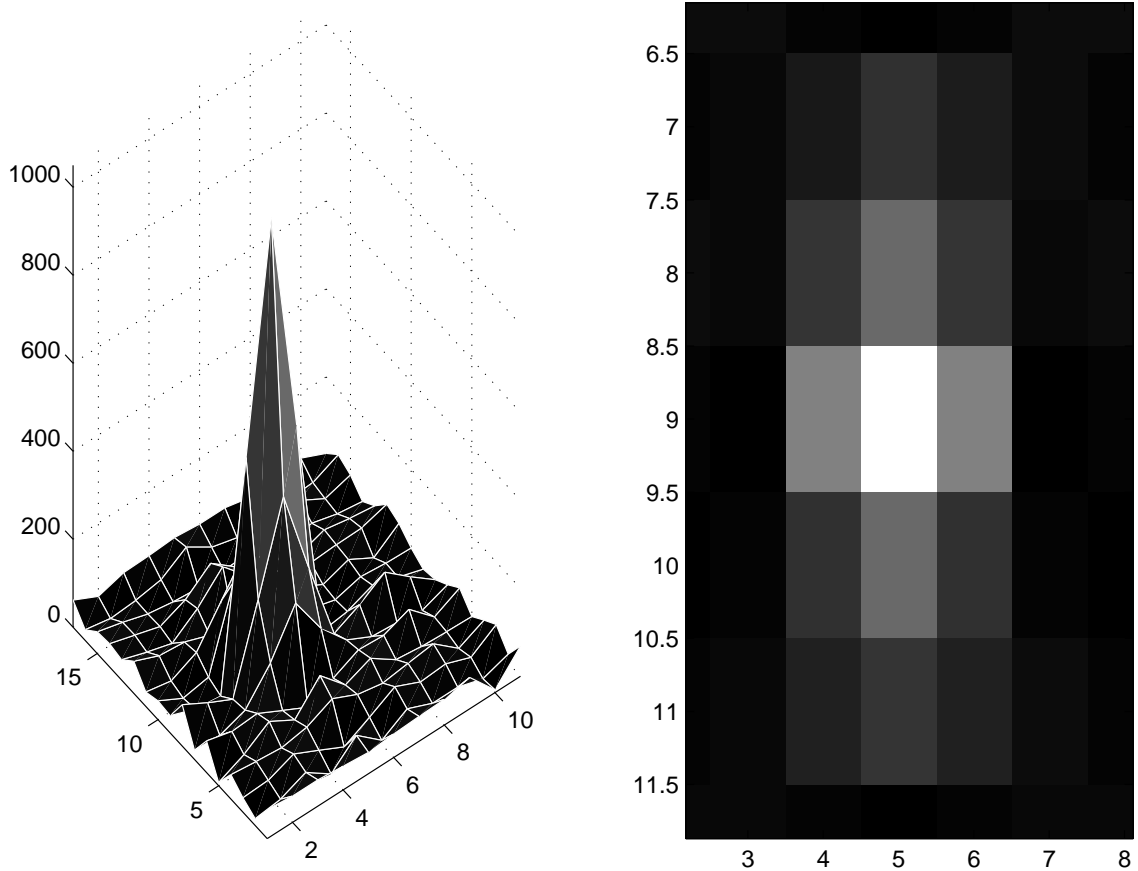


Figure 4.7. Part of a noiseless search space obtained with a GPS CA code with 2 samples/chip and a Doppler step of 666 Hz.

variables have a mean equal to μ , except the ones representing X_A and the four adjacent cells. The means of the four adjacent cells were set to the values measured by the squared root of a noiseless search space. In Figure 4.8 the comparison between ROCs obtained with the acquisition and the enhanced simulations is provided: results are very close, proving the impact of adjacent cells.

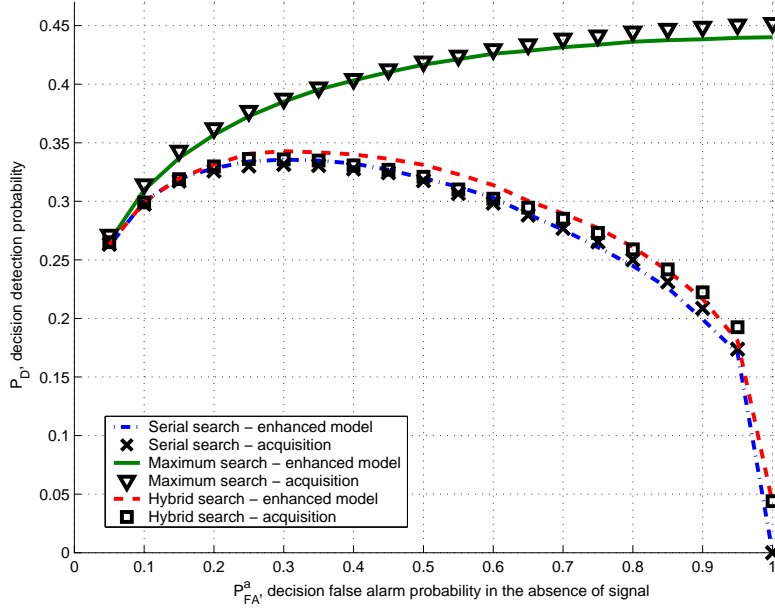


Figure 4.8. Decision detection probability vs decision false alarm probability in the absence of signal, enhanced model.

4.7 Network assisted GPS

The results reported in this chapter have been partially published in [27, 28] and they have been recently adopted by [29, 30] for quantifying the impact of network assistance on GNSS signal acquisition. Mobile phone networks have the capability of providing additional information to GNSS receivers and in particular they can provide direct or indirect information about code phases, Doppler shifts, and transmitted data bits. When the assistance is indirect, code delays and Doppler shifts are derived from it in the receiver [29]. Indirect assistance typically consists of satellite ephemerides, reference time, reference frequency, and an initial location estimate. The main effect of network assistance is to considerably reduce the size of the search space, reducing the set of satellites to be searched and restricting the range of possible code delays and Doppler frequencies. This principle is better highlighted in Figure 4.10 where the search space determined by the satellite, the code delay (time) and the Doppler shift (frequency) is essentially reduced by network assistance. Since the main impact of network assistance is to reduce the search space size, the statistic of a single cell is unaffected. As highlighted in [29, 30], the single cell probabilities are independent from the search space size and thus are not able to characterize the impact of network assistance. On the contrary decision probabilities result in an effective metric for characterizing acquisition performances.

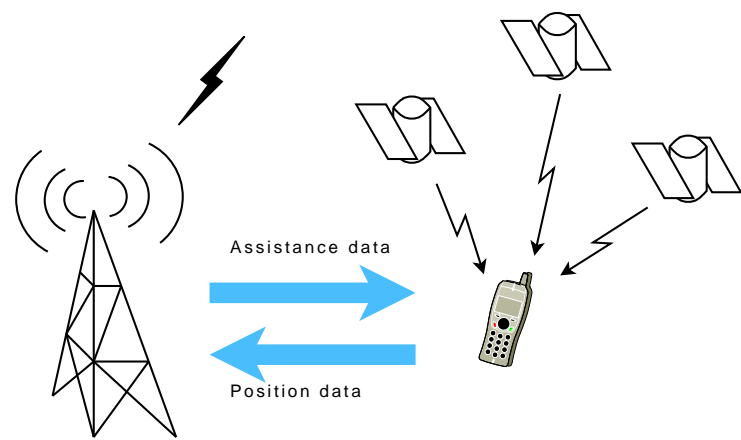


Figure 4.9. Principle of network assisted GPS (AGPS): mobile telephone network provides additional information to the GNSS receiver in order to reduce the size of the acquisition search space.

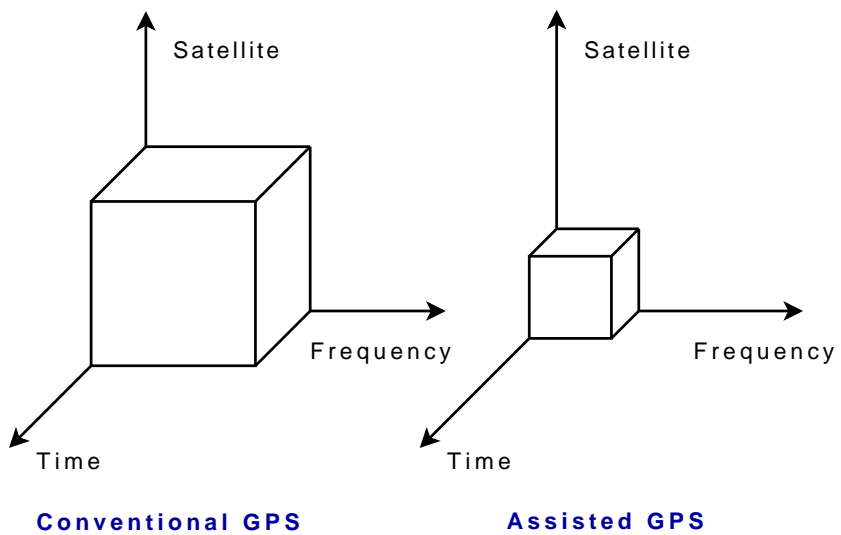


Figure 4.10. Reduction of the acquisition search space due to network assistance.

Chapter 5

Increasing the acquisition performance

In previous chapters the basic acquisition technique, based on coherent integration only, has been analyzed. The coherent integration time is however limited by different factors such as bit transition, signal dynamic and computational constraints. In fact the use of a long coherent integration time increases the computation load, not only because of the greater number of samples involved in the computation of the correlation function, but also because the width of the frequency bin for the Doppler search has to be reduced proportionally to the inverse of the integration time.

All these reasons have motivated the development of alternative integration strategies that allow to deal with the different signal imperfections mentioned above. Those techniques nonlinearly combine the input signal samples in a decision variable possibly hardened against phase and frequency errors and other signal impairments.

Two common techniques for increasing the search space quality that belong to the second stage (Envelope and Average) of the multi-layer approach described in Section 3.1, are:

- the **non-coherent signal combining**;
- the **differentially coherent signal combining**.

Those two techniques are well known in the literature and will be only briefly described in the first part of this chapter.

The second part of the chapter is devoted to the performance characterization of the these two integration strategies. In particular the problem of quantifying the impact of the two methods is discussed: although the ROC completely characterizes the detector performance [43] it is often useful to have a single metric, the output or equivalent coherent SNR, which encapsulates as much information about the detector performance as possible. This parameter characterizes the quality of the decision variable and different approaches have been adopted in the literature for its evaluation [36, 42, 43].

The case of non-coherent signal combining is considered and different methodologies from the literature are discussed. The impact of non-coherent integrations on the acquisition performance is studied in further detail. In particular the equivalent coherent SNR for acquisition systems employing non-coherent integrations is defined as the SNR that would yield similar performance in terms of ROCs if only coherent integrations were used. An analytical formulation of the problem is developed, and a new metric called *equivalent area criterion* is proposed. Closed-form formulas, relating the input SNR and the number of non-coherent integrations to the equivalent coherent SNR are then derived. To the best of our knowledge, this criterion has never been previously adopted in the literature for quantifying the impact of non-coherent integrations, and thus it represents the innovative contribution of this chapter. Results from radar and signal detection theory are adapted to the GNSS acquisition case and compared with formulas developed in the chapter. A methodology for testing the quality of the conversion formulas is developed and it is proved that the provided criterion usually gives better results than those present in the literature.

The problem of evaluating the number of non-coherent integrations from the equivalent coherent SNR is also addressed. Comparisons of the various criteria for non-coherent summations is a further contribution of this chapter and highlights that there are significant differences in the number of non-coherent integrations predicted according to the different criteria. Although the obtained results have been specifically derived for GNSS band-pass spread spectrum signals, they can be applied to the more general case of signal detection with coherent and non-coherent integrations [36].

5.1 Non-coherent signal combining

A first technique for increasing the acquisition performance consists in simply summing K instances of the output of the basic acquisition block. The squaring blocks remove the phase dependence and the CAFs are non-coherently summed. In Figure 5.1 the acquisition scheme with non-coherent integrations is reported. The final decision variable is obtained as

$$S_K(\tau, F_D) = \sum_{k=0}^{K-1} S_k(\tau, F_D) \quad (5.1)$$

where the subscript K indicates that K non-coherent integrations have been used. The index k has been used in the right side of Eq. (5.1) to distinguish different realizations of the basic CAF $S(\tau, F_D)$. Those realizations have been evaluated by using non-overlapping portions of the input signal $r[n]$.

In Section 3.6 it has been shown that, for $K = 1$, i.e. in absence of non-coherent integration, the cells of the CAF are χ^2 random variables with two degrees of freedom. Thus $S_K(\tau, F_D)$ is given by the sum of K independent χ^2 random variables with 2 degrees

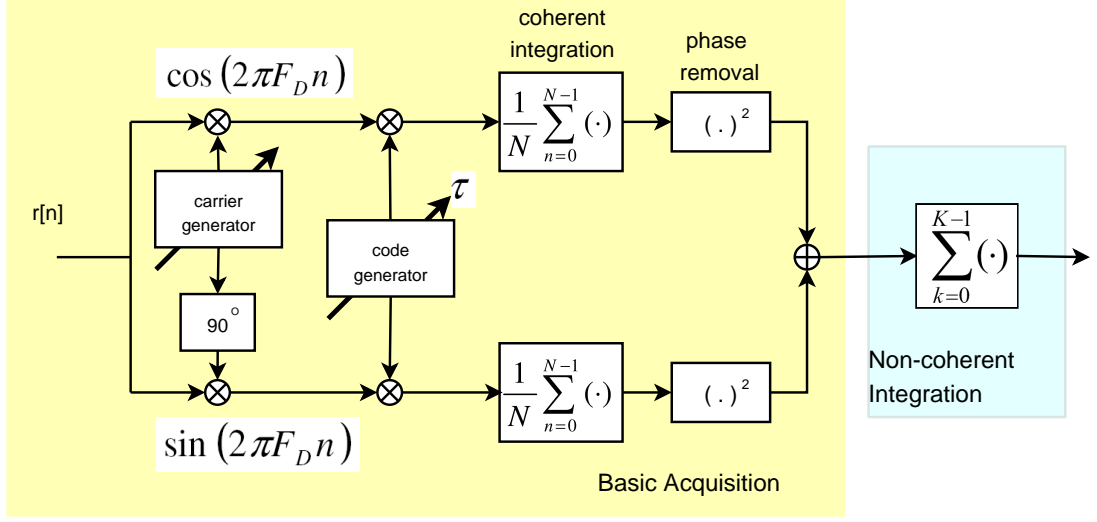


Figure 5.1. Acquisition scheme with non-coherent integrations.

of freedom. By using the properties of χ^2 random variables, $S_K(\tau, F_D)$ is a χ^2 random variable with $2K$ degrees of freedom.

When the code and the Doppler frequency of the local signal replica match the ones of the incoming signal, $S_K(\tau, F_D)$ is a non-central χ^2 random variable with non-central parameter

$$\lambda_K = K\lambda = K \frac{A^2}{4} \quad (5.2)$$

where λ is the non-centrality parameter defined in Section 3.6 and A is the useful signal amplitude. When the local replica and the incoming signal are not aligned $S_K(\tau, F_D)$ is a central χ^2 random variable.

By using properties of non-central and central χ^2 random variables [44, 55], it is possible to derive the detection and false alarm probabilities related to $S_K(\tau, F_D)$:

$$P_{fa,K}(\beta) = \exp \left\{ -\frac{\beta}{2\sigma_n^2} \right\} \sum_{i=0}^{K-1} \frac{1}{i!} \left(\frac{\beta}{2\sigma_n^2} \right)^i \quad (5.3)$$

$$P_{d,K}(\beta) = Q_K \left(\sqrt{K \frac{\lambda}{\sigma_n^2}}, \sqrt{\frac{\beta}{\sigma_n^2}} \right) = Q_K \left(\sqrt{K \rho_c}, \sqrt{\frac{\beta}{\sigma_n^2}} \right) \quad (5.4)$$

where $Q_K(a,b)$ is the generalized Marcum Q-function [37], σ_n^2 is the variance of the in-phase and quadrature outputs (see Section 3.6) and ρ_c , the coherent output SNR.

By applying the change of variable

$$\beta' = \frac{\beta}{\sigma_n^2}$$

it is possible to rewrite Eq.s (5.3) and (5.4) as

$$\begin{cases} P_{fa,K}(\beta') = \exp\left\{-\frac{\beta'}{2}\right\} \sum_{i=0}^{K-1} \frac{1}{i!} \left(\frac{\beta'}{2}\right)^i \\ P_{d,K}(\beta') = Q_K(\sqrt{K\rho_c}, \sqrt{\beta'}) \end{cases} \quad (5.5)$$

From Eq. 5.5 it emerges that the coherent SNR completely characterizes the ROC only when $K = 1$ that is when only coherent integration is used. Moreover ROCs obtained with different numbers of non-coherent integrations cannot be directly compared in terms of coherent SNR since, even if the coherent SNR is the same, two different detection probabilities are obtained for a fixed false alarm rate. It would be useful to have an unique indicator enabling an easy and intuitive analysis of the acquisition performance also when both coherent and non-coherent integrations are used. This is equivalent to determine an unique parameter, a function of the number of non-coherent integrations and of the coherent SNR, that completely characterizes the system performance. This parameter, that will be introduced in Section 5.3, is called equivalent coherent SNR and corresponds to the coherent SNR when $K = 1$.

5.2 Differentially coherent combining

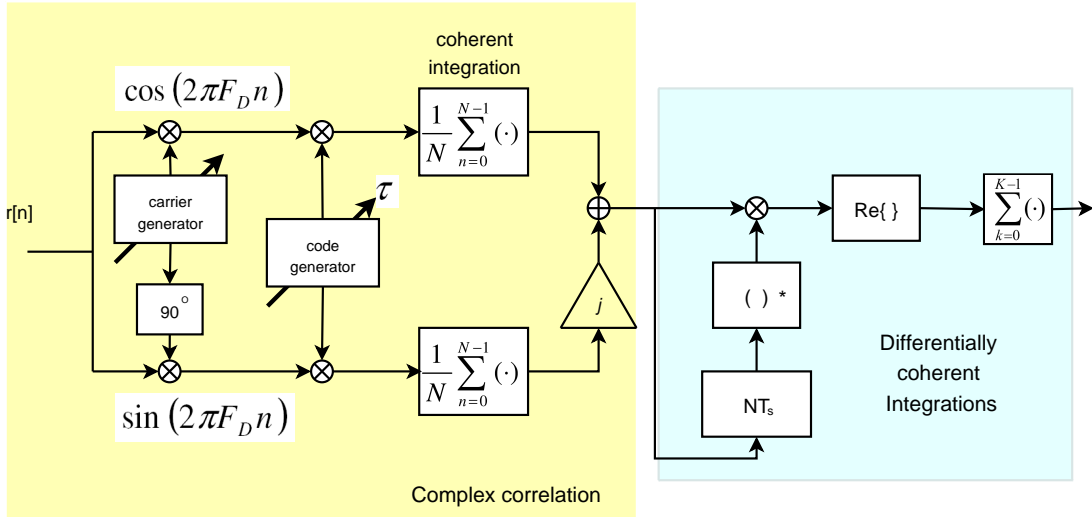


Figure 5.2. Acquisition scheme with differentially coherent integrations.

In the non-coherent integration strategy the phase dependence is removed by squaring the correlator outputs. In particular the final decision variable is obtained according

to Eq. (5.1), that can be rewritten as:

$$\begin{aligned}
 S_K(\tau, F_D) &= \sum_{k=0}^{K-1} S_k(\tau, F_D) = \sum_{k=0}^{K-1} [Y_{I,k}^2(\tau, F_D) + Y_{Q,k}^2(\tau, F_D)]^2 \\
 &= \sum_{k=0}^{K-1} |Y_{I,k}(\tau, F_D) + jY_{Q,k}(\tau, F_D)|^2 \\
 &= \sum_{k=0}^{K-1} [Y_{I,k}(\tau, F_D) + jY_{Q,k}(\tau, F_D)] [Y_{I,k}(\tau, F_D) + jY_{Q,k}(\tau, F_D)]^*
 \end{aligned} \tag{5.6}$$

where $Y_{I,k}(\tau, F_D)$ and $Y_{Q,k}(\tau, F_D)$ are the k th instances of the in-phase and quadrature correlator outputs. Eq. (5.6) can be interpreted as follows: the correlator outputs present residual phase effects that depend on the unknown phase of the input signal. These dependence is removed by squaring the correlator outputs. However, in this way, also the noise components are squared and the post-correlation averaging is less effective since the noise components do not cancel out any longer. In order to overcome this problem the decision variable (5.6) can be modified as follows:

$$\tilde{S}_K(\tau, F_D) = \sum_{k \in \mathcal{K}} [Y_{I,k}(\tau, F_D) + jY_{Q,k}(\tau, F_D)] [Y_{I,k-l}(\tau, F_D) + jY_{Q,k-l}(\tau, F_D)]^* \tag{5.7}$$

where \mathcal{K} defines the set of indexes that selects the complex correlations used for forming the variable $\tilde{S}_K(\tau, F_D)$. In Eq. (5.7) the complex correlation $Y_{I,k-l}(\tau, F_D) + jY_{Q,k-l}(\tau, F_D)$ evaluated on the $(k-l)$ th portion of the useful signal is used to correct the phase of the k th correlation $Y_{I,k}(\tau, F_D) + jY_{Q,k}(\tau, F_D)$. In this way independent noise components are multiplied by each other and the resulting noise process is still zero mean.

The decision variable (5.7) is the basic element that defines **differentially integrations**. Different forms of differential integrations are possible [9–12], depending on the separation, l , between complex correlations, the index set, \mathcal{K} , and the function used for determining the final decision variable. In fact Eq. (5.7) cannot be used for detection purposes since $\tilde{S}_K(\tau, F_D)$ is, in general, complex valued. The following cases are possible:

- differentially coherent integration [10–12]:

$$S_K(\tau, F_D) = \Re e \left\{ \sum_{k \in \mathcal{K}} [Y_{I,k}(\tau, F_D) + jY_{Q,k}(\tau, F_D)] [Y_{I,k-l}(\tau, F_D) + jY_{Q,k-l}(\tau, F_D)]^* \right\} \tag{5.8}$$

- differentially non-coherent integration [9, 10]:

$$S_K(\tau, F_D) = \left| \sum_{k \in \mathcal{K}} [Y_{I,k}(\tau, F_D) + jY_{Q,k}(\tau, F_D)] [Y_{I,k-l}(\tau, F_D) + jY_{Q,k-l}(\tau, F_D)]^* \right| \tag{5.9}$$

The detailed analysis of differentially integrations is out of the scope of this thesis and can be found in the literature. In particular an exhaustive analysis of differentially integrations can be found in [10] that provides a statistical characterization of the different strategies. In the context of this chapter differentially coherent combining with $\mathcal{K} = \{2,4,\dots,2K\}$ and $l = 1$ is considered. These results will be used in Chapter 7 for developing a new acquisition algorithm for composite GNSS signals.

Under the previous assumptions the decision variable becomes

$$\begin{aligned} S_K(\tau, F_D) &= \sum_{k=0}^{K-1} \Re \{ [Y_{I,2k+1}(\tau, F_D) + jY_{Q,2k+1}(\tau, F_D)] [Y_{I,2k}(\tau, F_D) + jY_{Q,2k}(\tau, F_D)]^* \} \\ &= \sum_{k=1}^K [Y_{I,2k+1}(\tau, F_D) Y_{I,2k}(\tau, F_D) + Y_{Q,2k+1}(\tau, F_D) Y_{Q,2k}(\tau, F_D)] \end{aligned} \quad (5.10)$$

and the corresponding acquisition scheme is depicted in Figure 5.2. The differentially coherent acquisition scheme assumes that the two complex correlations, $Y_{I,2k+1}(\tau, F_D) + jY_{Q,2k+1}(\tau, F_D)$ and $Y_{I,2k}(\tau, F_D) + jY_{Q,2k}(\tau, F_D)$ have the same phase and thus the signal component is concentrated on the real part of their product. However if some phase errors are present, differentially coherent integration become ineffective [10]. The analysis of phase and frequency errors on differentially coherent integration can be found in [10]. In [12] it is shown that Eq. (5.10) can be rewritten as the difference of two χ^2 random variables. In particular, when the signal is not present, i.e. under H_0 , $S_K(\tau, F_D)$ is the difference of two central χ^2 random variables with $2K$ degrees of freedom, whereas, under H_1 and in absence of phase errors, $S_K(\tau, F_D)$ is the difference of a non-central and a central χ^2 random variable. In particular, by introducing the notation

$$X_k(\tau, F_D) = Y_{I,k}(\tau, F_D) + jY_{Q,k}(\tau, F_D) \quad (5.11)$$

it is possible to rewrite Eq. (5.10) as follows:

$$\begin{aligned} S_K(\tau, F_D) &= \sum_{k=0}^{K-1} \Re \{ X_{2k+1}(\tau, F_D) X_{2k}^*(\tau, F_D) \} \\ &= \frac{1}{4} \sum_{k=0}^{K-1} \left[|X_{2k+1}(\tau, F_D) + X_{2k}(\tau, F_D)|^2 - |X_{2k+1}(\tau, F_D) - X_{2k}(\tau, F_D)|^2 \right] \\ &= \underbrace{\sum_{k=0}^{K-1} \left| \frac{X_{2k+1}(\tau, F_D) + X_{2k}(\tau, F_D)}{2} \right|^2}_{\chi_{2K}^2} - \underbrace{\sum_{k=0}^{K-1} \left| \frac{X_{2k+1}(\tau, F_D) - X_{2k}(\tau, F_D)}{2} \right|^2}_{\chi_{2K}^2} \\ &= C_1(\tau, F_D) - C_2(\tau, F_D) \end{aligned} \quad (5.12)$$

where $C_1(\tau, F_D)$ and $C_2(\tau, F_D)$ are two independent χ^2 random variables. The variance of the Gaussian random variables that generate $C_1(\tau, F_D)$ and $C_2(\tau, F_D)$ is given by

$$\begin{aligned} \text{Var} \left\{ \mathbb{R}e \left[\frac{X_{2k+1}(\tau, F_D) + X_{2k}(\tau, F_D)}{2} \right] \right\} &= \frac{1}{2} \text{Var} \left\{ \frac{X_{2k+1}(\tau, F_D) + X_{2k}(\tau, F_D)}{2} \right\} \\ &= \frac{1}{8} \text{Var} \{ X_{2k+1}(\tau, F_D) + X_{2k}(\tau, F_D) \} = \frac{1}{8} 4\sigma_n^2 = \frac{1}{2}\sigma_n^2 \end{aligned} \quad (5.13)$$

From [10, 12] the pdf of $S_K(\tau, F_D)$ under H_0 is given by:

$$p_{fa,K}(x) = \left(\frac{1}{\sigma_n^2} \right) \left(\frac{|x|}{2\sigma_n^2} \right)^{K-1/2} \frac{K_{K-1/2} \left(\frac{|x|}{\sigma_n^2} \right)}{\sqrt{\pi} \Gamma(K)} \quad (5.14)$$

where $K_i(\cdot)$ is the modified Bessel function of second kind and order i [45] and $\Gamma(\cdot)$ is the Euler's Gamma function [45].

The corresponding false alarm probability is obtained as

$$P_{fa,K}(\beta) = \int_{\beta}^{+\infty} p_{fa,K}(x) dx \quad (5.15)$$

For the special case $K = 1$

$$S_1(\tau, F_D) = \mathbb{R}e \{ X_1(\tau, F_D) X_0^*(\tau, F_D) \} \quad (5.16)$$

corresponds to the difference of two chi-square random variables with 2 degrees of freedom or equivalently to the difference of two exponential random variables. In this way $S_1(\tau, F_D)$ results Laplace distributed and equation (5.14) becomes:

$$p_{fa,1}(x) = \frac{1}{2\sigma_n^2} \exp \left\{ -\frac{|x|}{\sigma_n^2} \right\} \quad (5.17)$$

and the corresponding probability of false alarm results:

$$P_{fa,1}(\beta) = \begin{cases} 1 - \frac{1}{2} \exp \left\{ \frac{\beta}{\sigma_n^2} \right\} & \beta < 0 \\ \frac{1}{2} \exp \left\{ -\frac{\beta}{\sigma_n^2} \right\} & \beta \geq 0 \end{cases} \quad (5.18)$$

These results will be used as basic elements for the analysis of a new acquisition algorithm for composite GNSS signals.

The analysis of the detection probabilities results more complicated since the decision variable is obtained as the difference of a non-central and of a central χ^2 random variable. In [12] it is claimed that no analytical expression for this detection probability has been found. In [10] approximated expressions for this probability are provided. However in [56] the expression for the difference of independent non-central and central χ^2 random variables is reported. Those results can be used for deriving the detection probability associated to Eq. (5.12). In the following only the expression for $K = 1$ is reported.

This result will be better analyzed in Chapter 7 for the analysis of composite GNSS signals.

More in detail, the pdf of Eq. (5.12) under H_1 and for $k = 1$ is given by

$$p_{d,1}(x) = \frac{1}{2\sigma_n^2} \exp\left\{\frac{2x - \lambda}{2\sigma_n^2}\right\} Q_1\left(\sqrt{\frac{\lambda}{\sigma_n^2}}, \sqrt{\max\left(0, \frac{4x}{\sigma_n^2}\right)}\right) \quad (5.19)$$

where $\lambda = \frac{A^2}{4}$ is the non-centrality parameter defined in Section 3.6. The corresponding detection probability is given by

$$P_{d,1}(\beta) = Q_1\left(\sqrt{\frac{2\lambda}{\sigma_n^2}}, \sqrt{\max\left(0, \frac{2\beta}{\sigma_n^2}\right)}\right) - \frac{1}{2} \exp\left\{\frac{2\beta - \lambda}{2\sigma_n^2}\right\} Q_1\left(\sqrt{\frac{\lambda}{\sigma_n^2}}, \sqrt{\max\left(0, \frac{4\beta}{\sigma_n^2}\right)}\right) \quad (5.20)$$

5.3 Equivalent Coherent SNR

As discussed the performance of a signal detector is completely determined by its ROC and thus two detectors are equivalent only if their ROCs completely superimpose. Thus, in order to quantify the extent by which the performance of two detectors differs, it is possible to introduce the following metric

$$d^2(K_1, K_2, \rho_{c,1}, \rho_{c,2}) = \int_0^1 [P_{d,K_1}(\rho_{c,1}) - P_{d,K_2}(\rho_{c,2})]^2 dP_{fa} \quad (5.21)$$

that is the Euclidean square distance between two ROCs, the first one obtained with K_1 non-coherent integrations and a coherent SNR equal to $\rho_{c,1}$, and the second one characterized by K_2 and $\rho_{c,2}$. In Eq. (5.21) the dependence of the detection probability on the coherent output SNR has been explicitly reported. Since Eq. (5.21) corresponds to the square norm of the difference of two ROCs, $d^2(K_1, K_2, \rho_{c,1}, \rho_{c,2})$ is zero only if the two ROCs are the same, that is if the two detectors have the same performance.

Since the coherent output SNR completely characterizes a ROC when only coherent integration is used, it is possible to define the equivalent coherent SNR as

$$\begin{aligned} \rho_K &= \arg \min_{\rho} d(1, K, \rho, \rho_c) \\ &= \arg \min_{\rho} \left\{ \int_0^1 [P_{d,1}(\rho) - P_{d,K}(\rho_c)]^2 dP_{fa} \right\} \end{aligned} \quad (5.22)$$

that is the value, ρ , that minimizes the distance between the original ROC, the one obtained by K non-coherent integrations and a coherent SNR equal to ρ_c , and the ROC obtained by using coherent integration only. The idea beyond Eq. (5.22) is that a ROC can be approximated by another ROC obtained with coherent integration only, and that

the equivalent coherent SNR is the parameter that leads to the best fit [43]. By means of differentiation, Eq. (5.22) can be rewritten as

$$\rho_K = \rho : \int_0^1 2 [P_{d,1}(\rho) - P_{d,K}(\rho_c)] \frac{\partial P_{d,1}(\rho)}{\partial \rho} dP_{fa} = 0 \quad (5.23)$$

Problem (5.23) cannot be solved easily in closed form and numerical methods have to be employed. Thus alternative equivalence criteria should be utilized.

In this section three different criteria for obtaining an approximate expression for the equivalent SNR, when non-coherent integrations are considered, are presented. The first two criteria, the empirical formula and the generalized SNR, are from the literature and thus they will only be summarized. The third one, called *the equivalent area criterion*, is new and represents the original contribution of this section.

It can be noted that for many applications, such as for GNSS, only a limited region of the ROC (the one for low values of false alarm probability) is usually of interest. Thus more restrictive definitions of distance and consequently of equivalent coherent SNR can be adopted. A solution can be, for example, limiting the integral in Eq. (5.21) on the interval $[0, P_{\max}]$, that is equivalent to consider the square distance of ROCs for values of false alarm probability ranging from 0 to P_{\max} . However, by means of practical examples, we will show that, in the case of the equivalent area criterion, the choice of $P_{\max} = 1$ leads to closed-form formulas without compromising the ROC approximation for low values of false alarm probability.

5.3.1 Empirical formula

A first expression for empirically evaluating the equivalent SNR is provided in [43]. It can be noted that, once both false alarm and detection probabilities are fixed, then it is possible, by utilizing only coherent integrations, to invert Eq. (3.39), thus determining a value of coherent SNR denoted by ρ_K . In the same way, by utilizing K non-coherent integrations, another value of coherent SNR ρ_c can be found. From those two SNRs, an integration loss is defined as

$$L = 10 \log_{10} \frac{\rho_c}{\rho_K/K} \quad (5.24)$$

and thus, the equivalent SNR, that is the one that leads to similar performance when only coherent integrations are used, is obtained as:

$$\rho_K|_{dB} = \rho_c|_{dB} + 10 \log_{10} K - L \quad (5.25)$$

In [43] L is plotted for different values of K , as well as false alarm and detection probabilities and it is noticed that for $K \gg 1$ the loss is approximated by

$$L = 10 \log_{10} \sqrt{K} - 5.5 \text{dB} \quad (5.26)$$

Eq. (5.26) has been obtained empirically by fitting loss curves reported in [43], and is independent from the initial values of false alarm and detection probabilities used for defining L . From Eq. (5.26) it is then possible to evaluate a first expression of the equivalent SNR, that will be referred to as *empirical formula*, as a result of the derivation:

$$\begin{aligned}\rho_K|_{dB} &= \rho_c|_{dB} + 10 \log_{10} \sqrt{K} + 5.5 dB \\ \rho_K &= 10^{0.55} \sqrt{K} \rho_c = 3.548 \sqrt{K} \rho_c\end{aligned}\quad (5.27)$$

5.3.2 Generalized SNR

A second approach for evaluating the impact of non-coherent integrations on the signal quality has been utilized for GNSS by Lachapelle and Petovello in [42], and it is based on [57]. It notes that the coherent SNR, when only coherent integrations are used, is essentially the square mean distance between the signal peak and the noise floor, normalized with respect to the noise variance. In [42] an equivalent SNR is thus defined as

$$\rho_K = \frac{\mathbb{E} [S_K(\tau^0, F_{D,0}) - S_K(\tau \neq \tau^0, F_D \neq F_{D,0})]^2}{\text{Var}[S_K(\tau, F_D)]} \quad (5.28)$$

that is the mean square distance of the signal peak from the noise floor, normalized by the noise variance. In this case the decision statistic $S_K(F_D, \tau)$ is used and the phase dependence is removed by the squaring block in the acquisition process. The SNR defined in Eq. (5.28) will be also called generalized SNR since it defines a more general SNR with respect to Eq. (3.36), and the formula for deriving it, once given the coherent SNR and K , will be indicated as generalized SNR formula. In [42] Eq. (5.28) is used as an estimation of the equivalent SNR; however Eq. (5.28) has been obtained from general assumptions and it has not been directly derived from system performance indicators such as the false alarm and detection probabilities.

Similarly to the approach of the empirical formula, a squaring loss L is defined (see Eq. (5.24)) and, by using Eq. (5.28) and results from [57], the following expression is found

$$\begin{aligned}L &= 10 \log_{10} \frac{\rho_c}{\rho_K/K} = 10 \log_{10} \frac{4 - \pi}{\pi} + \rho_c|_{dB} - \\ &- 20 \log_{10} \left\{ \exp \left(-\frac{\rho_c}{4} \right) \left[\left(1 + \frac{\rho_c}{2} \right) I_0 \left(\frac{\rho_c}{4} \right) + \frac{\rho_c}{2} I_1 \left(\frac{\rho_c}{4} \right) \right] - 1 \right\}\end{aligned}\quad (5.29)$$

In Figure 5.3 the squaring loss L obtained according to Eq. (5.29) has been plotted. It is important to recognize that these results indicate that for a coherent output SNR greater than 10 dB the squaring loss becomes negative. This implies that for high coherent output SNR the use of non-coherent integrations is preferable to coherent integration, leading to a gain that tends to 3.67 dB. However this conclusion is never true since coherent integration leads to better performance in absence of bit transitions and other impairments. Therefore it can be concluded that this kind of approach [42] [57] is to be considered valid

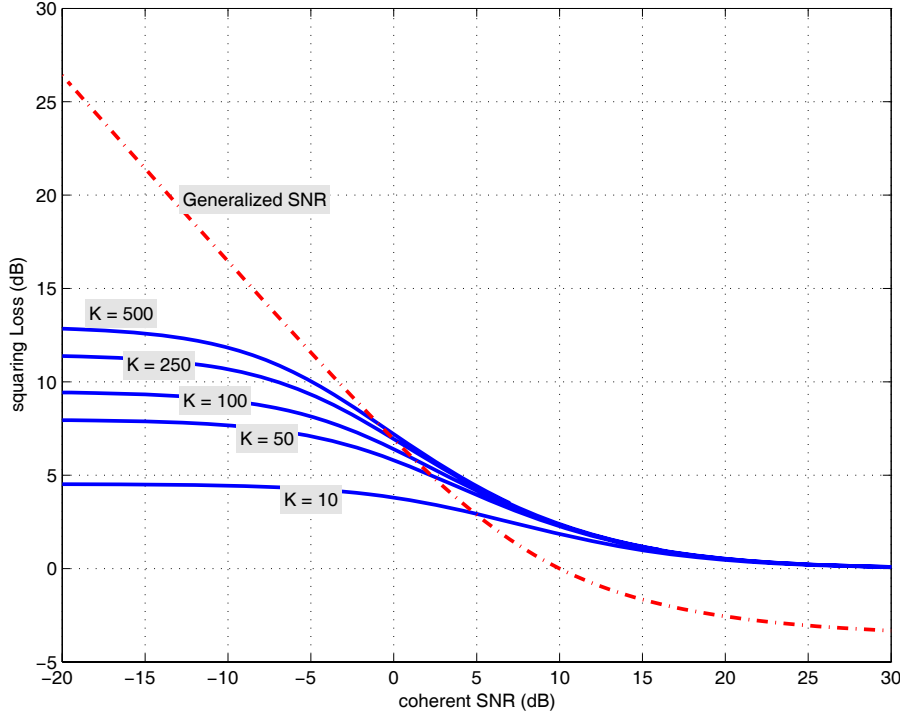


Figure 5.3. Squaring loss vs coherent SNR obtained from Eq.(5.24). The dashed line represents the loss evaluated according to Eq. (5.29) whereas the continuous curves refer to the loss obtained by using the equivalent coherent SNR evaluated according to the equivalent area criterion. In the latter case the loss depends on the number of non-coherent integrations.

only for coherent SNR $\ll 10$ dB. In Figure 5.3 the loss obtained according to definition Eq. (5.24) and the equivalent coherent SNR evaluated by means of the equivalent area criterion has been also depicted for comparison purposes. In this case the loss depends on the number of non-coherent integrations and becomes negligible for high coherent SNR.

5.3.3 Equivalent area criterion

ROCs are continuous, monotonically increasing curves constrained to pass through the points (0,0) and (1,1), since both detection and false alarm probabilities are obtained by integrating continuous probability density functions. These properties suggest a key observation: two ROCs are fairly superimposed if they are constrained to have the same area. This observation is also confirmed by the behaviors of the ROCs depicted in Figure 5.4. Previous considerations suggest that the equivalent coherent SNR evaluated according to the equivalent area criterion, is the one guaranteeing that the area under the ROC

with only coherent integration is equal to the one obtained with K non-coherent integrations:

$$\rho_K = \rho : \int_0^1 P_{d,1}(\rho) dP_{fa} = \int_0^1 P_{d,K}(\rho_c) dP_{fa} \quad (5.30)$$

Notice that Eq. (5.30) can be rewritten as

$$\rho_K = \rho : \int_0^1 [P_{d,1}(\rho) - P_{d,K}(\rho_c)] dP_{fa} = 0 \quad (5.31)$$

This condition is similar to Eq. (5.23), in which the area of the ROCs is pondered by the positive function $\frac{\partial P_{d,1}(\rho)}{\partial \rho}$. This function, $\frac{\partial P_{d,1}(\rho)}{\partial \rho}$, is positive since the detection probability monotonically increases as the coherent SNR increases.

Eq. (5.30) is simpler than Eq. (5.23) and allows a closed-form solution.

In order to solve Eq. (5.30) it is possible to verify that the area under a ROC can be expressed as

$$\int_0^1 P_{d,K}(\rho_c) dP_{fa} = 1 - \int_0^1 P_{fa} dP_{d,K}(\rho_c) \quad (5.32)$$

that is the difference between the area of the square with unitary side that contains the ROC and the area between the upper left side of the square and the ROC. In this way Eq. (5.30) becomes

$$\rho_K = \rho : \int_0^1 P_{fa} dP_{d,1}(\rho) = \int_0^1 P_{fa} dP_{d,K}(\rho_c) \quad (5.33)$$

This new condition is simpler than Eq. (5.30) since the derivative of the detection probability avoids the presence of the generalized Marcum Q-function in the computation of the integrals. In fact, by applying a variable change and expressing the integrals in terms of the normalized decision threshold β' , it results

$$\begin{aligned} \rho_K &= \rho : - \int_0^{+\infty} P_{fa,1}(\beta') \frac{\partial P_{d,1}(\beta', \rho)}{\partial \beta'} d\beta' \\ &= - \int_0^{+\infty} P_{fa,K}(\beta') \frac{\partial P_{d,K}(\beta', \rho_c)}{\partial \beta'} d\beta' \end{aligned} \quad (5.34)$$

Notice that, in the change of variable, two different expressions of the false alarm probability are adopted in the two integrals. In order to solve Eq. (5.34), it is necessary to evaluate the integral

$$A_K = - \int_0^{+\infty} P_{fa,K}(\beta') \frac{\partial P_{d,K}(\beta', \rho_c)}{\partial \beta'} d\beta' \quad (5.35)$$

By substituting Eq. (5.5) into Eq. (5.35), it follows:

$$\begin{aligned} A_K &= \int_0^{+\infty} \frac{1}{2} \left(\frac{\beta'}{K \rho_c} \right)^{\frac{K-1}{2}} \left[\sum_{i=0}^{K-1} \frac{1}{i!} \left(\frac{\beta'}{2} \right)^i \right] \cdot \\ &\quad \exp \left\{ -\frac{1}{2} (2\beta' + K\rho_c) \right\} I_{K-1} \left(\sqrt{K\rho_c \beta'} \right) d\beta' \end{aligned} \quad (5.36)$$

After some calculations and the substitution $\gamma = \sqrt{2\beta'}$ and $a_K = \sqrt{\rho_c/2}$, A_K becomes

$$A_K = \left(\frac{1}{2}\right)^K \exp\left\{-\frac{1}{2}Ka_K^2\right\} \sum_{i=0}^{K-1} \frac{1}{i!4^i} \cdot \int_0^{+\infty} \gamma^{2i} \gamma \left(\frac{\gamma}{\sqrt{Ka_K}}\right)^{K-1} \exp\left\{-\frac{1}{2}(\gamma^2 + Ka_K^2)\right\} \cdot I_{K-1}(\gamma\sqrt{Ka_K}) d\gamma \quad (5.37)$$

The term $\gamma \left(\frac{\gamma}{\sqrt{Ka_K}}\right)^{K-1} \exp\left\{-\frac{1}{2}(\gamma^2 + Ka_K^2)\right\} I_{K-1}(\gamma\sqrt{Ka_K})$ corresponds to the probability density function of a non-central χ random variable with $2K$ degrees of freedom and non-centrality parameter $\lambda = \sqrt{Ka_K}$. Thus the integrals involved in the summation in Eq. (5.37) correspond to the non-central moments of a χ -square random variable:

$$A_K = \left(\frac{1}{2}\right)^K \exp\left\{-\frac{1}{2}Ka_K^2\right\} \sum_{i=0}^{K-1} \frac{1}{i!4^i} E\left[(\chi_{2K}^2)^i\right] \quad (5.38)$$

and they can be evaluated by deriving its Moment Generating Function (MGF) [58]. Alternatively $E\left[(\chi_{2K}^2)^i\right]$ can be evaluated by using properties of the Gaussian random variables from which a χ_{2K}^2 random variable is generated.

When $K = 1$

$$A_1 = \frac{1}{2} \exp\left\{-\frac{1}{2}a_1^2\right\} = \frac{1}{2} \exp\left\{-\frac{1}{4}\rho_c\right\} \quad (5.39)$$

and thus, by solving Eq. (5.34), the following expression for the equivalent SNR is obtained:

$$\begin{aligned} \rho_K &= K\rho_c - 4 \log \left[\left(\frac{1}{2}\right)^{K-1} \sum_{i=0}^{K-1} \frac{1}{i!4^i} E\left[(\chi_{2K}^2)^i\right] \right] = \\ &= K\rho_c - 4 \log[P_{K-1}(\rho_c)] \end{aligned} \quad (5.40)$$

where $P_K(\rho_c)$ is a polynomial of degree $K - 1$ in ρ_c . In Appendix C a recursive algorithm for evaluating $P_K(\rho_c)$ is provided.

In Table 5.1 the expressions of the equivalent coherent SNR for $K = 1, 2, \dots, 5$ have been explicitly reported whereas in Figure 5.4 original ROCs are compared with the ones determined by the equivalent coherent SNR and coherent integration only. The ROCs almost superimpose for a wide range of false alarm probabilities assessing the validity of the equivalent area criterion.

As for the minimum distance case, the integrals in Eq. (5.30) can be limited in the interval $[0, P_{\max}]$ where P_{\max} is maximum false alarm probability of interest. However, by doing so, it is no longer possible to find a closed-form formula such as Eq. (5.40). Furthermore, as pointed out by Figure 5.4, the approximation given by the equivalent area criterion is

Table 5.1. Equivalent coherent SNR when K non-coherent integrations are employed.

K	A_K	Equivalent coherent SNR
1	$\frac{1}{2} \exp \left\{ -\frac{1}{4} \rho_c \right\}$	$\rho_1 = \rho_c$
2	$\frac{1}{2} \exp \left\{ -\frac{1}{2} \rho_c \right\} \left[1 + \frac{1}{8} \rho_c \right]$	$\rho_2 = 2\rho_c - 4 \log \left[1 + \frac{1}{8} \rho_c \right]$
3	$\frac{1}{2} \exp \left\{ -\frac{3}{4} \rho_c \right\} \left[1 + \frac{9}{32} \rho_c + \frac{9}{512} \rho_c^2 \right]$	$\rho_3 = 3\rho_c - 4 \log \left[1 + \frac{9}{32} \rho_c + \frac{9}{512} \rho_c^2 \right]$
4	$\frac{1}{2} \exp \left\{ -\rho_c \right\} \left[1 + \frac{29}{64} \rho_c + \frac{1}{16} \rho_c^2 + \frac{1}{384} \rho_c^3 \right]$	$\rho_4 = 4\rho_c - 4 \log \left[1 + \frac{29}{64} \rho_c + \frac{1}{16} \rho_c^2 + \frac{1}{384} \rho_c^3 \right]$
5	$\frac{1}{2} \exp \left\{ -\frac{5}{4} \rho_c \right\} \cdot \left[1 + \frac{325}{512} \rho_c + \frac{575}{4096} \rho_c^2 + \frac{213}{16751} \rho_c^3 + \frac{12}{30199} \rho_c^4 \right]$	$\rho_5 = 5\rho_c - 4 \log \left[1 + \frac{325}{512} \rho_c + \frac{575}{4096} \rho_c^2 + \frac{213}{16751} \rho_c^3 + \frac{12}{30199} \rho_c^4 \right]$

also accurate for low values of false alarm probability, without limiting the integrals in Eq. (5.30) on the interval $[0, P_{\max}]$. This result is confirmed by Figure 5.5 where a comparison of ROCs obtained by using different criteria for evaluating the equivalent SNR is depicted: also in this case the equivalent area criterion is the conversion formula providing the best results, providing a good approximation of the original ROCs also for low values of false alarm probability.

Eq. (5.40) allows the evaluation of the equivalent coherent SNR for different values of input SNR. However, for high values of K its computation can be burdensome. The difficulties in using Eq. (5.40) are in the evaluation of the polynomial $P_{K-1}(\rho_c)$ that involves the subsequent derivation of the MGF of a non-central χ^2 random variable.

However when the coherent SNR is lower than 0 dB, $P_{K-1}(\rho_c)$ can be truncated at the first two terms, and the logarithmic in Eq. (5.40) can be approximated by its Taylor expansion. In Appendix D it is shown that the constant term of $P_{K-1}(\rho_c)$ is always 1 and that the linear term equals

$$\frac{K}{4} \left[1 - \frac{1}{2^{2K-1}} \binom{2K}{K} \right] \rho_c \quad (5.41)$$

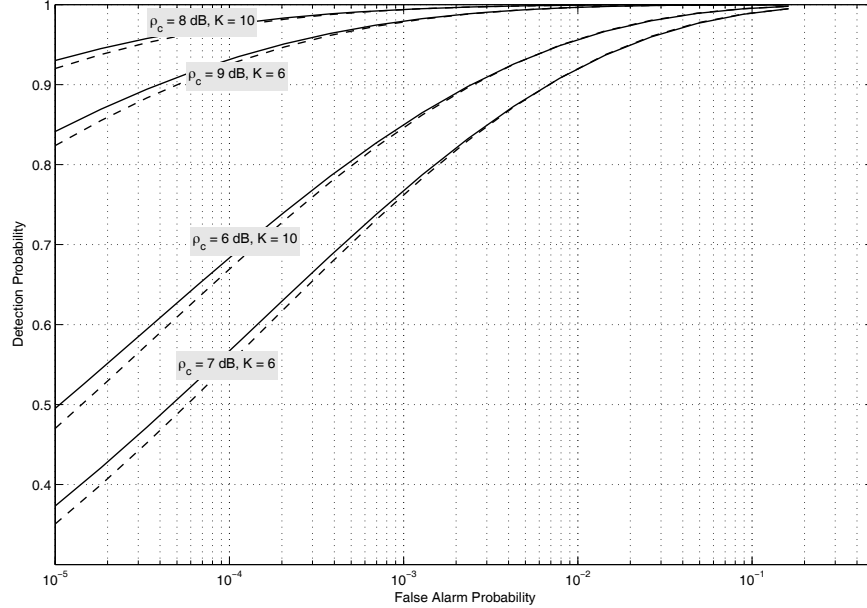


Figure 5.4. Comparisons between ROCs obtained with K non-coherent integrations (continuous curves) and the ones obtained by using only coherent integration and the corresponding equivalent coherent SNR (dashed curves). Parameter ρ_c is the coherent SNR.

From those results

$$P_{K-1}(\rho_c) = 1 + \frac{K}{4} \left[1 - \frac{1}{2^{2K-1}} \binom{2K}{K} \right] \rho_c + O(\rho_c^2) \quad (5.42)$$

For large values of K it is possible to apply the Stirling formula [59] for binomial, obtaining the following approximation:

$$P_{K-1}(\rho_c) \approx 1 + \frac{K}{4} \left[1 - \frac{2}{\sqrt{\pi K}} \right] \rho_c + O(\rho_c^2) \quad (5.43)$$

By substituting this result into Eq. (5.40), the following expression for the equivalent coherent SNR is found:

$$\begin{aligned} \rho_K &\approx K\rho_c - 4 \log \left(1 + \frac{K}{4} \left[1 - \frac{2}{\sqrt{\pi K}} \right] \rho_c \right) \\ &\approx \frac{2}{\sqrt{\pi}} \sqrt{K} \rho_c = 1.128 \sqrt{K} \rho_c \end{aligned} \quad (5.44)$$

Formula (5.44) states that the gain provided by non-coherent integrations is proportional to the square root of K . This result is similar to the one obtained by the empirical formula (5.27). However the coefficients that multiply the square-root of K are different, and the gains evaluated by the two formulas differ of 5 dB. Those formulas will be compared and tested in the next section.

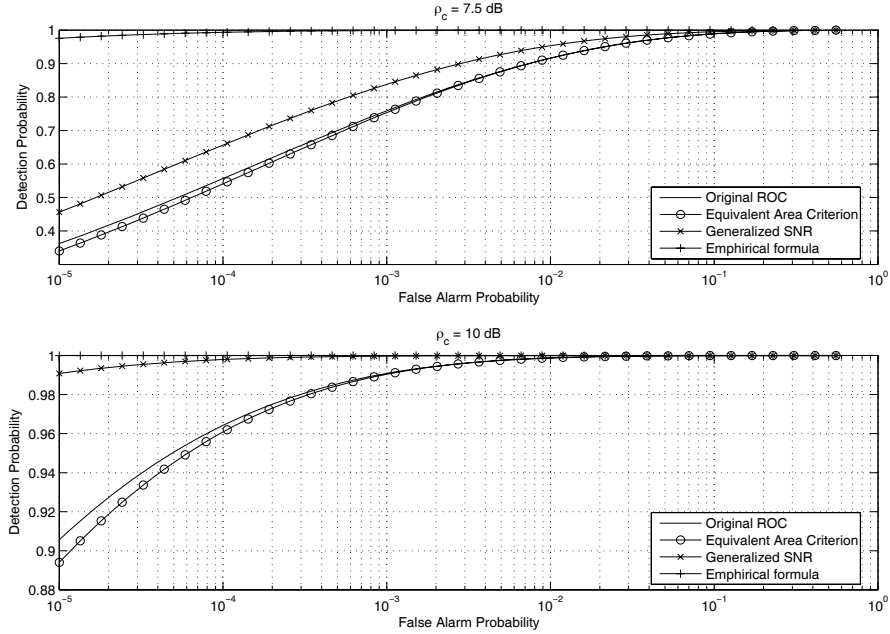


Figure 5.5. Comparisons of ROCs obtained by using different criteria for evaluating the equivalent coherent SNR. Continuous curves represent the original ROCs obtained by using K non-coherent integrations. The other curves are obtained by using only coherent integrations and the equivalent SNR evaluated according to different criteria. In the title, ρ_c is the coherent SNR, while the number of non-coherent integrations is $K = 5$ in both subplots.

5.4 Formulas validation

In previous sections, different strategies have been presented in order to find a suitable formula for determining the equivalent SNR. In Table 5.2 the three conversion formulas previously considered are reported. These formulas are quite different and a criterion for comparing their validity is necessary. In this section these formulas are tested by using two different approaches. Firstly the conversion formulas are compared by using target values of detection probability. Secondly the concept of *ROC distance* is defined and employed to directly compare the formulas.

5.4.1 Test for fixed false alarm probability

The validity of the conversion formulas has been firstly tested by considering single values of the ROC for a fixed false alarm probability. Further, the conversion formulas allow the determination of the number of non-coherent integrations needed to obtain a target equivalent SNR given an input coherent SNR. In the second column of Table 5.2 the conversion formulas have been inverted in order to find the expression of K as a function

Table 5.2. Conversion formulas for determining the equivalent SNR and the number of non-coherent integrations.

Empirical formula	$\rho_K = 3.548\sqrt{K}\rho_c$	$K = f_1(\rho_c, \rho_K)$ $= \left\lceil 0.282 \left(\frac{\rho_K}{\rho_c} \right)^2 \right\rceil$
Generalized SNR approach	$\rho_K = K\rho_c 10^{-L/10}$	$K = f_2(\rho_c, \rho_K)$ $= \left\lceil \frac{\rho_K}{\rho_c} 10^{L/10} \right\rceil$
Equivalent area approach	$\rho_K = 1.128\sqrt{K}\rho_c$	$K = f_3(\rho_c, \rho_K)$ $= \left\lceil 0.887 \left(\frac{\rho_K}{\rho_c} \right)^2 \right\rceil$

of an input coherent SNR, ρ_c , and of a target equivalent SNR ρ_K . $\lceil x \rceil$ is the ceiling operator, that corresponds to the smallest integer greater or equal to x . Thus these formulas have been used to determine K , once both target equivalent and coherent SNRs are fixed. Then, for each value of false alarm probability, a detection probability is determined. By using the target equivalent SNR and only coherent integration, another detection probability is obtained by inverting Eq. (5.5) with $K = 1$. This detection probability is denoted hereinafter as the target detection probability and the best conversion formula is the one that leads to the detection probability that better matches the target probability. In Figures 5.6 and 5.7 different detection probabilities have been plotted for $P_{fa} = 10^{-3}$. For each value of coherent SNR, four bars have been plotted, one representing the target detection probability fixed by the target equivalent SNR and the other three obtained by using the conversion formulas. In Figure 5.6 the case of a target equivalent SNR = 5 dB is considered, whereas in Figure 5.7 the target equivalent SNR is equal to 10 dB. The different bars in both figures have been obtained by Monte Carlo simulation. It has been verified that the estimated detection probabilities agree well with the theoretical values thus proving the validity of Eq. (5.5).

Figures 5.6 and 5.7 highlight that the equivalent area approach effectively quantifies the impact of non-coherent integrations when the target equivalent SNR is low, a scenario where non-coherent integrations can be quite valuable. The generalized SNR approach is preferable for high target equivalent SNR. It can also be noted that in this section only the approximated expression (5.44) is employed for testing the validity of the equivalent

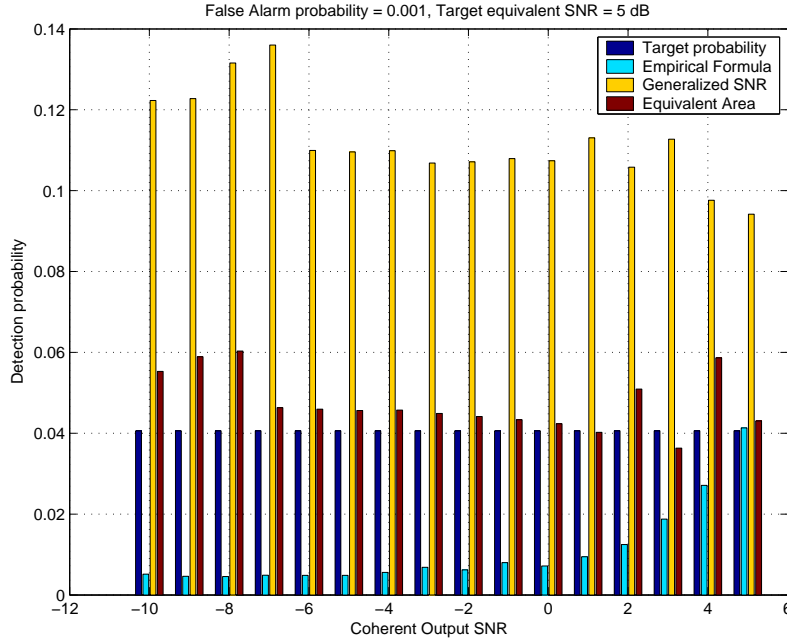


Figure 5.6. Comparison between different detection probabilities achieved with $P_{fa} = 10^{-3}$ and target equivalent SNR = 5 dB.

area criterion and that better results could be expected upon using Eq. (5.40).

5.4.2 ROC distance

In Section 5.3 the equivalent SNR is defined as the one that minimizes the Euclidean square distance between two ROCs: a ROC obtained by using only coherent integration and a ROC obtained by using K non-coherent integrations.

The validity of the conversion formulas can be thus measured by the Euclidean square distance between the ROC defined by the target equivalent SNR using coherent integration only and the one fixed by the input coherent SNR and the K non-coherent integrations determined by using the conversion formulas:

$$J_1(i) = \int_0^1 |P_{d,1}(\rho_K) - P_{d,K_i}(\rho_c)|^2 dP_{fa} \quad (5.45)$$

$$K_i = f_i(\rho_c, \rho_K) \quad i = 1, 2, 3.$$

where K_i is the number of non-coherent integrations determined by using the conversion formulas in the second column of Table 5.2. This metric is obtained by averaging the distance between detection probabilities with respect to all the possible values of false alarm probabilities. However, only relative low values of false alarm probability are of

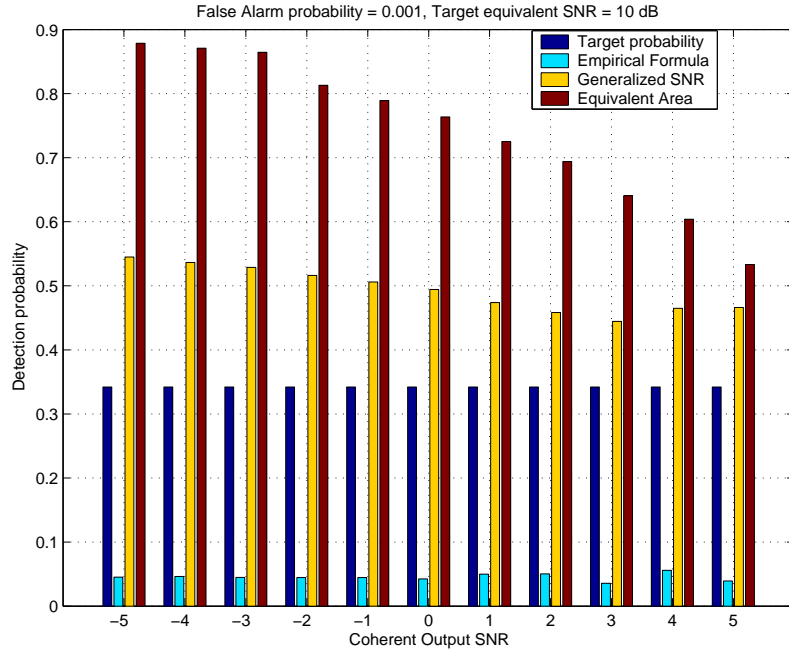


Figure 5.7. Comparison between different detection probabilities achieved with $P_{fa} = 10^{-3}$ and target equivalent SNR = 10 dB.

interest, thus Eq. (5.45) can be generalized to

$$J_{P_{max}}(i) = \int_0^{P_{max}} |P_{d,1}(\rho_K) - P_{d,K_i}(\rho_c)|^2 dP_{fa} \quad (5.46)$$

$$K_i = f_i(\rho_c, \rho_K) \quad i = 1, 2, 3.$$

where P_{max} is the maximum value of false alarm probability. In this way $J_{P_{max}}(i)$ is the mean distance between detection probabilities with respect to the false alarm probabilities in the range $[0, P_{max}]$. In Figure 5.8 the number of non-coherent integrations required for obtaining a target equivalent SNR = 5 dB (according to the different conversion formulas) has been plotted for different values of coherent SNR. The corresponding ROC distance, for $P_{max} = 0.1$, has been reported in Figure 5.9. In this case the equivalent area criterion is the one that gives the best performance. The ROC obtained with the number of non-coherent integrations determined by this formula is the closest to that fixed by the target equivalent SNR. In Figure 5.9 a horizontal line, indicated by the label “1-dB error threshold” is also present. This line represents the distance between two ROCs obtained by using only coherent integrations but whose coherent SNRs differ by 1 dB:

$$E_{1dB, P_{max}} = \int_0^{P_{max}} \left| P_{d,1}(\rho_K) - P_{d,1} \left(10^{-1dB/10} \rho_K \right) \right|^2 dP_{fa} \quad (5.47)$$

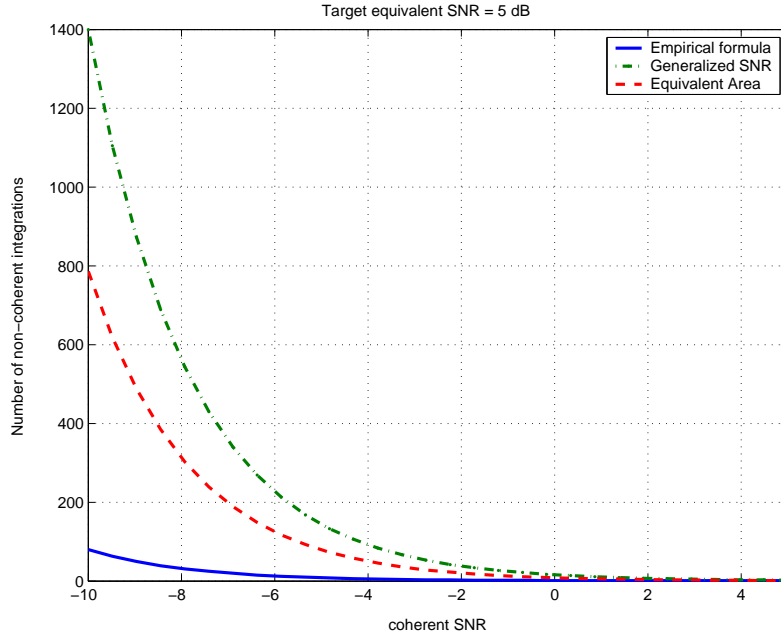


Figure 5.8. Number of non-coherent integrations vs coherent SNR for a target equivalent SNR = 5 dB.

This error allows a qualitative perception of the error resulting from using the conversion formulas in terms of the target equivalent SNR. In fact, if the ROC distance is below this threshold then the error in obtaining the target equivalent SNR is less than 1 dB.

In Figure 5.9 the ROC distance obtained by using the equivalent area conversion formula is quite close to the 1-dB error threshold, and below this threshold for coherent SNR greater than -6 dB, showing the validity of this approach.

In Figures 5.10 and 5.11 the case of a target equivalent SNR = 10 dB is considered. In this case the best performance is achieved by using the generalized SNR formula. The equivalent area criterion overestimates the number of non-coherent integrations, leading to an error greater than 1 dB with respect to the target equivalent SNR. The empirical formula always underestimates the number of non-coherent integrations and can be used as a lower bound on K .

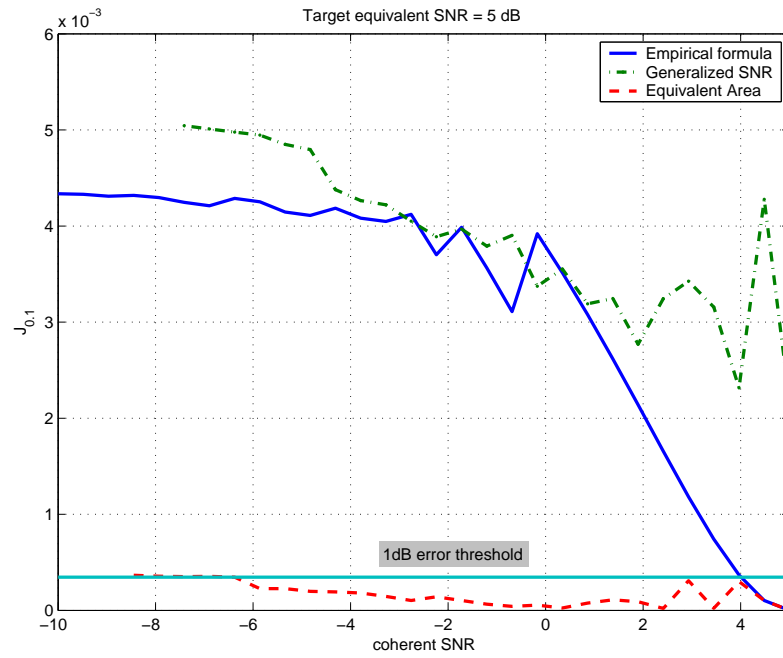


Figure 5.9. ROC distance with $P_{max} = 0.1$ vs coherent SNR for a target equivalent SNR = 5 dB.

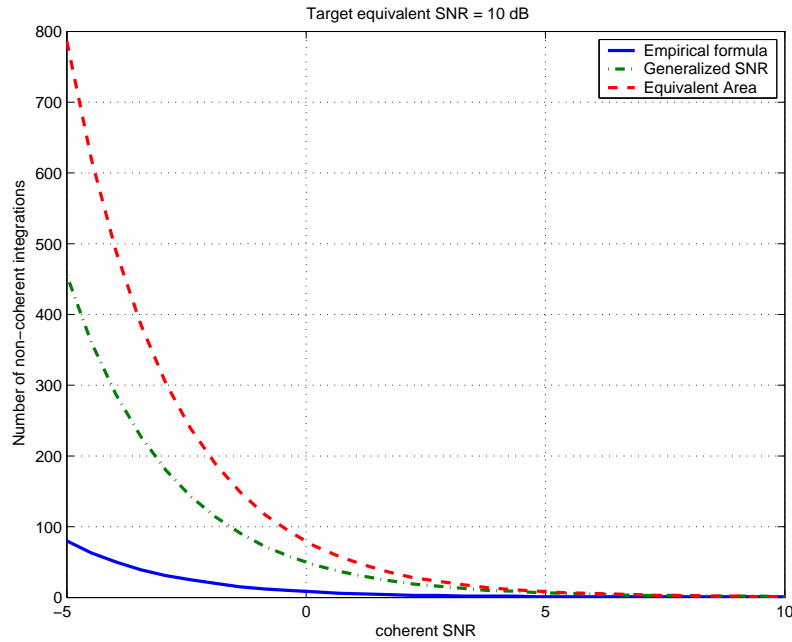


Figure 5.10. Number of non-coherent integrations vs coherent SNR for a target equivalent SNR = 10 dB.

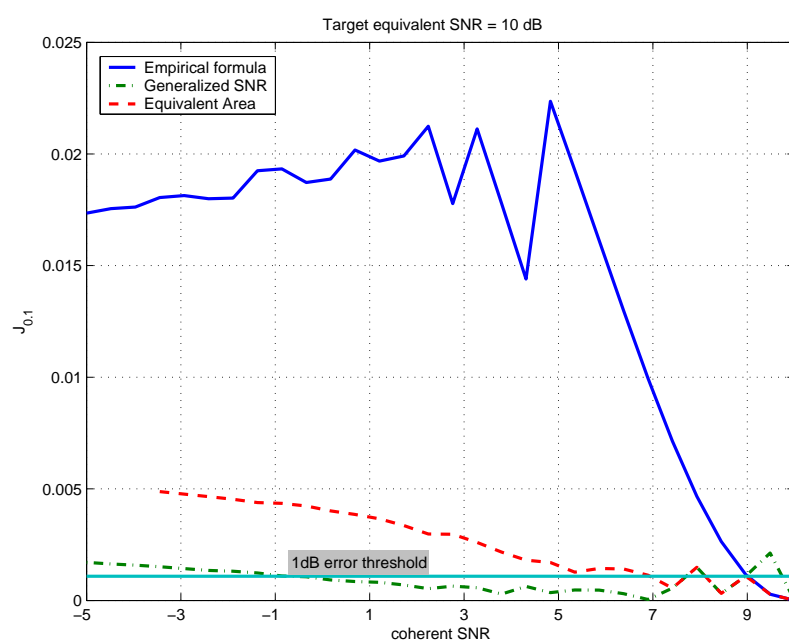


Figure 5.11. ROC distance with $P_{max} = 0.1$ vs coherent SNR for a target equivalent SNR = 10 dB.

Chapter 6

Acquisition losses

In previous chapters the acquisition process was analyzed under ideal conditions, i.e. different error sources were neglected. The following assumptions were made:

- the frontend does not essentially impact the signal component,
- the noise term entering the acquisition block is a white sequence,
- the quantization impact is essentially negligible,
- under the H_1 hypothesis the Doppler frequency and the delay of the local signal replica are exactly the same as that of the incoming signal.

In real applications none of these assumptions are strictly true and this has to be taken into account in order to correctly characterize the acquisition performance. In this chapter the effect of the frontend filtering on the useful signal and on the noise components is discussed. The quantization impact is also quantified in term of coherent output SNR and a general formula for the quantization loss is provided. Finally the effects of residual Doppler frequency and delay alignment error are briefly discussed.

6.1 Frontend filtering

The first stages of a GNSS receiver are the antenna and the frontend, which are used to recover the GNSS signal. The frontend downconverts, filters and amplifies the useful signal (Figure 6.1). The received signal is then AD converted. In this section the filtering effect of the frontend is considered. In particular it is assumed that the frontend can be modeled as a low-pass filter that introduces correlation among the noise samples and smoothes the useful signal.

Thus the signal at the input of the acquisition block is, in general, composed of a colored noise component and a filtered version of the transmitted GNSS signal. These effects can

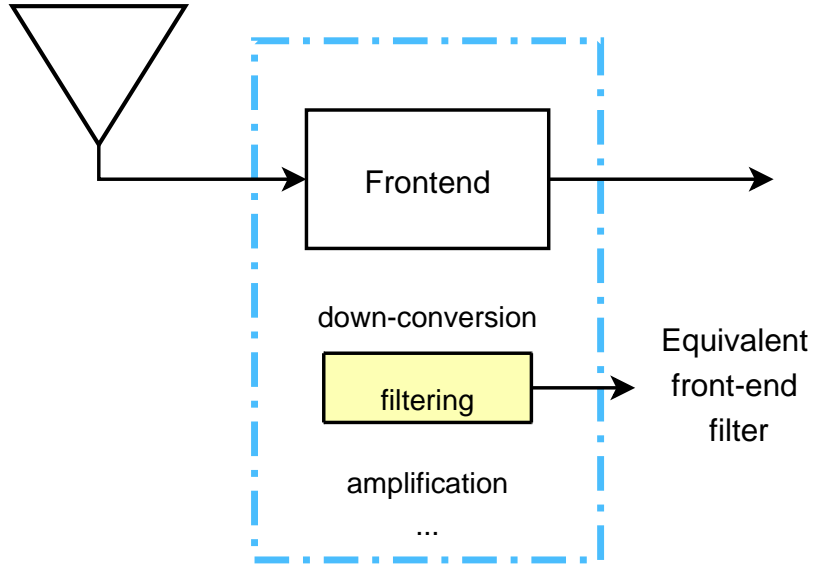


Figure 6.1. The first stages of a GNSS receiver are the antenna and the frontend, used to recover the GNSS signal. The frontend downconverts, filters and amplifies the received signal.

be accounted for an equivalent filter $h_f[n]$ that models the frontend filtering. In Figure 6.2 the equivalent model for the frontend filtering is reported. In this section the effect of the equivalent filter $h_f[n]$ on the coherent output SNR is derived.

6.1.1 Equivalent representation of the acquisition block

In order to simplify the analysis of the impact of the frontend filtering on the coherent output SNR it is useful to introduce an equivalent representation of the acquisition block. In particular, by considering Figure 3.5 it is possible to notice that all the operations before the squaring blocks are linear and thus can be modeled in terms of products and convolutions. Consider at first the code multiplication and the subsequent integration:

$$\begin{aligned} Y_I(\tau, F_D) &= \frac{1}{N} \sum_{n=0}^{N-1} Y_c[n, F_D] c[n - \tau] \\ Y_Q(\tau, F_D) &= \frac{1}{N} \sum_{n=0}^{N-1} Y_s[n, F_D] c[n - \tau] \end{aligned} \tag{6.1}$$

where $Y_I(\tau, F_D)$, $Y_Q(\tau, F_D)$, $Y_c[n, F_D]$ and $Y_s[n, F_D]$ are the signals introduced in Chapter 3. By manipulating Eq. (6.1) it clearly emerges that these operations can be expressed as

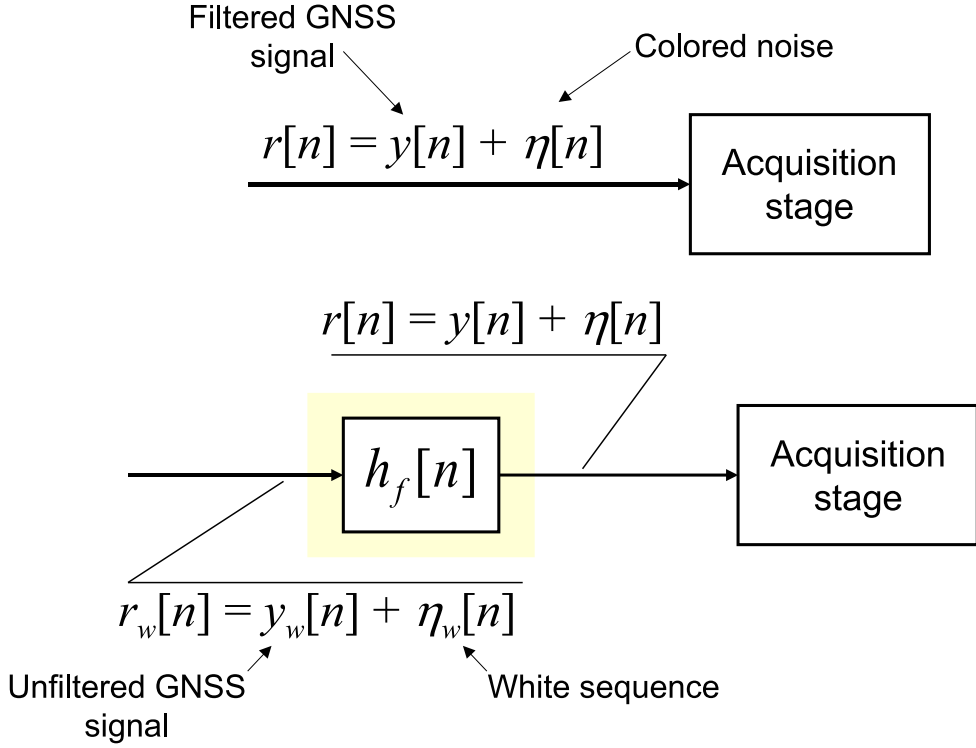


Figure 6.2. The signal at the input of the acquisition block is composed of the useful GNSS signal and a noise component. In general the noise component is a colored sequence and the useful signal is a filtered version of the transmitted GNSS signal. These effects can be accounted by an equivalent filter $h_f[n]$ that models the frontend filtering.

a convolution with a code equivalent filter as

$$\begin{aligned} Y_I(\tau, F_D) &= \sum_{n=0}^{N-1} r_c[n, F_D] \frac{1}{N} c[-(\tau - n)] = r_c[\tau, F_D] * h_c[\tau] \\ Y_Q(\tau, F_D) &= \sum_{n=0}^{N-1} r_s[n, F_D] \frac{1}{N} c[-(\tau - n)] = r_s[\tau, F_D] * h_c[\tau] \end{aligned} \quad (6.2)$$

where

$$h_c[\tau] = \frac{1}{N} c[-\tau] \quad (6.3)$$

is the equivalent code filter. This formulation of the code multiplication and of the subsequent integration leads to the equivalent acquisition scheme reported in Figure 6.3a). A second step in representing the acquisition block is obtained by introducing a complex notation for denoting the multiplications by the two local carriers and the final squaring operations. In fact the multiplication by the two local sinusoids on the in-phase and

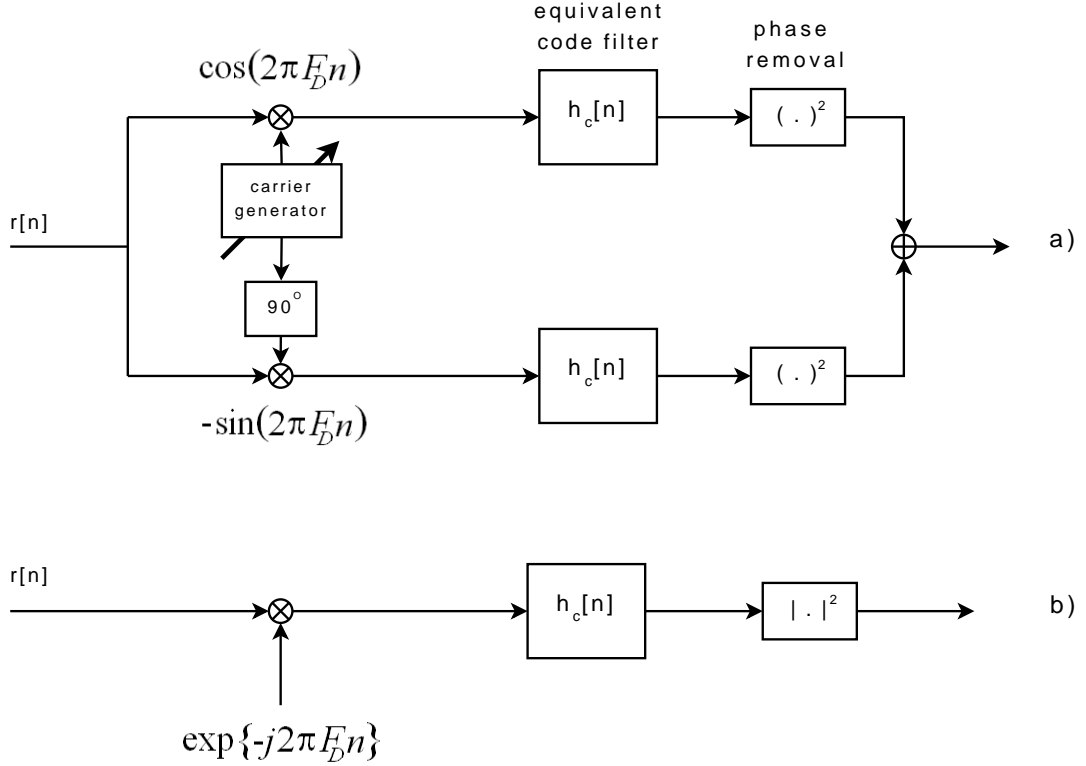


Figure 6.3. Equivalent representations of the basic acquisition scheme. a) the code multiplication and the subsequent integration can be interpreted as an equivalent filtering. b) Equivalent complex representation of the acquisition block.

quadrature branches can be represented by a multiplication by a complex sinusoid and the squaring operations can be substituted by a square modulus. These conventions lead to the representation depicted in Figure 6.3b) that shows that the acquisition block is a special form of the *quadrature matched filter* [60].

6.1.2 Coherent output SNR

In Section 3.7 the coherent output SNR has been defined as

$$\rho_c = \max_{\phi_0} \frac{\text{E}^2 [Y_I(\tau, F_D)]}{\text{Var}[Y_I(\tau, F_D)]} \quad (6.4)$$

where $Y_I(\tau, F_D)$ was obtained by neglecting the frontend filtering effect.

By using the equivalent representation developed in last section, one can possible to write:

$$Y_I(\tau, F_D) + jY_Q(\tau, F_D) = r[\tau] \exp \{-j2\pi F_D \tau\} * h_c[\tau]. \quad (6.5)$$

In the presence of frontend filtering, the input signal $r[n]$ can be written (see Figure 6.2) as

$$r[n] = r_w[n] * h_f[n] = y_w[n] * h_f[n] + \eta_w[n] * h_f[n] \quad (6.6)$$

where $h_f[n]$ is the equivalent filter that accounts for the effects of the frontend. $r_w[n] = y_w[n] + \eta_w[n]$ is the ideal input signal; $y_w[n]$ is the unfiltered GNSS signal and $\eta_w[n]$ is the input white noise characterized by power spectral density equal to $N_0 f_s / 2$. $r_w[n]$ is the ideal signal that follows the model described in Chapter 2. From Eq. (6.6) it is possible to derive the power spectral density of the noise component $\eta[n] = \eta_w[n] * h_f[n]$ as

$$G_\eta(f) = \frac{N_0}{2} f_s |H_f(f)|^2 \quad (6.7)$$

where $H_f(f)$ is the Discrete Fourier Transform (DFT) of the equivalent filter $h_f[n]$.

By using Eq. (6.5) it is then possible to evaluate the variance of $Y_I(\tau, F_D) + jY_Q(\tau, F_D)$:

$$\begin{aligned} \text{Var}\{Y_I(\tau, F_D) + jY_Q(\tau, F_D)\} &= 2\text{Var}\{Y_I(\tau, F_D)\} = \frac{N_0}{2} f_s \int_{-0.5}^{0.5} |H_f(f + F_D)|^2 |H_c(f)|^2 df \\ &\approx \frac{N_0}{2} f_s \int_{-0.5}^{0.5} |H_f(f + f_{IF} T_s)|^2 |H_c(f)|^2 df = \frac{N_0}{2} f_s \int_{-0.5}^{0.5} \tilde{G}(f) |H_c(f)|^2 df \end{aligned} \quad (6.8)$$

where $\tilde{G}(f) = |H_f(f + f_{IF} T_s)|^2$ is the noise PSD after modulation by the complex exponential $\exp\{-j2\pi F_D n\}$. In Figure 6.4 the process that leads to $\tilde{G}(f)$ is better explained. The frontend filter colors the input noise that can present a PSD similar to the one in Figure 6.4a). The complex exponential translates the noise component to the baseband and the equivalent code filter acts a low-pass filter. Since the Doppler frequency is usually small with respect to the intermediate frequency and since $|H_f(f + f_{IF} T_s)|^2$ is usually constant around the zero frequency, the effect of f_d can be neglected.

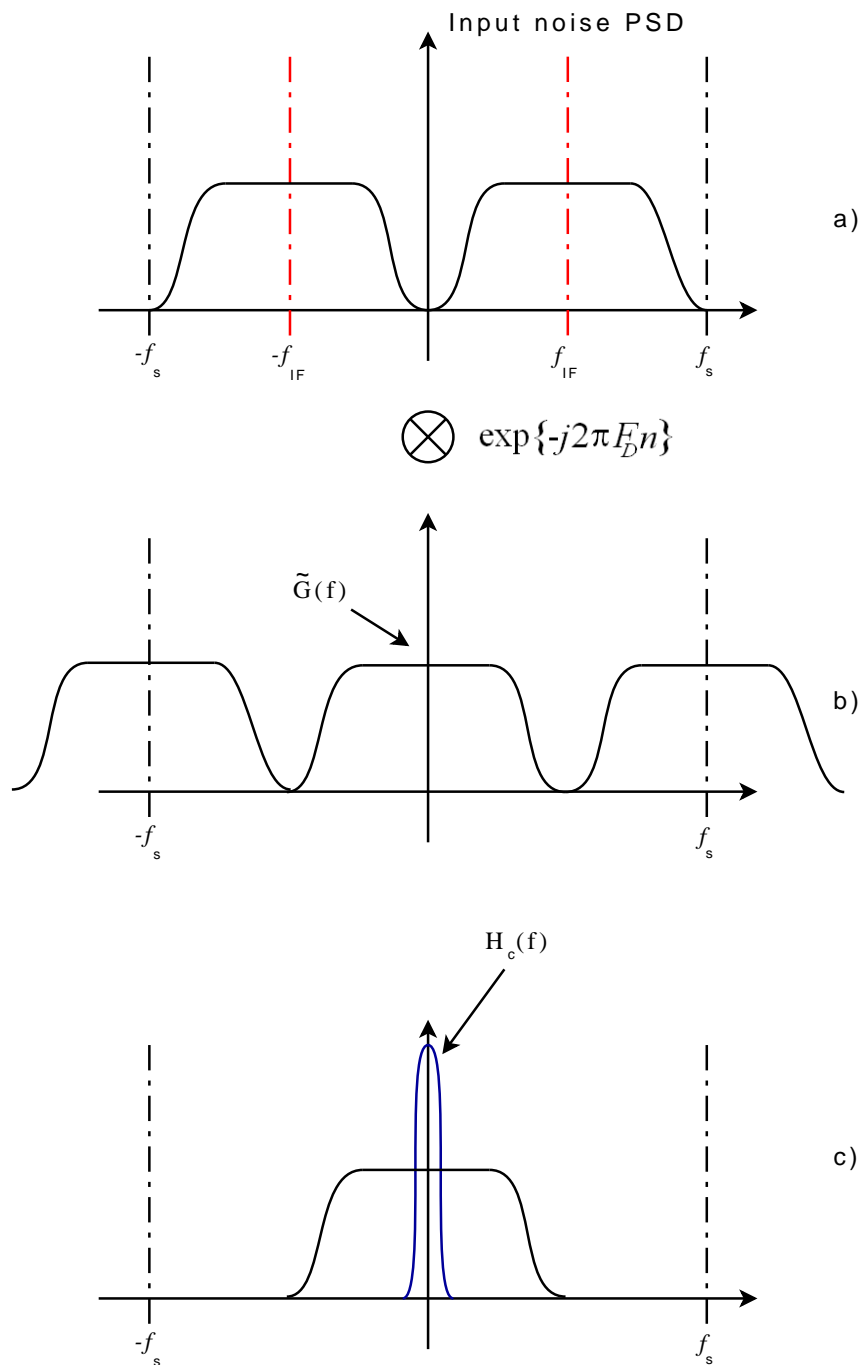


Figure 6.4. Effect of the different acquisition stage blocks on the noise PSD. a) Input signal PSD. b) Effect of the complex modulation. c) Effect of the equivalent code filtering.

Since the noise power is equally distributed on the in-phase and quadrature components it is possible to write:

$$\text{Var} \{Y_I(\tau, F_D)\} = \text{Var} \{Y_Q(\tau, F_D)\} = \frac{N_0}{4} f_s \int_{-0.5}^{0.5} \tilde{G}(f) |H_c(f)|^2 df \quad (6.9)$$

When the noise component is a white sequence $\tilde{G}(f) = 1$, Eq. (6.9) becomes

$$\begin{aligned} \text{Var} \{Y_I(\tau, F_D)\} &= \frac{N_0}{4} f_s \int_{-0.5}^{0.5} |H_c(f)|^2 df \\ &= \frac{N_0}{4} f_s \sum_{n=0}^{N-1} |h_c[n]|^2 = \frac{N_0}{4} f_s \sum_{n=0}^{N-1} \frac{1}{N^2} = \frac{N_0 f_s / 2}{2N} = \frac{\sigma_{IF}^2}{2N}. \end{aligned} \quad (6.10)$$

Eq. (6.10) corresponds to the ideal case discussed in Section 3.6.

The mean of $Y_I(\tau, F_D) + jY_Q(\tau, F_D)$ is given by

$$\begin{aligned} \text{E} \{Y_I(\tau, F_D) + jY_Q(\tau, F_D)\} &= (y[\tau] \exp \{-j2\pi F_D \tau\}) * h_c[\tau] \\ &= [(y_w[\tau] * h_f[\tau]) \exp \{-j2\pi F_D \tau\}] * h_c[\tau] \\ &= (y_w[\tau] \exp \{-j2\pi F_D \tau\}) * (h_f[\tau] \exp \{-j2\pi F_D \tau\}) * h_c[\tau] \\ &= [(y_w[\tau] \exp \{-j2\pi F_D \tau\}) * h_c[\tau]] * (h_f[\tau] \exp \{-j2\pi F_D \tau\}) \\ &= [(y_w[\tau] \exp \{-j2\pi F_D \tau\}) * h_c[\tau]] * \tilde{h}_f[\tau] \end{aligned} \quad (6.11)$$

where

$$\tilde{h}_f[\tau] = h_f[\tau] \exp \{-j2\pi F_D \tau\}.$$

The term

$$(y_w[\tau] \exp \{-j2\pi F_D \tau\}) * h_c[\tau]$$

corresponds to the correlation with the ideal signal considered in Chapter 3 and, under the condition of frequency alignment, $F_D = F_{D,0}$, it becomes

$$(y_w[\tau] \exp \{j2\pi F_D \tau\}) * h_c[\tau] = \frac{A}{2} R(\tau - \tau_0) \exp \{j\phi_0\} \quad (6.12)$$

By exploiting the equality (6.12), Eq. (6.11) becomes

$$\begin{aligned} \text{E} \{Y_I(\tau, F_D) + jY_Q(\tau, F_D)\} &= \frac{A}{2} R(\tau - \tau_0) \exp \{j\phi_0\} * \tilde{h}_f[\tau] \\ &= \frac{A}{2} [R(\tau - \tau_0) * \tilde{h}_f[\tau]] \exp \{j\phi_0\} = \frac{A}{2} [R(\tau) * \tilde{h}_f[\tau] * \delta(\tau - \tau_0)] \exp \{j\phi_0\} \\ &= \frac{A}{2} \tilde{R}(\tau) * \delta(\tau - \tau_0) \exp \{j\phi_0\} = \frac{A}{2} \tilde{R}(\tau - \tau_0) \exp \{j\phi_0\} \end{aligned} \quad (6.13)$$

where $\tilde{R}(\tau) = R(\tau) * \tilde{h}_f[\tau]$ is the cross-correlation between the filtered and unfiltered version of the GNSS code.

From Eq. (6.13) it is finally possible to derive the mean of $Y_I(\tau, F_D)$, which results in

$$\text{E} \{Y_I(\tau, F_D)\} = \frac{A}{2} \tilde{R}(\tau - \tau_0) \cos \phi_0. \quad (6.14)$$

Under the hypothesis of code alignment $\tau = \tau_0$ the mean $E\{Y_I(\tau, F_D)\}$ becomes

$$\begin{aligned} E\{Y_I(\tau, F_D)\} &= \frac{A}{2}\tilde{R}(0)\cos\phi_0 = \frac{A}{2}\int_{-0.5}^{0.5}\tilde{G}_s(f)df\cos\phi_0 \\ &= \frac{A}{2}\int_{-0.5}^{0.5}G_s(f)H_f(f+F_D)df\cos\phi_0 \approx \frac{A}{2}\int_{-0.5}^{0.5}G_s(f)H_f(f+f_{IFT}s)df\cos\phi_0 \end{aligned} \quad (6.15)$$

where $G_s(f)$ and $\tilde{G}_s(f)$ are the Fourier transforms of $R(\tau)$ and $\tilde{R}(\tau)$ respectively. It is noted that in the absence of frontend filtering, $\tilde{R}(\tau) = R(\tau)$. Thus, by exploiting $R(0) = 1$, Eq. (6.15) becomes

$$E\{Y_I(\tau, F_D)\} = \frac{A}{2}\cos\phi_0, \quad (6.16)$$

which corresponds to the result obtained in Chapter 3.

By using Eqs. (6.8) and (6.15) it is finally possible to evaluate the coherent output SNR in the presence of frontend filtering as:

$$\rho_{c,f} = \frac{\left[\frac{A}{2}\int_{-0.5}^{0.5}G_s(f)H_f(f+f_{IFT}s)df\right]^2}{\frac{N_0}{4}f_s\int_{-0.5}^{0.5}|H_f(f+f_{IFT}s)|^2|H_c(f)|^2df} = 2\frac{C}{N_0}T_c\frac{\left[\int_{-0.5}^{0.5}G_s(f)H_f(f+f_{IFT}s)df\right]^2}{N\int_{-0.5}^{0.5}|H_f(f+f_{IFT}s)|^2|H_c(f)|^2df} \quad (6.17)$$

Finally the associated loss, often denoted as *correlation loss*, is given by

$$L_f = \frac{\left[\int_{-0.5}^{0.5}G_s(f)H_f(f+f_{IFT}s)df\right]^2}{N\int_{-0.5}^{0.5}|H_f(f+f_{IFT}s)|^2|H_c(f)|^2df}. \quad (6.18)$$

6.2 Quantization loss

The digitalization process essentially consists of two operations: sampling and quantization. Sampling transforms the time-continuous received signal in a time-discrete sequence and usually, if the Nyquist's criterion is met, it does not affect the information present in the original signal. On the other hand, quantization irreversibly degrades the signal quality by mapping signal samples into a finite set of discrete values. Quantization is imposed by the fact that only a limited number of bits is available for representing the received signal. Even if in real receivers these two processes are simultaneously performed by Analog to Digital converters (ADC), their effects can be analyzed separately: in this section the quantization effect is considered.

Quantization effects have been extensively studied in the literature [61] and some useful results describing the statistical and spectral nature of the quantization noise have been derived [62]. However these results usually apply when a high number of bits for representing the received signal is available.

For mass-market applications, low-cost GNSS receivers with only a few bits are generally employed. In particular GNSS receivers equipped with 1-bit ADCs are still common, and 2-bit frontends are widespread. The wide use of this kind of ADCs is justified by their low cost and by the high sampling rate they can achieve. In these cases the statistical theory [61] for the quantization noise does not apply, since by using only 1 or 2 bits, the error committed in representing the signal is neither white nor uniform and its results are strongly dependent on the input signal. In [14] the quantization effect on the delay tracking loop is considered and the quantization loss for 1 and 2 bits is derived. In [3] the impact of the number of bits and of the quantization threshold on GPS receivers is studied. However no analytical results are reported and the study is essentially developed by simulations. All these investigations assume that the noise components entering the ADC are white and the impact of noise correlation is not accounted for. In [63] the joint effect of pre-filtering and quantization is studied, however only simulation results are provided.

In this section the quantization loss, when the input noise is white, is theoretically derived. The cases of 1 and 2 bits are reported and generalized to B bits. A general formula for the quantization loss is thus provided.

Analytical results are supported by simulations.

6.2.1 One-bit quantization

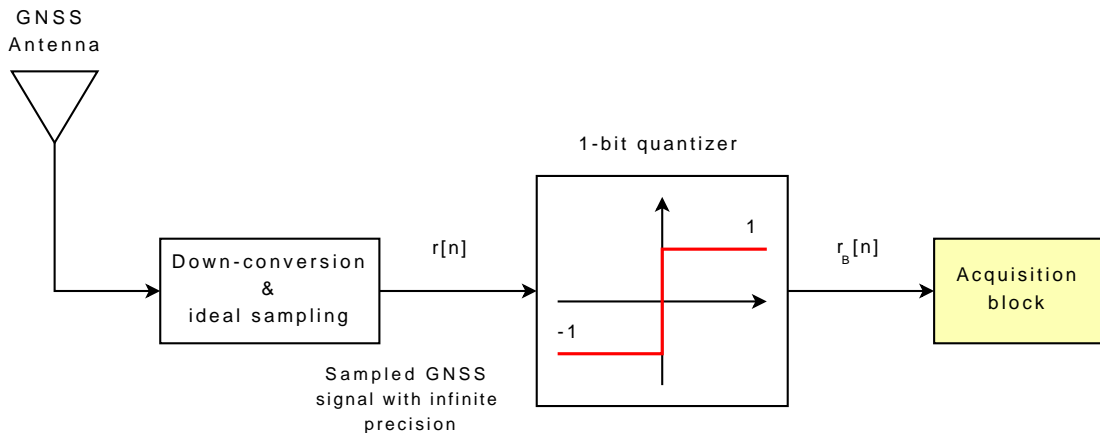


Figure 6.5. One-bit quantization for GNSS signal.

In this section the acquisition performance, achievable using only 1 bit for the input signal representation, is analyzed in terms of coherent output SNR. In Figure 6.5 the analog-to-digital conversion, when only one bit is used is depicted. The analog signal is at first downconverted and sampled. Then the 1-bit quantization is applied. The signal

$r[n]$ is supposed to be represented with an infinite precision and corresponds to the signal model (2.10), thus it is composed by a useful part, $y[n]$, and a noise term $\eta[n]$. $\eta[n]$ is a Gaussian random process supposed to be white and zero-mean. $r[n]$ enters the 1 bit quantizer that produces a new random process $r_B[n]$. $r_B[n]$ is a two-state random process that is still white, since the 1-bit quantizer is a memoryless nonlinear device and the samples of $r[n]$ are supposed independent. The two values that $r[n]$ can assume are $\{-1,1\}$; this convention does not cause any loss of generality and any set of the kind $\{-\Delta, \Delta\}$, with $\Delta \in \mathbb{R}^+$ would lead to the same expression for the coherent output SNR. $r_B[n]$ is characterized by the following probabilities:

$$\begin{aligned} p_{1,1} &= P(r_B[n] = 1) = P(r[n] > 0) = P(y[n] + \eta[n] > 0) = P(\eta[n] > -y[n]) \\ &= Q\left(-\frac{y[n]}{\sigma_{IF}}\right) \end{aligned} \quad (6.19)$$

$$\begin{aligned} p_{1,-1} &= P(r_B[n] = -1) = P(r[n] < 0) = P(y[n] + \eta[n] < 0) = P(\eta[n] < -y[n]) \\ &= Q\left(\frac{y[n]}{\sigma_{IF}}\right) \end{aligned} \quad (6.20)$$

where $Q(\cdot)$ is the surviving function of a Gaussian random variable with zero-mean and unit variance, defined as follows

$$Q(x) = \frac{1}{\sqrt{2\pi}} \int_x^{+\infty} \exp\left\{-\frac{t^2}{2}\right\} dt = \frac{1}{2} \operatorname{erfc}\left(\frac{x}{\sqrt{2}}\right)$$

$\operatorname{erfc}(\cdot)$ is the complementary error function [45]. σ_{IF} is the standard deviation of $\eta[n]$ defined in Chapter 2. In Figure 6.6a) the two probabilities (6.19) and (6.20) are represented as the two areas in which the probability density function of the noise component $\eta[n]$ is divided by the signal term $y[n]$. The expected value of $r_B[n]$ is given by

$$E(r_B[n]) = 1 \cdot p_{1,1} - 1 \cdot p_{1,-1} = Q\left(-\frac{y[n]}{\sigma_{IF}}\right) - Q\left(\frac{y[n]}{\sigma_{IF}}\right) \quad (6.21)$$

By considering Figure 6.6 it is clear that $E[r_B[n]]$ corresponds to the area under the Gaussian distribution of $\eta[n]$ in the interval $[-|y[n]|, |y[n]|]$ multiplied by the sign of $y[n]$. In GNSS applications the useful signal is generally buried in noise, and thus the condition $|y[n]| \ll \sigma_{IF}$ is usually verified. Under this condition the pdf of $\eta[n]$ is almost constant on the interval $[-|y[n]|, |y[n]|]$ and the expected value of $r_B[n]$ can be approximated by the area of the rectangle having sides $2|y[n]|$ and the maximum of the distribution of $\eta[n]$, multiplied by sign($y[n]$):

$$E(r_B[n]) \approx \operatorname{sign}(y[n]) 2|y[n]| \frac{1}{\sqrt{2\pi\sigma_{IF}^2}} = \sqrt{\frac{2}{\pi}} \frac{|y[n]|}{\sigma_{IF}} \quad (6.22)$$

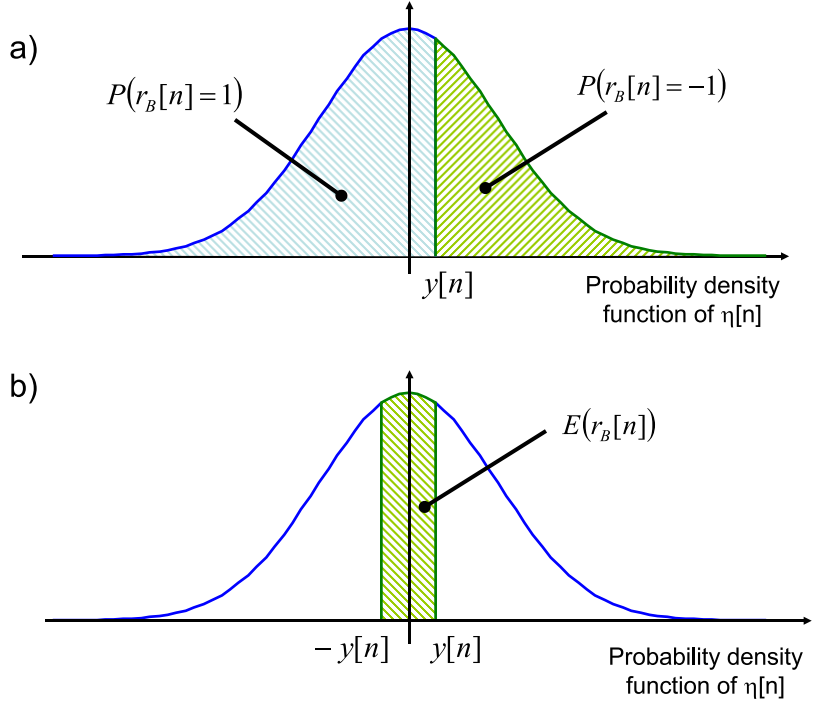


Figure 6.6. a) Representation of the probabilities characterizing the process $r_B[n]$ with respect to the noise probability density function. b) Representation of the expected value of $r_B[n]$ with respect to the noise probability density function.

The variance of $r_B[n]$ is given by

$$\text{Var}(r_B[n]) = E(r_B^2[n]) - E(r_B[n])^2 \approx E(1) - \frac{2}{\pi} \frac{y^2[n]}{\sigma_{IF}^2} \approx 1 \quad (6.23)$$

These results allow to characterize the signal $r_B[n]$ from the statistical point of view and illustrate why it is possible to acquire a GNSS signal also when only one bit is used for quantization. In fact the quantized signal results are, in average, proportional to the useful GNSS signal and thus can be used for acquisition.

The signal $r_B[n]$ enters the acquisition block where it is multiplied by the local carrier and code replica and then integrated in order to obtain the cross-correlation function that will be used for signal detection. The correlation blocks (Figure 3.5) combine many independent samples of $r_B[n]$ producing new random variables that can be considered Gaussian for the central limit theorem. As discussed in Section 3.7 the coherent SNR is

obtained by

$$\begin{aligned}\rho_{c,1} &= \max_{\phi_0} \frac{\text{E}^2 [Y_I(\tau, F_D)]}{\text{Var}[Y_I(\tau, F_D)]} \\ &= \max_{\phi_0} \frac{E \left\{ \frac{1}{N} \sum_{n=0}^{N-1} r_B[n] c[n] \cos(2\pi F_D n) \right\}^2}{\text{Var} \left\{ \frac{1}{N} \sum_{n=0}^{N-1} r_B[n] c[n] \cos(2\pi F_D n) \right\}}\end{aligned}\quad (6.24)$$

where $c[n]$ is the local code used to recover the transmitted signal. The received signal and the local code are supposed to be perfectly aligned in frequency, delay and phase. In this case

$$\begin{aligned}E \left\{ \frac{1}{N} \sum_{n=0}^{N-1} r_B[n] c[n] \cos(2\pi F_D n) \right\} &= \frac{1}{N} \sum_{n=0}^{N-1} E \{r_B[n]\} c[n] \cos(2\pi F_D n) \\ &\approx \frac{1}{N} \sum_{n=0}^{N-1} \sqrt{\frac{2}{\pi} \frac{A}{\sigma_{IF}}} c[n] \cos(2\pi F_D n) = \sqrt{\frac{2}{\pi} \frac{A}{2N\sigma_{IF}}} \sum_{n=0}^{N-1} c[n]^2 = \sqrt{\frac{2}{\pi} \frac{A}{N\sigma_{IF}}} \frac{N}{2} = \sqrt{\frac{2}{\pi} \frac{A}{2\sigma_{IF}}}\end{aligned}\quad (6.25)$$

and

$$\begin{aligned}\text{Var} \left\{ \frac{1}{N} \sum_{n=0}^{N-1} r_B[n] c[n] \cos(2\pi F_D n) \right\} &= \frac{1}{N^2} \sum_{n=0}^{N-1} E \{r_B^2[n]\} c^2[n] \cos^2(2\pi F_D n) - E \left\{ \frac{1}{N} \sum_{n=0}^{N-1} r_B[n] c[n] \cos(2\pi F_D n) \right\}^2 \\ &= \frac{1}{N^2} \sum_{n=0}^{N-1} c^2[n] \cos^2(2\pi F_D n) - \left[\frac{1}{N} \sum_{n=0}^{N-1} E \{r_B[n]\} c[n] \cos(2\pi F_D n) \right]^2 \\ &= \frac{1}{N^2} \frac{N}{2} - \left[\frac{1}{N} \sqrt{\frac{2}{\pi} \frac{A}{\sigma_{IF}}} \sum_{n=0}^{N-1} c^2[n] \cos^2(2\pi F_D n) \right]^2 = \frac{1}{2N}\end{aligned}\quad (6.26)$$

In Eq. (6.26) the condition $\frac{A}{\sigma_{IF}} \ll 1$ has been exploited. From Eqs. (6.25) and (6.26), it is finally possible to evaluate the expression of the coherent output SNR in the presence of 1-bit quantization. In particular the coherent output SNR is given by:

$$\rho_{c,1} = \frac{2}{\pi} \frac{NA^2}{2\sigma_{IF}^2}\quad (6.27)$$

By comparing Eq. (6.27) with expression (3.37) it emerges that quantizing the signal with 1 bit introduces a constant loss

$$L_1 = \frac{\rho_{c,1}}{\rho_c} = \frac{2}{\pi}\quad (6.28)$$

that corresponds to -1.96 dB.

6.2.2 Two-bit quantization

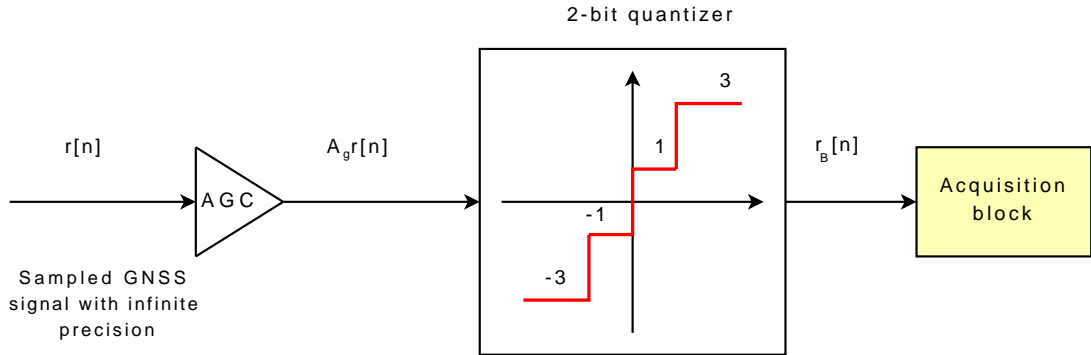


Figure 6.7. Two-bit quantization for GNSS signal.

When two bits are employed for signal quantization, the amplitude of the quantized signal can assume 4 values that, in this case, have been conventionally fixed to $-3, -1, 1$ and 3 . It can be noted that the choice of these values is arbitrary and equivalent to any set of the type $\{-3\Delta, -\Delta, \Delta, 3\Delta\}$ where Δ is any positive real number. The quantization function over 2 bits is defined as

$$Q_2^u(x) = \begin{cases} 3 & \text{for } x > 1 \\ 1 & \text{for } 0 < x \leq 1 \\ -1 & \text{for } -1 < x \leq 0 \\ -3 & \text{for } x \leq -1 \end{cases}. \quad (6.29)$$

In this case the quantization threshold has been fixed to 1. This choice does not reduce the generality of the analysis, in fact the input signal amplitude is adapted to the quantization function by means of the Automatic Gain Control (AGC) that is supposed to provide a constant gain A_g . Changing the AGC gain is equivalent to change the quantization threshold. After these preliminaries and by considering Figure 6.7 the quantized signal $r_B[n]$ is equal to

$$r_B[n] = Q_2^u(A_g r[n]), \quad (6.30)$$

which is a random variable with values in the set $\{-3, -1, 1, 3\}$. To each value of $r_B[n]$

is associated a probability as follows:

$$\begin{aligned}
 p_{2,3} &= P(r_B[n] = 3) = P(A_g r[n] > 1) = P(r[n] > 1/A_g) = P(y[n] + \eta[n] > 1/A_g) \\
 &= P(\eta[n] > 1/A_g - y[n]) = \frac{1}{\sqrt{2\pi\sigma_{IF}^2}} \int_{1/A_g - y[n]}^{+\infty} \exp\left\{-\frac{z^2}{\sigma_{IF}^2}\right\} dz \\
 &= Q\left(\frac{1/A_g - y[n]}{\sigma_{IF}}\right)
 \end{aligned} \tag{6.31}$$

$$\begin{aligned}
 p_{2,1} &= P(r_B[n] = 1) = P(0 < A_g r[n] \leq 1) \\
 &= P(0 < r[n] \leq 1/A_g) = P(0 < y[n] + \eta[n] \leq 1/A_g) = P(-y[n] < \eta[n] \leq 1/A_g - y[n]) \\
 &= \frac{1}{\sqrt{2\pi\sigma_{IF}^2}} \int_{-y[n]}^{1/A_g - y[n]} \exp\left\{-\frac{z^2}{\sigma_{IF}^2}\right\} dz = Q\left(\frac{-y[n]}{\sigma_{IF}}\right) - Q\left(\frac{1/A_g - y[n]}{\sigma_{IF}}\right)
 \end{aligned} \tag{6.32}$$

$$\begin{aligned}
 p_{2,-1} &= P(r_B[n] = -1) = P(-1 < A_g r[n] \leq 0) = P(-1/A_g < r[n] \leq 0) \\
 &= P(-1/A_g < y[n] + \eta[n] \leq 0) = P(-1/A_g - y[n] < \eta[n] \leq -y[n]) \\
 &= \frac{1}{\sqrt{2\pi\sigma_{IF}^2}} \int_{-1/A_g - y[n]}^{-y[n]} \exp\left\{-\frac{z^2}{\sigma_{IF}^2}\right\} dz = Q\left(\frac{-y[n] - 1/A_g}{\sigma_{IF}}\right) - Q\left(\frac{-y[n]}{\sigma_{IF}}\right)
 \end{aligned} \tag{6.33}$$

$$\begin{aligned}
 p_{2,-3} &= P(r_B[n] = -3) = P(A_g r[n] \leq -1) = P(r[n] \leq -1/A_g) = P(y[n] + \eta[n] \leq -1/A_g) \\
 &= P(\eta[n] \leq -1/A_g - y[n]) = \frac{1}{\sqrt{2\pi\sigma_{IF}^2}} \int_{-\infty}^{-1/A_g - y[n]} \exp\left\{-\frac{z^2}{\sigma_{IF}^2}\right\} dz \\
 &= Q\left(\frac{-1/A_g - y[n]}{\sigma_{IF}}\right)
 \end{aligned} \tag{6.34}$$

By using these probabilities it is possible to evaluate the mean value and the variance of

$r_B[n]$, in particular

$$\begin{aligned}
 E\{r_B[n]\} &= 1 \cdot [p_{2,1} - p_{2,-1}] + 3 \cdot [p_{2,3} - p_{2,-3}] \\
 &= \frac{1}{\sqrt{2\pi\sigma_{IF}^2}} \left[\int_{-y[n]}^{1/A_g - y[n]} \exp\left\{-\frac{z^2}{2\sigma_{IF}^2}\right\} dz - \int_{-1/A_g - y[n]}^{-y[n]} \exp\left\{-\frac{z^2}{2\sigma_{IF}^2}\right\} dz \right] \\
 &\quad + \frac{3}{\sqrt{2\pi\sigma_{IF}^2}} \left[\int_{1/A_g - y[n]}^{+\infty} \exp\left\{-\frac{z^2}{2\sigma_{IF}^2}\right\} dz - \int_{-\infty}^{-1/A_g - y[n]} \exp\left\{-\frac{z^2}{2\sigma_{IF}^2}\right\} dz \right] \\
 &= \frac{1}{\sqrt{2\pi\sigma_{IF}^2}} \left[\int_{-y[n]}^{+\infty} \exp\left\{-\frac{z^2}{2\sigma_{IF}^2}\right\} dz - \int_{-\infty}^{-y[n]} \exp\left\{-\frac{z^2}{2\sigma_{IF}^2}\right\} dz \right] \\
 &\quad + \frac{2}{\sqrt{2\pi\sigma_{IF}^2}} \left[\int_{1/A_g - y[n]}^{+\infty} \exp\left\{-\frac{z^2}{2\sigma_{IF}^2}\right\} dz - \int_{1/A_g + y[n]}^{+\infty} \exp\left\{-\frac{z^2}{2\sigma_{IF}^2}\right\} dz \right] \\
 &= \frac{1}{\sqrt{2\pi\sigma_{IF}^2}} \left[\int_{-y[n]}^{y[n]} \exp\left\{-\frac{z^2}{2\sigma_{IF}^2}\right\} dz + 2 \int_{1/A_g - y[n]}^{1/A_g + y[n]} \exp\left\{-\frac{z^2}{2\sigma_{IF}^2}\right\} dz \right] \\
 &= \frac{\text{sign}(y[n])}{\sqrt{2\pi\sigma_{IF}^2}} \left[\int_{-|y[n]|}^{|y[n]|} \exp\left\{-\frac{z^2}{2\sigma_{IF}^2}\right\} dz + 2 \int_{1/A_g - |y[n]|}^{1/A_g + |y[n]|} \exp\left\{-\frac{z^2}{2\sigma_{IF}^2}\right\} dz \right]
 \end{aligned} \tag{6.35}$$

In Figure 6.8 a pictorial representation of the integrals of Eq. (6.35) is provided. By

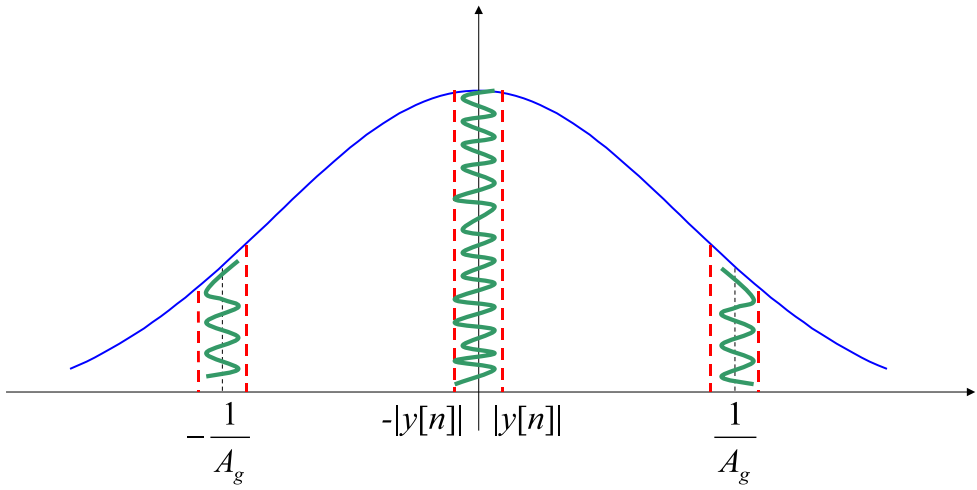


Figure 6.8. Pictorial representation of the integrals that lead to the expected value of the quantized signal $r_B[n]$.

exploiting the fact that $\frac{|y[n]|}{\sigma_{IF}} \ll 1$ it is possible to approximate the integrals in Eq. (6.35)

by the sum of rectangles, as for the one bit case. In this way Eq. (6.35) becomes

$$\begin{aligned} \mathbb{E}\{r_B[n]\} &\approx \frac{\text{sign}(y[n])}{\sqrt{2\pi\sigma_{IF}^2}} 2|y[n]| \left[1 + 2 \exp \left\{ -\frac{(1/A_g)^2}{2\sigma_{IF}^2} \right\} \right] \\ &= \frac{2y[n]}{\sqrt{2\pi\sigma_{IF}^2}} \left[1 + 2 \exp \left\{ -\frac{(1/A_g)^2}{2\sigma_{IF}^2} \right\} \right]. \end{aligned} \quad (6.36)$$

The mean square value of $r_B[n]$ is given by

$$\begin{aligned} \mathbb{E}\{r_B^2[n]\} &= 1 \cdot [p_{2,1} + p_{2,-1}] + 9 \cdot [p_{2,3} + p_{2,-3}] \\ &= 1 + 8[p_{2,3} + p_{2,-3}] \\ &= 1 + \frac{8}{\sqrt{2\pi\sigma_{IF}^2}} \left[\int_{1/A_g-y[n]}^{+\infty} \exp \left\{ -\frac{z^2}{2\sigma_{IF}^2} \right\} dz + \int_{-\infty}^{-1/A_g-y[n]} \exp \left\{ -\frac{z^2}{2\sigma_{IF}^2} \right\} dz \right]. \end{aligned} \quad (6.37)$$

By exploiting the condition $\frac{|y[n]|}{\sigma_{IF}} \ll 1$ and by considering that the AGC gain is inversely proportional to σ_{IF}^2 , the mean square value Eq. (6.37) can be approximated by

$$\begin{aligned} \mathbb{E}\{r_B^2[n]\} &\approx 1 + \frac{8}{\sqrt{2\pi\sigma_{IF}^2}} \left[\int_{1/A_g}^{+\infty} \exp \left\{ -\frac{z^2}{2\sigma_{IF}^2} \right\} dz + \int_{-\infty}^{-1/A_g} \exp \left\{ -\frac{z^2}{2\sigma_{IF}^2} \right\} dz \right] \\ &= 1 + 8\text{erfc}\left(\frac{1/A_g}{\sqrt{2}\sigma_{IF}}\right). \end{aligned} \quad (6.38)$$

The expression of the variance of $r_B[n]$ can be obtained by combining Eq.s (6.36) and (6.38), however, since $\frac{|y[n]|}{\sigma_{IF}} \ll 1$, the square of the mean value (6.36) is negligible with respect to Eq. (6.38), leading to the approximation

$$\text{Var}\{y_B[n]\} \approx 1 + 8\text{erfc}\left(\frac{1/A_g}{\sqrt{2}\sigma_{IF}}\right) \quad (6.39)$$

Given the mean and the variance of $y_B[n]$ it is possible to evaluate the coherent output SNR, by proceeding in the same way of the one bit case. In this case the coherent output SNR is equal to

$$\rho_{c,2} = \frac{2}{\pi} \frac{\left[1 + 2 \exp \left\{ -\frac{(1/A_g)^2}{2\sigma_{IF}^2} \right\} \right]^2}{1 + 8\text{erfc}\left(\frac{1/A_g}{\sqrt{2}\sigma_{IF}}\right)} \frac{A^2 N}{2\sigma_{IF}^2} \quad (6.40)$$

Thus the loss with respect to the ideal case is given by

$$L_2(A_g) = \frac{2}{\pi} \frac{\left[1 + 2 \exp \left\{ -\frac{(1/A_g)^2}{2\sigma_{IF}^2} \right\} \right]^2}{1 + 8\text{erfc}\left(\frac{1/A_g}{\sqrt{2}\sigma_{IF}}\right)} \quad (6.41)$$

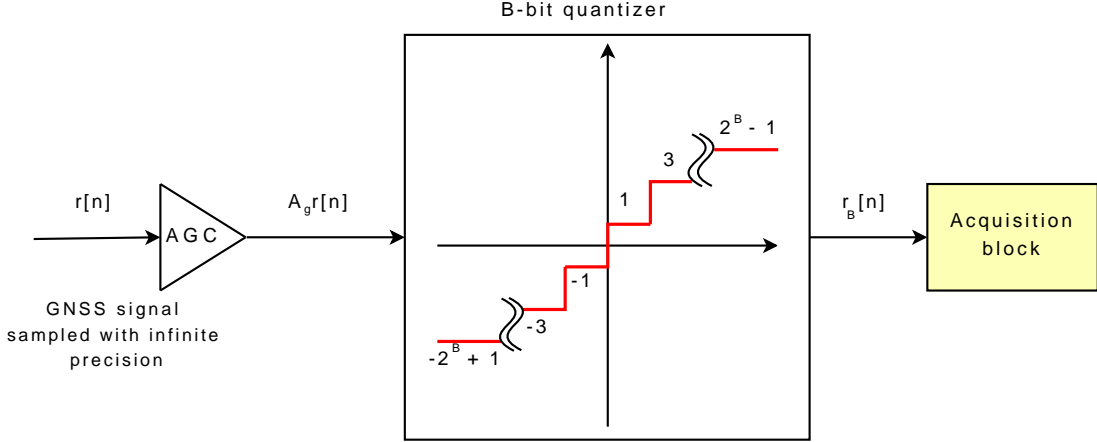


Figure 6.9. Signal quantization over B bits.

6.2.3 B-bit quantization

In this section a general formula, quantifying the loss introduced by quantizing the input signal with B bits is derived. In order to evaluate the coherent output SNR and derive the loss $L_B(A_g)$ it is necessary to statistically characterize the quantized signal $r_B[n]$, and in particular its mean and variance are required.

The quantized signal $r_B[n]$ is a discrete random variable that can assume the values in the set

$$B = \{-(2^B - 1), \dots, -3, -1, 1, 3, \dots, 2^B - 1\}$$

that are the odd numbers $\{2i + 1\}_{i=-2^{B-1}, -2^{B-1}+1, \dots, 2^{B-1}-1}$. A probability is associated to any of these values as

$$p_{B,2i+1} = P(r_B[n] = 2i + 1) = \begin{cases} \frac{1}{\sqrt{2\pi\sigma_{IF}^2}} \int_{(2^{B-1}-1)/A_g-y[n]}^{+\infty} \exp\left\{-\frac{z^2}{2\sigma_{IF}^2}\right\} dz & \text{for } i = 2^{B-1} - 1; \\ \frac{1}{\sqrt{2\pi\sigma_{IF}^2}} \int_{-\infty}^{-(2^{B-1}-1)/A_g-y[n]} \exp\left\{-\frac{z^2}{2\sigma_{IF}^2}\right\} dz & \text{for } i = -2^{B-1}; \\ \frac{1}{\sqrt{2\pi\sigma_{IF}^2}} \int_{i/A_g-y[n]}^{(i+1)/A_g-y[n]} \exp\left\{-\frac{z^2}{2\sigma_{IF}^2}\right\} dz & \text{otherwise} \end{cases} \quad (6.42)$$

where the quantization thresholds have been assumed uniformly spaced and correspond to the integers in the range $[-(2^{B-1} - 1); 2^{B-1} - 1]$. A_g is the gain provided by the AGC, as depicted in Figure 6.9.

By using the probabilities $p_{B,2i+1}$, it is possible to evaluate the expected value of $r_B[n]$ as

$$\begin{aligned}
 \mathbb{E}\{r_B[n]\} &= \sum_{i=-2^{B-1}}^{2^{B-1}-1} (2i+1)p_{B,2i+1} = \sum_{i=0}^{2^{B-1}-1} (2i+1) [p_{B,2i+1} - p_{B,-(2i+1)}] \\
 &= \sum_{i=0}^{2^{B-1}-1} [p_{B,2i+1} - p_{B,-(2i+1)}] + 2 \sum_{i=1}^{2^{B-1}-2} i [p_{B,2i+1} - p_{B,-(2i+1)}] \\
 &\quad + (2^B - 2) [p_{B,2^{B-1}} - p_{B,-(2^{B-1})}] \\
 &= \frac{1}{\sqrt{2\pi\sigma_{IF}^2}} \int_{-y[n]}^{y[n]} \exp\left\{-\frac{z^2}{2\sigma_{IF}^2}\right\} dz + \frac{2(2^{B-1}-1)}{\sqrt{2\pi\sigma_{IF}^2}} \int_{(2^{B-1}-1)/A_g-y[n]}^{(2^{B-1}-1)/A_g+y[n]} \exp\left\{-\frac{z^2}{2\sigma_{IF}^2}\right\} dz \\
 &\quad + \frac{2}{\sqrt{2\pi\sigma_{IF}^2}} \sum_{i=1}^{2^{B-1}-2} i \left[\int_{i/A_g-y[n]}^{i/A_g+y[n]} \exp\left\{-\frac{z^2}{2\sigma_{IF}^2}\right\} dz - \int_{(i+1)/A_g-y[n]}^{(i+1)/A_g+y[n]} \exp\left\{-\frac{z^2}{2\sigma_{IF}^2}\right\} dz \right] \\
 &= \frac{1}{\sqrt{2\pi\sigma_{IF}^2}} \int_{-y[n]}^{y[n]} \exp\left\{-\frac{z^2}{2\sigma_{IF}^2}\right\} dz + \frac{2}{\sqrt{2\pi\sigma_{IF}^2}} \sum_{i=1}^{2^{B-1}-1} \int_{i/A_g-y[n]}^{i/A_g+y[n]} \exp\left\{-\frac{z^2}{2\sigma_{IF}^2}\right\} dz \\
 &= \frac{\text{sign}\{y[n]\}}{\sqrt{2\pi\sigma_{IF}^2}} \left[\int_{-|y[n]|}^{|y[n]|} \exp\left\{-\frac{z^2}{2\sigma_{IF}^2}\right\} dz + 2 \sum_{i=1}^{2^{B-1}-1} \int_{i/A_g-|y[n]|}^{i/A_g+|y[n]|} \exp\left\{-\frac{z^2}{2\sigma_{IF}^2}\right\} dz \right] \\
 &= \frac{\text{sign}\{y[n]\}}{\sqrt{2\pi\sigma_{IF}^2}} \left[\sum_{i=-2^{B-1}+1}^{2^{B-1}-1} \int_{i/A_g-|y[n]|}^{i/A_g+|y[n]|} \exp\left\{-\frac{z^2}{2\sigma_{IF}^2}\right\} dz \right].
 \end{aligned} \tag{6.43}$$

By applying the fact that $\frac{|y[n]|}{\sigma_{IF}} \ll 1$, it is possible to approximate Eq. (6.43) by

$$\begin{aligned}
 \mathbb{E}\{r_B[n]\} &\approx \frac{\text{sign}\{y[n]\}}{\sqrt{2\pi\sigma_{IF}^2}} \left[\sum_{i=-2^{B-1}+1}^{2^{B-1}-1} 2|y[n]| \exp\left\{-\frac{(i/A_g)^2}{2\sigma_{IF}^2}\right\} \right] \\
 &= \frac{2y[n]}{\sqrt{2\pi\sigma_{IF}^2}} \left[1 + 2 \sum_{i=1}^{2^{B-1}-1} \exp\left\{-\frac{(i/A_g)^2}{2\sigma_{IF}^2}\right\} \right].
 \end{aligned} \tag{6.44}$$

In the same way it is possible to evaluate the mean square value of $r_B[n]$ as:

$$\begin{aligned}
 \mathbb{E}\{r_B^2[n]\} &= \sum_{i=0}^{2^{B-1}-1} (2i+1)^2 [p_{B,2i+1} + p_{B,-(2i+1)}] \\
 &= \frac{1}{\sqrt{2\pi\sigma_{IF}^2}} \sum_{i=0}^{2^{B-1}-2} (2i+1)^2 \left[\int_{i/A_g-y[n]}^{(i+1)/A_g-y[n]} \exp\left\{-\frac{z^2}{2\sigma_{IF}^2}\right\} dz \right. \\
 &\quad \left. + \int_{-(i+1)/A_g-y[n]}^{(-i+1)/A_g-y[n]} \exp\left\{-\frac{z^2}{2\sigma_{IF}^2}\right\} dz \right] \\
 &\quad + \frac{(2^B-1)^2}{\sqrt{2\pi\sigma_{IF}^2}} \left[\int_{(2^{B-1}-1)/A_g-y[n]}^{+\infty} \exp\left\{-\frac{z^2}{2\sigma_{IF}^2}\right\} dz + \int_{-\infty}^{-(2^{B-1}-1)/A_g-y[n]} \exp\left\{-\frac{z^2}{2\sigma_{IF}^2}\right\} dz \right]. \tag{6.45}
 \end{aligned}$$

As usual, by using the hypothesis $\frac{|y[n]|}{\sigma_{IF}} \ll 1$, it is possible to approximate Eq. (6.45) by

$$\begin{aligned}
 \mathbb{E}\{r_B^2[n]\} &\approx \frac{2}{\sqrt{2\pi\sigma_{IF}^2}} \sum_{i=0}^{2^{B-1}-2} (2i+1)^2 \int_{i/A_g}^{(i+1)/A_g} \exp\left\{-\frac{z^2}{2\sigma_{IF}^2}\right\} dz \\
 &\quad + \frac{2(2^B-1)^2}{\sqrt{2\pi\sigma_{IF}^2}} \int_{(2^{B-1}-1)/A_g}^{+\infty} \exp\left\{-\frac{z^2}{2\sigma_{IF}^2}\right\} dz \\
 &= \sum_{i=0}^{2^{B-1}-1} (2i+1)^2 \operatorname{erfc}\left(\frac{i/A_g}{\sqrt{2}\sigma_{IF}}\right) - \sum_{i=0}^{2^{B-1}-2} (2i+1)^2 \operatorname{erfc}\left(\frac{(i+1)/A_g}{\sqrt{2}\sigma_{IF}}\right) \tag{6.46} \\
 &= 1 + \left[\sum_{i=1}^{2^{B-1}-1} (2i+1)^2 \operatorname{erfc}\left(\frac{i/A_g}{\sqrt{2}\sigma_{IF}}\right) - \sum_{i=1}^{2^{B-1}-1} (2i-1)^2 \operatorname{erfc}\left(\frac{i/A_g}{\sqrt{2}\sigma_{IF}}\right) \right] \\
 &= 1 + \sum_{i=1}^{2^{B-1}-1} [(2i+1)^2 - (2i-1)^2] \operatorname{erfc}\left(\frac{i/A_g}{\sqrt{2}\sigma_{IF}}\right) \\
 &= 1 + 8 \sum_{i=1}^{2^{B-1}-1} i \cdot \operatorname{erfc}\left(\frac{i/A_g}{\sqrt{2}\sigma_{IF}}\right).
 \end{aligned}$$

As for the 2-bit case the variance of $r_B[n]$ can be calculated from Eqs. (6.44) and (6.46), however, since the square of the mean of $r_B[n]$ is negligible with respect to Eq. (6.46), the approximation

$$\operatorname{Var}\{r_B[n]\} \approx 1 + 8 \sum_{i=1}^{2^{B-1}-1} i \cdot \operatorname{erfc}\left(\frac{i/A_g}{\sqrt{2}\sigma_{IF}}\right) \tag{6.47}$$

holds.

From Eqs. (6.47) and (6.44) the coherent output SNR results in

$$\rho_c = \frac{2}{\pi} \frac{\left[1 + 2 \sum_{i=1}^{2^{B-1}-1} \exp \left\{ -\frac{(i/A_g)^2}{2\sigma_{IF}^2} \right\} \right]^2 A^2 N}{1 + 8 \sum_{i=1}^{2^{B-1}-1} i \cdot \operatorname{erfc} \left(\frac{i/A_g}{\sqrt{2}\sigma_{IF}} \right)} \frac{A^2 N}{2\sigma_{IF}^2}, \quad (6.48)$$

which corresponds to the loss

$$L_B(A_g) = \frac{2}{\pi} \frac{\left[1 + 2 \sum_{i=1}^{2^{B-1}-1} \exp \left\{ -\frac{(i/A_g)^2}{2\sigma_{IF}^2} \right\} \right]^2}{1 + 8 \sum_{i=1}^{2^{B-1}-1} i \cdot \operatorname{erfc} \left(\frac{i/A_g}{\sqrt{2}\sigma_{IF}} \right)}. \quad (6.49)$$

6.2.4 Analysis and Simulation

In this section the theoretical results obtained for the quantization loss are discussed and analyzed in detail. In particular Monte Carlo simulations are used to support the theoretical analysis.

In Figure 6.10 the quantization loss (dB) are depicted as a function of the product of

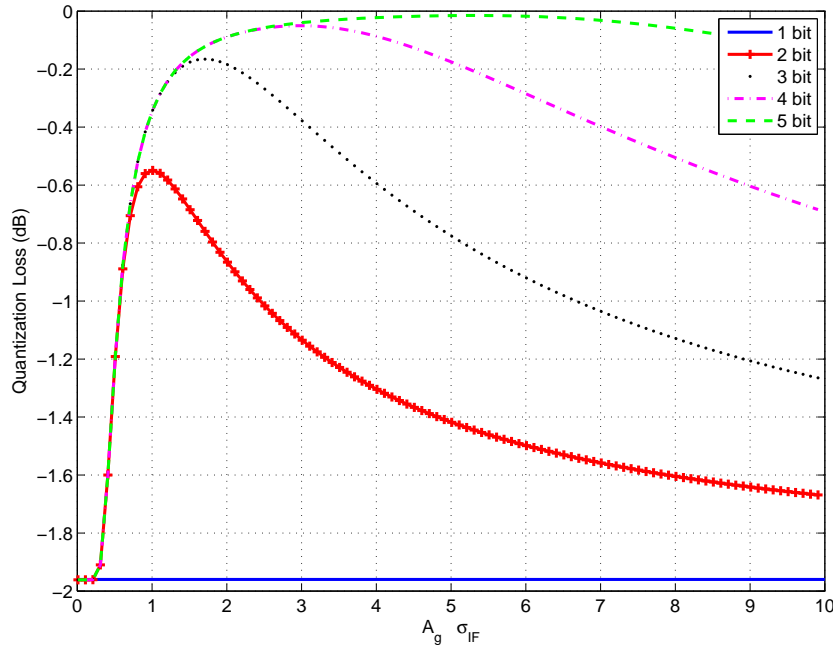


Figure 6.10. Quantization loss as a function of the normalized AGC gain ($A_g \sigma_{IF}$).

the AGC gain and the noise standard deviation σ_{IF} . In fact, by considering Eq. (6.49) it

clearly emerges that the quantization loss only depends on the product $A_g\sigma_{IF}$ that corresponds to the noise variance after the AGC and before the quantization block. From Figure 6.10 it emerges that, for $B > 1$, there is a value of A_g that minimizes the quantization loss. Moreover, as B increases, the quantization loss presents a larger region that is almost constant, thus the requirement for the AGC to provide the optimal gain A_g results less stringent for high values of B . The behavior of the quantization loss can be explained by the presence of a scaling error: an insufficient or excessive gain A_g results in an inappropriate use of the quantization function dynamic. An excessive gain A_g can also result in saturation phenomena. In Table 6.1 the optimal AGC gain and the relative minimum

Table 6.1. Optimal AGC gain.

Bit number	Optimal AGC Gain	Minimum Loss (dB)
1		-1.96
2	$1/\sigma_{IF}$	-0.55 dB
3	$1.71/\sigma_{IF}$	-0.165 dB
4	$2.98/\sigma_{IF}$	-0.05 dB
5	$5.315/\sigma_{IF}$	-0.015 dB

quantization loss are reported as a function of the number of bits. The results agree well with the minimum quantization losses reported by [2].

Table 6.2. Simulation Parameters

Parameter	Value
Sampling frequency	$f_s = 4.092$ MHz
Intermediate frequency	$f_{IF} = \frac{f_s}{4} = 1.023$ MHz
Code	GPS C/A
Code rate	1.023 Mchip/s

In order to validate the theoretical model developed in previous sections, the acquisition chain characterized by the parameters in Table 6.2 has been simulated. The input signal has been quantized with 2, 3 and 4 bits. Then the coherent output SNR has been estimated as a function of the AGC threshold and the quantization loss derived. The simulation results are depicted in Figures 6.11 and 6.12. In Figure 6.11 the case of $C/N_0 = 35$ dB has been considered: the quantization loss estimated by simulation and the theoretical curves overlap well, proving the validity of the model developed in previous sections. In Figure 6.12 a $C/N_0 = 45$ dB has been considered. Also in this case simulations and theoretical curves agree well although small deviations can be observed. These deviations can be explained by the fact that, for increasing C/N_0 , the assumption $\frac{|y[n]|}{\sigma_{IF}} \ll 1$

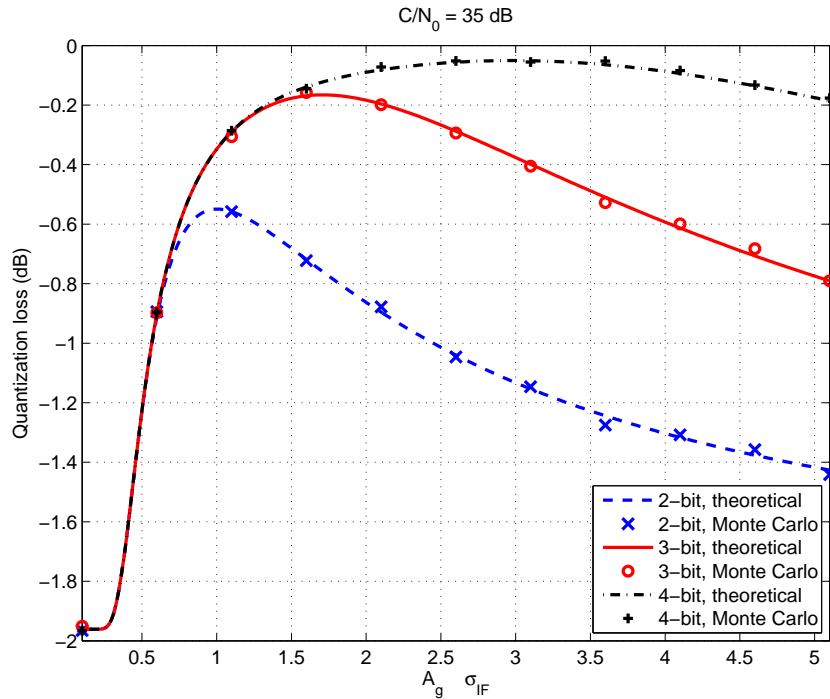


Figure 6.11. Quantization loss: comparison between theoretical and Monte Carlo results. ($C/N_0 = 35$) dB.

(the amplitude of the signal component is negligible with respect to the noise variance) is less and less valid, making formula (6.49) only approximately true.

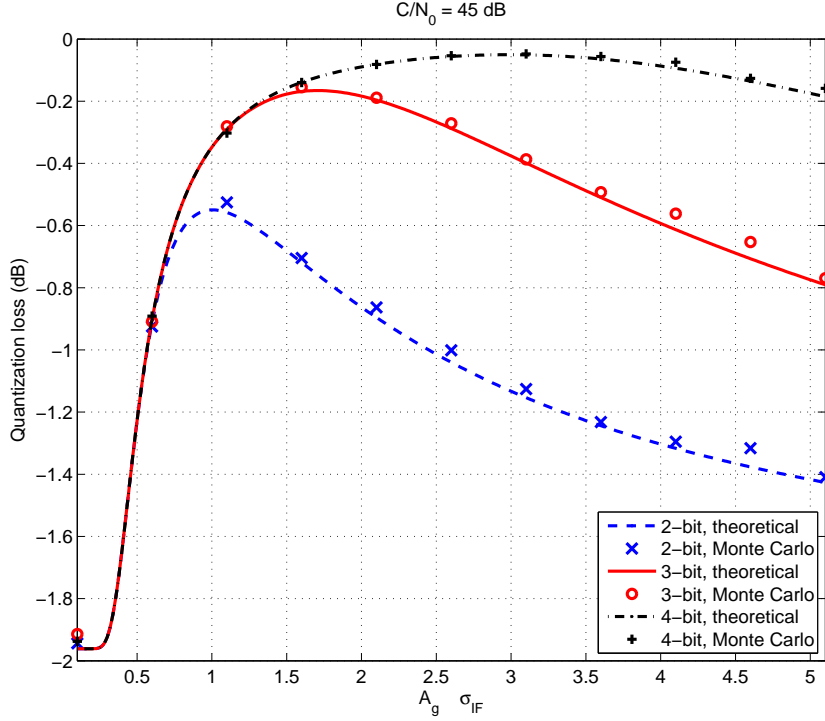


Figure 6.12. Quantization loss: comparison between theoretical and Monte Carlo results. ($C/N_0 = 45$) dB.

6.3 Doppler and delay residual errors

The detection law for an acquisition system is derived supposing the system able to perfectly recover the code delay and the Doppler frequency shift. However, in real applications, these conditions are rarely verified. Neither the code delay nor the Doppler shift is exactly in the set of delays and frequencies used in the search space evaluation. This condition is the cause of additional impairments, or losses, which reduce the amplitude of the correlation peak, reducing the coherent output SNR.

The effect of Doppler and code imperfect alignment has been thoroughly studied in the literature [3, 10, 34], and thus will be only briefly discussed in this section. In particular [10] investigates the impact of residual Doppler shift, code shift, Doppler dynamics and code Doppler. In [64] the analysis of these losses in presence of BOC modulated signals has been reported. This paper can be found in Appendix A.

In the presence of Doppler and code misalignment it is possible to show [3] that the in-phase and quadrature components, $Y_I(\tau, F_D)$ and $Y_Q(\tau, F_D)$, assume the following

expressions:

$$Y_I(\tau, F_D) = \frac{A \sin(\pi N \delta F)}{2 \pi N \delta F} R(\delta \tau) \cos \phi_0 + \eta_I \quad (6.50)$$

$$Y_Q(\tau, F_D) = \frac{A \sin(\pi N \delta F)}{2 \pi N \delta F} R(\delta \tau) \sin \phi_0 + \eta_Q \quad (6.51)$$

where

- A is the useful signal amplitude,
- δF is the normalized Doppler frequency error, $(F_{D,0} - F_D) T_s$,
- $\delta \tau$ is the code delay residual error and R is the normalized cross-correlation between the local replica and the input useful signal.

The frequency error is limited by the Doppler bin step size and in particular

$$-\frac{\Delta F}{2} \leq \delta F < \frac{\Delta F}{2}. \quad (6.52)$$

In the same way the code delay residual error is limited by the size of the step that the acquisition process uses to search all the possible code delays:

$$-\frac{\Delta \tau}{2} \leq \delta \tau < \frac{\Delta \tau}{2}. \quad (6.53)$$

By considering Eqs. (6.50) and (6.51) it is possible to evaluate the coherent output SNR which becomes:

$$\rho_{c,e} = \frac{A^2 \sin^2(\pi N \delta F)}{4 (\pi N \delta F)^2} R^2(\delta \tau) \frac{2N}{\sigma_{IF}^2} = 2 \frac{C}{N_0} T_c \frac{\sin^2(\pi N \delta F)}{(\pi N \delta F)^2} R^2(\delta \tau). \quad (6.54)$$

It can be noted that for $\delta F = 0$ and $\delta \tau = 0$ Eq. (6.54) equals expression (3.37). Moreover it is possible to define a loss associated to the Doppler frequency and code delay errors given by $\rho_{c,e}$ divided by the ideal coherent output SNR derived in Eq. (3.37). In particular the following expression is obtained:

$$L(\delta \tau, \delta F) = \frac{\sin^2(\pi N \delta F)}{(\pi N \delta F)^2} R^2(\delta \tau). \quad (6.55)$$

The loss (6.55) is given by the product of two terms that respectively depend on the Doppler frequency and the code delay errors. Thus it is possible to isolate the loss associated with the frequency residual error and the one associated with the code delay error namely

$$L_D(\delta F) = \frac{\sin^2(\pi N \delta F)}{(\pi N \delta F)^2} \quad (6.56)$$

and

$$L_C(\delta \tau) = R^2(\delta \tau). \quad (6.57)$$

By considering Eq. (6.56) one notices that the frequency error δF is multiplied by the factor N that represents the number of samples used to coherently integrate the input signal. Thus, as the coherent integration time increases, the effect of Doppler frequency residual errors becomes more and more severe. In order to limit this effect the Doppler bin size has to be lowered as the coherent integration time is increased and a common criteria, for setting ΔF , is the following

$$\Delta F \leq \frac{2}{3N} \quad \text{or equivalently } \Delta F \cdot f_s = \Delta f \leq \frac{2}{3T_c}. \quad (6.58)$$

Chapter 7

Acquisition of composite GNSS signals

With the advent of new Global Navigation Satellite Systems (GNSS), such as the European Galileo and the Chinese Compass, and with the modernization of the American GPS, new signals and new modulations have been introduced in order to provide better performance by fully exploiting the technology currently available.

Modern GNSS signals are usually made up of two different components, namely the data and pilot channels. The first one carries the navigation message, whereas the second is dataless and thus can be used for precisely determining the pseudoranges, allowing longer coherent integration time and the use of a pure PLL. Examples of such signals are the Galileo E1 Open Service signal (OS) [65, 66], the Galileo E5a and E5b signals [66] and the GPS L5 modulation [67]. In the Galileo E1 OS case, data and pilot are transmitted with the same phase and are separated only by different ranging codes, whereas in Galileo E5a, Galileo E5b and GPS L5 cases, the two components are broadcast with a phase difference of 90 degrees.

The drawback of using data and pilot components is that by processing each channel independently half of the transmitted power is lost. In order to overcome the power loss problem different techniques [17, 19, 68–71] have been proposed for combining data and pilot components to recover power from both channels. The acquisition of the Galileo E1 OS has been considered in [68] and [69] which propose to correlate the input signal with two different composite codes, given by the sum and difference of the data and pilot codes. However [68] and [69] do not characterize, from a statistical point of view, the performance of the proposed algorithm, which is analyzed only in terms of its impact on the architecture of a GNSS receiver. In [17] the data and pilot channels are acquired separately and the correlator outputs are non-coherently combined. The non-coherent combining of L5 data and pilot components is further analyzed in [18]. In [19] the optimal detector that combines pilot and data channels in the case of GPS L5 is derived. Then,

from the optimal detector, two sub-optimal algorithms, suitable for low and high SNR conditions, are developed. The sub-optimal algorithm in high SNR conditions consists of correlating the input signal with two appropriate combinations of data and pilot codes and using as decision variable the maximum between the two correlations. The detection algorithms described in [19] are characterized only by simulations. In [70] and [71] some implementations for the detection algorithms described in [19] are analyzed and some FFT based techniques are proposed.

In this chapter different techniques for the acquisition of composite GNSS signals are considered. At first the problem of data and pilot combining on a single code period is addressed and three different techniques are analyzed.

The first technique, non-coherent channel combining, is from the literature [17, 18] and it is used for comparison. The second strategy, coherent channel combining with relative sign recovery, corresponds to the sub-optimal detector for high SNR described in [19] whereas the last one, differentially coherent channel combining, is, to the best of the author's knowledge, new and represents one of the innovative contributions of this thesis. Differentially coherent channel combining is obtained by modifying the traditional differentially coherent acquisition technique [12] that exploits the correlation properties between two consecutive GNSS signal periods. In this case data and pilot components are used instead of the two consecutive signal periods. Some modifications have also been introduced to deal with the phase difference between the two components.

For each acquisition strategy the probabilities of detection and false alarm are provided. In particular closed-form expressions for the probabilities of coherent channel combining and of the differentially coherent integration strategy are derived. To the best of the author's knowledge these expressions are new.

Monte Carlo techniques have been used to support the theoretical analysis; simulations and analytical expressions agree well, proving the effectiveness of the developed theory.

In the second part of the chapter the problem of extending the integration time beyond one code period is discussed. In particular, for new GNSS signals, the navigation message can change the polarity of the transmitted signal every code period, essentially limiting the coherent integration time.

Two different integration strategies are considered:

- signal integration without sign recovery,
- signal integration with sign recovery.

The first strategy consists in removing the dependence on the navigation bits by using a non-linear function (squaring, absolute value) whereas, in the second one the bits are estimated and used to extend the coherent integration time.

7.1 Signal model

When considering composite GNSS signals with data and pilot components emitted with a 90-degree phase difference, the useful signal components, $y_i(t)$, of Eq. (2.5) can be modeled as [66,67]

$$y_i(t) = A_i e_{D,i} (t - \tau_{0,i}^a) \cos (2\pi (f_{IF} + f_{d,0}^i) t + \phi_{0,i}) + A_i e_{P,i} (t - \tau_{0,i}^a) \sin (2\pi (f_{IF} + f_{d,0}^i) t + \phi_{0,i}) \quad (7.1)$$

where $e_{D,i}(t)$ and $e_{P,i}(t)$ are the data and pilot components and the other parameters correspond to those defined in Chapter 2. In general the data and pilot components, $e_{D,i}(t)$ and $e_{P,i}(t)$, are given by the product of several terms

$$\begin{aligned} e_{D,i}(t) &= d_i(t) s_{b,i}(t) s_{D,i}(t) c_{D,i}(t) \\ e_{P,i}(t) &= s_{b,i}(t) s_{P,i}(t) c_{P,i}(t) \end{aligned} \quad (7.2)$$

where $d_i(t)$ is the navigation message, $s_{b,i}(t)$ is the signal obtained by periodically repeating the sub-carrier, $s_{D,i}(t)$ and $s_{P,i}(t)$ are the secondary codes or synchronization sequences for the data and pilot channels and $c_{D,i}(t)$ and $c_{P,i}(t)$ are the primary spreading sequences. In the L5, E5a and E5b cases the subcarrier is a rectangular window whose periodic repetition leads to $s_{b,i}(t) = 1$.

Since the signal in Eq. (7.1) is composed by two terms of the signal power C_i is given by

$$C_i = A_i^2. \quad (7.3)$$

The digital counterpart of Eq. (7.1) is given by

$$y_i[n] = \sqrt{C_i} e_{D,i}[n - \tau_{0,i}] \cos (2\pi F_{D,0}^i n + \phi_{0,i}) + \sqrt{C_i} e_{P,i}[n - \tau_{0,i}] \sin (2\pi F_{D,0}^i n + \phi_{0,i}) \quad (7.4)$$

where $\tau_{0,i} = \tau_{0,i}^a/T_s$ and $F_{D,0}^i = (f_{IF} + f_{d,0}^i) T_s$. As usual, due to the code orthogonality, the case of a single useful signal can be considered and the final signal model is

$$\begin{aligned} r[n] &= \sqrt{C} e_D[n - \tau_0] \cos (2\pi F_{D,0} n + \phi_0) \\ &+ \sqrt{C} e_P[n - \tau_0] \sin (2\pi F_{D,0} n + \phi_0) + \eta[n] \end{aligned} \quad (7.5)$$

where the index i has been dropped for ease of notation.

7.2 Single period acquisition

In the majority of the new composite GNSS signals the primary spreading code is modulated by a secondary code and, in the data channel case, by a navigation message. Those two modulations can change the polarity of the GNSS signal every primary code period.

Thus, without special integration strategies, the coherent integration time is limited to one primary code period. In fact the effect of bit transition over one primary code period can be easily managed by using the serial search and the parallel frequency search techniques discussed in Section 3.2. By sliding the input signal the maximum of the correlation is obtained when a whole primary code is aligned with the local signal replica and thus the bit transition occurs at the boundary of the input vector, without consequence for the acquisition process. Also the parallel search in the time domain can be modified, by using zero-padding techniques, in order to deal with the bit transition over one primary code period [72].

For these reason the acquisition on a single primary code represents the basic element for the acquisition of composite GNSS signals. In this section different combining strategies, over a single primary code period, are considered and analyzed.

7.2.1 Non-coherent channel combining

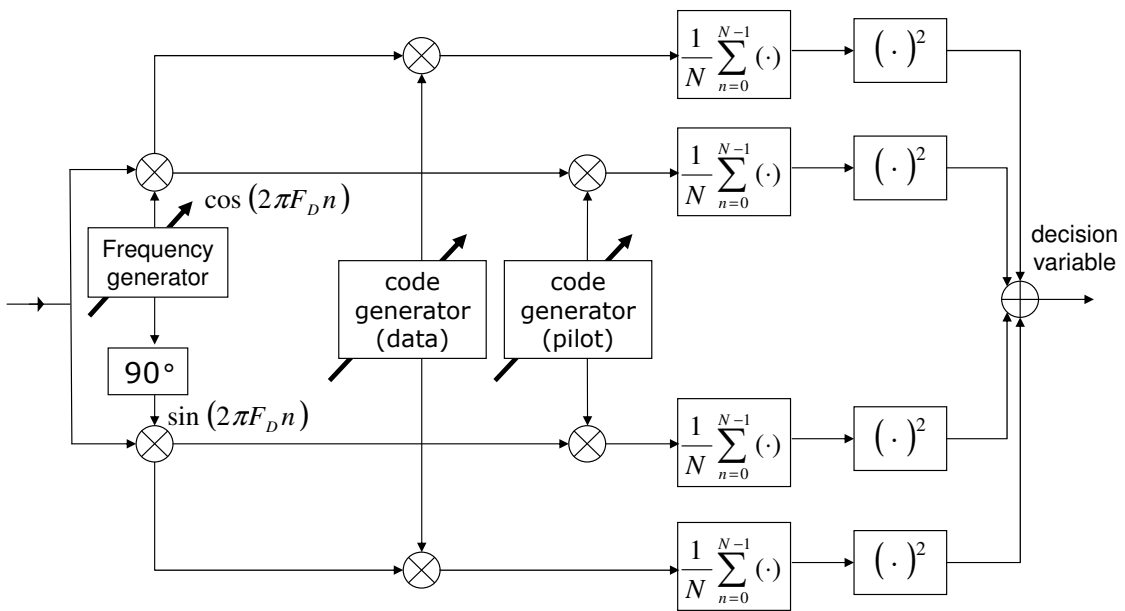


Figure 7.1. Acquisition scheme for non-coherent channel combining: the data and the pilot are acquired separately and the correlator outputs are non-coherently combined.

Non-coherent channel combining was originally proposed in [17] and consists of correlating separately the input signal with the data and pilot local replicas. The correlator outputs are then squared and non-coherently summed. A scheme for the non-coherent combining strategy is depicted in Figure 7.1.

As for the single channel acquisition, the correlator outputs can be written as

$$\begin{aligned} Y_{D,I}(\tau, F_D) &= \frac{\sqrt{C}}{2} d_D \frac{\sin(\pi N \delta F)}{\pi N \delta F} R(\delta\tau) \cos(\delta\phi_D) + \eta_{D,I} \\ Y_{D,Q}(\tau, F_D) &= \frac{\sqrt{C}}{2} d_D \frac{\sin(\pi N \delta F)}{\pi N \delta F} R(\delta\tau) \sin(\delta\phi_D) + \eta_{D,Q} \\ Y_{P,I}(\tau, F_D) &= \frac{\sqrt{C}}{2} d_P \frac{\sin(\pi N \delta F)}{\pi N \delta F} R(\delta\tau) \cos(\delta\phi_P) + \eta_{P,I} \\ Y_{P,Q}(\tau, F_D) &= \frac{\sqrt{C}}{2} d_P \frac{\sin(\pi N \delta F)}{\pi N \delta F} R(\delta\tau) \sin(\delta\phi_P) + \eta_{P,Q} \end{aligned} \quad (7.6)$$

where d_D and d_P are the signs of the data and pilot components. It has to be noted that data and pilot terms in Eq. (7.6) are characterized by a different phase difference, $\delta\phi_D$ and $\delta\phi_P$ respectively. This is due to the fact that pilot and data channels are transmitted with a phase difference of 90 degrees and thus, it can be assumed that

$$\delta\phi_P = \delta\phi_D + \frac{\pi}{2}. \quad (7.7)$$

$\eta_{D,I}$, $\eta_{D,Q}$, $\eta_{P,I}$ and $\eta_{P,Q}$ are four independent zero mean Gaussian random variables with variance given by Eq. (3.23):

$$\sigma_n^2 = \frac{\sigma_{IF}^2}{2N}.$$

The independence between components from different channels can be proven by exploiting the orthogonality properties of the primary spreading codes as reported in Appendix E.

The components from Eq. (7.6) are combined to form the decision statistic:

$$S(\tau, F_D) = Y_{D,I}^2(\tau, F_D) + Y_{D,Q}^2(\tau, F_D) + Y_{P,I}^2(\tau, F_D) + Y_{P,Q}^2(\tau, F_D) \quad (7.8)$$

In this case $S(\tau, F_D)$ is a χ^2 random variable with four degrees of freedoms. When the received and the local signals are aligned, with respect to the delay and the Doppler frequency, $S(\tau, F_D)$ is non-central with a non-centrality parameter equal to 2λ with

$$\lambda = \frac{C \sin^2(\pi \delta F)}{4 (\pi \delta F)^2} R^2(\delta\tau) \approx \frac{C}{4} = \frac{A^2}{4}. \quad (7.9)$$

Under H_0 , $S(\tau, F_D)$ can be assumed to be a central χ^2 random variable.

From these considerations it is possible to evaluate the probability of false alarm and detection in the case of non-coherent combining as

$$P_{fa}^{nc}(\beta) = \exp \left\{ -\frac{\beta}{2\sigma_n^2} \right\} \left(1 + \frac{\beta}{2\sigma_n^2} \right) \quad (7.10)$$

$$P_d^{nc}(\beta) = Q_2 \left(\frac{\sqrt{2\lambda}}{\sigma_n}, \frac{\sqrt{\beta}}{\sigma_n} \right) \approx Q_2 \left(\frac{A}{\sqrt{2}\sigma_n}, \frac{\sqrt{\beta}}{\sigma_n} \right). \quad (7.11)$$

7.2.2 Coherent channel combining with sign recovery

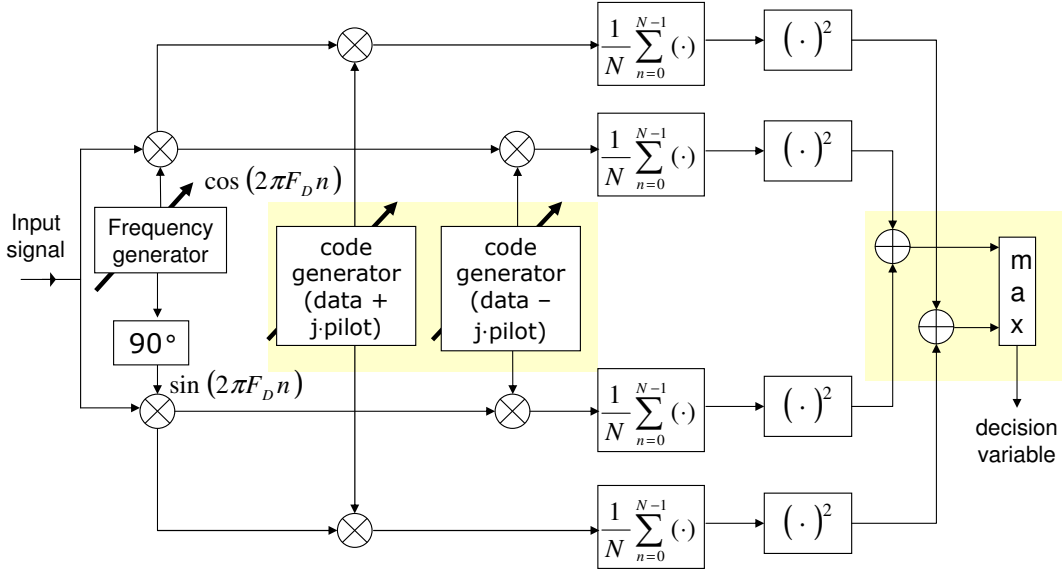


Figure 7.2. Acquisition scheme for coherent channel combining with sign recovery: data and pilot spreading sequences are combined to generate two equivalent codes. The maximum of the correlations with the two equivalent codes is used as decision variable.

Coherent channel combining with sign recovery has been considered in [71] and further analyzed in [19]. However in [71] only the acquisition principle is described without any statistical characterization of the combining method. In [19] it is shown that coherent channel combining is a near-optimal implementation of the likelihood ratio test. Moreover [19] analyzes the algorithm by simulation, showing that coherent channel combining leads to performance similar to the one of the optimal detector for a wide range of C/N_0 . Moreover, it can be easily shown [44, 60] that coherent channel combining is the optimal joint estimator for the code delay, Doppler shift and relative sign between data and pilot channels.

Coherent channel combining is based on the fact that, if the sign between data and pilot were known, all the useful signal power could be recovered by employing the correct composite local code:

$$\tilde{c}[n] = \begin{cases} c_D[n] + jc_P[n] \\ c_D[n] - jc_P[n]. \end{cases} \quad (7.12)$$

In Eq. (7.12) it has been assumed that $s_b[n] = 1$ and the navigation message, $d[n]$, and the

secondary codes, $s_D[n]$ and $s_P[n]$ are constant over a primary code period.

Due to the navigation message and the secondary codes, the relative sign between the data and the pilot channel is not known at the receiver and thus has to be estimated. In coherent channel combining the relative sign is estimated by correlating the input signal with both composite local codes (7.12): the sign estimate is the one that leads to the highest correlation. Thus the decision variable is given by

$$S(\tau, F_D) = \max \left\{ |Y^+(\tau, F_D)|^2, |Y^-(\tau, F_D)|^2 \right\} \quad (7.13)$$

where

$$\begin{aligned} Y^+(\tau, F_D) &= Y_D(\tau, F_D) + jY_P(\tau, F_D) \\ &= [Y_{D,I}(\tau, F_D) + jY_{D,Q}(\tau, F_D)] + j[Y_{P,I}(\tau, F_D) + jY_{P,Q}(\tau, F_D)] \\ Y^-(\tau, F_D) &= Y_D(\tau, F_D) - jY_P(\tau, F_D) \\ &= [Y_{D,I}(\tau, F_D) + jY_{D,Q}(\tau, F_D)] - j[Y_{P,I}(\tau, F_D) + jY_{P,Q}(\tau, F_D)] \end{aligned} \quad (7.14)$$

Eq. (7.13) states that the decision variable $S(\tau, F_D)$ is given by the maximum between the square modulus of the two correlations with the equivalent codes (7.12). Due to the linearity of the correlation process, the correlations $Y^+(\tau, F_D)$ and $Y^-(\tau, F_D)$ can be expressed as a linear combination of the correlations with the data and pilot local codes as stated in Eq. (7.14). In this way the decision variable can be evaluated by computing the four components $Y_{D,I}(\tau, F_D)$, $Y_{D,Q}(\tau, F_D)$, $Y_{P,I}(\tau, F_D)$ and $Y_{P,Q}(\tau, F_D)$ thus requiring the same computation load required by non-coherent channel combining. In Figure 7.2 the acquisition scheme for the coherent channel combining is depicted.

The false alarm and detection probabilities for the coherent combining can be easily determined by exploiting the following property:

$$\begin{aligned} P(S(\tau, F_D) > \beta) &= P \left(\max \left\{ |Y^+(\tau, F_D)|^2, |Y^-(\tau, F_D)|^2 \right\} > \beta \right) \\ &= 1 - P \left(\max \left\{ |Y^+(\tau, F_D)|^2, |Y^-(\tau, F_D)|^2 \right\} < \beta \right) \\ &= 1 - P \left(|Y^+(\tau, F_D)|^2 < \beta, |Y^-(\tau, F_D)|^2 < \beta \right) \\ &= 1 - P \left(|Y^+(\tau, F_D)|^2 < \beta \right) P \left(|Y^-(\tau, F_D)|^2 < \beta \right). \end{aligned} \quad (7.15)$$

The last line in Eq. (7.15) has been obtained by exploiting the independence between $|Y^+(\tau, F_D)|^2$ and $|Y^-(\tau, F_D)|^2$ that derives from the independence of $Y^+(\tau, F_D)$ and

$Y^- (\tau, F_D)$. In fact one has

$$\begin{aligned}
 \mathbb{E} \{ Y^+ (\tau, F_D) [Y^- (\tau, F_D)]^* \} &= \mathbb{E} \{ [Y_D (\tau, F_D) + jY_P (\tau, F_D)] [Y_D (\tau, F_D) - jY_P (\tau, F_D)]^* \} \\
 &= \mathbb{E} \{ [Y_D (\tau, F_D) + jY_P (\tau, F_D)] [Y_D^* (\tau, F_D) + jY_P^* (\tau, F_D)] \} \\
 &= \mathbb{E} \left\{ |Y_D (\tau, F_D)|^2 - |Y_P (\tau, F_D)|^2 \right\} \\
 &\quad + j\mathbb{E} \{ Y_D (\tau, F_D) Y_P^* (\tau, F_D) \} + j\mathbb{E} \{ Y_D^* (\tau, F_D) Y_P (\tau, F_D) \} \\
 &= 0
 \end{aligned} \tag{7.16}$$

In Eq. (7.16), the fact that $\mathbb{E} \{ |Y_D (\tau, F_D)|^2 \} = \mathbb{E} \{ |Y_P (\tau, F_D)|^2 \}$ has been exploited, since data and pilot channels have the same power and $Y_D (\tau, F_D)$ and $Y_P^* (\tau, F_D)$ are zero mean independent random variables. The independence of $Y_D (\tau, F_D)$ and $Y_P^* (\tau, F_D)$ derives from the orthogonality of the data and pilot codes. Eq. (7.16) proves that $Y^+ (\tau, F_D)$ and $Y^- (\tau, F_D)$ are uncorrelated, which also implies their independence, since both $Y^+ (\tau, F_D)$ and $Y^- (\tau, F_D)$ are Gaussian random variables [58]. $|Y^+ (\tau, F_D)|^2$ and $|Y^- (\tau, F_D)|^2$ are χ^2 distributed with two degrees of freedom and, when the signal is absent, or the local replicas are not aligned with the received signal, $|Y^+ (\tau, F_D)|^2$ and $|Y^- (\tau, F_D)|^2$ are both central. Since the equivalent codes (7.12) have twice the power of the single pilot and data codes, the variance of $Y^+ (\tau, F_D)$ and $Y^- (\tau, F_D)$ is $2\sigma_n^2$ and inserting Eq. (3.26) into Eq. (7.15) yields the false alarm probability

$$P_{fa}^{ch}(\beta) = 1 - \left[1 - \exp \left\{ -\frac{\beta}{4\sigma_n^2} \right\} \right]^2. \tag{7.17}$$

It can be noted that the exponential in Eq. (7.17) depends on $4\sigma_n^2$ instead of $2\sigma_n^2$ as for Eqs. (7.10) and (3.26).

When the signal is present and correctly aligned with the local replica, $|Y^+ (\tau, F_D)|^2$ and $|Y^- (\tau, F_D)|^2$ are non-central χ^2 random variables, and the respective non-centrality parameters have to be determined. In particular one can write:

$$\begin{aligned}
 \mathbb{E} [Y^+ (\tau, F_D)] &= \mathbb{E} \{ [Y_{D,I} (\tau, F_D) + jY_{D,Q} (\tau, F_D)] + j [Y_{P,I} (\tau, F_D) + jY_{P,Q} (\tau, F_D)] \} \\
 &= \begin{cases} \sqrt{C} \frac{\sin(\pi N \delta F)}{\pi \delta F} R(\delta \tau) \exp(j\delta \phi_D) & \text{relative data/pilot sign} = 1; \\ 0 & \text{otherwise.} \end{cases}
 \end{aligned} \tag{7.18}$$

and similarly,

$$\mathbb{E} [Y^- (\tau, F_D)] = \begin{cases} 0 & \text{relative data/pilot sign} = 1 \\ \sqrt{C} \frac{\sin(\pi N \delta F)}{\pi N \delta F} R(\delta \tau) \exp(j\delta \phi_D) & \text{otherwise.} \end{cases} \tag{7.19}$$

From these considerations it emerges that the decision variable $S(\tau, F_D)$, under H_1 , is given by the maximum between a central χ^2 and a non-central χ^2 random variables with two degrees of freedom. The non-centrality parameter of the non-central χ^2 random variable is given by

$$C \frac{\sin^2(\pi N \delta F)}{(\pi N \delta F)^2} R^2(\delta \tau) \approx C = 4\lambda. \quad (7.20)$$

Given these premises it is finally possible to express the detection probability as

$$P_d^{ch}(\beta) = 1 - \left[1 - \exp \left\{ -\frac{\beta}{4\sigma_n^2} \right\} \right] \left[1 - Q_1 \left(\sqrt{\frac{4\lambda}{2\sigma_n^2}}, \sqrt{\frac{\beta}{2\sigma_n^2}} \right) \right] \quad (7.21)$$

7.2.3 Differentially coherent channel combining

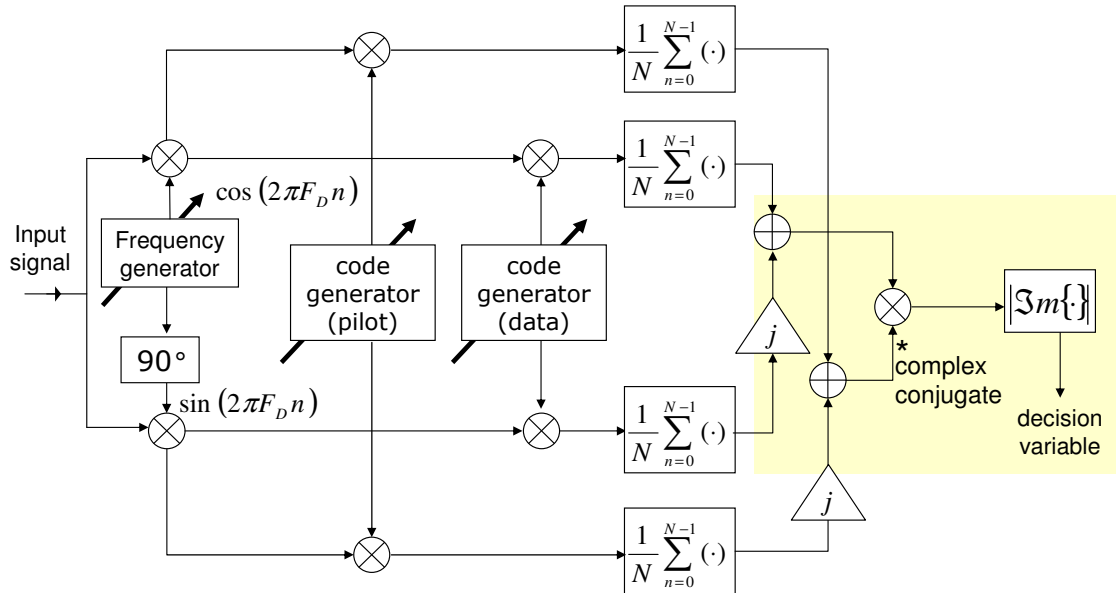


Figure 7.3. Acquisition scheme for differentially coherent channel combining with bit recovery: the correlations with the data and pilot local codes are performed separately and differentially coherent combined. Some modifications have been introduced to the traditional differentially coherent combining scheme in order to account for the phase difference between data and pilot channels.

In traditional differentially coherent combining [10, 12] correlations on two consecutive portions of the incoming signal are evaluated and the decision variable is obtained by taking the real part of the product of these two correlations. In this way the phase of

the second correlation is used to compensate the phase of the first one. Moreover, since the noise terms on the two correlations are independent, a lower noise amplification is expected, with respect to non-coherent combining [11]. Differential combining is effective as long as the hypothesis of constant phase on the two subsequent correlations holds; degradations are expected in presence of a time-varying phase.

When considering composite GNSS signals, data and pilot channels experience the same transmission channel and thus they are likely affected by the same delay and Doppler frequency. Moreover their phase is strictly related by Eq. (7.7). In this way the traditional differentially coherent acquisition scheme can be modified in order to employ the data and the pilot channel instead of two subsequent portions of the same signal. In Figure 7.3 the acquisition scheme employing differentially coherent channel combining is reported. The input signal is separately correlated with the data and the pilot local codes, and two complex correlations are formed, namely

$$\begin{aligned} Y_D(\tau, F_D) &= Y_{D,I}(\tau, F_D) + jY_{D,Q}(\tau, F_D); \\ Y_P(\tau, F_D) &= Y_{P,I}(\tau, F_D) + jY_{P,Q}(\tau, F_D) \end{aligned}$$

Finally the decision variable is obtained as

$$S(\tau, F_D) = |\mathbb{I}m\{Y_D(\tau, F_D) Y_P^*(\tau, F_D)\}|. \quad (7.22)$$

In Eq. (7.22) the imaginary part of the product $Y_D(\tau, F_D) Y_P^*(\tau, F_D)$ has been considered instead of the real part for the traditional differentially coherent acquisition scheme [12]. This modification has been introduced in order to account for the phase difference (7.7) between the data and pilot channels. Moreover in Eq. (7.22) the absolute value has been introduced in order to remove the dependence on the product of the navigation message and secondary codes.

In [12] it is shown that the real part of the product of two independent Gaussian random variables can be rewritten as the difference of two independent χ^2 random variables. Similarly

$$\begin{aligned} \mathbb{I}m\{Y_D(\tau, F_D) Y_P^*(\tau, F_D)\} &= \mathbb{R}e\{-jY_D(\tau, F_D) Y_P^*(\tau, F_D)\} = \mathbb{R}e\{Y_D(\tau, F_D) [jY_P(\tau, F_D)]^*\} \\ &= \left| \frac{Y_D(\tau, F_D) + jY_P(\tau, F_D)}{2} \right|^2 - \left| \frac{Y_D(\tau, F_D) - jY_P(\tau, F_D)}{2} \right|^2. \end{aligned} \quad (7.23)$$

When the useful GNSS signal is absent or not correctly aligned $\left| \frac{Y_D(\tau, F_D) + jY_P(\tau, F_D)}{2} \right|^2$ and $\left| \frac{Y_D(\tau, F_D) - jY_P(\tau, F_D)}{2} \right|^2$ are two independent central χ^2 random variables with two degrees of freedom and thus $\mathbb{I}m\{Y_D(\tau, F_D) Y_P^*(\tau, F_D)\}$ is Laplace distributed [12, 56] as

$$\mathbb{I}m\{Y_D(\tau, F_D) Y_P^*(\tau, F_D)\} | H_0 \sim \text{Laplace}\left(0, \frac{1}{\sigma_n^2}\right).$$

It can then be shown that the decision variable $Y(\tau, F_D) = |\mathbb{I}m \{Y_D(\tau, F_D) Y_P^*(\tau, F_D)\}|$ is exponentially distributed under H_0 . By exploiting these properties it is then possible to write the probability of false alarm as

$$P_{fa}^{dc}(\beta) = \exp \left\{ -\frac{\beta}{\sigma_n^2} \right\}. \quad (7.24)$$

When the signal is present, depending on the relative sign between data and pilot channels, either $\left| \frac{Y_D(\tau, F_D) + jY_P(\tau, F_D)}{2} \right|^2$ or $\left| \frac{Y_D(\tau, F_D) - jY_P(\tau, F_D)}{2} \right|^2$ is a non-central χ^2 random variable with two degrees of freedom and non-centrality parameter equal to λ . In order to determine the probability density function of the decision statistic under H_1 , it is possible to assume that $Y(\tau, F_D)$ is given by the absolute value of the difference of a non-central and a central χ^2 random variable. In fact, the absolute value in Eq. (7.22) removes the dependence on the relative sign between data and pilot channels making the case in which $\left| \frac{Y_D(\tau, F_D) + jY_P(\tau, F_D)}{2} \right|^2$ is non-central equivalent to the case in which $\left| \frac{Y_D(\tau, F_D) - jY_P(\tau, F_D)}{2} \right|^2$ is non-central. From [56] (Chapter 4.C) the pdf of the difference between a non-central and a central χ^2 random variables with two degrees of freedom is given by

$$p_d(x) = \frac{1}{2\sigma_n^2} \exp \left\{ \frac{2x - \lambda}{2\sigma_n^2} \right\} Q_1 \left(\sqrt{\frac{\lambda}{\sigma_n^2}}, \max \left(0, \sqrt{\frac{4x}{\sigma_n^2}} \right) \right) \quad (7.25)$$

Finally, by applying the modulus transformation to the difference of non-central and central random variables, it is possible to determine the pdf of $|\mathbb{I}m \{Y_D(\tau, F_D) Y_P^*(\tau, F_D)\}|$ as

$$p_S(s) = \frac{1}{2\sigma_n^2} \exp \left\{ -\frac{2s + \lambda}{2\sigma_n^2} \right\} + \frac{1}{2\sigma_n^2} \exp \left\{ \frac{2s - \lambda}{2\sigma_n^2} \right\} Q_1 \left(\sqrt{\frac{\lambda}{\sigma_n^2}}, \sqrt{\frac{4s}{\sigma_n^2}} \right) (s > 0). \quad (7.26)$$

The probability of detection is obtained by integrating by parts Eq. (7.26):

$$P_d^{dc}(\beta) = \frac{1}{2} \exp \left\{ -\frac{2\beta + \lambda}{2\sigma_n^2} \right\} - \frac{1}{2} \exp \left\{ \frac{2\beta - \lambda}{2\sigma_n^2} \right\} Q_1 \left(\sqrt{\frac{\lambda}{\sigma_n^2}}, \sqrt{\frac{4\beta}{\sigma_n^2}} \right) + Q_1 \left(\sqrt{\frac{2\lambda}{\sigma_n^2}}, \sqrt{\frac{2\beta}{\sigma_n^2}} \right) \quad (7.27)$$

To the best of our knowledge expression (7.27) is new.

7.2.4 Simulation analysis and comparison

In previous sections three different schemes for the acquisition of composite GNSS signals have been analyzed by characterizing the respective probabilities of detection and false alarm. The results are summarized in Table 7.1.

In this section the different acquisition schemes are compared in terms of ROCs and the performance of each strategy is analyzed by simulation.

Table 7.1. False alarm and detection probabilities for different acquisition schemes. The symbol “■” denotes the original contributions of this chapter.

Scheme	$P_{fa}(\beta)$	$P_d(\beta)$
Single channel acquisition	$P_{fa}^{sc}(\beta) = \exp\left\{-\frac{\beta}{2\sigma_n^2}\right\}$	$P_d^{sc}(\beta) = Q_1\left(\sqrt{\frac{\lambda}{\sigma_n^2}}, \sqrt{\frac{\beta}{\sigma_n^2}}\right)$
Non-coherent combining	$P_{fa}^{nc}(\beta) = \exp\left\{-\frac{\beta}{2\sigma_n^2}\right\} \left(1 + \frac{\beta}{2\sigma_n^2}\right)$	$P_d^{nc}(\beta) = Q_2\left(\sqrt{\frac{2\lambda}{\sigma_n^2}}, \sqrt{\frac{\beta}{\sigma_n^2}}\right)$
Coherent combining ■	$P_{fa}^{ch}(\beta) = 1 - \left[1 - \exp\left\{-\frac{\beta}{4\sigma_n^2}\right\}\right]^2$	$P_d^{ch}(\beta) = 1 - \left[1 - \exp\left\{-\frac{\beta}{4\sigma_n^2}\right\}\right] \cdot \left[1 - Q_1\left(\sqrt{\frac{2\lambda}{\sigma_n^2}}, \sqrt{\frac{\beta}{2\sigma_n^2}}\right)\right]$
Differentially coherent combining ■	$P_{fa}^{dc}(\beta) = \exp\left\{-\frac{\beta}{\sigma_n^2}\right\}$	$P_d^{dc}(\beta) = \frac{1}{2} \exp\left\{-\frac{2\beta + \lambda}{2\sigma_n^2}\right\} - \frac{1}{2} \exp\left\{\frac{2\beta - \lambda}{2\sigma_n^2}\right\} Q_1\left(\sqrt{\frac{\lambda}{\sigma_n^2}}, \sqrt{\frac{4\beta}{\sigma_n^2}}\right) + Q_1\left(\sqrt{\frac{2\lambda}{\sigma_n^2}}, \sqrt{\frac{2\beta}{\sigma_n^2}}\right)$

7.2.5 Simulation results

Table 7.2. Simulation parameters.

Parameter	Value
Sampling frequency, f_s	40.92 MHz
$B_{IF} = f_s/2$	20.46 MHz
Intermediate frequency, $f_{IF} = f_s/4$	10.23 MHz
Code length N	10230 chip
Pre-detection integration time	1 ms
Samples/chip	4

The analytical results of the previous sections have been tested by simulation and

particular false alarm and detection probabilities for the different strategies have been evaluated by means of Monte Carlo simulations. For all simulations the parameters reported in Table 7.2 have been adopted. The parameters of Table 7.2 reflect the code rate and the bandwidth that will be adopted for GPS L5 and Galileo E5a and E5b signals. The effect of the frontend filter has been neglected and the composite signal has been simulated as an ideal QPSK modulation, using the spreading codes from [66].

Simulation results are reported in Figure 7.4. In particular the ROC curves for the different acquisition methods have been estimated by means of Monte Carlo simulations and compared with the theoretical models provided in previous sections: the false alarm and detection probabilities evaluated by Monte Carlo simulations always overlap with the theoretical curves highlighting the validity of the models provided in previous sections.

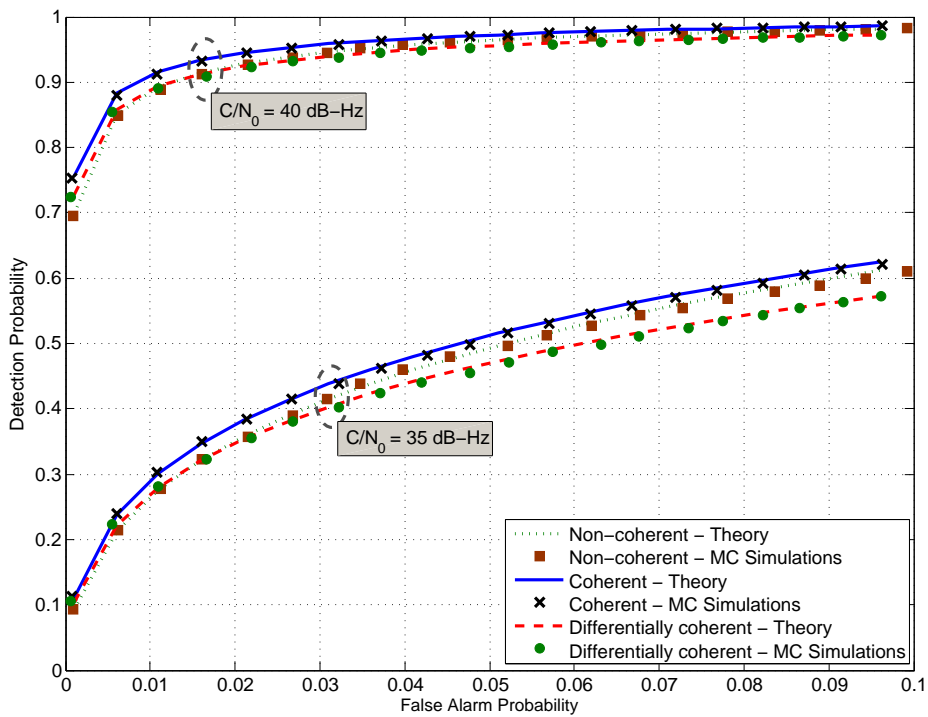


Figure 7.4. Theoretical and simulated ROCs for the different acquisition methods.

7.2.6 ROC comparison

The three acquisition methods analyzed in previous sections have been compared in terms of the ROC curves; ROCs for the single channel acquisition have been added as

a comparison term. As expected, and as already reported [17], the single channel acquisition always leads to the worst performance. This is due to the fact that only half of the available signal power is exploited. The advantage of the single channel acquisition is the relative simplicity of the algorithm, which requires only half of the computational load needed by the other methods.

In Figures 7.5 and 7.6 the ROC comparison is reported for C/N_0 of 40, 35 and 30 dB-Hz. The plots are in log-log scale in order to enhance the differences among the different algorithms. In all considered cases, coherent combining outperforms the other strategies although all the methods that combine both channels tend to converge to the same curve for low C/N_0 . Differentially coherent and non-coherent combining show similar performance, although the non-coherent combining algorithm works slightly better for high values of false alarm probability whereas the differentially coherent is preferable for low P_{fa} . The cross-over point between the differentially coherent and the non-coherent ROC is located around a value of false alarm probability of 10^{-2} . In Figure 7.7 the detection

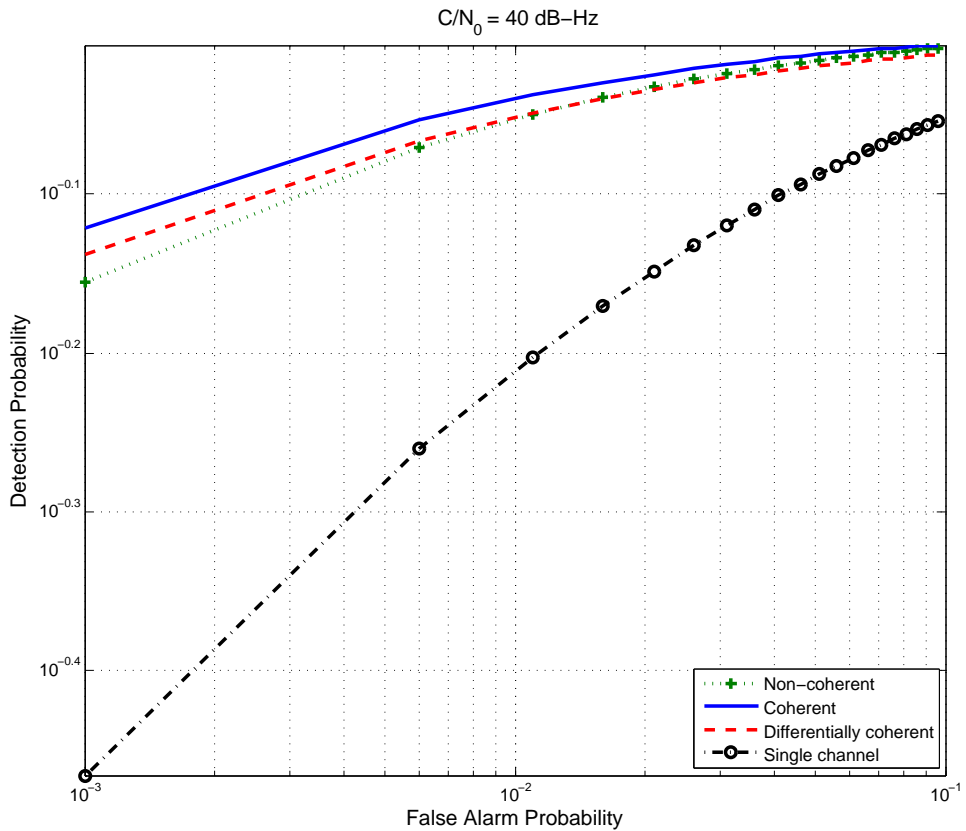


Figure 7.5. ROC comparison among the different acquisition strategies. $C/N_0 = 40$ dB-Hz.

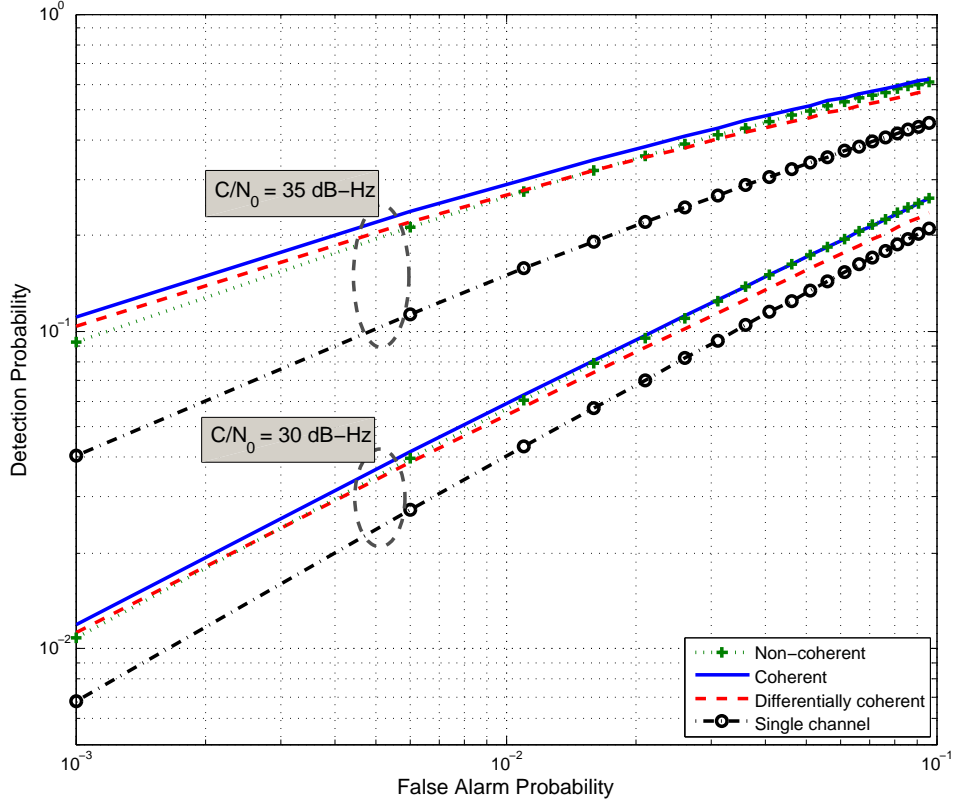


Figure 7.6. ROC comparison among the different acquisition strategies. $C/N_0 = 35$ and $C/N_0 = 30 \text{ dB-Hz}$.

probabilities for the different acquisition techniques have been plotted for different values of C/N_0 and for a fixed false alarm rate $P_{fa} = 10^{-3}$. From this plot it emerges clearly that coherent channel combining outperforms the other acquisition strategies, since, for a given C/N_0 , it yields the highest detection probability. In this case, since the probability of false alarm is lower than 10^{-2} , differentially coherent combining outperforms the non-coherent channel combining strategy.

From this analysis it emerges that, when acquisition on a single code period is considered, coherent channel combining with bit recovery is the most effective acquisition strategy. For low C/N_0 , the sign estimation is no longer reliable and coherent channel combining tends to have the same performance as non-coherent combining.

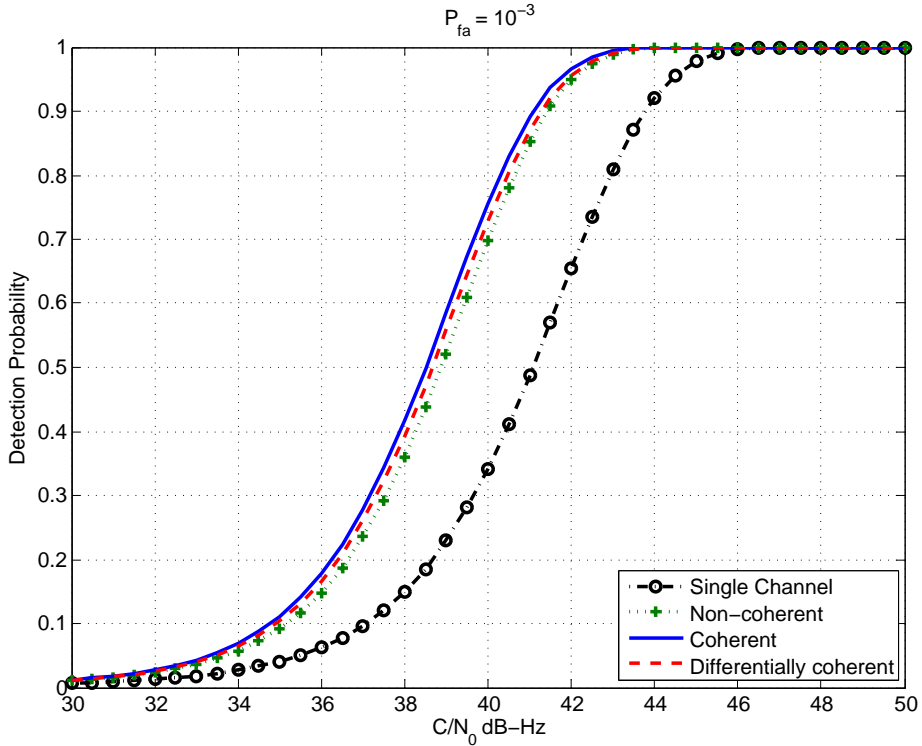


Figure 7.7. Detection probability vs. C/N_0 for a fixed false alarm rate, $P_{fa} = 10^{-3}$.

7.3 Multiple code period integration

In order to increase the acquisition performance, different instances of the decision variable $S(\tau, F_D)$ can be combined in order to reduce the noise impact. However, since the sign of the navigation message and of the secondary code can change each primary code period, an adequate strategy to deal with this problem has to be adopted. In the following the notation

$$S_k(\tau, F_D)$$

will indicate the decision variable evaluated on k th input signal portion and

$$S(\tau, F_D) = F [Y_{D,1}(\tau, F_D), Y_{D,2}(\tau, F_D), \dots, Y_{D,K}(\tau, F_D), Y_{P,1}(\tau, F_D), Y_{P,2}(\tau, F_D), \dots, Y_{P,K}(\tau, F_D)]$$

will indicate the final decision variable obtained by opportunely combining K independent instances of the complex correlations of the data and pilot channels.

7.3.1 Signal integration without sign recovery

This section is devoted to the analysis of different acquisition strategies that employ a non-linear function in order to remove the dependence of the variables $Y_{D,k}(\tau, F_D)$ and $Y_{P,k}(\tau, F_D)$ from the navigation message and the secondary codes. In particular a non-linear function is used to remove the dependence from the signs $d_{D,k}$ and $d_{P,k}$ in Eq. (7.6), where the index k has been added to denote time dependence. The principle of

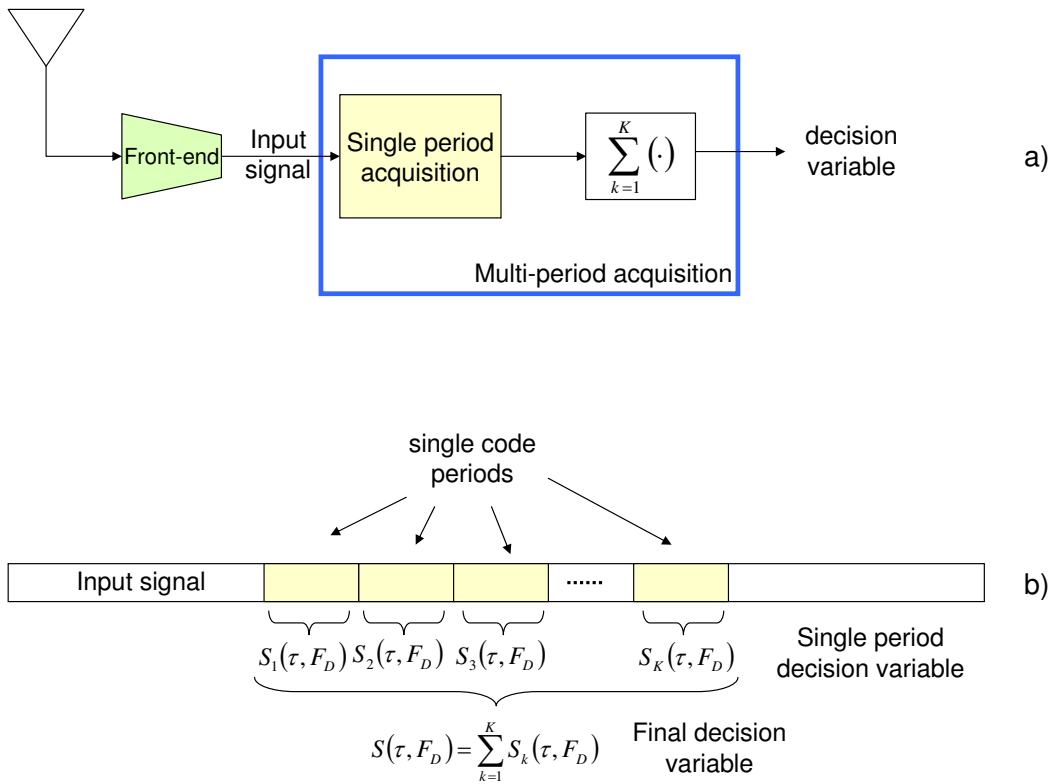


Figure 7.8. Principle of signal integration without sign recovery. A phase/sign independent random variable $S_k(\tau, F_D)$ is produced for each primary code period. These random variables are then directly summed producing the final decision statistic $S(\tau, F_D)$.

this kind of signal integration is reported in Figure 7.8. A sign independent random variable $S_k(\tau, F_D)$ is produced for each primary code period and the final decision random variable is given by

$$S(\tau, F_D) = \sum_{i=1}^K S_i(\tau, F_D). \quad (7.28)$$

7.3.2 Non-coherent integration

By applying the non-coherent channel combining strategy to Eq. (7.28) the final decision random variable assumes the following expression:

$$S(\tau, F_D) = \sum_{k=1}^K S_k(\tau, F_D) = \sum_{k=1}^K |Y_{D,k}(\tau, F_D)|^2 + \sum_{k=1}^K |Y_{P,k}(\tau, F_D)|^2. \quad (7.29)$$

The expressions of the false alarm and detection probabilities for Eq. (7.29) are well known from the literature [17] and are

$$P_{fa}(\beta, K) = \exp \left\{ -\frac{\beta}{2\sigma_n^2} \right\} \sum_{i=0}^{2K-1} \frac{1}{i!} \left(\frac{\beta}{2\sigma_n^2} \right)^i \quad (7.30)$$

$$P_d(\beta, K) = Q_{2K} \left(\sqrt{\frac{2K\lambda}{\sigma_n^2}}; \sqrt{\frac{\beta}{\sigma_n^2}} \right) \quad (7.31)$$

where λ is the non-centrality parameter (7.9).

7.3.3 Semi-coherent integration

Semi-coherent integration was considered at first by [71] that only proposed the method, without providing a rigorous analysis of its performance. In this section the semi-coherent integration technique is further detailed and a closed-form formula for the false alarm probability is provided. A technique, based on the numerical inversion of the characteristic function (chf), is also provided for the evaluation of the detection probability.

In the semi-coherent integration strategy the decision variables on the single code period are obtained as

$$S_k(\tau, F_D) = \max \left\{ |Y_k^+(\tau, F_D)|^2, |Y_k^-(\tau, F_D)|^2 \right\}$$

i.e. the decision variables obtained by employing coherent channel combining with sign recovery, as discussed in Section 7.2.2. The final decision variable for the semi-coherent integration strategy is given by

$$S(\tau, F_D) = \sum_{k=1}^K S_k(\tau, F_D) = \sum_{k=1}^K \max \left\{ |Y_k^+(\tau, F_D)|^2, |Y_k^-(\tau, F_D)|^2 \right\}. \quad (7.32)$$

In order to determine the expression for the false alarm and detection probabilities for a generic K the following approach can be adopted. At first the chfs, $Ch_{fa}(t,1)$ and $Ch_d(t,1)$, for the case $K = 1$ can be evaluated from Eqs. (7.17) and (7.21). The chfs for a generic K are then obtained by raising to the power K $Ch_{fa}(t,1)$ and $Ch_d(t,1)$:

$$\begin{aligned} Ch_{fa}(t, K) &= Ch_{fa}^K(t, 1) \\ Ch_d(t, K) &= Ch_d^K(t, 1) \end{aligned} \quad (7.33)$$

Property (7.33) is a direct consequence of the independence of the single period decision variables $S_k(\tau, F_D)$.

The pdfs, and consequently the detection and false alarm probabilities, can be finally obtained by inverting the chfs (7.33).

By deriving Eq. (7.17), the pdf of the decision variable under H_0 and for $K = 1$ is given by

$$\begin{aligned} f_{fa}(x,1) &= -\frac{d}{dx} P_{fa}(x,1) \\ &= 2 \left[\frac{1}{4\sigma_n^2} \exp \left(-\frac{x}{4\sigma_n^2} \right) \right] - \left[\frac{1}{2\sigma_n^2} \exp \left(-\frac{x}{2\sigma_n^2} \right) \right] \end{aligned} \quad (7.34)$$

Eq. (7.34) can be interpreted as the difference of two weighted exponential distributions and thus the chf of $S_k(\tau, F_D)$ under H_0 is given by the following combination of exponential chfs [44]:

$$Ch_{fa}(t,1) = \frac{2}{(1-j4\sigma_n^2 t)} - \frac{1}{(1-j2\sigma_n^2 t)} = \frac{1}{(1-j4\sigma_n^2 t)(1-j2\sigma_n^2 t)} \quad (7.35)$$

Thus the chf of $S(\tau, F_D)$ is given by:

$$Ch_{fa}(t,K) = \frac{1}{(1-j4\sigma_n^2 t)^K (1-j2\sigma_n^2 t)^K} = \sum_{i=1}^K \left[\frac{a_{K,i}}{(1-j4\sigma_n^2 t)^i} - \frac{b_{K,i}}{(1-j2\sigma_n^2 t)^i} \right] \quad (7.36)$$

where the second part of Eq. (7.36) is the partial fraction expansion of $\frac{1}{(1-j4\sigma_n^2 t)^K (1-j2\sigma_n^2 t)^K}$. $\{a_{K,i}\}_{i=1}^K$ and $\{b_{K,i}\}_{i=1}^K$ are the coefficients of the partial fraction expansion of Eq. (7.36). A recursive algorithm for the determination of the coefficients $\{a_{K,i}\}_{i=1}^K$ and $\{b_{K,i}\}_{i=1}^K$ is reported in Appendix F.

The chf (7.36) can be interpreted as the linear combination of chfs of central χ^2 random variables with different degrees of freedom. Thus the probability density function of $S(\tau, F_D)$ is a linear combination of central χ^2 probability density functions:

$$\begin{aligned} f_{fa}(x,K) &= \sum_{i=1}^K \left[a_{K,i} \left(\frac{1}{4\sigma_n^2} \right)^i \frac{x^i}{(i-1)!} \exp \left\{ -\frac{x}{4\sigma_n^2} \right\} - b_{K,i} \left(\frac{1}{2\sigma_n^2} \right)^i \frac{x^i}{(i-1)!} \exp \left\{ -\frac{x}{2\sigma_n^2} \right\} \right] \\ &= \sum_{i=1}^K \left(\frac{1}{4\sigma_n^2} \right)^i \frac{x^i}{(i-1)!} \exp \left\{ -\frac{x}{4\sigma_n^2} \right\} \left[a_{K,i} - b_{K,i} 2^i \exp \left\{ -\frac{x}{4\sigma_n^2} \right\} \right] \end{aligned} \quad (7.37)$$

From Eq. (7.37) it is finally possible to evaluate the false alarm probability related to $S(\tau, F_D)$ under H_0 as

$$\begin{aligned} P_{fa}(\beta, K) &= \int_{\beta}^{+\infty} f_{fa}(x, K) dx \\ &= \exp \left\{ -\frac{\beta}{4\sigma_n^2} \right\} \sum_{i=1}^K \sum_{m=0}^{i-1} \left(\frac{1}{4\sigma_n^2} \right)^m \frac{1}{m!} \left[a_{K,i} - b_{K,i} 2^m \exp \left\{ -\frac{\beta}{4\sigma_n^2} \right\} \right]. \end{aligned} \quad (7.38)$$

Eq. (7.38) can be easily inverted by using a Newton-Raphson based algorithm. In this way, the decision threshold β can be determined. A first approximated solution for the threshold β can be obtained by using a normal approximation for $S(\tau, F_D)$. In particular, from Eqs. (7.32) and (7.34), it is possible to evaluate the mean and the variance of $S(\tau, F_D)$ under H_0 :

$$\begin{aligned} \mathbb{E}[S(\tau, F_D) | H_0] &= 6K\sigma_n^2; \\ \text{Var}\{S(\tau, F_D) | H_0\} &= 10K\sigma_n^4. \end{aligned} \quad (7.39)$$

and thus

$$P_{fa}(\beta, K) \approx \frac{1}{2} \operatorname{erfc} \left(\frac{\beta - 6K\sigma_n^2}{\sqrt{2 \cdot 10K\sigma_n^4}} \right) \quad \text{for } K \gg 1 \quad (7.40)$$

where $\operatorname{erfc}(\cdot)$ is the complementary error function [45].

Under H_1 the pdf of $S_k(\tau, F_D)$ assumes the following expression:

$$\begin{aligned} f_d(x, 1) &= -\frac{d}{dx} P_d(x, 1) \\ &= \frac{1}{4\sigma_n^2} \exp \left\{ -\frac{x}{4\sigma_n^2} \right\} + \frac{1}{4\sigma_n^2} \exp \left\{ -\frac{x+4\lambda}{4\sigma_n^2} \right\} I_0 \left(\frac{\sqrt{4\lambda x}}{2\sigma_n^2} \right) \\ &\quad - \exp \left\{ -\frac{2\lambda}{4\sigma_n^2} \right\} \frac{1}{4\sigma_n^2} \exp \left\{ -\frac{x+\lambda}{2\sigma_n^2} \right\} I_0 \left(\frac{\sqrt{\lambda x}}{\sigma_n^2} \right) \\ &\quad - \frac{1}{4\sigma_n^2} \exp \left\{ -\frac{x}{4\sigma_n^2} \right\} Q_1 \left(\sqrt{\frac{4\lambda}{2\sigma_n^2}}, \sqrt{\frac{x}{2\sigma_n^2}} \right) \end{aligned} \quad (7.41)$$

The evaluation of $Ch_d(t, 1)$ can be obtained by computing the Fourier transform of Eq. (7.41) that, after a significant effort of calculus, leads to

$$\begin{aligned} Ch_d(t, 1) &= \frac{1}{1 - j4\sigma_n^2 t} \left[\exp \left\{ \frac{j4\lambda t}{1 - j4\sigma_n^2 t} \right\} + \exp \left\{ -\frac{\lambda}{2\sigma_n^2} \right\} \exp \left\{ \frac{j\lambda t}{1 - j2\sigma_n^2 t} \right\} \right] \\ &\quad - \frac{1}{1 - j2\sigma_n^2 t} \exp \left\{ -\frac{\lambda}{2\sigma_n^2} \right\} \exp \left\{ \frac{j\lambda t}{1 - j2\sigma_n^2 t} \right\} \end{aligned} \quad (7.42)$$

It can be noted that Eq. (7.42) degenerates to Eq. (7.35) when the non-centrality parameter λ is equal to 0. By using Eq. (7.33), the chf for $S(\tau, F_D)$ under H_1 assumes the following expression:

$$\begin{aligned} Ch_d(t, K) &= \left[\frac{1}{1 - j4\sigma_n^2 t} \left[\exp \left\{ \frac{j4\lambda t}{1 - j4\sigma_n^2 t} \right\} + \exp \left\{ -\frac{\lambda}{2\sigma_n^2} \right\} \exp \left\{ \frac{j\lambda t}{1 - j2\sigma_n^2 t} \right\} \right] \right]^K \\ &\quad - \frac{1}{1 - j2\sigma_n^2 t} \exp \left\{ -\frac{\lambda}{2\sigma_n^2} \right\} \exp \left\{ \frac{j\lambda t}{1 - j2\sigma_n^2 t} \right\} \end{aligned} \quad (7.43)$$

Although Eq. (7.43) could be eventually inverted by using a partial fraction expansion, the resulting process is complex and a different approach should be taken. A solution is

represented by numerical algorithms for the inversion of the characteristic function [73]. In this way, by using efficient FFT algorithms [73], the probability of detection $P_d(\beta, K)$ can be easily evaluated.

7.3.4 Differentially coherent integration

In the differentially coherent acquisition scheme the decision variable on a single code period is given by:

$$S_k(\tau, F_D) = |\Im \{Y_{D,k}(\tau, F_D) [Y_{P,k}(\tau, F_D)]^*\}|. \quad (7.44)$$

The acquisition over several periods can be performed by directly summing K independent realizations of $S(F_D, \tau)$:

$$S(\tau, F_D) = \sum_{k=0}^{K-1} S_k(\tau, F_D) = \sum_{k=0}^{K-1} |\Im \{Y_{D,k}(\tau, F_D) [Y_{P,k}(\tau, F_D)]^*\}| \quad (7.45)$$

As proven in Section 7.2.3 $S_k(\tau, F_D)$ are exponentially distributed and thus $S(\tau, F_D)$ is χ^2 distributed with $2K$ degrees of freedom. Thus the false alarm probability for the non-coherent differential combining assumes the following expression:

$$P_{fa}(\beta, K) = \exp \left\{ -\frac{\beta}{\sigma_n^2} \right\} \sum_{i=0}^{K-1} \frac{1}{i!} \left(\frac{\beta}{\sigma_n^2} \right)^i. \quad (7.46)$$

The detection probability for a generic K does not admit a easy expression, but it can be evaluated by using a numerical method for the inversion of the characteristic function. In particular, it has been proven in Section 7.2.3 that the detection probability for $K = 1$ is given by

$$P_d(\beta, 1) = \frac{1}{2} \exp \left\{ -\frac{2\beta + \lambda}{2\sigma_n^2} \right\} - \frac{1}{2} \exp \left\{ \frac{2\beta - \lambda}{2\sigma_n^2} \right\} Q_1 \left(\sqrt{\frac{\lambda}{\sigma_n^2}}, \sqrt{\frac{4\beta}{\sigma_n^2}} \right) + Q_1 \left(\sqrt{\frac{2\lambda}{\sigma_n^2}}, \sqrt{\frac{2\beta}{\sigma_n^2}} \right) \quad (7.47)$$

The corresponding chf is obtained by deriving Eq. (7.47) and by evaluating its Fourier transform. This computation leads to

$$Ch_d(t, 1) = \frac{\exp \left\{ -\frac{\lambda}{2\sigma_n^2} \right\}}{1 + j\sigma_n^2 t^2} \left[j\sigma_n^2 t + \exp \left\{ \frac{\lambda}{2\sigma_n^2} \right\} \exp \left\{ \frac{j\lambda t}{1 - j\sigma_n^2 t} \right\} \right] \quad (7.48)$$

It is noted that, for $\lambda = 0$, Eq. (7.48) degenerates to the chf of a exponential random variable [44]. The chf for a generic K is obtained by raising to the power K Eq. (7.48):

$$Ch_d(t, 1) = \frac{\exp \left\{ -\frac{K\lambda}{2\sigma_n^2} \right\}}{(1 + j\sigma_n^2 t^2)^K} \left[j\sigma_n^2 t + \exp \left\{ \frac{\lambda}{2\sigma_n^2} \right\} \exp \left\{ \frac{j\lambda t}{1 - j\sigma_n^2 t} \right\} \right]^K \quad (7.49)$$

The detection probability can be then evaluated by numerically inverting [73] the chf (7.49). It has to be remarked that the pdf corresponding to Eq. (7.47) is not, in general, equal to zero initially. This corresponds to a discontinuity that would be hardly managed by the FFT based inversion algorithm. The problem can be solved by considering the regularized chf

$$\tilde{Ch}_d(t, K) = Ch_d(t, K) + Ch_d(-t, K). \quad (7.50)$$

The Fourier transform of Eq. (7.50) is given by

$$\tilde{f}_d(x, K) = f_d(x, K) + f_d(-x, K) \quad (7.51)$$

that is the sum of the pdf $f_d(x, K)$ and of its symmetric $f_d(-x, K)$. $\tilde{f}_d(x, K)$ does not present discontinuities in the origin and thus it can be easily evaluated by means of FFT based techniques. Moreover $f_d(x, K)$ and $f_d(-x, K)$ have disjoint supports and thus $f_d(x, K)$ can be easily recovered from $\tilde{f}_d(x, K)$.

7.3.5 Signal integration with sign recovery

In previous sections the total integration time has been extended by removing the sign dependence by a non-linear operation such as squaring. This strategy is not, in general, optimal [19] since the non-linear operation usually amplifies the noise components. In [19] optimal and near-optimal detectors for composite GNSS signals have been studied, showing that a near-optimal detection strategy consists in estimating the relative signs between data and pilot channel and among different consecutive portions of the incoming signals. This kind of strategy is further analyzed in this section considering two different methodologies. The first one, denoted as “exhaustive bit search” tests all possible sign combinations without considering the additional information provided by the secondary code. The second one, denoted as “secondary code partial correlation”, exploits the constraints imposed by the secondary code on the possible bit combinations. Those two strategies are better analyzed in the following paragraphs.

7.3.6 Exhaustive bit search

In order to increase the coherent integration time to K ms, it is possible to use the following decision statistic:

$$S(\tau, F_D) = \max_{\mathcal{D}_K} \left| \sum_{k=1}^K d_{D,k} Y_{D,k}(\tau, F_D) + j d_{P,k} Y_{P,k}(\tau, F_D) \right|^2 \quad (7.52)$$

where

$$\mathcal{D}_K = \{d_{D,k}, d_{P,k}\}_{k=0}^{K-1} \quad (7.53)$$

is the set of the possible signs of the data and pilot components. $Y_{D,k}(\tau, F_D)$ and $Y_{P,k}(\tau, F_D)$ are the correlations over the k th input signal period with the data and the pilot local replicas defined as

$$\begin{aligned} Y_{D,k}(\tau, F_D) &= Y_{D,I,k}(\tau, F_D) + jY_{D,Q,k}(\tau, F_D) \\ Y_{P,k}(\tau, F_D) &= Y_{P,I,k}(\tau, F_D) + jY_{P,Q,k}(\tau, F_D) \end{aligned} \quad (7.54)$$

where the components in Eq. (7.54) have been defined in Eq. (7.6).

If there were no secondary codes all the sign sequences would be possible and the exhaustive bit search would correspond to the Maximum Likelihood estimator for the code delay, the Doppler shift and the bit sequence (7.53). However, since secondary codes are foreseen for both the data and the pilot channel the exhaustive search algorithm results suboptimal since it does not account for the constraints imposed by the secondary codes. This strategy is analyzed in order to provide a comparison for the secondary code based partial correlations. Moreover, for low values of K , secondary codes do not introduce any constraints on possible bit combinations; in those cases the exhaustive search is the optimal estimator for the code delay, the Doppler frequency and the bit combination (7.53). In [19] it is shown that the decision statistics (7.52) is a near-optimum detector for establishing the signal presence, estimating the code delay and the Doppler frequency. The sub-optimality is given by the fact that Eq. (7.52) also provides the set

$$\hat{D}_K = \arg \max_{\mathcal{D}_K} \left| \sum_{k=1}^K d_{D,k} Y_{D,k}(\tau, F_D) + j d_{P,k} Y_{P,k}(\tau, F_D) \right|^2$$

that is an estimation of the sequence of bits transmitted by the GNSS satellites.

In order to evaluate Eq. (7.52) all the possible sign combinations \mathcal{D}_K have to be evaluated and tested. It is possible to construct, for each code delay and Doppler frequency the following vectors:

$$\begin{aligned} D(\tau, F_D) &= \begin{bmatrix} Y_{D,1}(\tau, F_D) \\ Y_{D,2}(\tau, F_D) \\ \vdots \\ Y_{D,K}(\tau, F_D) \end{bmatrix}; \quad P(\tau, F_D) = \begin{bmatrix} Y_{P,1}(\tau, F_D) \\ Y_{P,2}(\tau, F_D) \\ \vdots \\ Y_{P,K}(\tau, F_D) \end{bmatrix} \\ R(\tau, F_D) &= \begin{bmatrix} D(\tau, F_D) \\ jP(\tau, F_D) \end{bmatrix} \end{aligned} \quad (7.55)$$

that are the vectors containing the correlations of K code periods of the received signal with the local data and pilot codes. For each bit combination it is also possible to define

the column vector

$$d_{i,K} = \begin{bmatrix} d_{D,1} \\ d_{D,2} \\ \vdots \\ d_{D,K} \\ d_{P,1} \\ d_{P,2} \\ \vdots \\ d_{P,K} \end{bmatrix} \quad (7.56)$$

that accounts for the different signs that the data and the pilot components can assume. The index i has been added in order to enumerate all the possible sign combinations: each value of i univocally defines a sign combination. In this case $i = 0, 1, \dots, 2^{2K-1} - 1$ since half of the possible combinations is discarded because obtained by reversing the sign of the components of another vector $d_{i,K}$. Vectors only differing by the sign lead to the same decision variable and thus half of the bit combinations are discharged leading to 2^{2K-1} different d_i^K .

By using Eqs. (7.56) and (7.55), (7.52) can be written as

$$S(\tau, F_D) = \max_i |d_{i,K}^T R(\tau, F_D)|^2 \quad (7.57)$$

where $(\cdot)^T$ denotes transposition. For each set of signs $d_{i,K}$ a random variable

$$S_i(\tau, F_D) = d_{i,K}^T R(\tau, F_D)$$

is obtained and thus

$$S(\tau, F_D) = \max_i |S_i(\tau, F_D)|^2 \quad (7.58)$$

Since each $S_i(\tau, F_D)$ is a linear combination of the Gaussian random variables contained in the vector $R(F_D, \tau)$, they are still Gaussian random variables that are however strongly correlated. In fact the vectors containing all the different $S_i(\tau, F_D)$ can be obtained as

$$V(F_D, \tau) = \begin{bmatrix} d_{0,K}^T \\ d_{1,K}^T \\ \vdots \\ d_{2^{K-1}-1,K}^T \end{bmatrix} R(\tau, F_D) = M \cdot R(\tau, F_D) \quad (7.59)$$

and thus

$$\mathbb{E}[V(F_D, \tau)V^H(F_D, \tau)] = M\mathbb{E}[R(\tau, F_D)R(\tau, F_D)^H]M^H = \sigma_n^2 M M^H \quad (7.60)$$

where σ_n^2 is the variance of the components of $R(\tau, F_D)$ that have been assumed independent. From Eq. (7.60) clearly emerges the correlation among the components of $V(F_D, \tau)$. This correlation prevents the evaluation of an analytical expression for the false alarm and detection probabilities relative to Eq. (7.52). These probabilities will be analyzed by simulations in Section 7.3.9.

7.3.7 Secondary code partial correlation

In the previous section the decision statistic is formed by taking the maximum of a set of random variables obtained by considering all possible sign combinations occurring when considering K consecutive signal periods. However both data and pilot components of the composite GNSS signal can be modulated by a secondary code. The secondary code limits the number of possible sign combinations reducing the computational load required for the evaluation of the decision statistic.

In [19] the case relative to the GPS L5 modulation is considered and in particular the problem of optimally combining the data and pilot components is addressed. [19] considers the case of $K = M \cdot N_d$ where M is an integer greater than zero and $N_d = 10$ is the length of the secondary code of data channel expressed in terms of primary code periods. In this way the tiered code, obtained by combining the primary and the secondary codes, of the data channel is fully acquired whereas the pilot signal is processed by means of partial correlation. In this context we consider the case of partial correlations performed on both data and pilot codes.

7.3.8 Number of bit combinations with secondary code constraints

As already pointed out, the secondary codes reduce the number of possible bit combinations. The number of such combinations has to be kept as low as possible in order to

- reduce the computational load,
- improve the system performance since, when only a few candidates are possible, there are fewer opportunities to have a false alarm.

When both data and pilot channels are employed, the input block data, of duration K ms, can assume one of the different positions shown in Figure 7.9. Moreover the data secondary codes can assume any sign value, because of the navigation message. Let N_d be the length of the data secondary code, N_p the length of the pilot secondary code and $H = \frac{N_p}{N_d}$. When K is lower or equal to N_d it is possible to treat separately each segment in which the pilot code is divided by the data code. For each segment of secondary code, there are two possible cases depending if the input signal block crosses or not the data secondary code boundary. In the first case there are $2(N_d - K + 1)$ possible combinations

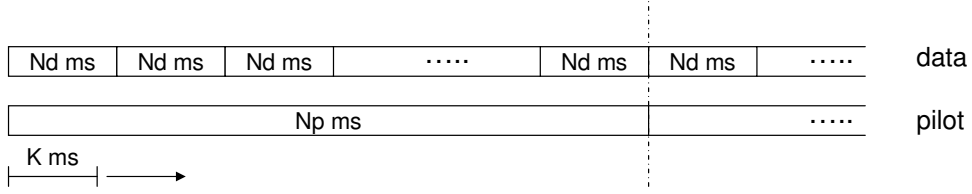


Figure 7.9. Possible positions of the input signal block with respect to the data and pilot secondary code.

since the input data block can assume $N_d - K + 1$ different delays without crossing the boundary of the data secondary code. The factor 2 is due to the fact that the sign of the data secondary code can be either positive or negative. When the input data block crosses the data secondary code boundary there are $4(K - 1)$ possible combinations: the factor 4 is due to the different signs that the two consecutive secondary codes of the data channel can assume with respect to the pilot channel. $K - 1$ is the number of delays that makes the input signal block cross the secondary code boundary. In this way, when considering both data and pilot channel and $K \leq N_d$ there are

$$2H(N_d + K - 1) \quad (7.61)$$

possible combinations.

When only the data channel is considered only

$$N_d + K - 1 \quad (7.62)$$

combinations have to be tested. In Table 7.3 the number of possible bit combinations to be tested with and without the constraints imposed by the secondary codes are compared. In order to have a fair comparison with the pilot and data case, the integration time for the case of the data channel alone has been doubled. It can be noted that, when the data channel alone is considered, the number of bit combinations is much lower than in the case in which both channels are considered. It has also to be noted that formulas (7.61) and (7.62) do not account for possible repetitions. In fact some combinations of data and pilot secondary codes can lead to the same bit sequence. For this reason, when $K = 2$ the number of possible sign combinations foreseen by Eqs. (7.61) and (7.62) is greater than the number of all possible combinations. However, as K increases, due to the pseudo-random nature of the secondary codes, the number of repetitions decreases and Eqs. (7.61) and (7.62) become more and more accurate.

From formulas (7.61) and (7.62), it clearly emerges that the search over a single channel results is more convenient than the dual channel combining. The drawback is seen by the fact that the integration time K has to be doubled since half of the useful power is

Table 7.3. Comparison of the number of possible bit combinations to be tested with and without the constraints imposed by the secondary codes. In order to have a fair comparison with the other two cases the integration time for the data channel alone has been doubled.

K	Data + Pilot channels	Data channel	Exhaustive search
2	210	23	8
3	220	25	32
4	230	27	128
5	240	29	512
6	250	31	2048
7	260	33	8192
8	270	35	32768
9	280	37	131072

discarded. In the context of this thesis only the partial correlation over the data channel is considered. As for the exhaustive bit search the false alarm and detection probability cannot be easily derived and will be studied by simulations in the next section.

7.3.9 Simulation results

The integration strategies described in previous sections have been analyzed by means of Monte Carlo simulations. The simulations parameters are reported in Table 7.4 and correspond to those already used for the analysis of the acquisition on a single code period. In Figures 7.10 and 7.11 the case of $K = 3$ is considered. As expected the exhaustive bit

Table 7.4. Simulation parameters.

Parameter	Value
Sampling frequency, f_s	40.92 MHz
$B_{IF} = f_s/2$	20.46 MHz
Intermediate frequency, $f_{i,E5} = f_s/4$	10.23 MHz
Code length N	10230 chip
Integration time	K ms
Samples/chip	4

search and the secondary code partial correlation strategies outperform the other techniques. This gain however results in an additional computational load, required by the search for the different bit combinations and by the reduced Doppler bin size. The secondary code partial correlation strategy has been implemented considering six periods of the data channel and ignoring the pilot channel. This choice, as already pointed out in Section 7.3.7, limits the number of bit combinations, reducing the search space dimension

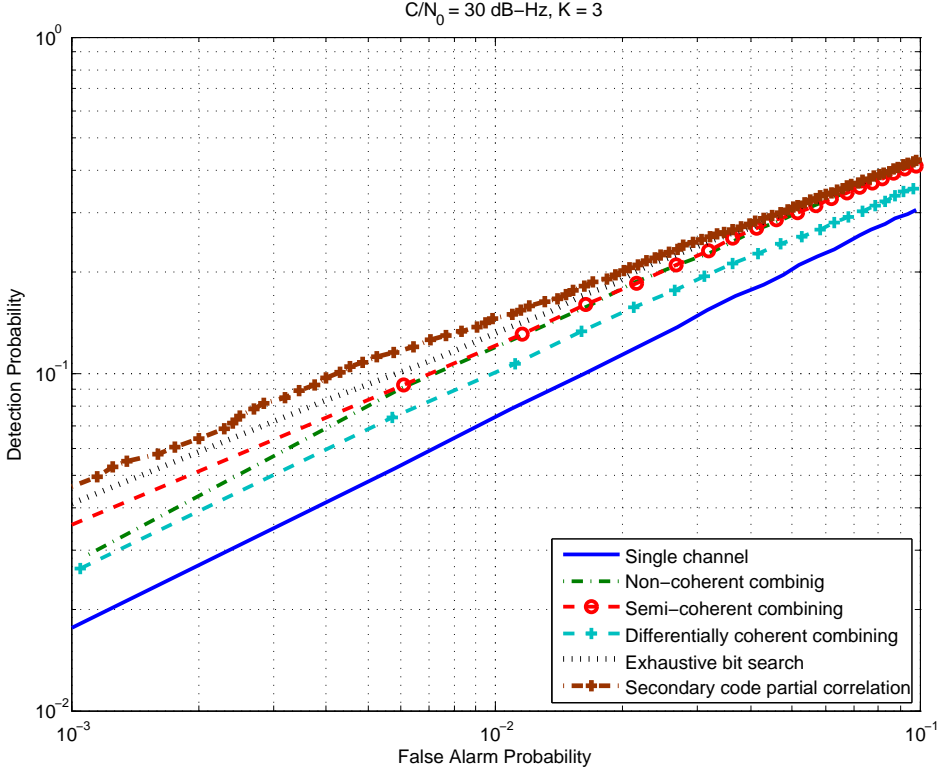


Figure 7.10. ROC comparison among different acquisition strategies. $C/N_0 = 30 \text{ dB-Hz}$, $K = 3$.

and providing a better immunity against noise. For this reason the secondary code partial correlation strategy outperforms the exhaustive bit search acquisition that also requires a heavier computational load.

The non-coherent, the semi-coherent and the differentially coherent integrations techniques require similar computational loads. Among these strategies the semi-coherent leads to the best performance. However, as the C/N_0 decreases, the difference between non-coherent and semi-coherent integrations tends to disappear. This is due to the fact that, for low C/N_0 , it is not possible to effectively recover the relative sign between data and pilot channels. Further investigations are required for establishing if non-coherent integration is preferable to semi-coherent integration for very low C/N_0 . In Figures 7.12 and 7.13 the case of $K = 5$ has been considered. The results are similar to those found for $K = 3$. The secondary code partial correlation strategy gives the best results in terms of ROC. Without the secondary code constraint, the number of bit combinations increases exponentially with respect to K . When the secondary code is considered the number of possible bit combinations grows linearly with K . Thus the performance gain of the

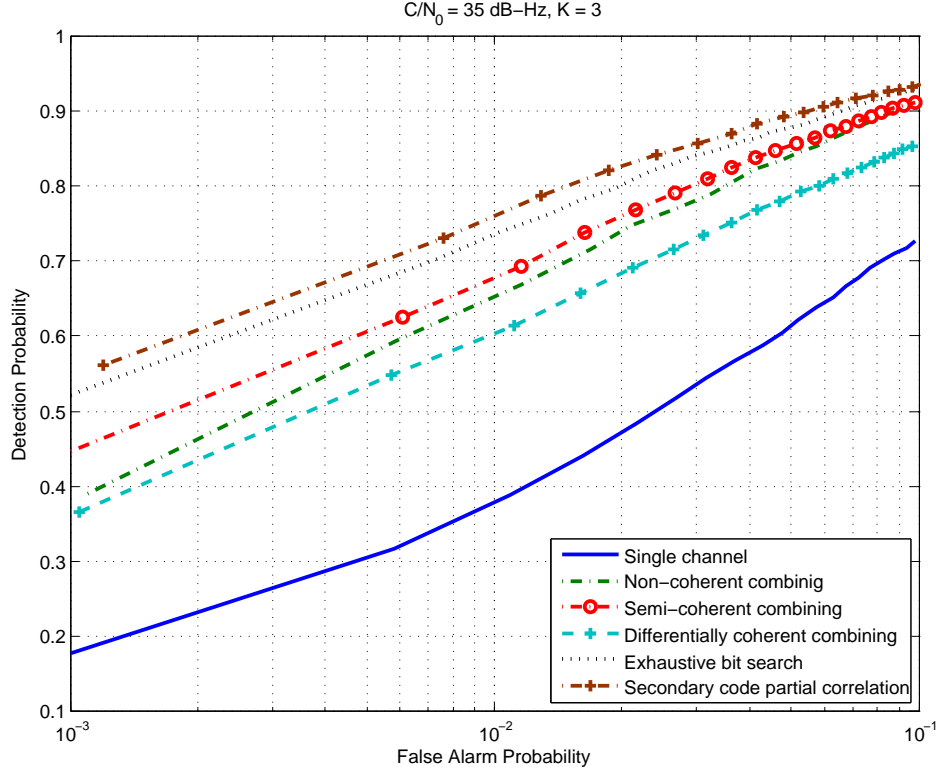


Figure 7.11. ROC comparison among different acquisition strategies. $C/N_0 = 35 \text{ dB-Hz}, K = 3$.

secondary code partial correlation with respect to the exhaustive bit search acquisition increases as K increases. This fact emerges clearly by comparing Figures 7.10 and 7.11 with Figures 7.12 and 7.13. In Figures 7.14, 7.15 and 7.16 the case of $K = 10$ is considered. The exhaustive bit search and the secondary code partial correlation strategies have not been considered because of their computational load. The simulation results agree with the previous analysis: non-coherent and semi-coherent integrations are preferable to the other techniques and semi-coherent integration outperforms the traditional non-coherent integration for high C/N_0 .

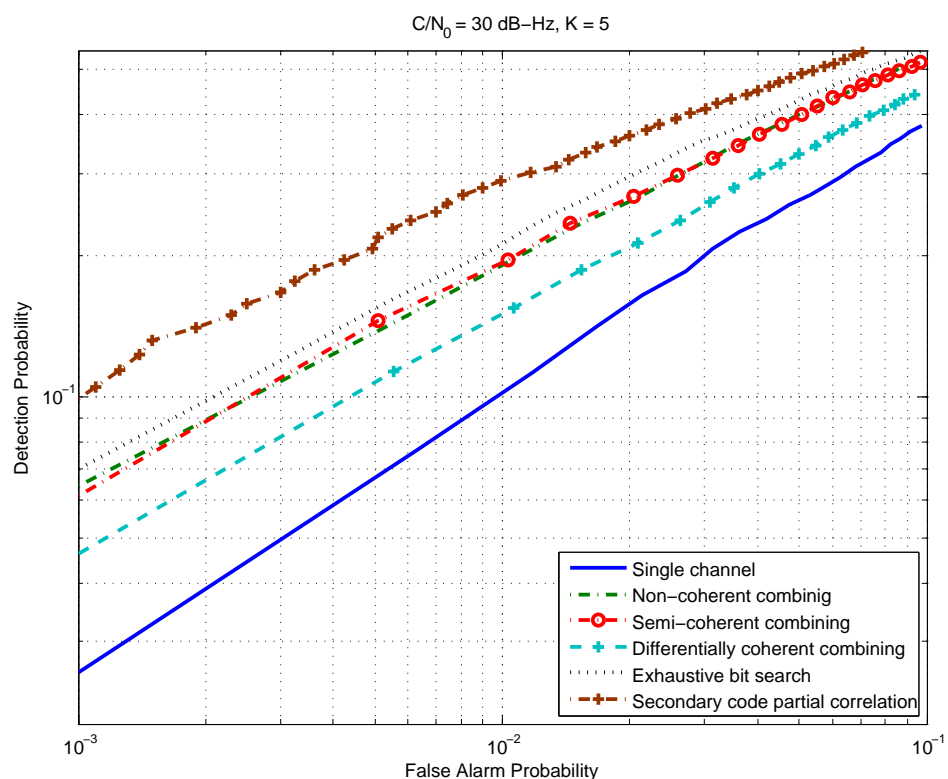


Figure 7.12. ROC comparison among different acquisition strategies. $C/N_0 = 30 \text{ dB-Hz}, K = 5$.

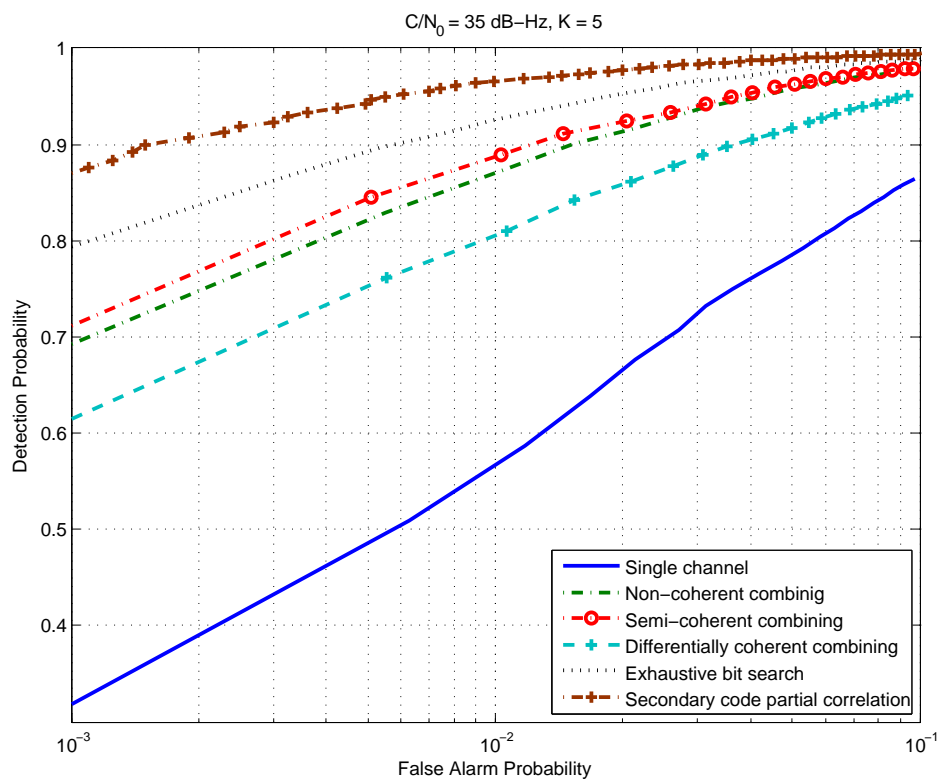


Figure 7.13. ROC comparison among different acquisition strategies. $C/N_0 = 35 \text{ dB-Hz}, K = 5$.

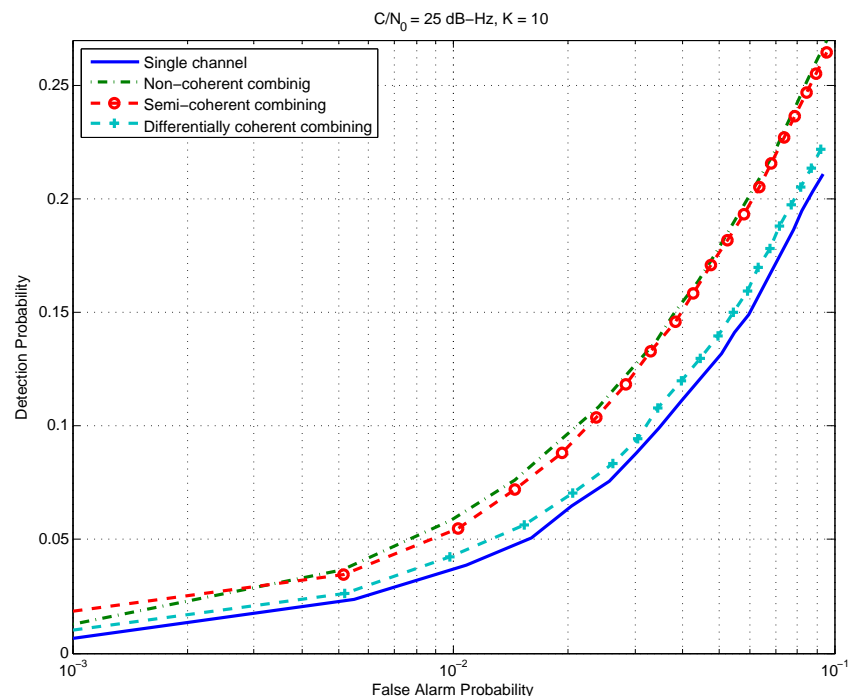


Figure 7.14. ROC comparison among different acquisition strategies.
 $C/N_0 = 25 \text{ dB-Hz}, K = 10$.

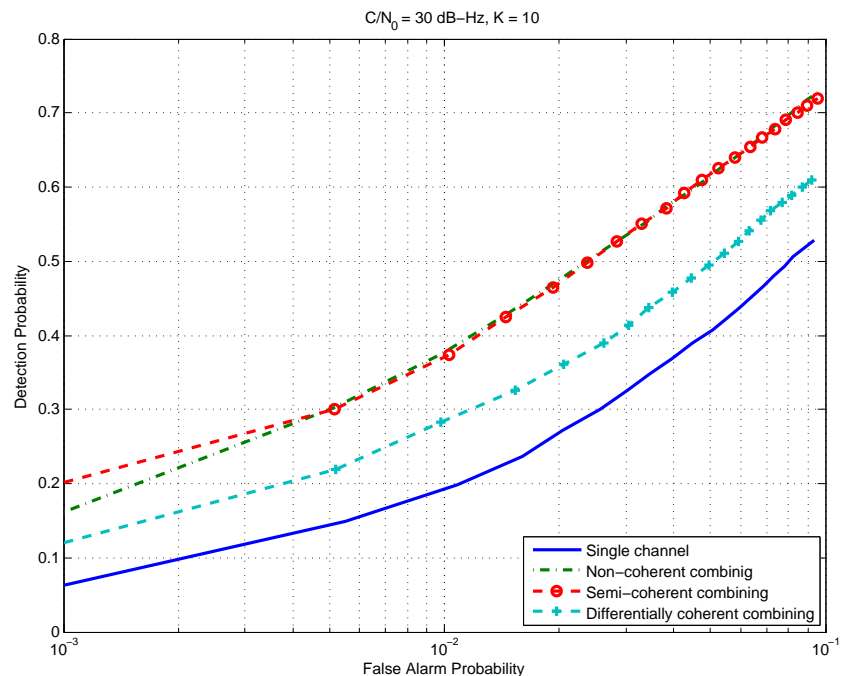


Figure 7.15. ROC comparison among different acquisition strategies.
 $C/N_0 = 30 \text{ dB-Hz}, K = 10$.

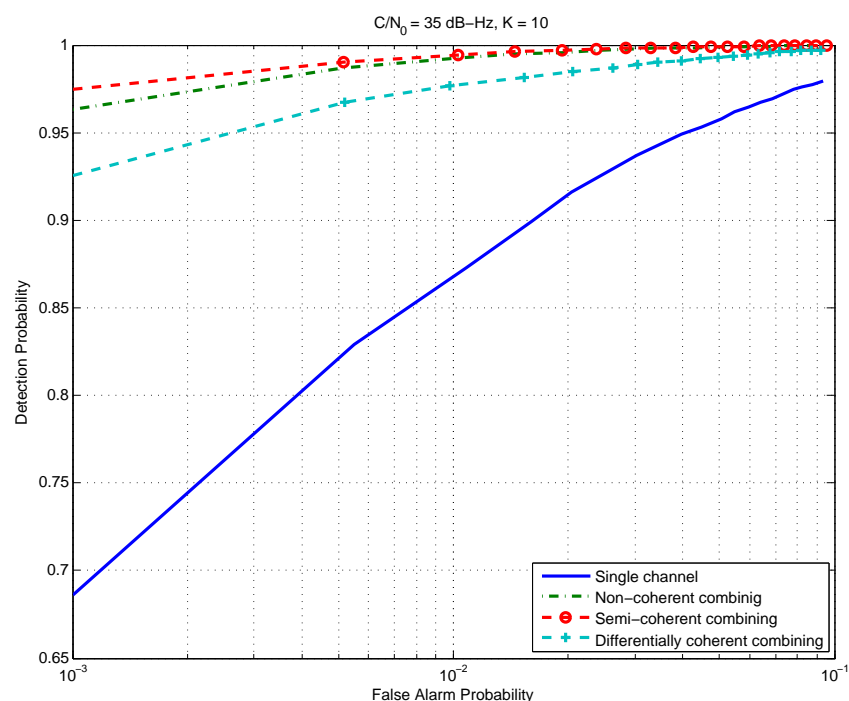


Figure 7.16. ROC comparison among different acquisition strategies.
 $C/N_0 = 35 \text{ dB-Hz}, K = 10$.

Chapter 8

Conclusions

In this chapter, conclusions regarding the first part of this thesis are drawn. Recommendations for future works are also provided.

Different tools for analyzing the acquisition process have been provided. More specifically the acquisition block has been formalized as a multi-layer process operating in two different domains: the cell and the decision domains. The distinction between these two domains was not clearly stated in the previous literature and represents one of the main contributions of this part. The distinction between cell and decision probabilities has been also introduced and the relationship between those two sets of probabilities has been investigated. In the context of the multi-layer description of the acquisition block, the last stage, i.e. the “Multi-trial and Verification” stage, has been briefly described and a complete analysis of the verification strategies is desirable. This part of the decision process should be further investigated in future works. Other aspects of the acquisition process have also been investigated such as the acquisition losses due to the frontend filtering and quantization. A general formula, quantifying the quantization loss when B bits are used for representing the input signal, has been provided and verified by simulation. Quantization and frontend filtering losses have been analyzed separately and further studies will be devoted to their interaction. The theoretical developments of the first chapters have been used to design new acquisition algorithms for composite GNSS signals. Each acquisition strategy has been characterized from a statistical point of view through the derivation of the cell false alarm and detection probabilities. From the analysis presented the following remarks on the acquisition of composite GNSS signals emerge:

- When the acquisition on a single code period is considered the coherent channel combining with bit recovery results in a more effective acquisition strategy. For low C/N_0 the bit estimation is no more reliable and the coherent channel combining tends to have the same performance of the non-coherent combining.

- Non-coherent and differentially coherent channel combining show similar performance, although the non-coherent combining algorithm works slightly better for high values of false alarm probability whereas the differentially coherent is preferable for low P_{fa} .
- When considering acquisition on multiple code periods two classes of algorithms can be identified: with and without bit recovery.
- The pure non-coherent, the semi-coherent and the differentially coherent combining belong to the first class, and require a reduced computational load with respect to the other strategies since the bit combinations do not have to be searched and the Doppler bin size does not have to be reduced. Among these strategies the semi-coherent integration gives better performance for high C/N_0 . For low C/N_0 , semi-coherent and non-coherent integration leads to similar performances.
- Among the second class, the secondary code partial correlation outperforms all the other techniques requiring a lower computational load with respect to the exhaustive search of all the possible bit combinations.

The analysis has also considered composite GNSS signals characterized by two distinct channels, namely the data and pilot channels, transmitted at the same time and separated by different codes and phases. The new GNSS modulations are not limited to this class of signals. An example is represented by the new L2C signal [74] that has adopted time multiplex data and pilot channels. For this kind of signals new acquisition techniques have to be designed.

Part II

GNSS Acquisition in the presence of interference

Chapter 9

Interference source classification

It is known that RF Interference is generally unpredictable and represents an impairing factor in GNSS applications mainly because of the low power of the GNSS signal at the Earth's surface (at present the power of the GPS L1 civil code is -158.5 dBW and the power of Galileo L1 signal is -152 dBW). A direct consequence of this fact is that not only are the in-band interference sources likely to affect Galileo receivers, but also strong out-of-band signals with their spectral side lobes and harmonics can have an effect. The latters are due to the non-linearity of strong RF emitters in faraway bands but geographically located close to the end-user GNSS receiver; in these cases the power level of the harmonics could be high enough to seriously interfere with the GNSS band.

The RFI may be intentional or unintentional. Moreover GNSS receivers are vulnerable to spoofing, that is, the intentional transmission of a false but stronger version of the GNSS signal.

In the context of this thesis the analysis is limited to unintentional interference and, in particular, to RFI due to communication and electronic systems. This chapter deals with the classification of different types and different sources of interference. In particular two different classifications are possible: the first is based on the statistical, spectral and temporal characteristics of the interference whereas the second is relative to the source that generates the disturbing signal.

When considering the statistical, spectral and temporal characteristics of the interference signal, four main classes can be identified:

- **Narrow-band Gaussian interference** [20–22],
- **Continuous Wave interference (CWI)** [22],
- **Pulsed interference** [75–79],
- **Swept interference** [22].

The term “narrow-band Gaussian” denotes all those interfering signals that can be effectively characterized by a normal pdf. The adjective “narrow-band” refers to the fact that this kind of interference occupies only a portion of the GNSS signal band. Thus the disturbing signal can have a wide band that is however relatively narrow with respect to the GNSS signals.

The class of CWI includes all those disturbing signals that can be effectively modeled as pure sinusoids. This kind of interference can be generated by a wide variety of electronic systems. In fact almost every electronic device and communication system relies on oscillators for the generation of sinusoidal signals that are used as carriers for the transmission of the communication message or for synchronization purposes. Due to the presence of non-linearities and imperfections in the electronic components harmonics can be generated in the GNSS bands. Those signals are then perceived as CWI.

All those disturbing signals that are concentrated in the time domain can be included into the class of “pulsed interference”. Examples of these signals are Ultra Wide Band (UWB) signals that are used for indoor localization and for short range communications between personal electronic devices (PED). Pulsed signals are also used by radar and navigation systems. Distance Measuring Equipment (DME) and TACtical Air Navigation (TACAN) signal consists of the sequence of pairs of Gaussian pulses and are used for navigation and landing operations. These signals are transmitted in the same frequency band of Galileo E5 and GPS L5 signals, representing a potential treat [78,79] for these GNSSs.

The term “swept interference” denotes all those disturbing signals characterized by an instantaneous narrow band and by a time-varying central frequency. An example of swept interference recorded in proximity of VHF emitters is reported in Section 13.2.

The main sources of unintentional RFI in GNSS applications are:

- **FM, VHF and UHF emitters** such as TV and radio transmitters;
- **Personal electronic devices (PED);**
- **Satellite based Services;**
- **Radar and Navigation systems.**

These sources will be better discussed in the next sections. In Table 9.1 the different types of interference are related to the different sources. It can be noted that PEDs can generate all types of interference, due to the great variety of devices that are included into this class. In Figure 9.1 the frequency plan of Galileo and GPS is depicted together with the different interference signals that can affect the different frequency bands.

Table 9.1. Interference type and source classification.

Source Type	Narrow- band Gaussian Interference	CWI	Pulsed Interference	Swept Interference
FM, VHF, UHF emitters	✓	✓		✓
PED	✓	✓	✓	✓
Satellite based Services	✓			
Radar			✓	

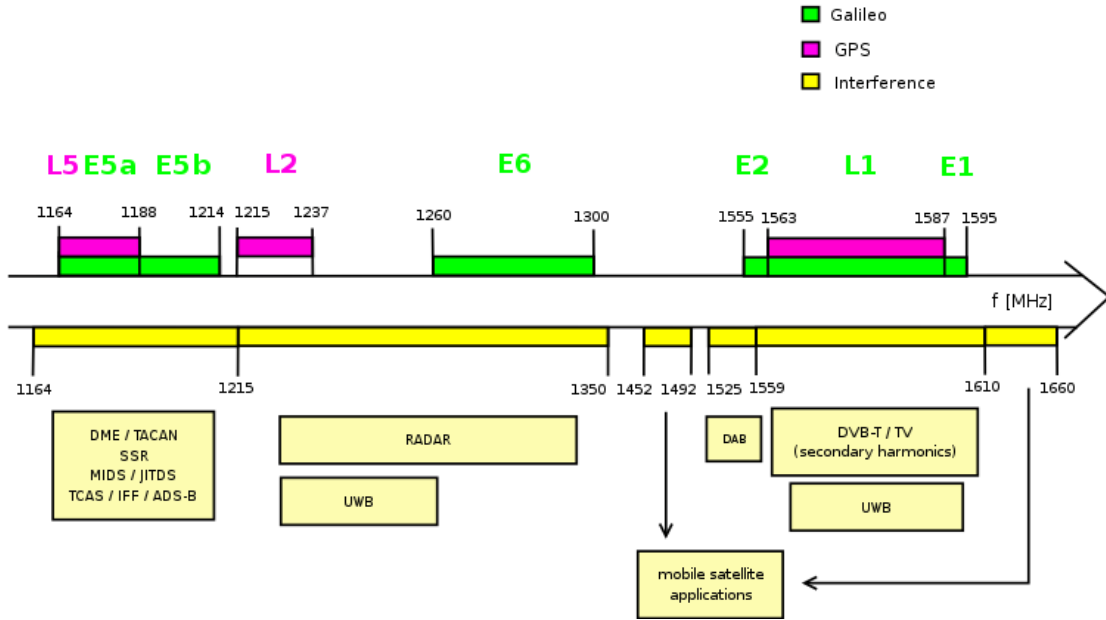


Figure 9.1. Interference source frequency bands.

9.1 Interference from FM, VHF and UHF emitters

One of the main sources of GNSS interference is due to harmonics and spurious emissions from FM, VHF and UHF stations. In [22] the potential impact of FM, VHF and UHF emitters on GNSS is analyzed in detail. It is shown that different harmonics can enter

GNSS bands possibly degrading GNSS receiver functioning. In Table 9.2 the order and the source of the different harmonics that can enter the L1 band is reported, showing that almost each FM, VHF and UHF emitter can produce disturbing signals in the GNSS frequencies.

Table 9.2. Harmonics from FM, VHF and UHF emitters, from [22].

Order	Band (MHz)	Usage
L1	1571.42 - 1579.42	C/A-GPS
2th	785.71 - 788.71	UHF TV
3th	523.807 - 526.473	UHF TV
4th	392.855 - 394.855	Mobile/Station
5th	314.284 - 315.884	Mobile/Station
6th	261.903 - 263.237	Mobile/Station
7th	224.488 - 225.631	Broadcasting
8th	196.427 - 197.428	VHF TV
9th	174.602 - 175.491	VHF TV
10h	157.142 - 157.942	VHF Maritime
11th	142.856 - 143.584	VHF Military
12th	130.952 - 131.618	VHFCOM
13th	120.878 - 121.494	VHFCOM
14th	112.244 - 112.816	VOR/ILS
15th	104.761 - 105.295	FM
16th	98.214- 98.714	FM

9.1.1 Interference from TV emitters

Different harmonics from TV ground stations can generate potentially dangerous interference for both GPS and Galileo receivers. In [22], five TV channels, generating harmonics in the GPS L1 band, are reported with their relative power impact (Figure 9.2). TV emissions are veritable sources of interference for GNSS receivers and they can generate both wide and narrow band interference: the video carriers can be considered as medium/wide band signals whereas the sound carriers are considered as CWI.

In [80] and [81] a case of interference from TV signals is reported. In that case, however, the interference signal did not enter the antenna. It entered the power connection for the active antenna Low Noise Amplifier (LNA) and caused harmonic distortion in the LNA that resulted in an average 5 dB decrease in C/N_0 .

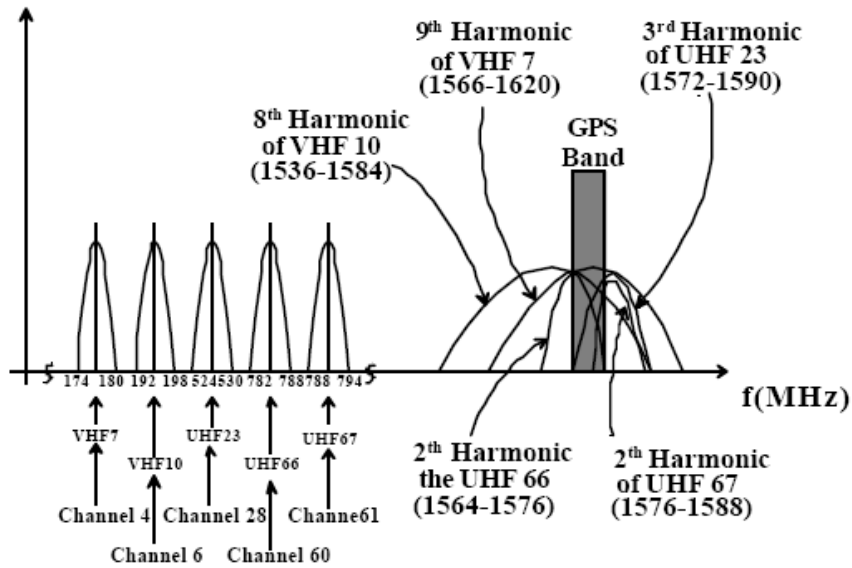


Figure 9.2. Potential interference from TV emitters (from [22]).

9.2 Personal Electronic Devices

There are two types of PEDs: those that intentionally transmit signals and that are known as intentional transmitters and those that are unintentional radiators.

Intentional transmitters have to emit a signal in order to accomplish their function and include:

- cell phones,
- pagers,
- two-way radios,
- remote-control toys,
- laptop connected to a wireless network.

Future intentional PEDs generations may be based on UWB signal allowing the development of high bit rate personal devices, which should be monitored as new possible interference sources for GNSS receivers.

PEDs that can be classified as unintentional transmitters, do not need to transmit a signal in order to accomplish their function, but, as any electrical device, they emit some level of radiation.

Examples of unintentional transmitters include:

- compact-disc players,
- tape recorders,
- game-boys,
- laptop computers and palm pilots (not connected to a wireless network but radiating other kinds of signals),
- laser pointers.

The proximity of GNSS receivers to other electronic devices emitting intentional or unintentional signals can cause a disruption of GNSS signal reception.

9.2.1 Ultra Wide-Band (UWB) interference

The FCC (Federal Communications Commission) defines UWB any signal that occupies more than 500 MHz bandwidth in the 3.1 to 10.6 GHz band and meets the spectrum mask in Figure 9.3 [82].

UWB signals emerged as a potential solution for low-complexity, low-cost, low-power

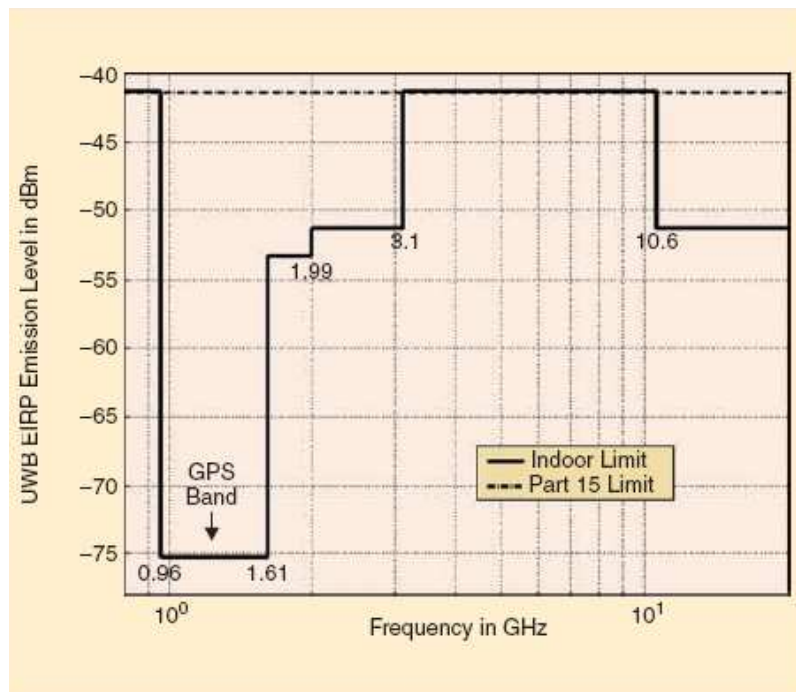


Figure 9.3. UWB spectral mask for indoor communication systems.

consumption, and high-data-rate wireless connectivity among devices within or entering the personal operating space. With the possibility to offer data transmission rates of

100–500 Mbps at distances of 2–10 m using average radiated power of a few hundred microwatts, and the possibility of miniaturized low cost mass production, UWB technology is currently seen by many to be the backbone of future short-range wireless communication systems. In addition, UWB signals have been utilized in imaging radar techniques because of their wall penetration capability, and are being studied for indoor location and navigation purposes because of their performance in multipath environment [83]. With all these potential applications and advantages, ubiquitous UWB devices are becoming reality.

The problem with UWB signals is their impact on existing spectral users, especially for users of Galileo and GPS whose signal power is far below the noise floor.

Generally UWB signals are generated using very narrow pulses in the time domain, their spectral properties depend on the pulse waveform, as well as on the pulse-width and the duty-cycle. The use of very narrow pulses spreads the transmitted signal energy to an extremely wide frequency band that can interfere with GNSS receiver bands.

Several studies [75–77] have concluded that UWB signals degrade GPS receiver performance and for this reason, they can be potentially detrimental, especially for indoor GNSS users. However these studies are mainly focused on the power portion of the UWB signals interfering with the GNSS bands. In [84] a simulation approach is proposed in order to take into account the UWB pulse waveform, the pulse repetition rate and other parameters characterizing UWB signals; performances in terms of GPS receivers acquisition success rate are drawn demonstrating that interference effects can be reduced by opportunely choosing the modulation parameters. In [76] an entire Wireless Personal Area Network (WPAN) based on UWB signals is considered and its impact on GPS receiver is studied. Also in this case the impact on GPS receivers strongly depends on UWB modulation parameters.

9.3 Satellite-based Services

Radio Frequency (RF) emissions from satellite systems can represent a source of interference for GNSSs. This kind of interference source can be divided in two classes:

- interference from Mobile Satellite Service (MSS) communications systems,
- interference among GNSSs.

MSS communications systems pose two distinct interference threats to the GNSS signals [85]. Mobile Earth Stations (MSEs), transmitting in the 1610-1660.5 MHz band, can introduce wideband power in the GNSS band, raising the noise power level. Another potential source of GNSS interference are the spurious harmonic emissions from geostationary satellites that transmit in the 1525-1559 MHz band. These emissions are yet unregulated by the ITU.

The second class of interference is due to the fact that different GNSSs can broadcast in the same frequency bands and thus the signal transmitted by one GNSS can jam another. This problem has been seriously considered for the SIS of Galileo, which has been designed to be compatible with the preexisting GPS. Two different types of effects can be further identified: **intersystem** and **intrasytem** interference [86–89].

9.3.1 Intersystem and Intrasytem Interference

Galileo has been designed to be interoperable and compatible with GPS. Compatibility implies that the two systems should operate with as little impact on each other as possible. However unintentional imperfections in the transmitter design can produce intrasytem and intersystem interference. The term intersystem refers to interference produced by GPS transmitter on the Galileo signal and vice versa, whereas the term intrasytem refers to those impairments impacting the same system they are produced by. For example an incomplete carrier suppression can produce an undesired narrowband component with power concentrated around the carrier frequency.

Another type of imperfection involves intermodulation products caused by nonlinear combinations of multiple signals at the transmitter.

Different works (e.g. [88] and [89]) have tested the impact of the Galileo signals and of intersystem interference on the GPS system, but additional work has to be performed on the Galileo robustness to GPS interference.

9.4 Radar and Navigation systems

The Galileo E5a/E5b and the GPS L5 signals will be located within the 960-1215 MHz frequency band that is already used worldwide for Aeronautical Radionavigation Services (ARNS) such as Distance Measuring Equipment (DME), TACtical Air Navigation (TACAN) and Secondary Surveillance Radar (SSR), as well as by the U.S. Department of the Defense (DoD) Joint Tactical Information Distribution System (JTIDS) and Multifunction Information Distribution System (MIDS).

The DME/TACAN systems consist of an airborne interrogator and a ground-based transponder that emits high-power pulsed signals constituting a real threat. In [78,79] a thorough survey of this kind of interference has been performed showing the need to develop mitigation techniques for this kind of impairments; the reallocation of DME/TACAN signals has also been proposed as an alternative solution.

9.5 Other sources

Several other interference sources can degrade GNSS receiver performance, such as impulsive radars, power lines, military transmission and also natural electromagnetic phenomena. In general these sources broadcast signals that can be generally described as narrow or wide band signals and detected/mitigated by using appropriate techniques. Some works deals with the impact of these specific interference sources, such as [90] which analyzes the power line case.

Chapter 10

Gaussian narrow-band interference

When an interfering signal is present an additional term has to be added to Eq. (2.10) in order to account for the impact of the disturbing signal. In particular Eq. (2.10) becomes

$$r[n] = y[n] + \eta[n] + i[n] \quad (10.1)$$

where $i[n]$ models the disturbing signal. $i[n]$ can assume different expressions depending on the time/frequency and statistical characteristics of the disturbing signal. $i[n]$ will be better specified in the next chapters depending on the type of interference under analysis.

The first class of disturbing signals considered in this thesis is represented by narrow-band Gaussian interference. This class of interferences includes all those signals that can be effectively characterized by a Gaussian pdf, where the term “narrow-band” refers to the fact that the spectrum of these signals occupies only a portion of the GNSS signal band. Thus the disturbing signal can have a relatively wide band that is, however, narrow with respect to the one of the GNSS signal under consideration.

In the context of this chapter the interference is assumed to be zero mean and wide sense stationary (WSS). In this way the disturbing signal $i[n]$ can be modeled as a colored Gaussian process

$$i[n] \sim \mathcal{N}(0, \sigma_{INT}^2) \quad (10.2)$$

characterized by a Power Spectral Density (PSD) $G_l(f)$ and an autocorrelation function $R_l[n]$. $G_l(f)$ and $R_l[n]$ allow to characterize the time/frequency characteristics of $i[n]$.

This characterization of the disturbing signal is extremely general and allows to describe a wide variety of interference.

Although quantifying the interference impact on the acquisition block is, in general, a complex problem, under the assumption of narrow-band Gaussian interference the development of a consistent theory, allowing comparative analysis, is possible. Moreover the acquisition process within the GNSS receiver modifies the shape of the interfering

signal, either mitigating or amplifying its impact and a reliable measure of the interfering degradation should account these interactions.

Different parameters have been investigated in order to quantify the effect of this kind of interference on the signal quality, and in particular a quantity called “effective C/N_0 ” was introduced to reflect the effect of interference at the input of the receiver, avoiding receiver-specific details such as integration time and the use of coherent or non-coherent processing. Furthermore a parameter called **Spectral Separation Coefficient** (SSC) was introduced [20, 21] to distinguish the effects of the interference spectral shape from effects due to the interfering power. These parameters were first introduced by Betz in [20, 21] and then became widely accepted as reliable and effective measures of interference degradation. In particular, both Galileo Signal Task Force and ESA adopted them to investigate mutual system interference between GPS and Galileo signals.

When narrow-band Gaussian interference is present, the acquisition performance is completely characterized by the coherent output Signal to Noise and Interference Ratio (SNIR) that represents a generalization of the coherent output SNR introduced in Section 3.7 and better analyzed in Section 6.1. The Gaussian nature of the interference does not modify the statistic of the correlator output and the ROCs maintain the same functional structure of Eq. (3.39).

In this chapter the coherent output SNR in presence of narrow-band Gaussian interference is derived for digital receivers and the concept of SSC is revised. It is important to highlight that in [21] the concepts of SNIR and therefore of the SSCs were not directly related to the receiver functional blocks. In addition, such parameters were derived in the analog domain without taking into account the specific features of digital receivers. The contribution of this chapter can be then summarized into two points:

- the definition and the analysis of the coherent output SNIR and SSCs for digital receivers is provided,
- the chapter explains and analyzes the meaning and the effects of the SNIR and SSCs considering the impact of such parameters on the acquisition block. It has been proved that the acquisition performance directly depends on the SNIR and so on SSCs.

Further details on the subject can be found in [91].

10.1 Digital SCCs

As already discussed in Section 6.1, all the operations in an acquisition system, prior to the squaring blocks, are linear and the code correlation can be represented as an equivalent filter characterized by an impulse response, namely

$$h_c[\tau] = \frac{1}{N}c[-\tau].$$

Since all the operations prior the squaring blocks are linear, the correlator output in presence of interference can be written as

$$\begin{aligned} Y_I(\tau, F_D) &= S_I(\tau, F_D) + \eta_I + \nu_I \\ Y_Q(\tau, F_D) &= S_Q(\tau, F_D) + \eta_Q + \nu_Q \end{aligned} \quad (10.3)$$

where

- $S_I(\tau, F_D), S_Q(\tau, F_D)$ are the useful signal components,
- η_I and η_Q are the noise terms,
- ν_I and ν_Q derive from the interference term $i[n]$.

More specifically,

$$\begin{aligned} \nu_I + j\nu_Q &= \frac{1}{N} \sum_{n=0}^{N-1} i[n] c[n - \tau] \exp\{-j2\pi F_D n\} \\ &= (i[\tau] \exp\{-j2\pi F_D n\}) * h_c[\tau] = g(\tau, F_D) * h_c[\tau] \end{aligned} \quad (10.4)$$

where $g(\tau, F_D) = i[\tau] \exp\{-j2\pi F_D n\}$. Since $i[n]$ is a Gaussian random process, ν_I and ν_Q are Gaussian random variables. Moreover, it is possible to show [44] that ν_I and ν_Q are independent since multiplication by sine and cosine and the subsequent low-pass filtering project the interference on two orthogonal functions.

The interference $i[n]$ is characterized by the PSD $G_l(f)$. Now it is possible to evaluate the variance of $\nu_I + j\nu_Q$ considering that the signal $g[n]$, obtained by modulating $i[n]$, has the PSD

$$G_j(f) = G_l(f + F_D) \quad (10.5)$$

and the interference term at the correlator output is characterized by

$$G_\nu(f) = G_l(f + F_D) |H_c(f)|^2. \quad (10.6)$$

Finally the variance of $\nu_I + j\nu_Q$ is given by

$$\text{Var}[\nu_I + j\nu_Q] = \int_{-0.5}^{0.5} G_\nu(f) df = \int_{-0.5}^{0.5} G_l(f + F_D) |H_c(f)|^2 df. \quad (10.7)$$

By introducing the normalized PSD

$$\bar{G}_l(f) = \frac{1}{C_l} G_l(f + F_D) \quad (10.8)$$

where $C_l = \int_{-0.5}^{0.5} G_l(f) df = \sigma_{INT}^2$ is the interference power, it is possible to express Eq. (10.7) as

$$\text{Var}[\nu_I + j\nu_Q] = C_l \int_{-0.5}^{0.5} \bar{G}_l(f) |H_c(f)|^2 df. \quad (10.9)$$

The narrow-band Gaussian interference increases the variance of the noise term at the correlator output, which in this case is given by

$$\sigma_{out}^2 = \text{Var}[Y_I(\tau, F_D)] = \sigma_n^2 + \sigma_i^2 \quad (10.10)$$

where σ_n^2 is the variance of the noise term given by Eq. (6.9)

$$\sigma_n^2 = \frac{N_0}{4} f_s \int_{-0.5}^{0.5} \tilde{G}(f) |H_c(f)|^2 df$$

and σ_i^2 is given by

$$\sigma_i^2 = \text{Var}[\nu_I] = \frac{1}{2} \text{Var}[\nu_I + j\nu_Q] = \frac{1}{2} C_l \int_{-0.5}^{0.5} \bar{G}_l(f) |H_c(f)|^2 df. \quad (10.11)$$

From Eqs. (6.9), (10.10) and (10.11) the variance at the correlator output is given by

$$\sigma_{out}^2 = \frac{N_0}{4} f_s \int_{-0.5}^{0.5} \tilde{G}(f) |H_c(f)|^2 df + \frac{1}{2} C_l \int_{-0.5}^{0.5} \bar{G}_l(f) |H_c(f)|^2 df. \quad (10.12)$$

In Section 6.1 the contribution of the useful signal term was evaluated and is given by Eq. (6.15) as

$$\begin{aligned} \text{E}\{Y_I(\tau, F_D)\} &= \frac{A}{2} \tilde{R}(0) \cos \phi_0 = \frac{A}{2} \int_{-0.5}^{0.5} \tilde{G}_s(f) df \cos \phi_0 \\ &= \frac{A}{2} \int_{-0.5}^{0.5} G_s(f) H_f(f + F_D) df \cos \phi_0 \approx \frac{A}{2} \int_{-0.5}^{0.5} G_s(f) H_f(f + f_{IF} T_s) df \cos \phi_0 \end{aligned}$$

where $\tilde{R}(\tau)$, $\tilde{G}_s(f)$ and $R(\tau)$, $G_s(f)$ are the correlation functions and the PSDs introduced in Section 6.1. $H_f(f)$ is the transfer function of the equivalent filter modeling the effect of the frontend. Using these results, it is possible to evaluate the coherent output SNIR defined as

$$\rho_c^d = \max_{\phi_0} \frac{\text{E}^2[Y_I(\tau, F_D)]}{\text{Var}[Y_I(\tau, F_D)]} \quad (10.13)$$

that is the same definition as Eq. (3.36) but in the presence of interference.

By using previous results the coherent output SNIR assumes the following expression

$$\begin{aligned} \rho_c^d &= \frac{\left[\frac{A}{2} \int_{-0.5}^{0.5} G_s(f) H_f(f + f_{IF} T_s) df \right]^2}{\frac{N_0}{4} f_s \int_{-0.5}^{0.5} \tilde{G}(f) |H_c(f)|^2 df + \frac{1}{2} C_l \int_{-0.5}^{0.5} \bar{G}_l(f) |H_c(f)|^2 df} \\ &= \frac{C \left[\int_{-0.5}^{0.5} G_s(f) H_f(f + f_{IF} T_s) df \right]^2}{\frac{N_0}{2NT_s} \int_{-0.5}^{0.5} \tilde{G}(f) N |H_c(f)|^2 df + \frac{C_l}{NT_s} T_s \int_{-0.5}^{0.5} \bar{G}_l(f) N |H_c(f)|^2 df} \\ &= 2 \frac{C}{N_0} T_c \frac{\left[\int_{-0.5}^{0.5} G_s(f) H_f(f + f_{IF} T_s) df \right]^2}{\int_{-0.5}^{0.5} \tilde{G}(f) G_s(f) df + 2 \frac{C_l}{N_0} T_s \int_{-0.5}^{0.5} \bar{G}_l(f) G_s(f) df} \end{aligned} \quad (10.14)$$

where

$$G_s(f) = N |H_c(f)|^2$$

is the normalized PSD of the local code $c[n]$. $G_s(f)$ is normalized since

$$\int_{-0.5}^{0.5} G_s(f) df = \int_{-0.5}^{0.5} N |H_c(f)|^2 = \frac{1}{N} \sum_{n=0}^{N-1} |c[n]|^2 = 1 \quad (10.15)$$

The term

$$k_d = \int_{-0.5}^{0.5} \tilde{G}_l(f) G_s(f) df \quad (10.16)$$

represents the projection of the interference normalized PSD over the local code PSD and it is called **digital spectral separation coefficient** (SSC). The digital SSC accounts for the effect of the spectral shape of the interference on the acquisition performance. The acquisition block filters the interference, thus only a portion of the disturbing signal power impacts the coherent SNIR. The digital SSC quantifies this portion of the interference signal. By using Eq. (10.16), the coherent output SNIR (10.14) can be rewritten as

$$\rho_c^d = 2 \frac{C}{N_0} T_c \frac{\left[\int_{-0.5}^{0.5} G_s(f) H_f(f + f_{IF} T_s) df \right]^2}{\int_{-0.5}^{0.5} \tilde{G}(f) G_s(f) df + 2 \frac{C_l}{N_0} T_s k_d}. \quad (10.17)$$

In absence of interference $k_d = 0$ Eq. (10.17) is equal to Eq. (6.17). If the effect of the frontend is negligible, i.e.

$$\int_{-0.5}^{0.5} G_s(f) H_f(f + f_{IF} T_s) df = \int_{-0.5}^{0.5} G_s(f) df = 1$$

and

$$\int_{-0.5}^{0.5} \tilde{G}(f) G_s(f) df = \int_{-0.5}^{0.5} G_s(f) df = 1,$$

the coherent output SNIR assumes the following expression

$$\rho_c^d = 2 \frac{C}{N_0} T_c \frac{1}{1 + 2 \frac{C_l}{N_0} T_s k_d} \quad (10.18)$$

and the loss due to the interference can be quantified as

$$L_{INT} = \left[1 + 2 \frac{C_l}{N_0} T_s k_d \right]^{-1} = \left[1 + \frac{C_l}{N_0 f_s / 2} k_d \right]^{-1}. \quad (10.19)$$

The term $2 \frac{C_l}{N_0} T_s = \frac{C_l}{N_0 f_s / 2} = \frac{C_l}{N_0 B_s}$ represents the Jammer to Noise ratio (J/N) in ideal conditions, i.e. when the receiver bandwidth is equal to $f_s/2$. Thus the coherent output SNR reduction is proportional to one plus the product between the SSC and the Jammer to Noise ratio.

10.2 ROC analysis and SSCs interpretation

As previously highlighted the correlator outputs, in the presence of narrow-band Gaussian interference, are still independent Gaussian random variables, thus the detection and false alarm probabilities have the same structure as that of Eq. (3.39) and can be expressed as

$$P_{fa}(\beta) = \exp\left\{-\frac{\beta}{2\sigma_{out}^2}\right\} \quad (10.20)$$

$$P_{det}(\beta) = \int_{-\sqrt{\beta}}^{+\infty} \frac{z}{\sigma_{out}^2} \exp\left\{-\frac{z^2 + \alpha^2}{2\sigma_{out}^2}\right\} I_0\left(\frac{z\alpha}{\sigma_{out}^2}\right) dz = Q_1\left(\sqrt{\frac{\alpha^2}{\sigma_{out}^2}}, \sqrt{\frac{\beta}{\sigma_{out}^2}}\right) \quad (10.21)$$

with $\alpha = \sqrt{\mu_I^2 + \mu_Q^2}$ and

$$\sigma_{out}^2 = \sigma_n^2 + \sigma_i^2.$$

μ_I and μ_Q are the means of the random variables on the in-phase and quadrature branches in case of perfect a delay/frequency alignment:

$$\begin{aligned} \mu_I &= \sigma_{out} \sqrt{\rho_c^d} \cos \theta \\ \mu_Q &= -\sigma_{out} \sqrt{\rho_c^d} \sin \theta \\ \alpha &= \sigma_{out} \sqrt{\rho_c^d} \end{aligned} \quad (10.22)$$

Eqs. (10.10) and (10.22) prove that the ROCs in the presence of interference are completely determined by the knowledge of the SSCs and of the output coherent SNIR.

10.3 Simulation results

The above analysis is now supported by simulations. An acquisition system like the one represented in Figure 3.5 has been implemented and both false alarm and detection probabilities have been evaluated using error count techniques. The system has been fed with the useful signal, white noise and different types of interference. The narrow band interference has been simulated filtering white Gaussian noise. A base-band model has been used since the demodulation and the Doppler frequency removal produce base-band signals. For this reason the notation “low-pass” interference indicates a signal whose central frequency was originally close to the GNSS signal carrier and that has assumed a spectrum concentrated around the zero frequency after the demodulation and the Doppler removal. The simulations have been carried out for different kinds of interference and for both GPS BPSK and Galileo BOC(1,1) modulations, always leading to results in agreement with the theoretical model. In Figures 10.1 and 10.2 the analysis of the impact of a band-pass and a low-pass interference for the Galileo and GPS signal acquisition is reported; the simulation parameters are given in Table 10.1 and the digital SSC values in

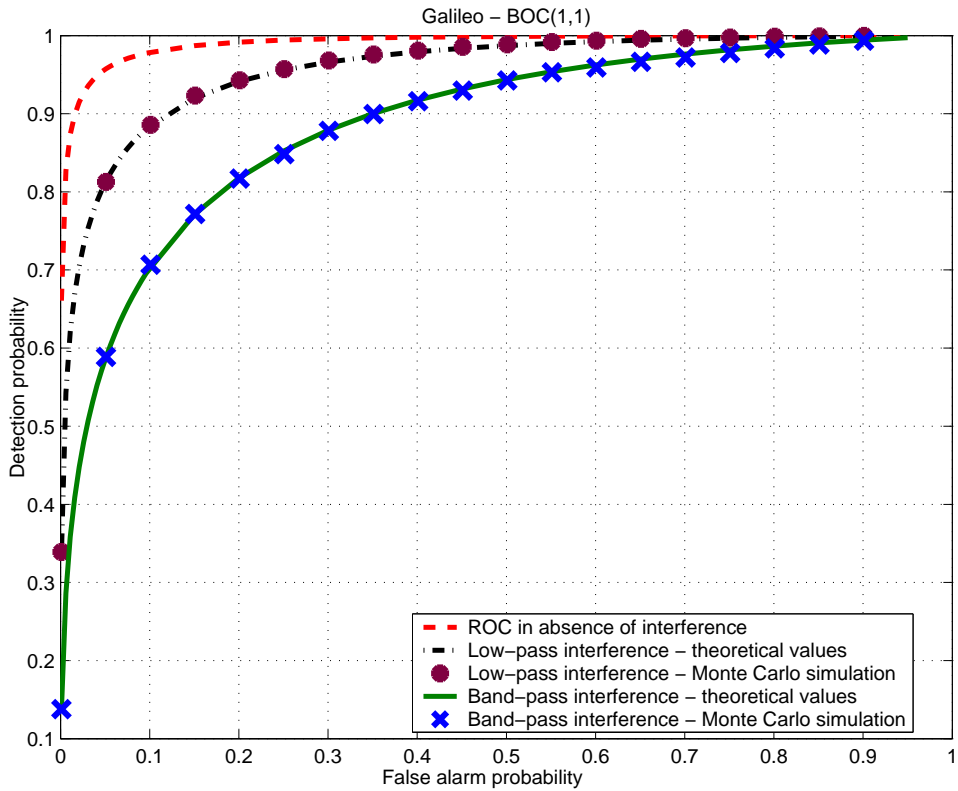


Figure 10.1. ROC curves for the BOC(1,1) Galileo signal.

Table 10.1. Simulation parameters.

C/N_0 Galileo	30 dB-Hz
C/N_0 GPS	36 dB-Hz
samples per chip	4
sampling frequency	$f_s = 4.092$ MHz
Low-pass interference cut-off frequency	$f_c = 0.125f_s$
Band-pass interference frequency interval	$[0.125f_s; 0.375f_s]$
Interference to noise ratio $C_l/(N_0 f_s)$	0 dB

Table 10.2. SSCs values, pure number.

	GPS	Galileo
Low-pass interference	3.198	0.617
Band-pass interference	0.337	1.661

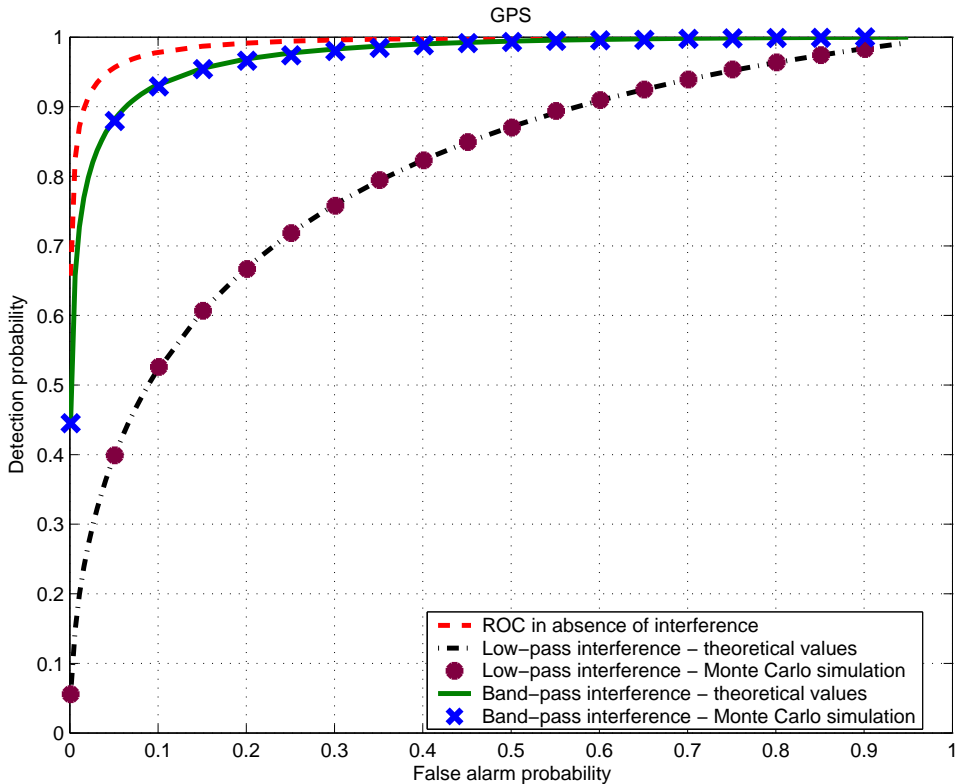


Figure 10.2. ROC curves for the GPS signal.

Table 10.2. As expected the GPS signal is more sensitive to interfering signals with spectra concentrated around its carrier. This is due to the spectral shape of the GPS signal that has a main lobe at the frequency carrier: in this case the SSC is greater than the one of the BOC(1,1) that presents a zero at those frequencies and the ROCs worsen. On the contrary the Galileo signal is more fragile with respect to interference centered on its side lobes.

Chapter 11

Continuous Wave Interference (CWI)

In the previous chapter, the case of narrow-band Gaussian interference has been analyzed. In particular it has been shown that the presence of Gaussian interference does not alter the statistical properties of the correlator outputs, which are independent Gaussian random variables. When this condition is true the coherent output SNR allows to quantify the interference impact. The validity of the coherent output SNR is however limited to those interfering signals that lead to Gaussian random variables at the correlator outputs and this condition is not, in general, true. Thus the acquisition block needs to be characterized by means of the ROCs that represent a more general metric for quantifying the performance of a detection system.

The presence of disturbing signals during GNSS acquisition is similar to the problem of clutter in radar detection. Indeed, GNSS interference and radar clutter are both unwanted signals that affect the detection process [39]. However, to the best of the author's knowledge, the radar and in general the detection literature is lacking models to effectively characterize GNSS interference. For instance, clutter is generally characterized by K, Gamma or Gamma-derived distributions [26,39]; these models cannot however be directly applied to GNSS interferences.

This chapter is devoted to the development of a consistent model evaluating the performance of GNSS signal acquisition in the presence of continuous wave (CW) interference. The class of CW interferences includes all those narrowband signals that can be reasonably represented as pure sinusoids with respect to the GNSS bands. This kind of interfering signals can be generated by UHF and VHF TV, VHF Omni-directional Radio-range (VOR) and Instrument Landing System (ILS) harmonics, by spurious signals caused by power amplifiers working in non-linearity regions or by oscillators present in many electronic devices [22].

The problem of CW detection and mitigation has been extensively considered in the recent literature [23–25]. However a model focusing on the detection and false alarm probabilities has never been previously proposed and thus it is the focus of this chapter. The

case of a basic acquisition scheme, without non-coherent integration is considered. In [3] the CW impact in presence of a limited number of bits for the input signal quantization is considered. [3] notes that the CW signal, in the GPS case, is most disturbing when the interference is coherent with the GPS carrier frequency. In this case the CW is downconverted to a constant by the frontend and thus only the case of a constant offset at the input of the ADC is considered.

In this chapter the number of bits used for quantization is assumed to be large enough to neglect the effect of the quantization noise. This assumption holds for new generations of GPS receivers that can be equipped with ADCs with 8 or more bits [2].

The developed model is general and accounts for the impact of the CW frequency and of the GNSS code. In particular it is shown that the acquisition performance strongly depends on two parameters that can be interpreted as the generalization of the Spectral Separation Coefficients (SSC) analyzed in the previous chapter.

The chapter also investigates the evolution of the CW through the acquisition chain along with the impact of the coherent integration time. The analogy with models for radar detection in clutter environments [39] and the role of the GNSS signal phase are finally described.

When a real CWI is present, the disturbing signal of Eq. (10.1) assumes the expression

$$i[n] = A_{INT} \cos(2\pi f_i n T_s + \theta_{int}) = A_{INT} \cos(2\pi F_{int} n + \theta_{int}) \quad (11.1)$$

where A_{INT} and f_i are the interference amplitude and frequency. θ_{int} is a uniformly distributed random variable of the form

$$\theta_{int} \sim \mathcal{U}[-\pi, \pi]. \quad (11.2)$$

The power of the interference with respect to the noise variance is defined by the Jammer to Noise ratio as follows:

$$\frac{J}{N} = \frac{A_{INT}^2}{2} \frac{1}{\sigma_{IF}^2} = \frac{A_{INT}^2}{2N_0 B_{IF}}. \quad (11.3)$$

11.1 Detection and false alarm probabilities

In order to determine the probability of detection, it is necessary to determine the probability distribution of the decision variable $S(\tau, F_D)$ under the hypothesis of perfect code and frequency alignment. When the interference and useful signal phases are known, $S(\tau = \tau_0, F_D = F_{D,0})$ is a non-central χ^2 random variable whose non-centrality parameter depends on both the interference and useful signals. The distribution of $S(\tau = \tau_0, F_D = F_{D,0})$ is obtained by removing the hypothesis of knowing the useful signal and interference, and by integrating over their random parameters.

In this chapter the complex representation of the acquisition block will be used. This representation has been discussed in Section 6.1.1 and depicted in Figure 6.3. In this way the decision variable $S(\tau, F_D)$ is obtained as the square absolute value of a complex correlator output. Thus, in order to determine the distribution of $S(\tau = \tau_0, F_D = F_{D,0})$ it is necessary to evaluate the mean and variance of the correlator output when the GNSS signal and the interference are assumed known. In the previous chapter the complex correlator output has been denoted by $Y(\tau, F_D)$ and, under the hypothesis of knowing the signal and interference parameters, it is a complex Gaussian random variable.

For the linearity properties highlighted in the previous chapters it is possible to consider the impact of the three components in Eq. (10.1) separately.

11.1.1 Useful signal contribution

When the code delay and the Doppler shift are correctly recovered the useful signal contribution is given by

$$S_y = \frac{1}{N} \sum_{n=0}^{N-1} A c[n - \tau_0]^2 d[n - \tau_0] \cos(2\pi F_{D,0} n + \phi_0) \exp\{-j2\pi F_{D,0} n\}. \quad (11.4)$$

The spreading code assumes only the values ± 1 and vanishes when squared. The navigation message is supposed to be constant over the integration interval and thus it is neglected. From these considerations,

$$S_y = \frac{A}{N} \sum_{n=0}^{N-1} \frac{\exp\{j\phi_0\} + \exp\{-j4\pi F_{D,0} n - j\phi_0\}}{2} \approx \frac{A}{2} \exp\{j\phi_0\}. \quad (11.5)$$

In Eq. (11.5) the Euler formula for the cosine has been employed and the high frequency complex exponential has been considered filtered by the summation.

11.1.2 Interference contribution

By using the Euler formula the interference can be expressed as

$$i[n] = \frac{A_{INT}}{2} \exp\{j2\pi F_{int} n + j\theta_{int}\} + \frac{A_{INT}}{2} \exp\{-j2\pi F_{int} n - j\theta_{int}\}. \quad (11.6)$$

The multiplication by the complex exponential at the frequency $F_{D,0}$ produces the new signal

$$i_D[n] = \frac{A_{INT}}{2} \exp\{j2\pi(F_{int} - F_{D,0})n + j\theta_{int}\} + \frac{A_{INT}}{2} \exp\{-j2\pi(F_{int} + F_{D,0})n - j\theta_{int}\}. \quad (11.7)$$

In this way two complex exponentials at two different frequencies are produced. This signal enters the equivalent filter whose output is given by

$$S_{int} = k_1 \frac{A_{INT}}{2} \exp \{j2\pi(F_{int} - F_{D,0})\tau_0 + j\theta_{int} + j\theta_1\} \\ + k_2 \frac{A_{INT}}{2} \exp \{-j2\pi(F_{int} + F_{D,0})\tau_0 - j\theta_{int} + j\theta_2\} \quad (11.8)$$

where

- $k_1 = |H_c(F_{int} - F_{D,0})|$ and $\theta_1 = \angle\{H_c(F_{int} - F_{D,0})\}$;
- $k_2 = |H_c(-F_{int} - F_{D,0})|$ and $\theta_2 = \angle\{H_c(-F_{int} - F_{D,0})\}$.

In Eq. (11.8) the fact that complex sinusoids are the eigenfunctions of linear and time invariant systems has been exploited. $H_c(f)$ is the Fourier Transform of the equivalent filter $h_c[n]$.

Notice that the square of k_1 and k_2 can be written as

$$k_{1,2}^2 = |H_c(\pm F_{int} - F_{D,0})|^2 = \int_{-\infty}^{\infty} |H_c(f)|^2 \delta(f - (\pm F_{int} - F_{D,0})) df \\ = \frac{1}{N} \int_{-\infty}^{\infty} N |H_c(f)|^2 \delta(f - (\pm F_{int} - F_{D,0})) df = \frac{1}{N} \int_{-\infty}^{\infty} G_s(f) G_i(f) df \quad (11.9)$$

where $\delta(\cdot)$ denotes the Dirac's delta, $G_s(f) = N |H_c(f)|^2$ and $G_i(f) = \delta(f - (\pm F_{int} + F_{D,0}))$. Expression (11.9) shows that k_1^2 and k_2^2 are proportional to the Spectral Separation Coefficients [20, 21] of the two components of the interfering signal. However, in this case, a different functional relation relates these parameters to the false alarm and detection probabilities with respect to the case of Gaussian interference developed in Chapter 10.

11.1.3 Noise contribution

As already discussed in previous chapters, the multiplication by the complex exponential equally splits the noise power on the two acquisition branches. The equivalent filter $h_c[n]$ is low-pass and thus the real and imaginary parts of the process at its output can be considered independent. The total variance of the output process is given by

$$2\sigma_n^2 = \frac{1}{N} \sigma_{IF}^2 = \frac{1}{N} N_0 B_{IF} \quad (11.10)$$

and thus

$$S_W \sim \mathcal{N}_c(0, \sigma_n^2 \mathbf{I}_2) \quad (11.11)$$

where \mathbf{I}_2 is the 2×2 identity matrix. The symbol \mathcal{N}_c indicates that the process is both complex and Gaussian.

11.1.4 Detection probability

The input of the complex modulus is thus given by the sum of the three components discussed above, namely

$$Y(\tau_0, F_{D,0}) = Y_I(\tau_0, F_{D,0}) + jY_Q(\tau_0, F_{D,0}) = S_y + S_{int} + S_W \quad (11.12)$$

which, given the phases of the useful signal and of the interference, is the Gaussian process

$$Y(\tau_0, F_{D,0})|\phi_0, \theta_{int} \sim \mathcal{N}_c(S_y + S_{int}, \sigma_n^2 \mathbf{I}_2). \quad (11.13)$$

The square absolute value of Eq. (11.13) is a χ^2 random variable characterized by the probability distribution

$$Y(\tau, F_D)|\varphi_0, \theta_{int} \sim p_S(x|\alpha, \sigma_n^2) = \frac{1}{2\sigma_n^2} \exp\left\{-\frac{x+\alpha^2}{2\sigma_n^2}\right\} I_0\left(\frac{\sqrt{x\alpha^2}}{\sigma_n^2}\right) \quad x > 0 \quad (11.14)$$

where

$$\begin{aligned} \alpha^2 &= |S_y + S_I|^2 \\ &= \frac{A^2}{4} + \frac{A_{INT}^2 k_1^2}{4} + \frac{A_{INT}^2 k_2^2}{4} + \frac{A_{INT}^2 k_1 k_2 \cos(\varphi_1 - \varphi_2)}{2} \\ &\quad + \frac{AA_{INT} k_1 \cos \varphi_1}{2} + \frac{AA_{INT} k_2 \cos \varphi_2}{2} = \alpha^2(\varphi_1, \varphi_2). \end{aligned} \quad (11.15)$$

φ_1 and φ_2 are two new parameters given by

$$\varphi_1 = \theta_1 + 2\pi(F_{int} - F_{D,0})\tau_0 + \theta_{int} - \phi_0 \quad (11.16)$$

$$\varphi_2 = \theta_2 - 2\pi(F_{int} + F_{D,0})\tau_0 - \theta_{int} - \phi_0. \quad (11.17)$$

By integrating the distribution (11.14) it is possible to find the detection probability given the useful signal and the interference phases, as

$$P_{det}(\beta|\varphi_0, \theta_{int}) = Q\left(\frac{\alpha}{\sigma_n}; \frac{\sqrt{\beta}}{\sigma_n}\right) \quad (11.18)$$

where $Q(\cdot; \cdot)$ is the Marcum Q-function introduced in [37].

In order to evaluate the overall detection probability it is necessary to remove the hypothesis of knowing ϕ_0 and θ_{int} and average (11.18) with respect to the probability densities of these two random variables. By considering Eqs. (11.16) and (11.17) it is easy to note that between the couples (φ_1, φ_2) and (ϕ_0, θ_{int}) there is a linear injective map and thus a convenient and equivalent strategy for obtaining the detection probability is represented by averaging Eq. (11.18) with respect to φ_1 and φ_2 . Furthermore, in Appendix G, it is shown

that, due to the cosine periodicity, φ_1 and φ_2 can be considered as two independent random variables uniformly distributed over the interval $[-\pi, \pi]$. From these considerations the final expression of the detection probability is

$$P_{det}(\beta) = \frac{1}{4\pi^2} \int_{-\pi}^{\pi} \int_{-\pi}^{\pi} Q\left(\frac{\alpha(\varphi_1, \varphi_2)}{\sigma_n}; \frac{\sqrt{\beta}}{\sigma_n}\right) d\varphi_1 d\varphi_2. \quad (11.19)$$

When φ_1 and φ_2 are considered as random variables, $\alpha(\varphi_1, \varphi_2)$ defined by Eq. (11.15) is a random variable as well. α represents the amplitude of the cell used for the detection in absence of the Gaussian noise and, in this case, fluctuates because of the presence of the interference. Thus model (11.19) has a structure similar to the one of the detection probabilities of fluctuating targets in the radar theory [26, 55].

In Appendix H it is shown that α^2 can be expressed as

$$\alpha^2 = p_1 + \sqrt{C}p_2 \cos \varphi_2 + \sqrt{p_3 + \sqrt{C}p_4} \cos \varphi_2 \cos \varphi_3 \quad (11.20)$$

where p_1, p_2, p_3 and p_4 are the four positive constants

$$\begin{aligned} p_1 &= \frac{A^2}{4} + \frac{A_{INT}^2 k_1^2}{4} + \frac{A_{INT}^2 k_2^2}{4} \\ p_2 &= \frac{A_{INT}}{\sqrt{2}} k_2 \\ p_3 &= \frac{A_{INT}^4 k_1^2 k_2^2}{4} + \frac{A_{INT}^2 A^2}{4} k_1^2 \\ p_4 &= \frac{A_{INT}^3}{\sqrt{2}} k_1^2 k_2. \end{aligned} \quad (11.21)$$

φ_2 and φ_3 are two independent random variables uniformly distributed over the interval $[-\pi; \pi]$. From this expression it is possible to evaluate the maximum and minimum values for α , namely

$$\begin{aligned} \alpha_{\max} &= \sqrt{p_1 + A/\sqrt{2}p_2 + \sqrt{p_3 + A/\sqrt{2}p_4}} = \sqrt{p_1 + \sqrt{C}p_2 + \sqrt{p_3 + \sqrt{C}p_4}} \\ &= \sqrt{\frac{C}{2} + \frac{A_{INT}}{2} (k_1 + k_2)} \end{aligned} \quad (11.22)$$

$$\alpha_{\min} = \left(\frac{A}{2} - \frac{A_{INT}}{2} (k_1 + k_2) \right)^+ = \left(\sqrt{\frac{C}{2}} - \frac{A_{INT}}{2} (k_1 + k_2) \right)^+ \quad (11.23)$$

where the relationship $C = \frac{A^2}{2}$ has been used. $(x)^+ = \max(x, 0)$ denotes the *positive part* operator. The maximum value is obtained when both cosines in Eq. (11.20) are equal to 1 and represents the case in which the useful signal and the filtered interference are aligned in phase. For the minimum, two cases are possible: either the interference is

strong enough to completely cancel the signal contribution and thus $\alpha_{\min} = 0$, or the signal term dominates and $\alpha_{\min} = \sqrt{\frac{C}{2}} - \frac{A_{INT}}{2}(k_1 + k_2)$. In the latter case, the signal and interference contributions are in opposition of phase. Eq. (11.23) summarizes these two cases and can be obtained by substituting the two cosines in Eq. (11.20) by two new variables, $x = \cos \varphi_2$ and $y = \cos \varphi_3$. By minimizing with respect to x and y and by verifying the boundary conditions $-1 \leq x, y \leq 1$ the two minimum cases are found and finally Eq. (11.23) is obtained.

The detection probability (11.19) can also be expressed as

$$P_{det}(\beta) = \int_{\alpha_{\min}}^{\alpha_{\max}} Q\left(\frac{a}{\sigma_n}; \frac{\sqrt{\beta}}{\sigma_n}\right) f_{\alpha,d}(a) da \quad (11.24)$$

where $f_{\alpha,d}$ denotes the probability density function of α under the hypothesis of signal presence. This kind of expression is common in the radar literature [26,55] and once again it highlights the analogy between this model and radar detection probabilities. However, even if Eq. (11.20) allows to determine $f_{\alpha,d}$, its expression results quite complex and requires numerical methods for its evaluation. In Figure 11.1 an example of the probability distribution of α is shown. In this case $C = 1$, $A_{INT} = 2$, $k_1 = 0.5$ and $k_2 = 0.2$. All those parameters along with the values of α in Figure 11.1 are considered dimensionless since one is dealing with digital signals. The dimension of the signals is lost during the AD conversion and only the fundamental information about power and amplitude ratios is preserved. In Figure 11.1 the probability distribution of α has been determined either by Monte Carlo simulations or by numerically evaluating the $f_{\alpha,d}$ derived from Eq. (11.20) and the distributions of φ_2 and φ_3 .

11.1.5 False Alarm probability

The false alarm probability can be easily derived from the detection probability by constraining C , the signal power, to zero. Eq. (11.15) then becomes

$$\alpha^2 = \frac{A_{INT}^2 k_1^2}{4} + \frac{A_{INT}^2 k_2^2}{4} + \frac{A_{INT}^2 k_1 k_2 \cos(\varphi_1 - \varphi_2)}{2} = \alpha^2(\varphi_1 - \varphi_2), \quad (11.25)$$

which depends only on the phase difference $\varphi_1 - \varphi_2$. In Appendix H it is shown that $\varphi_1 - \varphi_2$ can be substituted, due to the periodicity of the cosine, by a random variable θ uniformly distributed in the range $[-\pi, \pi]$. Since in this case the amplitude of the decision cell depends only on one random variable, Eq. (11.19) becomes

$$P_{fa}(\beta) = \frac{1}{2\pi} \int_{-\pi}^{\pi} Q\left(\frac{1}{\sigma_n} \sqrt{\frac{A_{INT}^2 k_1^2}{4} + \frac{A_{INT}^2 k_2^2}{4} + \frac{A_{INT}^2 k_1 k_2 \cos \theta}{2}}; \frac{\sqrt{\beta}}{\sigma_n}\right) d\theta. \quad (11.26)$$

An alternative expression for Eq. (11.26) can be obtained by employing the distribution of the decision cell $\alpha(\varphi_1 - \varphi_2)$. By substituting $C = 0$ in Eqs. (11.20) and (11.21) or,

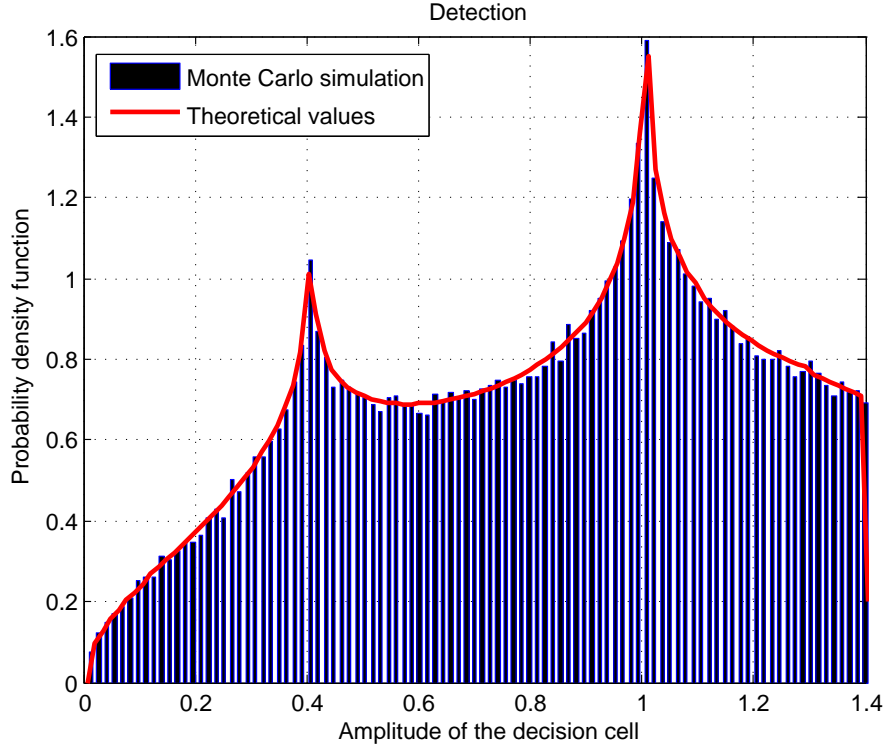


Figure 11.1. Probability density function of the decision cell amplitude α under the hypothesis of useful signal presence. $A_{INT} = 2$, $C = 1$, $k_1 = 0.5$ and $k_2 = 0.2$.

equivalently, by considering Eq. (11.25), it follows that the decision cell amplitude is given by

$$\alpha = \frac{A_{INT}}{2} \sqrt{k_1^2 + k_2^2 + 2k_1^2 k_2^2 \cos \theta}. \quad (11.27)$$

Eq. (11.27) states that the amplitude of a decision cell, in the absence of noise and under the false alarm hypothesis, varies in the range $\left[\frac{A_{INT}}{2} |k_1 - k_2|, \frac{A_{INT}}{2} (k_1 + k_2) \right]$ as the square root of a translated sinusoid. θ is a random variable uniformly distributed in the range $[-\pi, \pi]$, thus, by applying Eq. (11.27) it is possible to find the probability density function of α under the hypothesis of useful signal absence as

$$\alpha \sim f_{\alpha,fa}(a) = \frac{2a}{\pi \sqrt{\frac{A_{INT}^4 k_1^2 k_2^2}{4} - \left[a^2 - \frac{A_{INT}^2}{4} (k_1^2 + k_2^2) \right]^2}}, \quad \frac{A_{INT}}{2} |k_1 - k_2| < a < \frac{A_{INT}}{2} (k_1 + k_2) \quad (11.28)$$

Finally an equivalent expression for Eq. (11.26) is found by integrating the conditional probability with respect to α :

$$P_{fa}(\beta) = \int_{\frac{A_{INT}}{2}|k_1-k_2|}^{\frac{A_{INT}}{2}(k_1+k_2)} \frac{2aQ\left(\frac{a}{\sigma_n}; \frac{\sqrt{\beta}}{\sigma_n}\right)}{\pi \sqrt{\frac{A_{INT}^4 k_1^2 k_2^2}{4} - \left[a^2 - \frac{A_{INT}^2}{4} (k_1^2 + k_2^2)\right]^2}} da. \quad (11.29)$$

In Figure 11.2 an example of $f_{\alpha,fa}(a)$ is shown reported with $A_{INT} = 2$, $k_1 = 0.5$ and

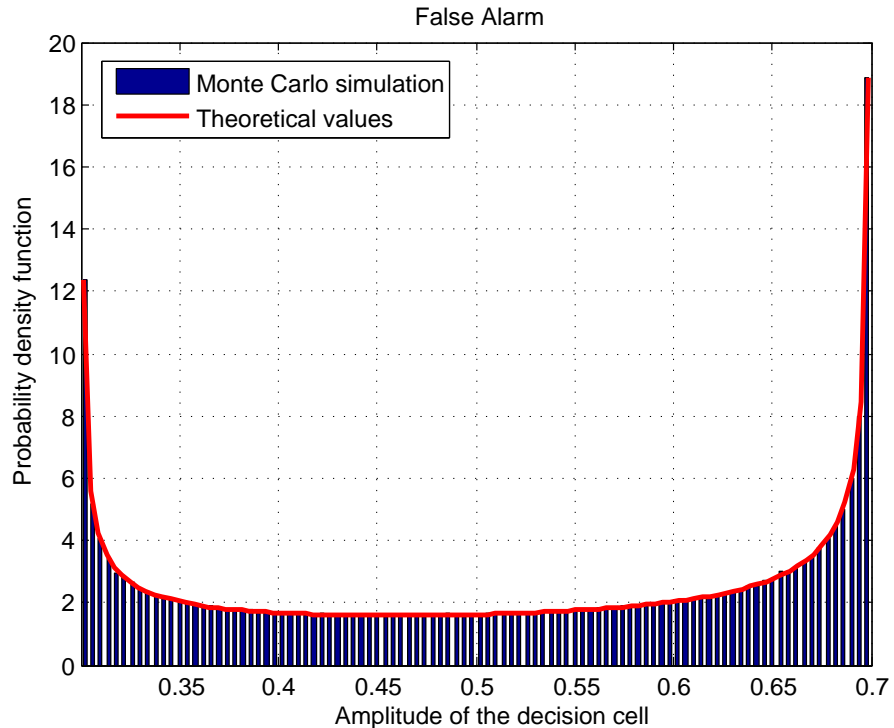


Figure 11.2. Probability density function of the decision cell amplitude α under the hypothesis of useful signal absence. $A_{INT} = 2$, $k_1 = 0.5$ and $k_2 = 0.2$.

$k_2 = 0.2$.

11.2 Impact of the acquisition parameters

The impact of the CW interference essentially depends on

- the interference amplitude and frequency,
- the Doppler frequency of the useful signal,

- the GNSS code,
- the coherent integration time,
- the subcarrier, that is for example the BOC or the BPSK.

The role of the interference amplitude is evident from Eqs. (11.15) and (11.26) in the determination of the false alarm and detection probabilities, whereas the impact of the other parameters is implicit in the coefficients k_1 and k_2 . In this section, the role of the system parameters that impact k_1 and k_2 under the hypothesis of a sampling rate multiple of the code rate is discussed. It is noted that Eq. (11.9) is general as it defines k_1 and k_2 without any hypothesis regarding the sampling rate and it can be used also for GNSS signals that employ multilevel modulations. In fact, the impact of the coherent integration time of the GNSS code and of the modulation is included in the spectrum of the equivalent filter $h_c[n]$. The case analyzed in this section is aimed at giving a better insight on the impact of the different parameters when their roles can be easily isolated.

The spreading sequence $c[n]$ refers to the base-band local code modulated by the subcarrier and repeated $L = N/(O_v N_c)$ times, where N is the total length of $c[n]$, N_c is the spreading code length and O_v is the number of samples per chip. When the sampling rate is a multiple of the code period $c[n]$, it can be written as

$$c[n] = c_{code}[n] * s_c[n] * h_L[n] \quad (11.30)$$

where $c_{code}[n]$ is the local code defined as

$$c_{code}[n] = \sum_{i=0}^{N_c-1} c_i \delta[n - O_v i] \quad (11.31)$$

that is the spreading sequence $\{c_i\}_{i=0}^{N_c-1}$ spaced of $O_v T_s$. $s_c[n]$ is an equivalent subcarrier signal of duration $O_v T_s$ and $h_L[n]$ is the sequence

$$h_L[n] = \sum_{i=0}^{L-1} \delta[n - O_v N_c i] \quad (11.32)$$

that accounts for the use of more than one code period. $s_c[n]$ is not to be confused with the signal $s_b[n]$ introduced in Chapter 2 where a different signal representation was used.

Eq. (11.30) is better explained in Figure 11.3 where the convolution of the spreading code with the subcarrier signal is reported. The convolution with the subcarrier modulates the spreading code producing one period of local replica.

Since the equivalent filter $h_c[n]$ is equal to $\frac{1}{N} c[-n]$ it can also be expressed as the convolution of three terms as

$$h_c[n] = \frac{1}{N_c} h_{code}[-n] * \frac{1}{O_v} s_c[-n] * \frac{1}{L} h_L[-n] \quad (11.33)$$

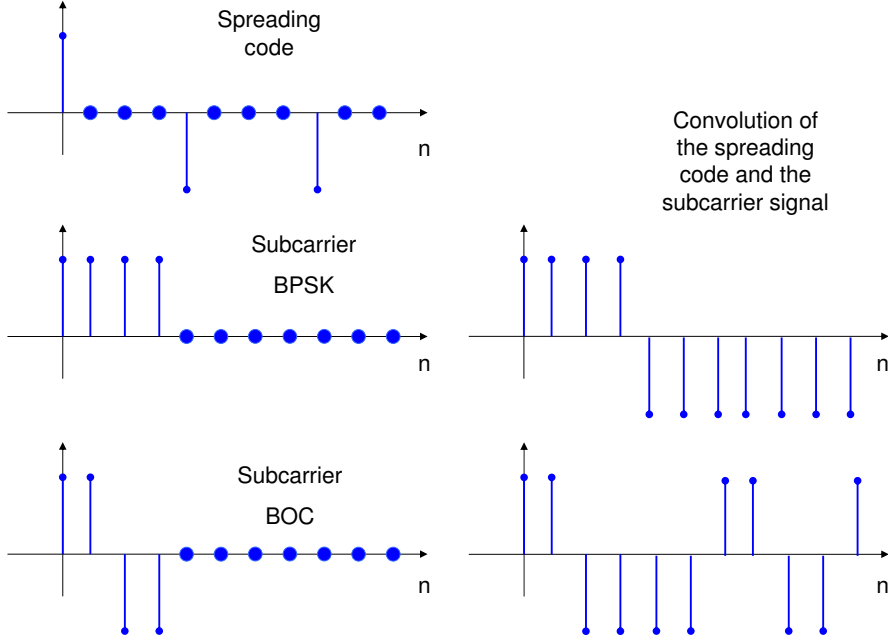


Figure 11.3. Pictorial representation of the convolution of the spreading sequence $c_{code}[n]$ with the subcarrier signal $s_c[n]$.

Thus the coefficients k_1 and k_2 can be expressed as

$$k_i = |H_{code}(\mp F_{int} - F_{D,0})| \cdot |S_c(\mp F_{int} - F_{D,0})| \cdot |H_L(\mp F_{int} - F_{D,0})| \quad (11.34)$$

where $H_{code}(f)$, $S_c(f)$ and $H_L(f)$ are the Fourier Transforms of $h_{code}[n]$, $s_c[n]$ and $h_L[n]$, respectively. Eq. (11.34) allows one to separate the different effects of the GNSS code, the subcarrier and the coherent integration time. Figures (11.4) and (11.5) show the different factors noted in Eq. (11.34) as a function of the frequency. The Fourier Transform of the code behaves like a Gaussian process since each value of $H_{code}(f)$ is given by the combination of several samples of a pseudo-random sequence. Thus $H_{code}(f)$ represents random-like oscillations and its impact on the CW can change drastically when two different codes are used. The spectrum of the subcarrier presented in Figure 11.4 has a sinc-like shape and refers to a BPSK modulation. In this case it is clear that the interference is most disturbing when its frequency equals the frequency of the useful signal and $|S_c(f)|$ is maximized. As $L \rightarrow +\infty$, $H_L(f)$ tends to an impulse train and spectral lines at the frequency multiple of $1/(N_c O_v T_s)$ clearly appear. Since L is finite each spectral line of $H_L(f)$ is convolved with a sinc function whose main support narrows as L increases. Thus, by using long coherent integration time and consequently large L , the acquisition process is more robust with respect to an interference whose frequency is not a multiple of the inverse of the code period $N_c O_v T_s$.

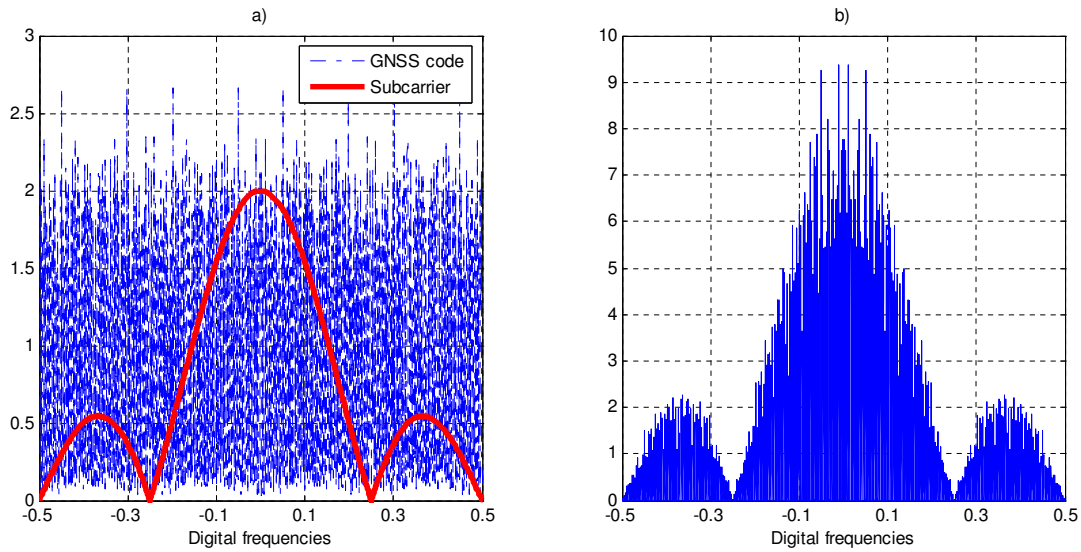


Figure 11.4. a) Modulus of the DFTs of the GNSS code and of the subcarrier. b) Spectrum of the equivalent filter $h_c[n]$

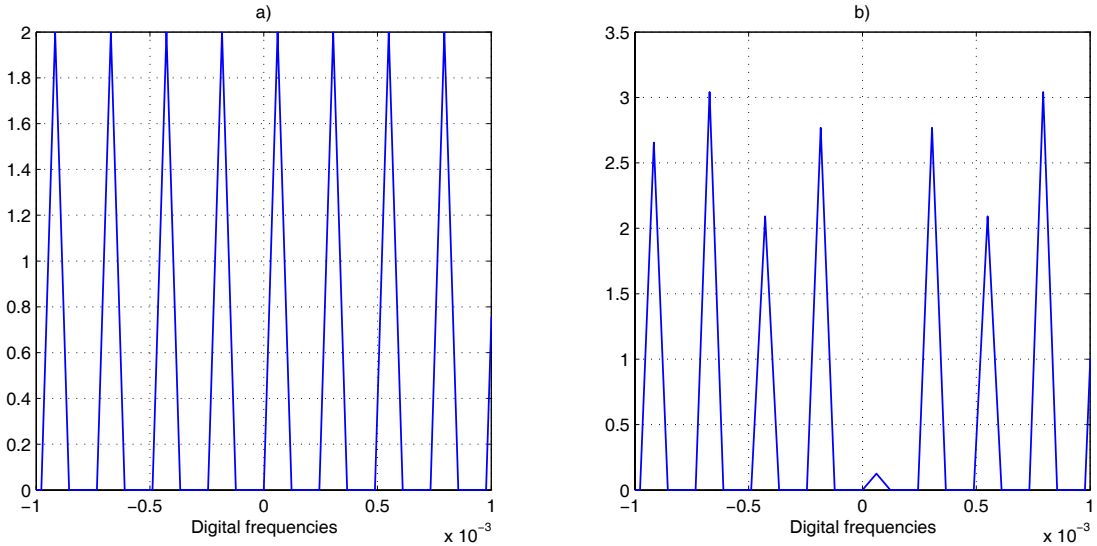


Figure 11.5. a) Zoom of the DFT of the $h_L[n]$ with $L = 4$. As $L \rightarrow +\infty$, $H_L(f)$ tends to an impulse train and spectral lines clearly appear. b) Zoom of the DFT of the equivalent filter $h_c[n]$.

11.3 Simulations

This section presents simulation results for supporting the model discussed in Section 11.1. The acquisition process described in Section 3.1 has been simulated by employing the system setup with the parameters listed in Table 11.1.

The distributions of the decision cell in the presence and absence of a useful signal are

Table 11.1. Simulation parameters

Sampling frequency	$f_s = 4.092 \text{ MHz}$
Intermediate frequency	$f_{IF} = 38.5 \text{ KHz}$
Number of samples per chip	$O_v = 4 \text{ samples/chip}$
Modulation	BPSK
C/N_0	40 dB-Hz
J/N	10 dB
Receiver Bandwidth	$B_{IF} = f_s/2$
Code length	$N_c = 1023$
Number of code periods	$L = 4$

reported in Figures 11.6 and 11.7. Notice that the theoretical model fits the distributions obtained by Monte Carlo simulations proving the validity of the previous analysis.

ROCs have been also derived, either by simulations or by using Eqs. (11.19) and (11.26).

Curves are reported by using a linear scale and the ROCs are evaluated for values of false alarm probability on the whole range [0,1]. Even if in practice the false alarm probability should be set to a value close to zero, the aim of these simulations was to validate the theoretical model provided in previous sections for every false alarm probability, and thus the whole range [0,1] has been investigated. The linear scale has been adopted since no appreciable representation enhancement was found by using the logarithmic scale. In Figure 11.8, two cases have been investigated: the first one considers the CW frequency equal to the useful signal one, whereas in the second one, the two frequencies differ by 500 Hz. As expected, the CW impact is greater in the first case than in the second one. Furthermore, in the case in which the interference is coherent to the GNSS signal, the system performance is at its lowest. ROCs estimated by Monte Carlo simulations coincide with the theoretical model, supporting the validity of both Eqs. (11.19) and (11.26).

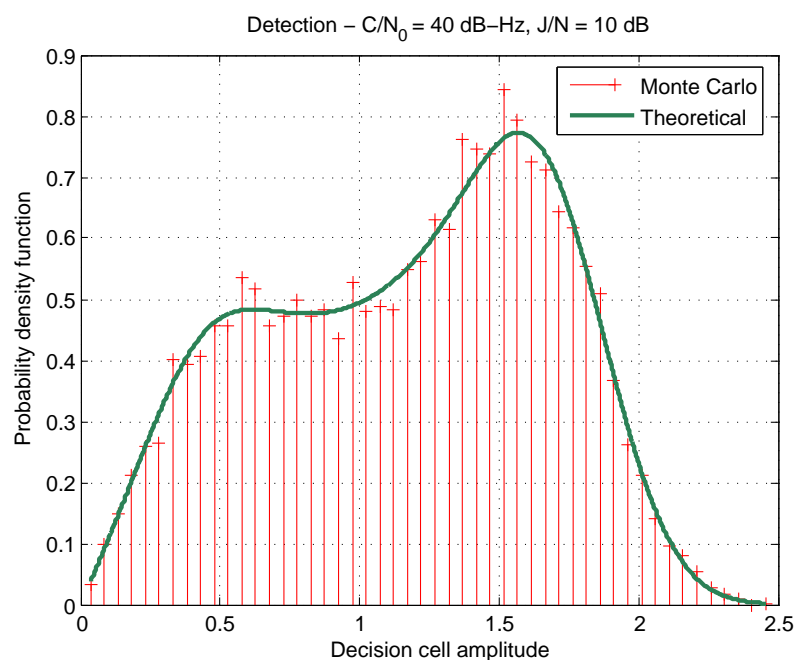


Figure 11.6. Probability distribution of the decision cell under detection hypothesis, i.e., in the presence of useful signal. The theoretical model fits Monte Carlo simulations.

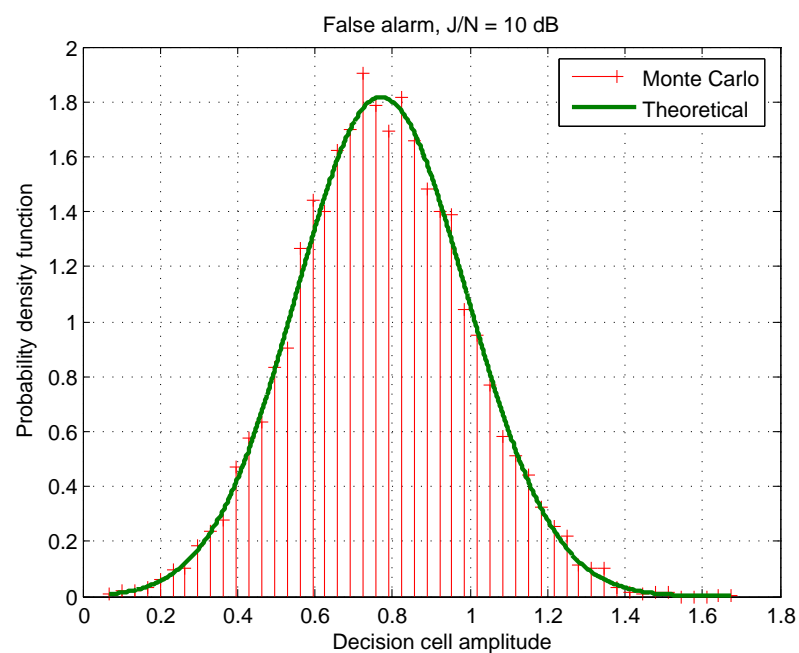


Figure 11.7. Probability distribution of the decision cell under the false alarm hypothesis, i.e., in the absence of useful signal. The theoretical model fits Monte Carlo simulations.

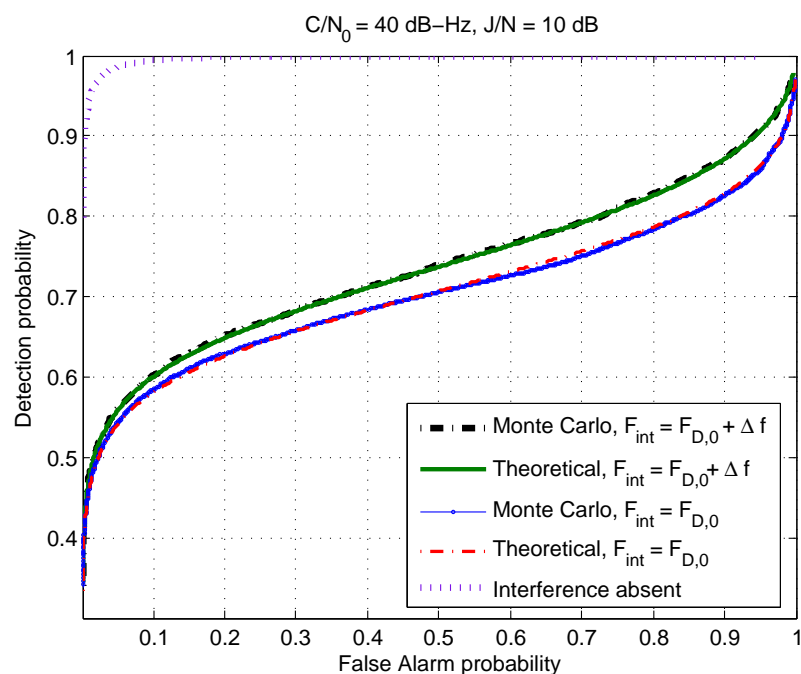


Figure 11.8. Comparison between theoretical ROCs and Monte Carlo simulations. The ROC in the absence of interference is reported as reference. $\Delta f \cdot f_s = 500 \text{ Hz}$.

Chapter 12

CWI mitigation

12.1 General Overview

An advanced receiver should be able to operate even in the presence of strong interference. This kind of receiver should be equipped with additional units able to detect and, under certain conditions, mitigate the impact of interfering signals. When present, these units are generally placed before the traditional blocks of a GNSS receiver: only when the interfering components are eliminated the received signal should be used to determine the user's position. If the detection/mitigation units are digital devices, then they are placed after the frontend and are fed by the digitalized received signal. In Figure 12.1 the scheme of a GNSS receiver equipped with digital detection/mitigation units is shown.

One of the cases in which mitigation units can effectively remove the interfering signal is that CWI. In the frequency domain these signals are almost orthogonal with respect to the GNSS signals, thus they can be removed from the useful signal with limited distortion.

For this kind of disturbing signals the notch filter has proven to be an efficient mitigation technique, for its capability of attenuating the CWI and essentially preserving the useful signal PSD. In the literature the notch filter has been widely used for interference removal [92] in different contexts, such as biomedical applications [93] and DSSS communications [25, 94, 95] to cite but a few.

The most important classes of notch filter-based CWI excision algorithms are:

- adaptive transversal FIR filters in time domain [96, 97],
- FFT-based FIR filters [97, 98],
- constrained poles and zeros IIR notch filters [99–101],
- unconstrained zeros IIR notch filters [95, 102].

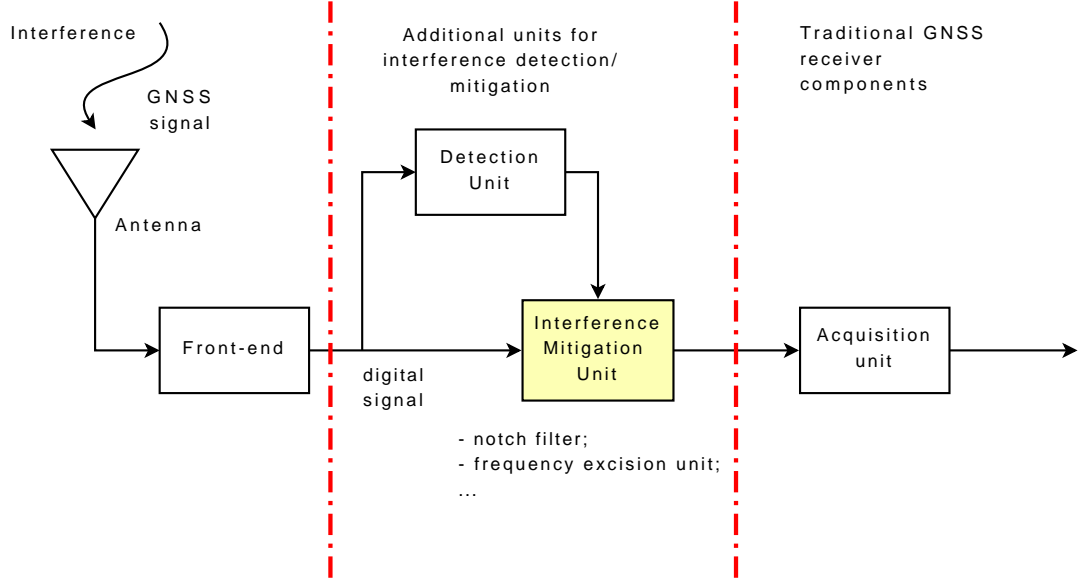


Figure 12.1. High-level scheme of a GNSS receiver equipped with interfering detection/mitigation units. In this context digital detection/mitigation units are considered and additional devices are added between the frontend and the traditional receiver units.

The first class of notch filters is based on a FIR filter whose taps are iteratively evaluated by different adaptive algorithms, such as the direct inversion matrix method proposed by [97] and the Least Mean Square (LMS) algorithm of [96]. FIR notch filters do not have stability problems but are computationally complex since the number of taps, required for a thin notch, is relatively high, involving a high number of additions/multiplications. FFT-based FIR filters exploit the efficiency of the FFT algorithm in order to evaluate a spectral estimation of the signal components. When a frequency component passes a fixed threshold a CWI is considered detected at this frequency and it is then excised. Different criteria for fixing the detection threshold are discussed in [98]. After frequency excision the signal is IFFT-transformed into the time domain. Such a technique corresponds to circular filtering, and the equivalent impulse response presents notches corresponding to the canceled components. This method presents the advantage of being able to deal with multiple CWI.

A widely spread class of notch filters is represented by Infinite Impulse Response (IIR) filters with constrained poles and zeros [103]. The diffusion of such filters is essentially due to their low computational requirements, to their efficient implementation and to the low number of parameters to be adapted. For these notch filters the zeros are constrained on the unit circle and the poles lay on the same radial line of the zeros. Tracking performance and convergence properties have been extensively studied [99, 104] however, due

to the IIR nature of these notch filters, several issues still remain unexplored [99]. In the GNSS context, the use of IIR notch filters has been recently proposed [25, 95] for interference removal. However some simplistic hypotheses are often assumed. For example the problem of interference detection is usually not addressed and one CW presence at the time is often assumed. The presence of more than one CWI is rarely considered and the analysis is often limited to one complex interfering signal.

This chapter deals with design of an efficient CWI detection/mitigation technique based on adaptive IIR notch filters. In particular the problem of determining the number of disturbing CWIs that affect the received signals and of activating an appropriate notch filter for their removal is thoroughly analyzed. This problem has been rarely treated in literature and is the focus of this chapter. The proposed detection algorithm is based on the removal of the constraint on the location of the filter zeros whose amplitude is adjusted by an adaptive unit. The zeros amplitude is adjusted on the basis of the Jammer to Noise ratio (J/N) and thus it can be used as a metric for the detection of the disturbing signals. At first the case of a single complex interference is considered and the one-pole notch filter is introduced. A complex interfering signal implies the presence of a single spectral line that can be easily eliminated by a single pole notch filter. Thus the behavior of the one-pole notch filter is examined. The system proposed by [95] has been used as starting point. The notch bandwidth and depth (transfer function maximum and minimum values) are analytically derived and some considerations are made. Another novel part presented here is the evaluation of the Wiener solution related to the notch approach, in order to analyze the asymptotical behavior of the filter. In fact, in [95] only an approximated solution is given, since the autoregressive (AR) part of the filter is neglected for simplicity. A complete Wiener solution that is an extended version with respect to the one reported in [95] is provided, and it is worth mentioning that such a solution is valid for every pole contraction factor that regulates the width of the notch. Simulation results prove the exactness of the formula, providing curves that coincides with the theoretical ones.

The results relative to the one-pole notch filter are extended to the case of a single real CWI. This kind of signal presents two spectral lines in correspondence of the frequencies f_i and $-f_i$, and thus two zeros are necessary to mitigate its impact. In this case a two-pole notch filter is required. This kind of filter is characterized by two complex conjugate zeros, z_0 and z_0^* , that are continuously adapted in order to track the real CWI. The impact of the two zeros on the useful GNSS signal is partially compensated by the presence of two complex conjugate poles that have the same phase of z_0 and z_0^* , and modulus contracted by a factor k_α , the pole contraction factor. The zeros are progressively adapted by a LMS algorithm that minimizes the notch filter output power. In fact the CWI is expected to carry high power concentrated at the frequencies f_i and $-f_i$ and the minimization of the output power is obtained when two deep notches are placed in correspondence of those

frequencies. Thus the minimization of the output power involves the interfering cancellation. The characteristic of the two-pole notch filter, the adaptive criterion employed for tracking the real interferer and the loss introduced on the useful GNSS signal are studied. When the interferer is not present, the two-pole notch filter can introduce degradation in the GNSS signal and should be deactivated. Thus a detection algorithm is proposed and coupled with the two-pole notch filter. The proposed detection criterion is simple and requires a very low computational load. The detection unit is essentially based on the convergence properties of z_0 . In fact, in absence of interference, the minimization of the output power is obtained by enlarging the notch and removing as much noise power as possible. The LMS can enlarge the notch because the modulus of the zeros is not constrained to unity and thus, in absence of interferer, z_0 and z_0^* tend to zero. Absence of interference is declared when the modulus of the zeros is below a fixed threshold: in this case the notch filter is deactivated. In this way the two-pole notch filter is able to autonomously detect the interfering presence and to initiate its activation or deactivation. Finally a multi-pole notch filter, able to deal with multiple CWI is proposed. This algorithm is obtained by cascading two or more two-pole notch filters. When more than one CWI is present, the first two-pole notch filter in the chain mitigates the most powerful disturbing signal, whereas the other filters remove the other interferers with progressively decreasing power. The detection units coupled with each notch filter in the chain allow the activation of only a number of filters equal to the number of interfering signals, thus minimizing the loss on the useful GNSS signal.

12.2 One-pole notch filter

The one-pole notch filter is designed for filtering a complex sinusoidal interference that can be modeled as

$$i[n] = A_{INT} \exp \{j2\pi f_i T_s n + j\phi_i\} \quad (12.1)$$

where:

- n is the discrete-time index,
- A_{INT} is the amplitude of the complex sinusoid,
- f_i and ϕ_i are the interference frequency and phase,
- T_s is the sampling interval corresponding to the sampling frequency $f_s = \frac{1}{T_s}$.

Considering expression (12.1), one notices that the interference corresponds to only one point on the unit circle of the z-plane, thus only one zero ($z = z_0$) is required to mitigate the interfering spectral line corresponding to the interference frequency. At the same time a pole in $z = k_\alpha z_0$ is required to compensate for the effects of the zero, where the

parameter k_α allows the regulation of the notch bandwidth. For stability reasons $k_\alpha < 1$. Therefore, the transfer function of the filter is given by

$$H_n(z) = \frac{1 - z_0 z^{-1}}{1 - k_\alpha z_0 z^{-1}}. \quad (12.2)$$

The structure of the filter, shown in Figure 12.2, takes the following form where $r[n]$ is

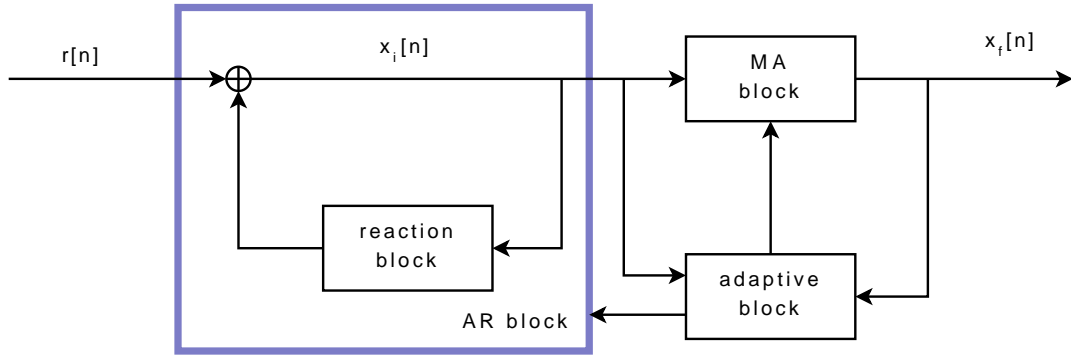


Figure 12.2. Notch filter structure: $r[n]$ is the digital input signal, $x_i[n]$ is the signal after the AR block and $x_f[n]$ is the final filtered signal.

the input signal (10.1):

$$z[n] = y[n] + \eta[n] + i[n].$$

For this analysis the contribution of the GNSS signal, $y[n]$, will be neglected due to its weakness with respect to the interference signal.

$r[n]$ is filtered by an Autoregressive Moving Average (ARMA) structure composed of three blocks: the AR, the Moving Average (MA) and the adaptive block. The MA and AR transfer functions are given by

$$H_{MA}(z) = 1 - z_0 z^{-1} \quad (12.3)$$

and

$$H_{AR}(z) = \frac{1}{1 - k_\alpha z_0 z^{-1}}. \quad (12.4)$$

12.2.1 The adaptive criterion

The core of the notch filter is represented by the adaptive block that tracks the interference frequency and adjusts the filter parameters in order to achieve the minimization of a specific cost function. In this section the algorithm reported in [95] is discussed and the adaptive criterion is determined. In particular the only free parameters of the one-pole

notch filter are the phase and the absolute value of the zero z_0 . The adaptive technique chosen in [95] is a normalized LMS [105] technique that iteratively minimizes the cost function

$$J[n] = E \left\{ |x_f[n]|^2 \right\} \quad (12.5)$$

where $x_f[n]$ is the output of the notch filter. The minimization is performed with respect to the complex parameter z_0 using the iterative rule

$$z_0[n+1] = z_0[n] - \mu[n]g(J[n]) \quad (12.6)$$

where $g(J[n])$ is the stochastic gradient of the cost function $J[n]$,

$$g(J[n]) = \nabla_{z_0} \left\{ |x_f[n]|^2 \right\} \quad (12.7)$$

and $\mu[n]$ is the algorithm step, set to

$$\mu[n] = \frac{\delta}{E_{x_i[n]}}. \quad (12.8)$$

$E_{x_i[n]}$ is an estimate of $E[|x_i[n]|^2]$ and δ is the non-normalized LMS algorithm step. $x_i[n]$ is the output of the AR block as shown in Figure 12.2. δ controls the convergence properties of the algorithm and it should be accurately chosen in order to guarantee fast convergence and reduced misadjustment. Since $x_f[n]$ is a complex signal and z_0 is a complex variable, the complex generalized derivative rules should be used in order to correctly evaluate the stochastic gradient (12.7) as

$$\nabla f(x) = \frac{\partial f}{\partial \Re e\{x\}} + j \frac{\partial f}{\partial \Im m\{x\}} = 2 \frac{\partial f}{\partial x^*}. \quad (12.9)$$

Further details on the complex generalized derivative rules can be found in [105]. Using this definition it is possible to compute

$$g(J[n]) = -4x_f[n](x_i^*[n-1]). \quad (12.10)$$

This LMS algorithm has been implemented and tested in MATLAB, proving the validity of the notch filter criterion. In Figure 12.3 an example of transfer function of the implemented notch filter is shown: a sinusoid hidden in noise with $J/N = 6$ dB is isolated and canceled by the frequency response of the filter. The transfer function is obtained in steady state conditions. It can be seen that the width of the rejection band is regulated by the factor k_α : the more k_α is close to 1 the more the rejection band narrows; however values of k_α too close to 1 cannot be employed for stability and convergence reasons. In Figure 12.4 and Figure 12.5 the spectrum of the noisy input signal and of the filtered output signal are reported. It is noted how the interference peak has been eliminated.

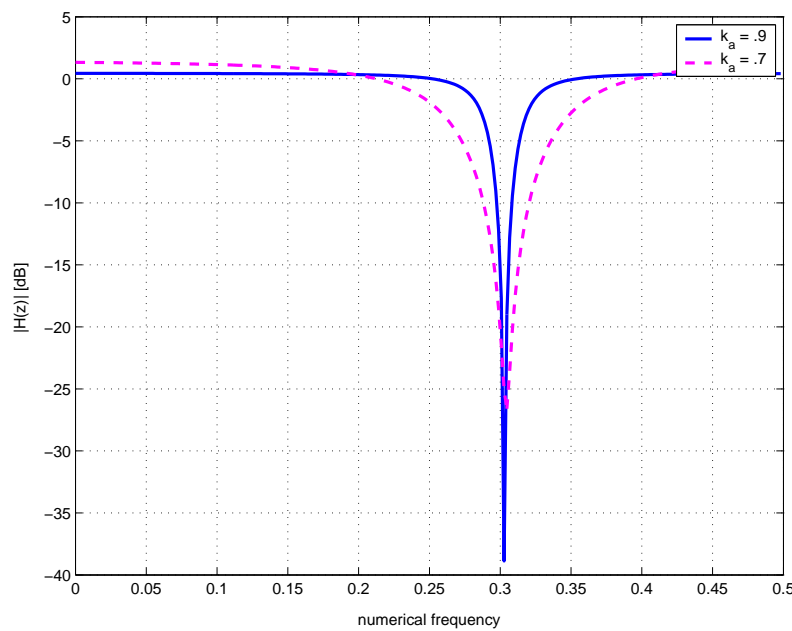


Figure 12.3. Transfer function of the notch filter, $k_\alpha = 0.9$ and $k_\alpha = 0.7$.

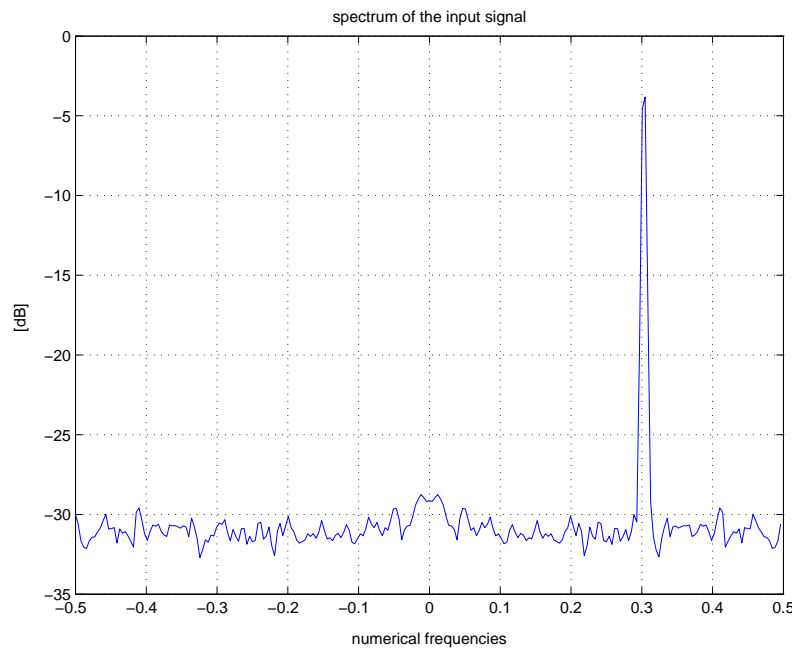


Figure 12.4. Normalized spectrum of the input signal [dB]. The signal power has been normalized to unity.

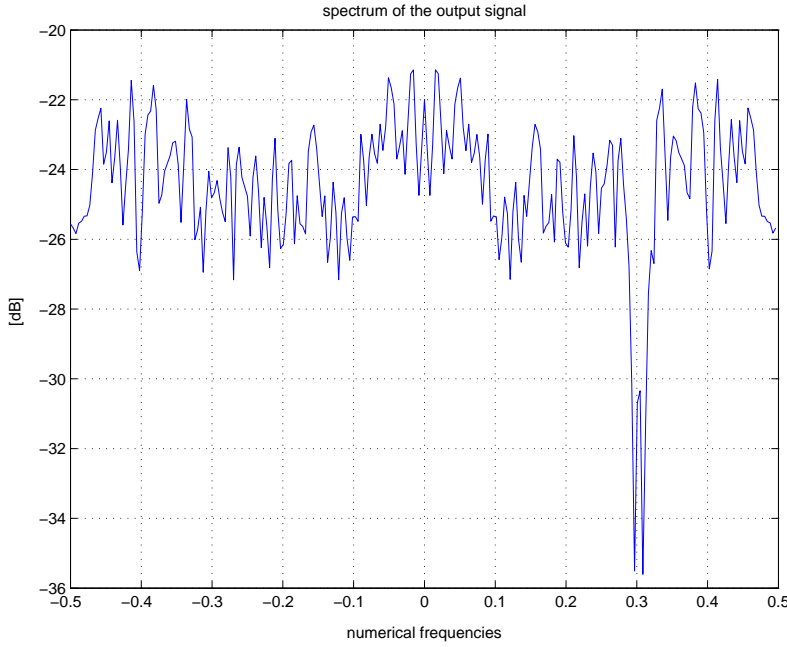


Figure 12.5. Normalized spectrum of the filtered signal [dB]. The signal power has been normalized to unity.

12.2.2 Wiener solution

As already pointed out the LMS algorithm tries to minimize the cost function

$$J[n] = E \{ |x_f[n]|^2 \}$$

following the opposite direction of the stochastic gradient. However the LMS cannot exactly find the optimal z_0 that minimizes $J[n]$, for the intrinsic nature of the algorithm and for a residual misadjustment due to the adaption step of the method. The z_0 that exactly minimizes $J[n]$ is called Wiener solution and it is in general not easy to evaluate, either because in a real context the expectation present in the cost function requires a delicate estimation process or because the relevant computational load does not allow real time applications. In some cases however it is possible to theoretically evaluate the Wiener solution. This is extremely useful for studying the asymptotical performance of the LMS algorithm; in fact it is possible to show that in steady state conditions the LMS solution tends to the Wiener one. Therefore the complete Wiener solution for the one-pole notch filter is analyzed here, starting from the preliminary and approximated results of [95]. The explicit evaluation of the Wiener solution is reported and the results are compared with simulations.

The Wiener solution for z_0 is obtained by imposing that the gradient of the cost function

$J[n]$ be zero, namely

$$\nabla J[n] = E[g(J[n))] = 0, \quad (12.11)$$

which corresponds to solving the following equation:

$$\begin{aligned} E\{x_f[n]x_i^*[n-1]\} &= E\{(x_i[n] - z_0x_i[n-1])x_i^*[n-1]\} \\ &= E\{x_i[n]x_i^*[n-1]\} - z_0E\{|x_i[n-1]|^2\} = 0. \end{aligned} \quad (12.12)$$

The Wiener solution given in [95] is approximated in the sense that is obtained by neglecting the AR part of the notch filter. In fact, in [95] the signal $x_i[n]$ corresponds to the input signal $r[n]$ and thus Eq. (12.12) reduces to

$$E\{r[n]r^*[n-1]\} - z_0E\{|r[n-1]|^2\} = 0 \quad (12.13)$$

Substituting $r[n] = \eta[n] + A_{INT} \exp\{j2\pi f_i T_s n + j\phi_i\}$ one obtains

$$E\{r[n]r^*[n-1]\} = E\{\eta[n]\eta^*[n-1]\} + A_{INT}^2 \exp\{j2\pi f_i T_s\} = A_{INT}^2 \exp\{j2\pi f_i T_s\} \quad (12.14)$$

and

$$\begin{aligned} E\{|r[n-1]|^2\} &= E\{|r[n]|^2\} \\ &= E\{(\eta[n] + A_{INT} \exp\{j2\pi f_i T_s n + j\phi_i\})(\eta^*[n] + A_{INT} \exp\{-j2\pi f_i T_s n - j\phi_i\})\} \\ &= E\{\eta[n]\eta^*[n]\} + A_{INT}^2 = \sigma_{IF}^2 + A_{INT}^2 \end{aligned} \quad (12.15)$$

where σ_{IF}^2 is the variance of the input noise. Substituting Eqs. (12.14) and (12.15) into Eq. (12.13) yields

$$A_{INT}^2 \exp\{j2\pi f_i T_s\} - z_0\sigma_{IF}^2 - z_0A_{INT}^2 = 0 \quad (12.16)$$

from which

$$z_0 = \frac{A_{INT}^2 \exp\{j2\pi f_i T_s\}}{\sigma_{IF}^2 + A_{INT}^2} = \frac{A_{INT}^2 / \sigma_{IF}^2}{A_{INT}^2 / \sigma_{IF}^2 + 1} \exp\{j2\pi f_i T_s\}. \quad (12.17)$$

It is noted that this solution is independent on the value of k_α . As it will be shown below, the experimental results are not in agreement with this. In Figure 12.6 the Wiener solution according to [95] is shown.

In order to obtain the complete Wiener solution the autoregressive part of the filter cannot be neglected, and therefore the approximation $x_i[n] = r[n]$ is no longer valid. So the expression for $x_i[n]$ as function of the components of $r[n]$ has to be evaluated. Therefore, the impulse response of the AR block for Eq. (12.4) has to be derived as

$$h_{AR}[n] = \sum_{i=0}^{+\infty} (k_\alpha z_0)^i \delta[n-i]. \quad (12.18)$$

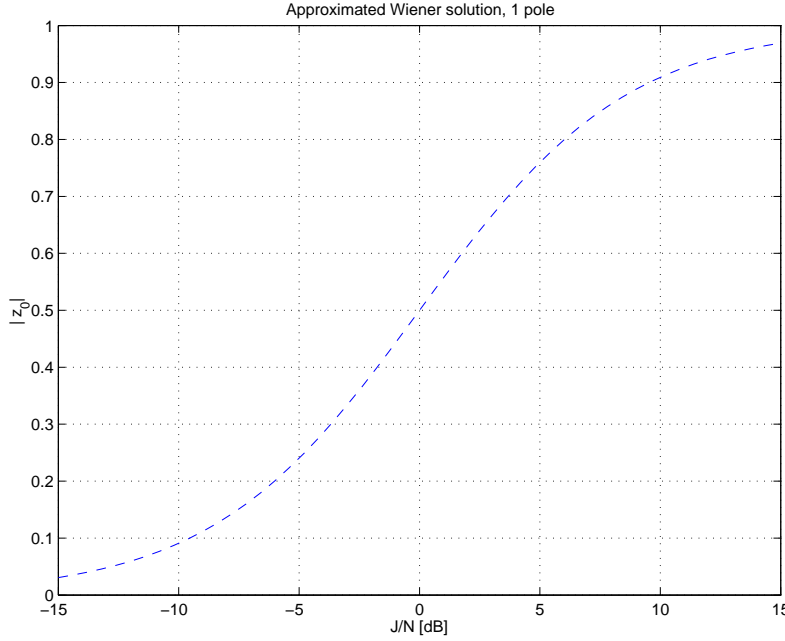


Figure 12.6. Wiener solution according to [95].

In this way

$$\begin{aligned}
 x_i[n] &= r[n] * h_{AR}[n] = \sum_{i=0}^{+\infty} (k_\alpha z_0)^i \eta[n-i] + A_{INT} \sum_{i=0}^{+\infty} (k_\alpha z_0)^i \exp\{j2\pi f_i T_s(n-i) + j\phi_i\} \\
 &= \sum_{i=0}^{+\infty} (k_\alpha z_0)^i \eta[n-i] + \frac{A_{INT} \exp\{j2\pi f_i T_s n + j\phi_i\}}{1 - k_\alpha z_0 \exp\{-j2\pi f_i T_s\}}
 \end{aligned} \tag{12.19}$$

Using this result it is now possible to evaluate the terms in Eq. (12.12):

$$\begin{aligned}
 E\{|x_i[n-1]|^2\} &= \sum_{i=0}^{+\infty} \sum_{k=0}^{+\infty} (k_\alpha z_0)^i (k_\alpha z_0^*)^k E\{\eta[n-i-1] \eta^*[n-k-1]\} \\
 &\quad + \frac{A_{INT} \exp\{j2\pi f_i T_s(n-1) + j\phi_i\}}{1 - k_\alpha z_0 \exp\{-j2\pi f_i T_s\}} \frac{A_{INT} \exp\{-j2\pi f_i T_s(n-1) - j\phi_i\}}{1 - k_\alpha z_0^* \exp\{j2\pi f_i T_s\}} \\
 &= \sum_{i=0}^{+\infty} (k_\alpha^2 |z_0|^2)^i \sigma_{IF}^2 + \frac{A_{INT}^2}{1 - 2k_\alpha \Re\{z_0 \exp\{-j2\pi f_i T_s\}\} + k_\alpha^2 |z_0|^2} \\
 &= \frac{\sigma_{IF}^2}{1 - k_\alpha^2 |z_0|^2} + \frac{A_{INT}^2}{1 - 2k_\alpha \Re\{z_0 \exp\{-j2\pi f_i T_s\}\} + k_\alpha^2 |z_0|^2}
 \end{aligned} \tag{12.20}$$

$$\begin{aligned}
 E\{x_i[n]x_i^*[n-1]\} &= \sum_{i=0}^{+\infty} \sum_{k=0}^{+\infty} (k_\alpha z_0)^i (k_\alpha z_0^*)^k E\{\eta[n-i]\eta^*[n-1-k]\} \\
 &\quad + \frac{A_{INT} \exp\{j2\pi f_i T_s n + \phi_i\}}{1 - k_\alpha z_0 \exp\{-j2\pi f_i T_s\}} \frac{A_{INT} \exp\{-j2\pi f_i(n-1)T_s - j\phi_i\}}{1 - k_\alpha z_0^* \exp\{j2\pi f_i T_s\}} \\
 &= \sum_{i=1}^{+\infty} (k_\alpha z_0)^i (k_\alpha z_0^*)^{i-1} \sigma_{IF}^2 + \frac{A_{INT}^2 \exp\{j2\pi f_i T_s\}}{1 - 2k_\alpha \Re\{z_0 \exp\{-j2\pi f_i T_s\}\} + k_\alpha^2 |z_0|^2} \\
 &= \frac{k_\alpha z_0 \sigma_{IF}^2}{1 - (k_\alpha^2 |z_0|^2)} + \frac{A_{INT}^2 \exp\{j2\pi f_i T_s\}}{1 - 2k_\alpha \Re\{z_0 \exp\{-j2\pi f_i T_s\}\} + k_\alpha^2 |z_0|^2}
 \end{aligned} \tag{12.21}$$

In Eqs. (12.20) and (12.21) the cross-components between noise and complex exponential have not been considered, since they are statistically independent and the noise has zero mean.

Substituting expressions (12.20) and (12.21) into Eq. (12.12) yields:

$$\frac{z_0 \sigma_{IF}^2 (k_\alpha - 1)}{1 - (k_\alpha^2 |z_0|^2)} + \frac{A_{INT}^2 [\exp\{j2\pi f_i T_s\} - z_0]}{1 - 2k_\alpha \Re\{z_0 \exp\{-j2\pi f_i T_s\}\} + k_\alpha^2 |z_0|^2} = 0 \tag{12.22}$$

Eq. (12.22) cannot be easily solved directly, however some simplifications can be made by imposing that the phase of z_0 be $2\pi f_i T_s$. This assumption is justified by the fact that the phase of z_0 does not affect the power of the noise component at the output of the notch filter, because a change in the phase only changes the rejection band location but not the overall shape of the transfer function, that results circularly shifted. Since the remaining noise power is always the same, one can choose the phase that minimizes the exponential component power and that corresponds to $2\pi f_i T_s$. Using the condition

$$z_0 = \rho \exp\{j2\pi f_i T_s\}$$

and, applying some simplifications, Eq. (12.22) becomes

$$\begin{aligned}
 \frac{\rho \sigma_{IF}^2 (k_\alpha - 1)}{1 - k_\alpha^2 \rho^2} + \frac{A_{INT}^2 (1 - \rho)}{1 - 2k_\alpha \rho + k_\alpha^2 \rho^2} &= 0 \\
 \frac{\rho \sigma_{IF}^2 (k_\alpha - 1)}{1 + k_\alpha \rho} + \frac{A_{INT}^2 (1 - \rho)}{1 - k_\alpha \rho} &= 0,
 \end{aligned}$$

which leads to the following second degree equation:

$$\rho(1 - k_\alpha \rho) - \frac{A_{INT}^2}{\sigma_{IF}^2 (1 - k_\alpha)} (1 - \rho)(1 + k_\alpha \rho) = 0. \tag{12.23}$$

This equation has two solutions but only one is acceptable for the condition $\rho \geq 0$, namely

$$\rho = \frac{-\gamma(1 - k_\alpha) - 1 + \sqrt{[\gamma(1 - k_\alpha) + 1]^2 + 4k_\alpha \gamma(\gamma - 1)}}{2k_\alpha(\gamma - 1)} \tag{12.24}$$

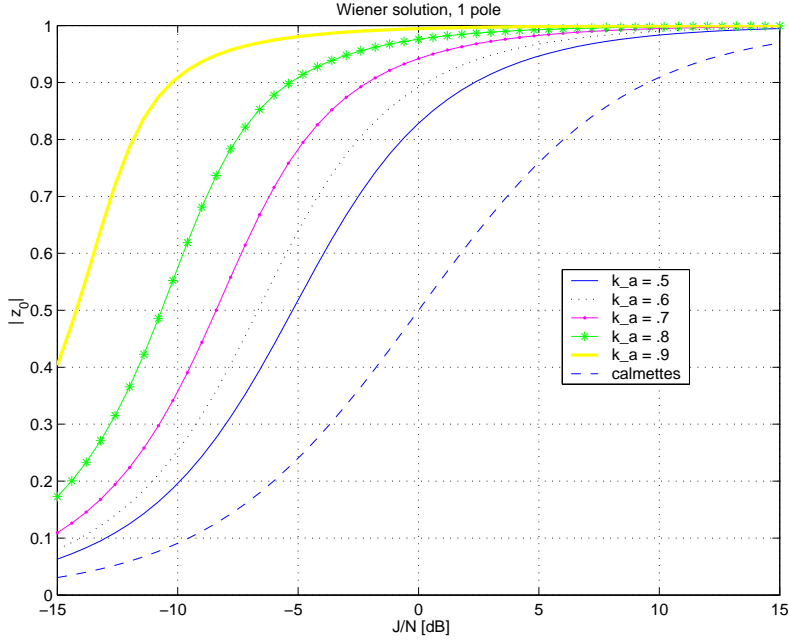


Figure 12.7. Notch filter Wiener solution: the absolute value of the notch filter zero z_0 that minimizes the output power is reported as function of J/N for different values of k_α . The label “calmettes” refers to the solution reported in [95] that is independent from k_α .

with $\gamma = \frac{A_{INT}^2}{\sigma_{IF}^2(1-k_\alpha)}$.

In Figure 12.7 the Wiener solution is represented. It is noted that, contrary to the solution provided in [95], this solution depends on k_α , so curves obtained for different values of k_α are shown. The solution provided in [95] is also depicted; it is observed that the solution provided in [95] is the limit solution for k_α tending to zero, that is when the autoregressive block degenerates to a constant. In Section 12.2.4 the matching between this Wiener solution and the experimental curves will be shown.

12.2.3 Bandwidth and attenuation

In this section some of the one-pole notch filter properties are analyzed, and more specifically the shape of its transfer function, the minimum, the maximum, and its bandwidth, namely

$$z_0 = \rho \exp\{j\omega_0\}$$

and

$$z^{-1} \cdot z_0 = \exp\{-j\omega\} \rho \exp\{j\omega_0\} = \rho \exp\{j(\omega_0 - \omega)\} = \rho \exp\{j\Delta_\omega\}.$$

The minimum and maximum values of $|H_n(z)|^2$ on the unit circle, are calculated by evaluating the derivative of the function and finding where it is equal to zero, more specifically, by solving

$$\frac{d|H_n(\exp\{j\omega\})|^2}{d\omega} = 0 \quad (12.25)$$

with

$$H_n(\exp\{j\omega\}) = \frac{1 - \rho \exp\{j\omega_0\} \exp\{-j\omega\}}{1 - \rho k_\alpha \exp\{j\omega_0\} \exp\{-j\omega\}}$$

In this way

$$|H_n(\exp\{j\omega\})|^2 = \frac{1 - 2\rho \cos(\omega_0 - \omega) + \rho^2}{1 - 2\rho k_\alpha \cos(\omega_0 - \omega) + \rho^2 k_\alpha^2}. \quad (12.26)$$

Performing the derivative yields

$$\begin{aligned} & \frac{d|H_n(\exp\{j\omega\})|^2}{d\omega} = \\ &= \frac{2\rho \sin(\omega_0 - \omega)(1 - 2\rho k_\alpha \cos(\omega_0 - \omega) + \rho^2 k_\alpha^2) - 2\rho k_\alpha \sin(\omega_0 - \omega)(1 - 2\rho \cos(\omega_0 - \omega) + \rho^2)}{(1 - 2\rho k_\alpha \cos(\omega_0 - \omega) + \rho^2 k_\alpha^2)^2} \\ &= 0 \end{aligned} \quad (12.27)$$

that is

$$\begin{aligned} & 2\rho \sin(\omega_0 - \omega)(1 - 2\rho k_\alpha \cos(\omega_0 - \omega) + \rho^2 k_\alpha^2 - k_\alpha + 2\rho k_\alpha \cos(\omega_0 - \omega) - \rho^2 k_\alpha) \\ &= 2\rho \sin(\omega_0 - \omega)(1 + \rho^2 k_\alpha^2 - k_\alpha - \rho^2 k_\alpha) = 0 \end{aligned} \quad (12.28)$$

and finally

$$\sin(\omega_0 - \omega) = 0$$

Therefore the solutions are $\omega = \omega_0$ and $\omega = \omega_0 + \pi$, which give the positions of the maximum and minimum values. In conclusion the minimum of $|H_n(z)|^2$ is in $z = \exp\{j\omega_0\}$, giving an attenuation of

$$A_t = |H_n(z = \exp\{j\omega_0\})| = \left| \frac{1 - \rho}{1 - k_\alpha \rho} \right|$$

and the maximum is in $z = \exp\{j(\omega_0 + \pi)\}$, giving

$$M = |H_n(z = \exp\{j\omega_0 + j\pi\})| = \left| \frac{1 + \rho}{1 + k_\alpha \rho} \right|.$$

Figures 12.8 and 12.9 show the evolution of the maximum and minimum values of the notch filter transfer function as a function of k_α . It can be noted that A_t increases with k_α . On the contrary, M decreases with k_α and tends to 1 when k_α tends to 1. In conclusion, lower values of k_α mean both a deeper notch and a higher M . Since the filter distortion increases as a function of M as the latter takes on values larger than 1, the choice of k_α

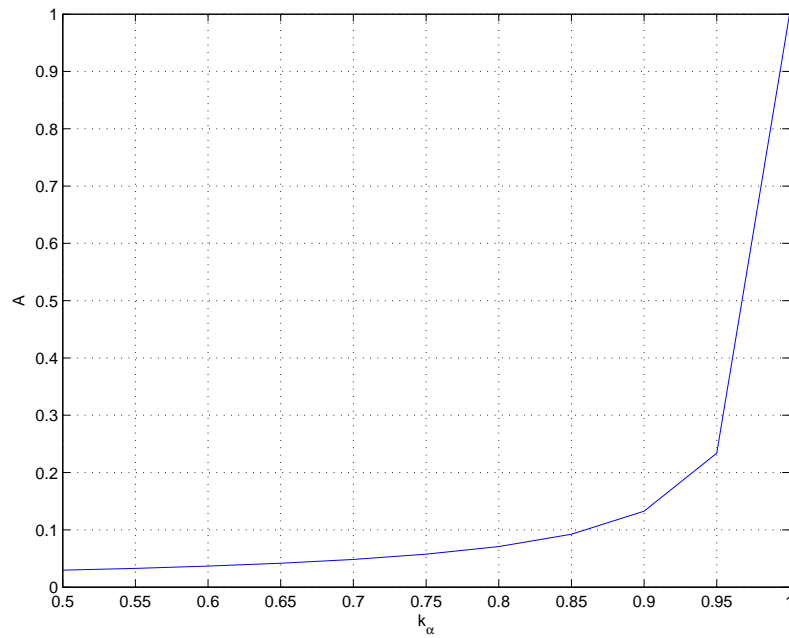


Figure 12.8. $|H_n(z)|$ minimum vs k_α , $\rho = 0.985$.

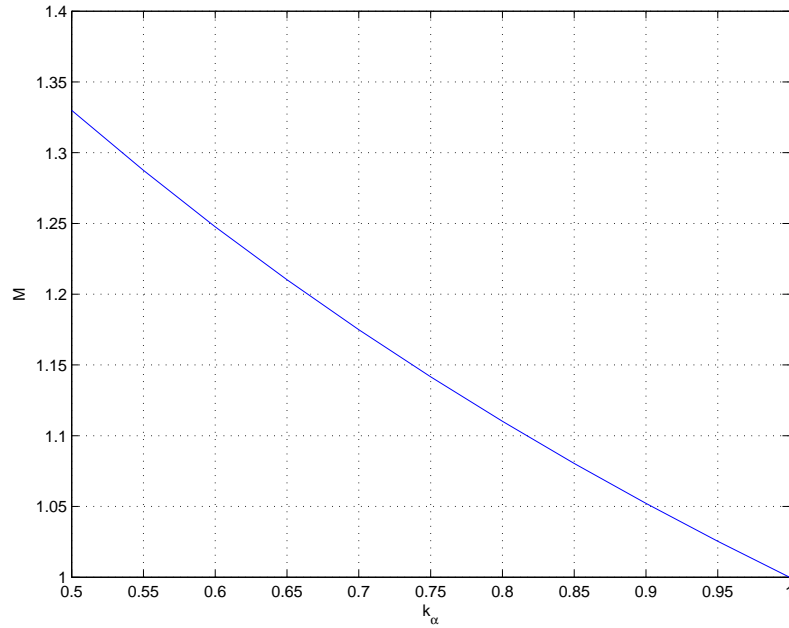


Figure 12.9. $|H_n(z)|$ maximum vs k_α , $\rho = 0.985$.

requires a tradeoff between notch depth and introduced distortion.

Now the 3 dB bandwidth, B_{3dB} , is calculated and again a comparison with the solution given in [95] is provided. In order to calculate the 3 dB bandwidth, the equation

$$|H_n(j\omega)|^2 = \frac{1}{2}M \quad (12.29)$$

has to be solved. The squared module of $|H_n(z)|$ is given by

$$|H_n(z)|^2 = \left| \frac{1 - z_0 z^{-1}}{1 - k_\alpha z_0 z^{-1}} \right|^2 = \frac{1 + \rho^2 - 2\rho \cos(\Delta_\omega)}{1 + \rho^2 k_\alpha^2 - 2\rho k_\alpha \cos(\Delta_\omega)} \quad (12.30)$$

and, after some manipulations, it is possible to rewrite Eq. (12.29) as

$$\cos(\Delta_\omega) = \frac{.5M + .5Mk_\alpha^2\rho^2 - 1 - \rho^2}{-2\rho + Mk_\alpha\rho}. \quad (12.31)$$

Given the shape of the notch filter and the proximity of the two frequencies laying at a distance B_{3dB} , the approximation $\omega \approx \omega_0$, and therefore $\Delta_\omega \approx 0$, is valid. This leads to the approximation $\cos(\Delta_\omega) \approx 1 - \frac{1}{2}\Delta_\omega^2$. Substituting these results into Eq. (12.31), the value of Δ_ω^2 can be obtained as

$$\Delta_\omega^2 = 2 + \frac{2 + 2\rho^2 - M - Mk_\alpha^2\rho^2}{\rho(Mk_\alpha - 2)}. \quad (12.32)$$

This equation has two solutions $\Delta_{\omega,1}$ and $\Delta_{\omega,2}$, with the same absolute value and opposite sign, so $\Delta_{\omega,1} = -\Delta_{\omega,2} = \Delta_\omega$ and $\Delta_{\omega,1} - \Delta_{\omega,2} = 2\Delta_\omega$.

Now,

$$\Delta_\omega = \omega_0 - \omega = \omega_0 - 2\pi f T_s$$

from which

$$f = \frac{\omega_0 - \Delta_\omega}{2\pi T_s}$$

and equivalently

$$f_{1,2} = \frac{\omega_0 - \Delta_{\omega,1,2}}{2\pi T_s}.$$

B_{3dB} can be obtained as the distance between the two frequencies solution of Eq. (12.32) as

$$B_{3dB} = f_1 - f_2 = \frac{\omega_0 - \Delta_{\omega,1}}{2\pi T_s} - \frac{\omega_0 - \Delta_{\omega,2}}{2\pi T_s} = \frac{\Delta_{\omega,2} - \Delta_{\omega,1}}{2\pi} = \frac{\Delta_\omega}{\pi T_s} \quad (12.33)$$

and finally

$$B_{3dB} = \frac{1}{\pi T_s} \sqrt{2 + \frac{2 + 2\rho^2 - M - Mk_\alpha^2\rho^2}{\rho(Mk_\alpha - 2)}}. \quad (12.34)$$

Figure 12.10 shows the shape of B_{3dB} versus k_α for different values of ρ . It is noted that for $\rho = 1$ the curve is a straight line. In fact Eq. (12.34) becomes:

$$B_1 = \frac{|k_\alpha - 1|}{\pi T_s} \quad (12.35)$$

This is the approximated formula for the 3 dB bandwidth given by Calmettes et al in an earlier work [102], where the modulus of z_0 was fixed to one.

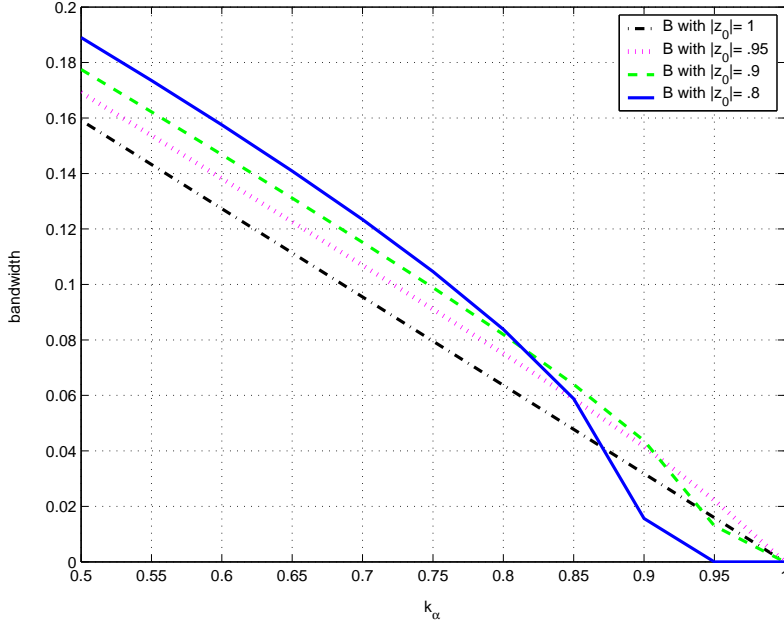
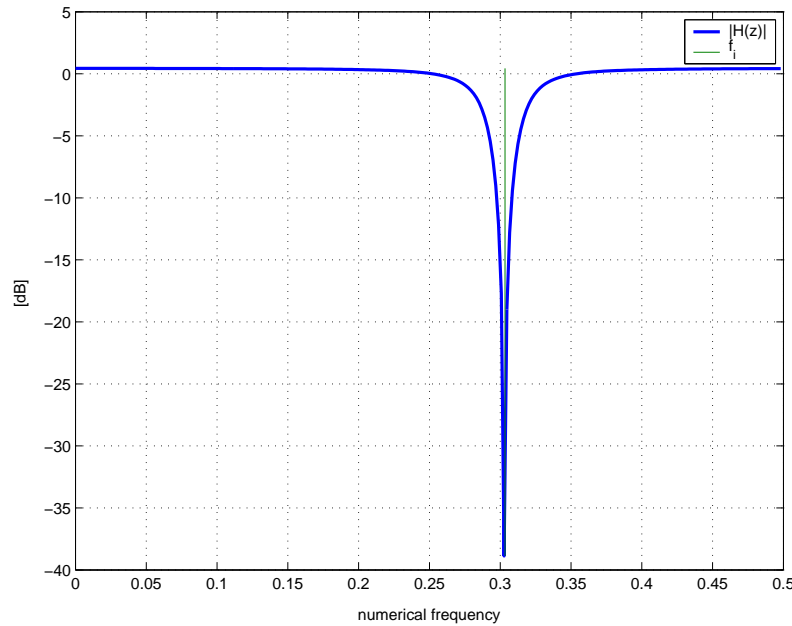
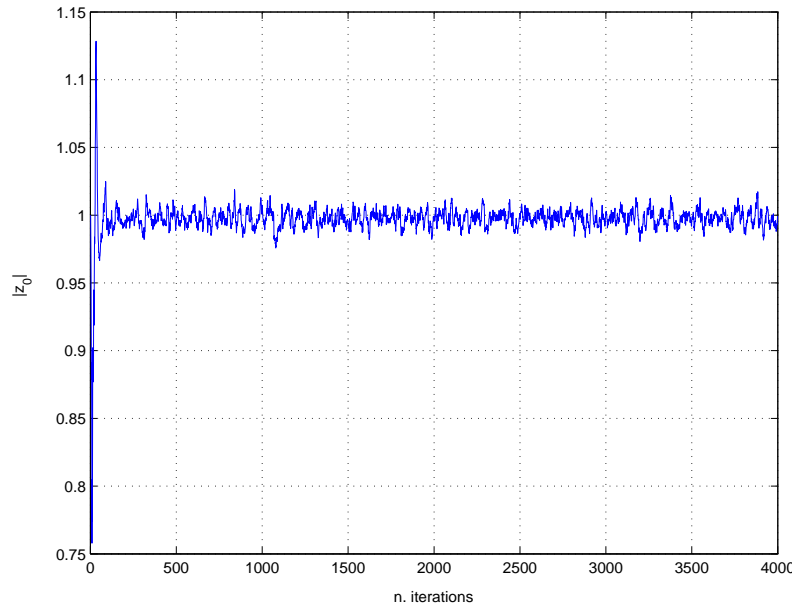


Figure 12.10. Normalized 3 dB bandwidth vs k_α , for different values of ρ . The 3 dB bandwidth is normalized with respect to the sampling frequency.

12.2.4 Performance analysis and test on real data

The performance of the filter has been tested imposing the amplitude and phase of the interferer, and monitoring outputs like the filter transfer function and the position of the zeros. Some of the most interesting results are reported below. The figures have been obtained in steady state conditions, and with $A_{INT} = 10$, $J/N = 6$ dB, $k_\alpha = 0.9$ and $\delta = 0.07$; moreover the frequencies have been normalized with respect to the sampling frequency f_s . Figure 12.11 shows the transfer function of the filter, together with the line indicating the interfering frequency f_i , proving that the filter has correctly detected the complex sinusoid. Figure 12.12 shows how the modulus of z_0 settles around one, proving the convergence of the algorithm. Some results of the comparison of the experimental curves and the Wiener solution are also provided. The J/N has been made varying in


 Figure 12.11. Transfer function of the notch filter, $k_\alpha = 0.9$ and $\delta = 0.07$.

 Figure 12.12. Convergence of modulus of the zero z_0 , $k_\alpha = 0.9$ and $\delta = 0.07$.

the range $(-15 \text{ dB}, 15 \text{ dB})$, the total power of the signal has been held constant and k_α

has been successively fixed to 0.7, 0.8 and 0.9. Some 4000 iterations have been performed and the steady state condition maintained. Figure 12.13 shows how the modulus of the z_0

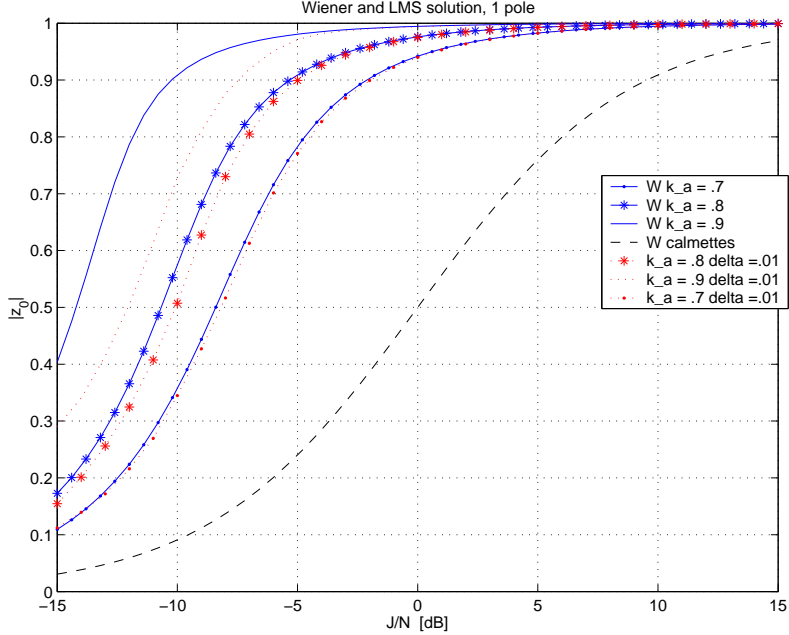


Figure 12.13. LMS and Wiener solution for different values of k_α and comparison between theoretical and simulation results.

changes with the varying of the J/N . It can be seen that the curves change for different k_α . Moreover the curves have been superposed to the Wiener solutions: it can be immediately noted that the Wiener solutions provided with the complete analysis are very close to the ones obtained by simulations.

The one-pole notch filter has been tested on real GPS data, collected with the Nord-Nav R30 receiver [1]. Such data contain a narrowband interference. The interference was generated by using the analog signal generator Agilent E4428C directly connected to an antenna and irradiating in the proximity of the receiver antenna. The experimental setup adopted for collecting the GPS data corrupted by CWI is depicted in Figure 12.14: the Agilent E4428C signal generator was used to produce the CWI and the GPS signal corrupted by the interference was collected by using the NordNav frontend. The GPS signal was stored and post-processed by using MATLAB. Since the input signal is real, with a real interfering, the one-pole notch filter is unable to directly deal with this kind of signal. One way to successfully use it is to apply an Hilbert transform at the input signal before the filtering. The procedure adopted for processing the collected GPS samples is depicted in Figure 12.15: the Hilbert transform was used in order to produce a complex

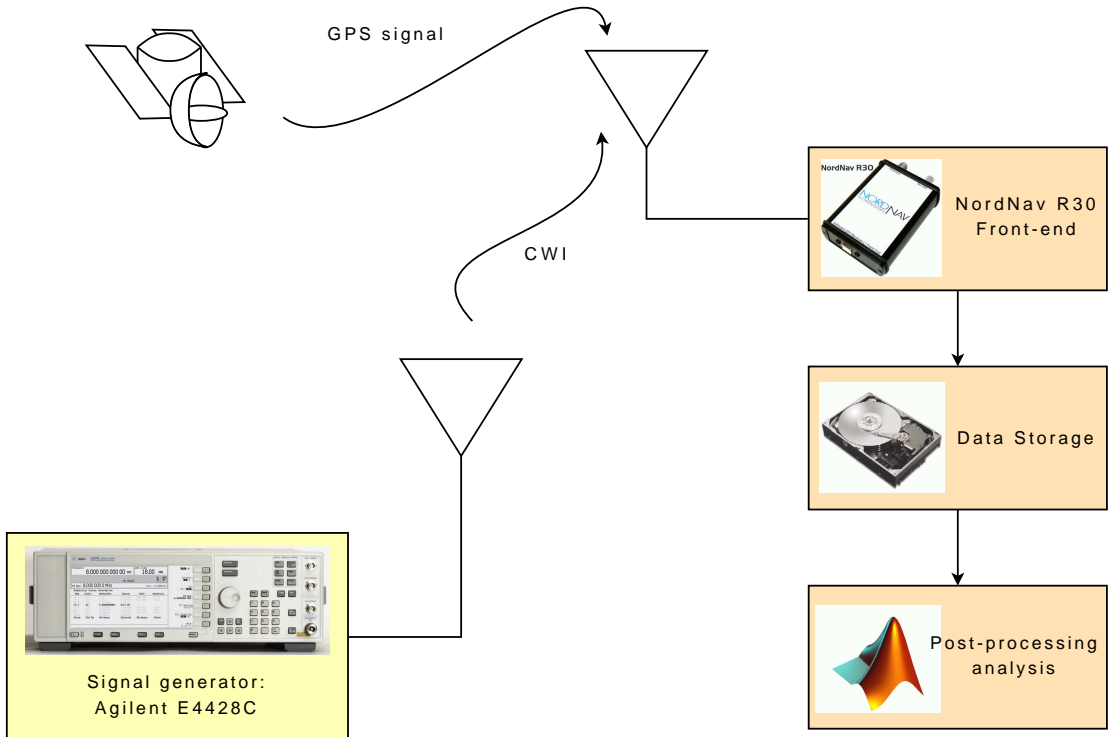


Figure 12.14. Scheme of experimental setup used for collecting and processing the GPS data corrupted by CWI.

signal that can be processed by the one-pole notch filter. The one-pole notch filter has then been used to excise the CWI from the complex signal that was then re-transformed into a real sequence. This sequence was then fed into the acquisition block.

In Figure 12.16 the power spectral densities of the input signal and of the signal processed by the one-pole notch filter, according to the scheme reported in Figure 12.15, are depicted. The one-pole notch filter correctly determines the interference frequency effectively excising the CWI. The effectiveness of the one-pole notch filter is still more evident when considering Figures 12.17 and 12.18, which provide the CAFs evaluated on the unfiltered and filtered GPS signal. Without a mitigation unit, it is not possible to detect the signal peak whereas, as it clearly emerges from Figure 12.18, the one-pole notch filter effectively removes the CWI allowing a correct and more reliable signal acquisition. Both search spaces have been evaluated by using a coherent integration time of 1 ms and $K = 3$ non-coherent integrations.

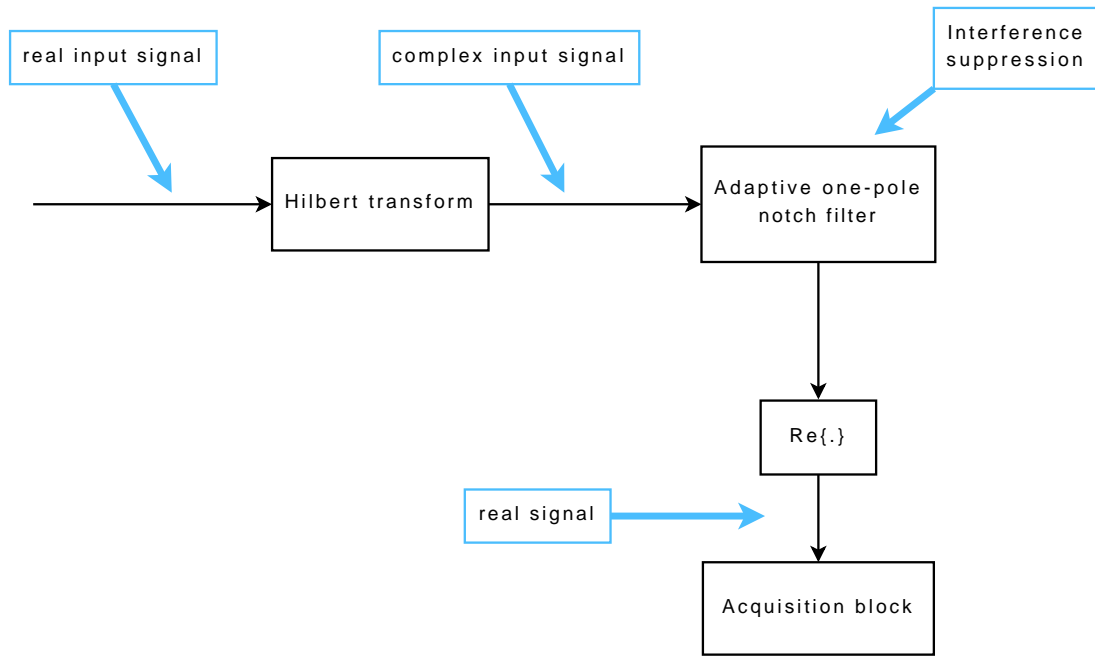


Figure 12.15. Procedure adopted for processing the GPS samples. An Hilbert transform was used in order to produce a complex signal that can be processed by the one-pole notch filter.

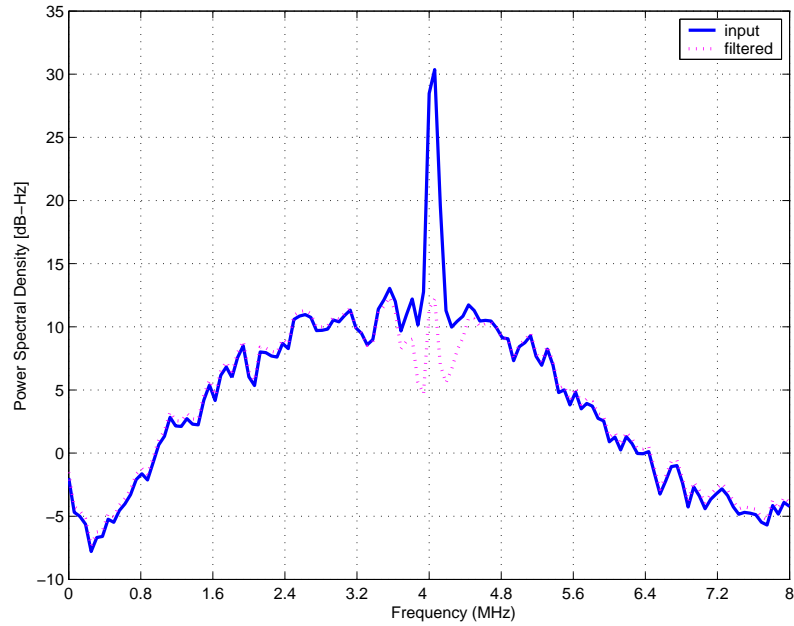


Figure 12.16. PSD of the input and output signals.

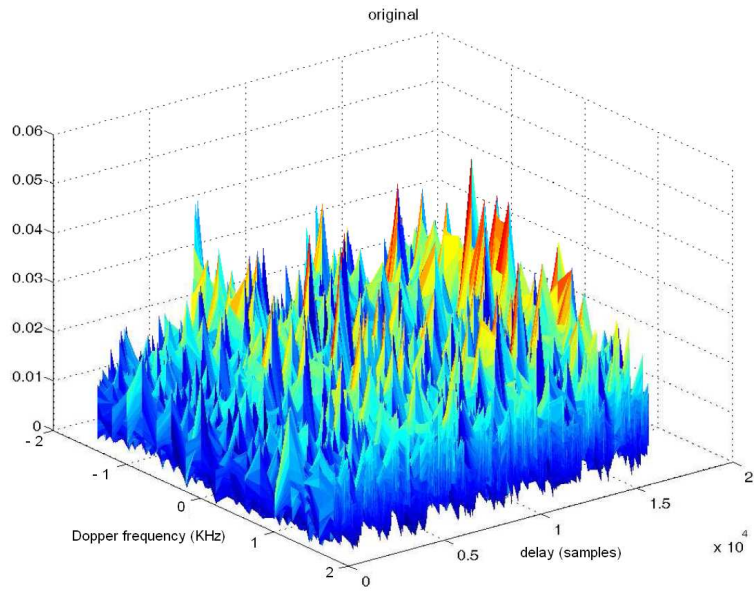


Figure 12.17. CAF obtained by processing the GPS signal corrupted by the CWI. Without mitigation unit is not possible to detect the signal peak. The search space has been evaluated by using a coherent integration time of 1 ms and $K = 3$ non-coherent integrations.

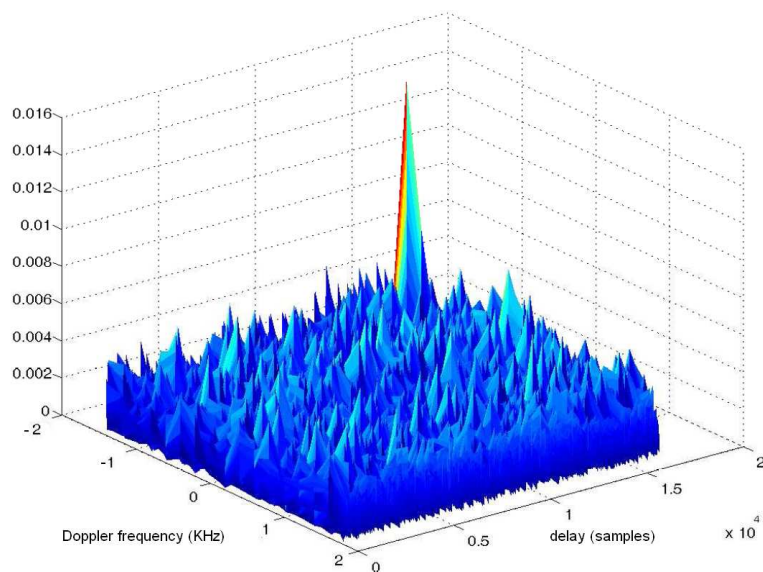


Figure 12.18. CAF obtained by processing the GPS signal corrupted by the CWI after interference mitigation. The one-pole notch filter effectively removes the CWI and the signal peak emerges from the search space. The search space has been evaluated by using a coherent integration time of 1 ms and $K = 3$ non-coherent integrations.

12.3 Two-pole notch filter

The case of a complex sinusoidal interference is extremely interesting for some preliminary analysis but with limited applicability. In fact the signal at the output of the GNSS frontend is real and thus some additional devices, as the Hilbert transform employed in Section 12.2.4, are required in order to produce a complex CWI. For these reasons the one-pole notch filter has been modified in order to directly deal with real CWIs.

The presence of a real CWI means that two spectral lines have to be mitigated, thus requiring two zeros in the transfer function. The structure of the two-pole notch filter is similar to the one reported for the one-pole filter: an ARMA structure composed of three blocks, namely the AR, the MA and the adaptive unit (see Figure 12.2). The filter is designed for filtering the real sinusoidal interference as

$$i[n] = A_{INT} \cos(2\pi f_i n T_s + \phi_i) \quad (12.36)$$

where:

- A_{INT} is the interfering signal amplitude,
- f_i and ϕ_i are the frequency and phase of the continuous wave,
- T_s the sampling interval,
- n is the time index.

The MA transfer function is then given by

$$H_{MA}(z) = (1 - z_0 z^{-1})(1 - z_0^* z^{-1}) = 1 - 2\Re e\{z_0\}z^{-1} + |z_0|^2 z^{-2}. \quad (12.37)$$

The AR block is constrained to compensate for the effects of the MA block other than the zeros frequencies and its transfer function is given by

$$H_{AR}(z) = \frac{1}{(1 - k_\alpha z_0 z^{-1})(1 - k_\alpha z_0^* z^{-1})} = \frac{1}{1 - 2k_\alpha \Re e\{z_0\}z^{-1} + k_\alpha^2 |z_0|^2 z^{-2}}. \quad (12.38)$$

In this way the transfer function of the whole filter is given by

$$H_n(z) = \frac{1 - 2\Re e\{z_0\}z^{-1} + |z_0|^2 z^{-2}}{1 - 2k_\alpha \Re e\{z_0\}z^{-1} + k_\alpha^2 |z_0|^2 z^{-2}}. \quad (12.39)$$

The same LMS algorithm used for the complex case and consisting in the minimization of the cost function $E\{|x_f[n]|^2\}$ with respect to the complex parameter z_0 has been adopted. In this case, the expression of the stochastic gradient is given by

$$g(J[n]) = 4x_f[n](z_0 x_i[n-2] - x_i[n-1]). \quad (12.40)$$

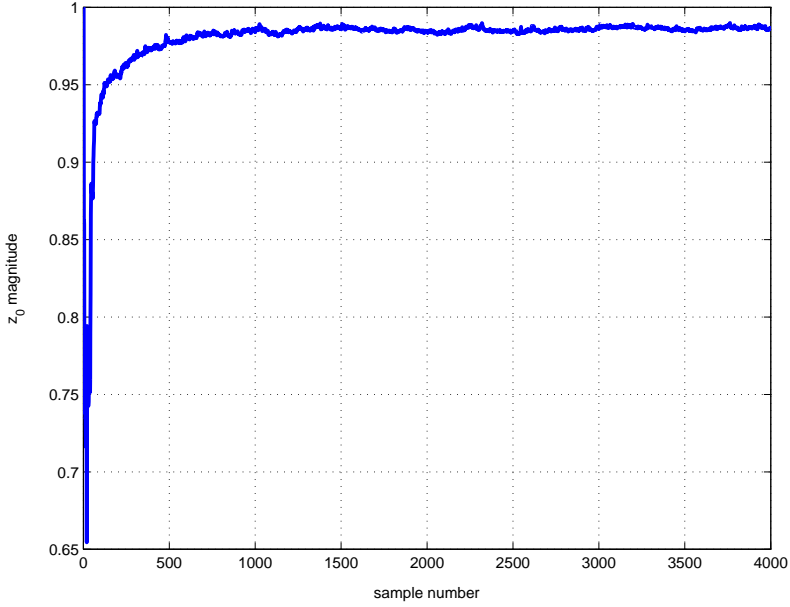


Figure 12.19. Magnitude of the adjusted parameter z_0 through the LMS convergence process.

This LMS algorithm, according to expressions (12.6) and (12.40) has been implemented and tested in MATLAB. The convergence of the adapted parameter z_0 is shown in Figure 12.19 where the magnitude of the adjusted parameter z_0 is reported. The magnitude of z_0 converges to a value close to unity that creates two zeros in the transfer function of the filter corresponding to the frequencies $\pm f_i$. In Figure 12.20 an example of transfer function of the implemented notch filter is reported where the system has reached the steady state condition and the interfering sinusoid is isolated and canceled by the frequency response of the filter. The J/N was equal to 0 dB.

12.3.1 The detection unit

In Figure 12.19 the convergence process of the modulus of the notch filter zero has been reported. In this case the amplitude converges to a value that is close to unity. This is due to the fact that a strong interference is present and thus the minimization of the power of the notch filter output is achieved by narrowing the notch and removing as much interfering power as possible. However as the interfering power decreases cost function minimum is no longer achieved by removing only the interference but also by attenuating a part of the noise and GNSS signal components. In this way the adaptive algorithm chooses a wider notch that is able to capture not only the interference but also part of the noise and signal power. Thus the amplitude of the notch filter zeros is extremely dependent on the interfering power. In Figure 12.21 the convergence of the z_0 amplitude

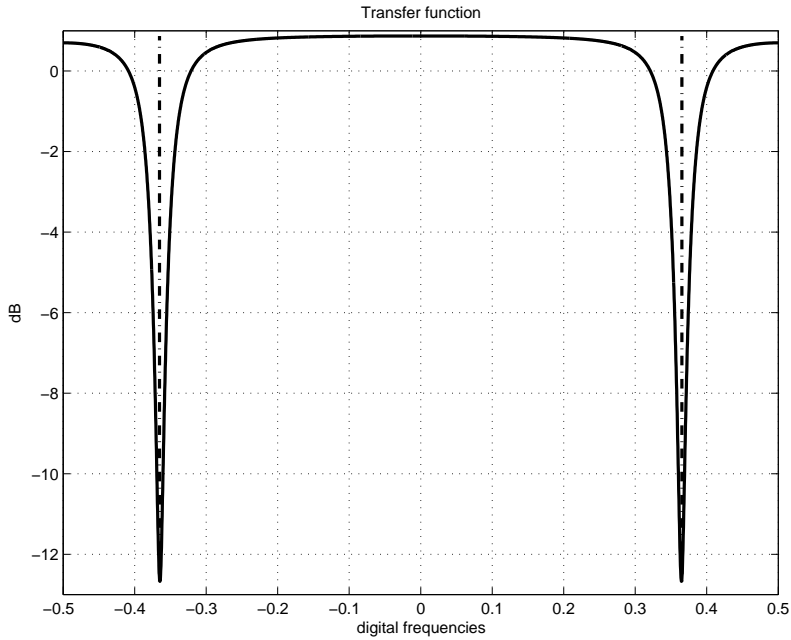


Figure 12.20. Transfer function of the notch filter, $k_\alpha = 0.9$, steady state conditions.

is reported for different values of J/N . The zero amplitude is strongly dependent on the interfering power and thus it can be used for detection purposes. The proposed detection algorithm consists in verifying if the mean value of the amplitude of z_0 passes a fixed threshold. If that happens it means that the notch filter is tracking a CWI and thus its output has to be used for positioning operation. Otherwise the unfiltered signal has to be employed. In Figure 12.22 the mean magnitude of z_0 has been reported as a function of J/N for two different values of the pole contraction factor k_α . The detection threshold can be fixed by choosing a $J/N = L$ that may however be considered harmful for the GNSS receiver. By using Figure 12.22 the threshold T is determined as the value to which the notch filter zero converges when a J/N of L is present. In this way the notch filter is activated only if an interference characterized by $J/N > L$ is present. In Figure 12.23 the scheme of the adaptive notch filter coupled with the interfering detection unit is reported. The notch filter is always active but the detection unit decides if the GNSS receiver should use the filtered signal or not. In Figure 12.24 the detection algorithm is better described: the subsequent values of z_0 produced by the adaptive unit of the notch filter are low-pass filtered, obtaining an estimation of its mean. Then a simple test verifies the condition $|\hat{z}_0| > T$, where \hat{z}_0 is the estimation of the mean of z_0 and T is the detection threshold. Then the detection unit decides if the filtered signal is better than the original one according to the test result.

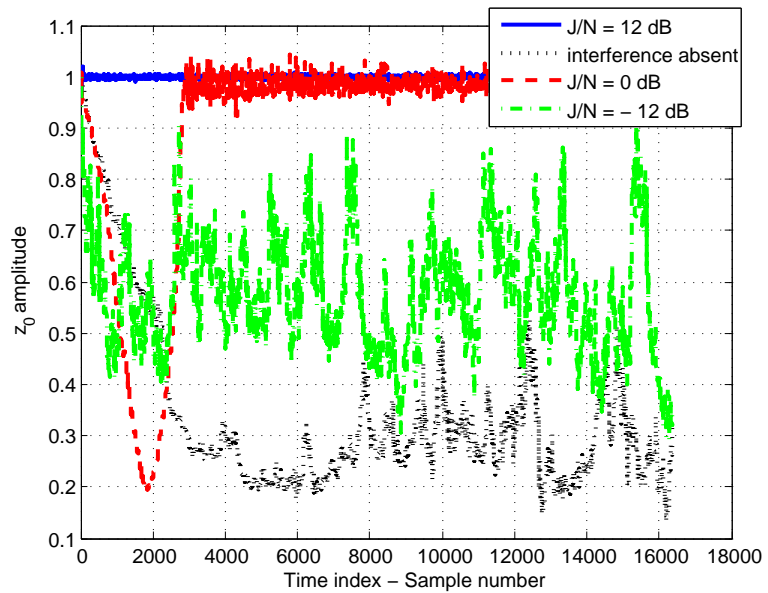


Figure 12.21. Convergence characteristics of the amplitude of the notch filter zero for different J/N . $k_\alpha = 0.9$.

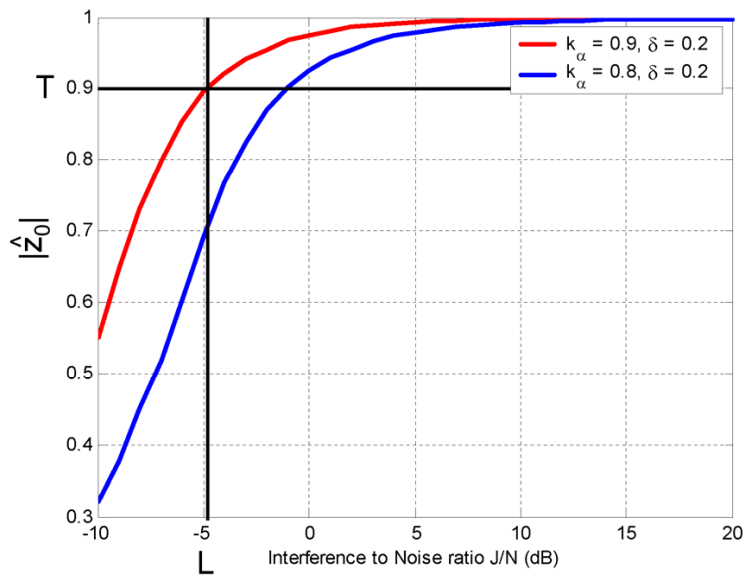


Figure 12.22. Mean magnitude of the adjusted parameter z_0 : threshold setting.

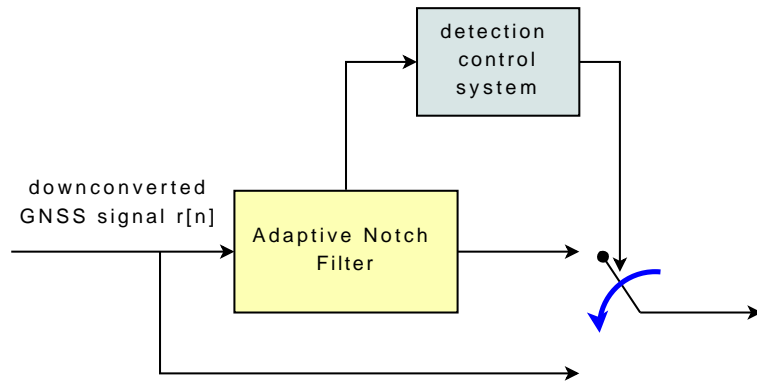


Figure 12.23. Scheme of the adaptive notch filter coupled with the detection unit. The notch filter is always active but the detection unit decides if it is better to use the original or the filtered signal.

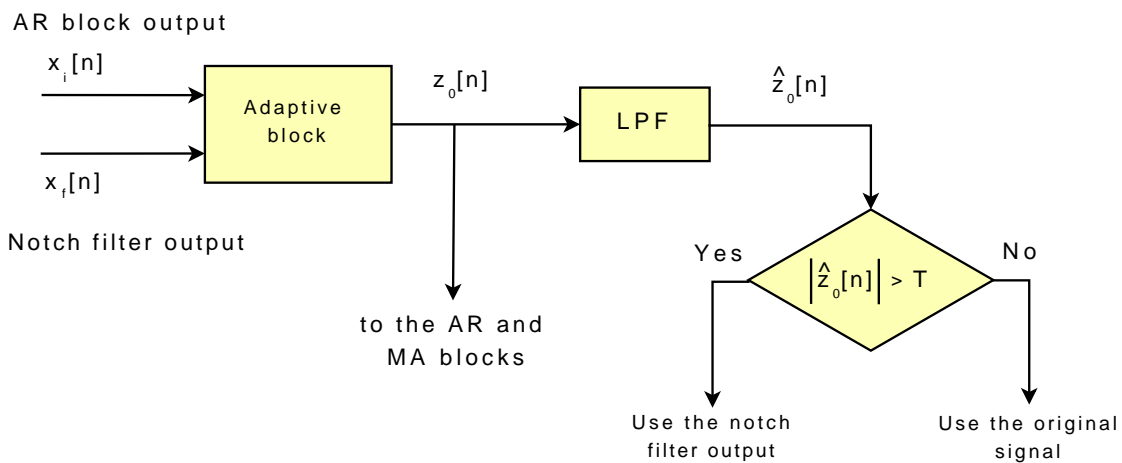


Figure 12.24. Detection algorithm based on the convergence characteristics of the zero of the two-pole notch filter.

12.4 Multi-pole notch filter

When the disturbing signal is given by the sum of several CWIs, namely

$$i[n] = \sum_{k=1}^H A_{INT,k} \cos(2\pi f_{i,k} n T_s + \phi_{i,k}) \quad (12.41)$$

a multi-pole notch filter is required. In Eq. (12.41)

- $A_{INT,k}$ is the amplitude of the k th CWI,
- $f_{i,k}$ and $\phi_{i,k}$ are the frequency and phase of the k th component,
- T_s the sampling interval,
- n is the time index.

A multi-pole notch filter can be obtained by employing several two-pole notch filters in cascade, one for each interfering signal. The first two-pole notch filter in the chain mitigates the most powerful disturbing signal, whereas the other filters remove the other interferers with progressively decreasing power. This solution is not optimal in terms of performance, since the minimization of the output signal power is not achieved globally but by using different stages that work separately. The design of a global adaptive algorithm results very complex and it would not exploit the detection capability of the algorithm proposed on the previous section. The solution of cascading two-pole notch filters coupled with their detection unit is very simple to implement and allows one to activate only the filters that are strictly necessary for removing the interfering signal. In fact, if the number of interferences is less than the number of cells in the chain, the notch filters in excess would distort the useful GNSS signal by removing portions of its spectrum. An easy and efficient solution of the multi-pole notch filter is presented in Figure 12.25. This implementation exploits the detection capabilities of the algorithm proposed above; the excess notch filters are ignored when the interferences are no longer detected in the filtering chain.

12.4.1 Multi-pole notch filter performance

In order to determine the multi-pole notch filters performance, different tests have been performed using both real and simulated data. In this section the test performed by using real GPS samples collected using the NordNav frontend is described. In Figure 12.26 the experimental setup used for testing the multi-pole notch filter is shown. Three CWIs have been simulated and added to the GPS samples collected by the NordNav frontend. Then the resulting signal has been fed to the multi-pole notch filter. In Figure 12.27 the PSD of the signal that enters the multi-pole notch filter is shown. The detection units coupled

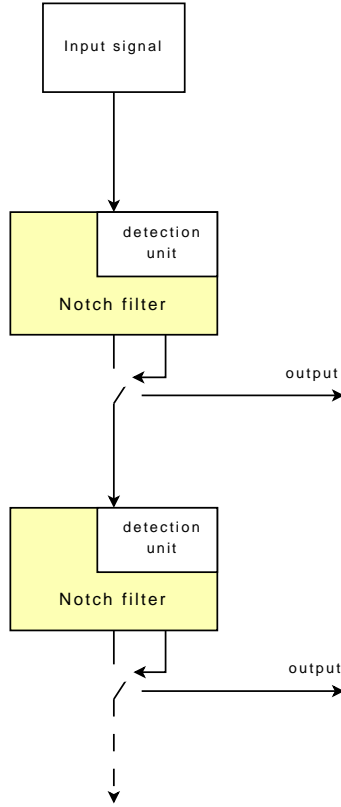


Figure 12.25. Scheme of the multi-pole notch filter.

with the two-pole notch filters correctly activate three mitigation units that progressively remove the three disturbing signals. In order to show how the multi-pole notch filter operates, the outputs of the three active cells have been monitored and their PSDs reported in Figure 12.28. As already stated, the filter cancels the interferers in power order, accordingly to the principle of the minimum output energy. The first peak to be attenuated is the most powerful, then the one with medium power and finally the weakest one. The fact that the third peak is quite weak is reflected in the third notch filter transfer function shown in Figure 12.29: the notch is quite broad and not specially deep; the adaptive algorithm is trying to remove not only the interfering power but also the noise and the useful signal one. The performed tests show the feasibility of the method and its good performances. The detection units activate the correct number of two-pole notch filters and the CW interferences are efficiently removed.

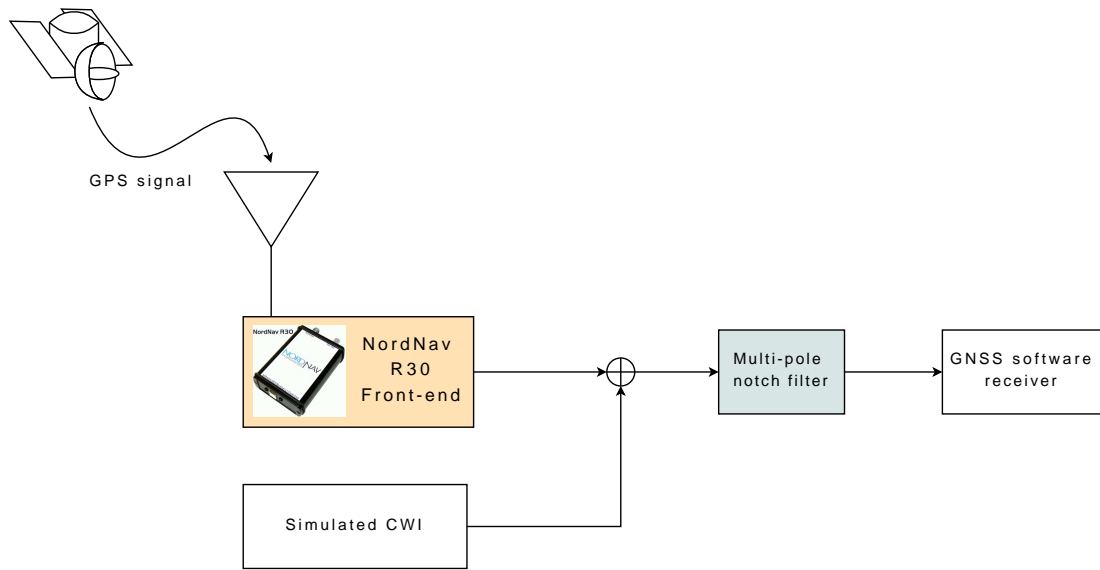


Figure 12.26. Experimental setup used for testing the multi-pole notch filter.

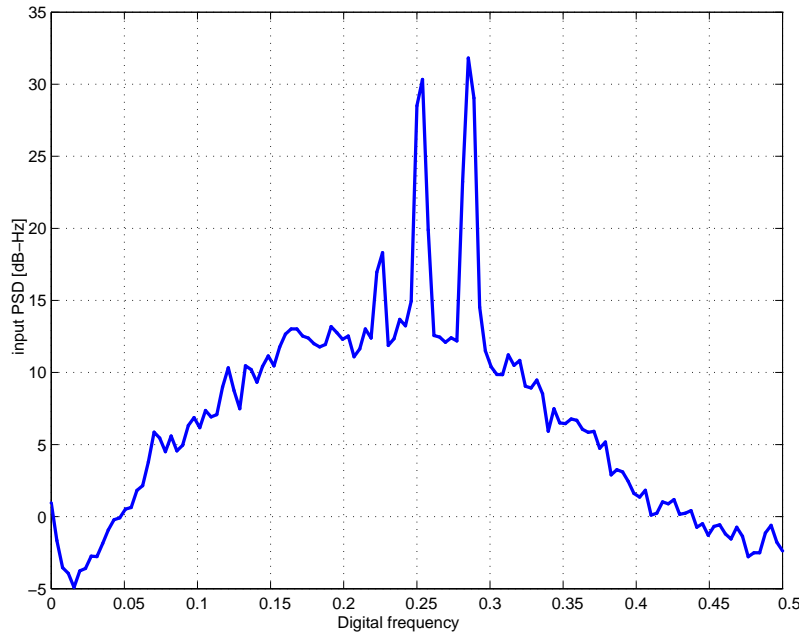


Figure 12.27. Resulting power spectral density of the input signal of the multi-pole notch filter.

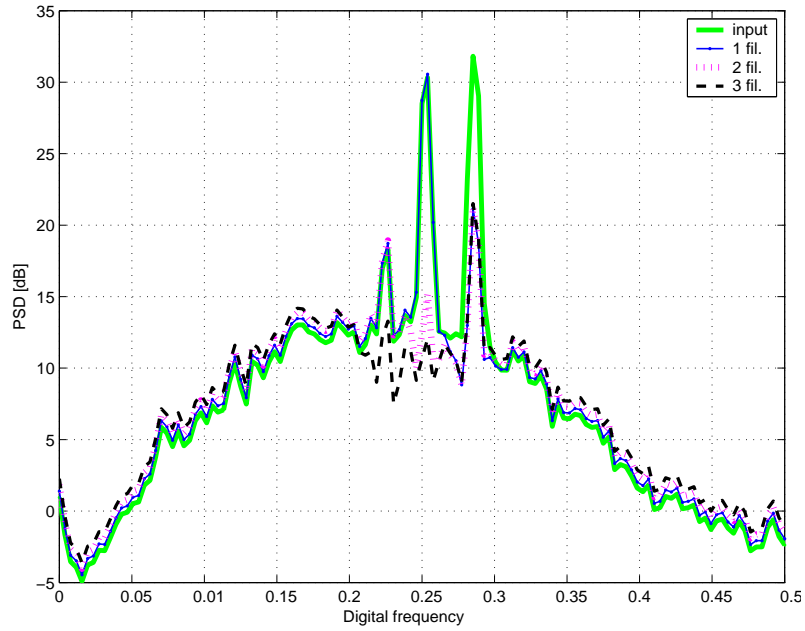


Figure 12.28. Resulting power spectral densities of the output signals of the three two-pole notch filters activated by the detection units.

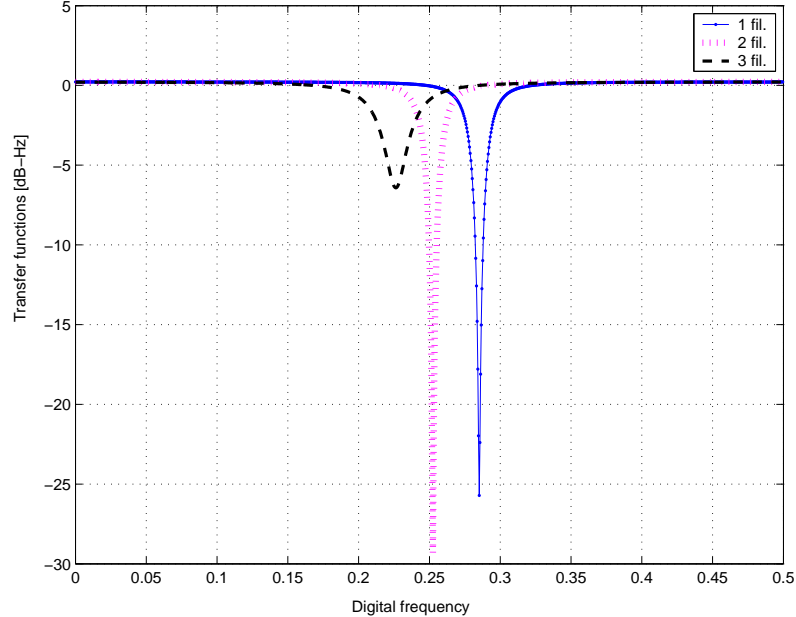


Figure 12.29. Resulting transfer functions of the three notch filters activated by the detection units.

Chapter 13

Time-frequency analysis for interference detection and mitigation

13.1 General Overview

In previous chapters Gaussian narrowband and continuous wave interference have been thoroughly analyzed. However these two classes represent only a small fraction of the possible disturbing signals that can degrade the performance of a GNSS receiver. Due to its weakness, the GNSS signal is subject to interferences that are extremely different in terms of time and frequency characteristics [22]. Thus the design of a general detector/mitigator, able to efficiently deal with different kinds of interference, is a complex problem.

A solution is found through Time-Frequency (TF) analysis [106] that allows to detect and efficiently remove a great variety of disturbing signals. Time-Frequency representations (TFRs) map a one-dimensional signal of time, $x(t)$ into a two-dimensional function of time and frequency, $T_x(t, f)$. In this way the signal is characterized over a time-frequency plane yielding to a potentially more revealing picture of the temporal localization of the signals spectral components.

In the past, great interest has been devoted to TF excision techniques in the context of DSSS communications [107–112]. This interest is justified by the fact that the power of DSSS signals is spread over a bandwidth that is much wider than the original information bandwidth. As a result, DSSS signals present power spectral densities that can be completely hidden under the noise floor and, consequently, only marginally impact the interference detection/estimation on the TF plane.

In the context of GNSS, the use of TF analysis has been limited by the heavy computational load required by these techniques. The length of spreading sequences, up to several thousands of symbols [2, 4], and the consequent memory and computational loads, along with stringent real-time constraints, often leave an extremely limited amount of

computational resources for additional units, for example for interference detection and mitigation. Thus other techniques, less computationally demanding, such as notch filtering [95] and frequency excision [98], have been preferred to TF analysis. However, the use of these detection/mitigation techniques is often confined to a specific class of disturbing signals resulting in a completely ineffective processing for those interferences presenting time/frequency characteristics different from the ones for which the algorithms were designed.

In the literature some TF algorithms have been specifically developed for GNSS applications. However the implementation aspects are often only marginally discussed. [113] proposes a TF detection/excision algorithm for GPS receivers based on the Wigner-Ville distribution. Although the method is promising, [113] does not discuss any implementation issue as well as the computational requirements of the proposed method.

In [114] an excision algorithm based on the Short Time Fourier Transform (STFT) and spectrogram is proposed. The method is implemented by exploiting the structure of the FFT-based acquisition scheme [115] that is suitable only for those receivers that evaluate correlations using the FFT. Moreover the method from [114] does not allow the use of analysis windows different from the rectangular one. The size of the analysis windows is also fixed and corresponds to the FFT size, potentially resulting in spectral leakage [116] and poor TFR's.

In this chapter the use of TF techniques for GNSS interference detection/mitigation is considered. In particular a solution for efficiently implementing TF techniques in GNSS receivers is proposed. This solution is based on the key observation that the acquisition block implicitly performs a sort of TF analysis. More specifically, it is shown that the evaluation of the search space for the delay and Doppler frequency corresponds to the evaluation of a spectrogram, whose analysis window is adapted to the received signal. Thus the adoption of a different analysis window allows for the detection/estimation of disturbing signals. Based on this principle, this method proposes a slight modification of the basic acquisition scheme that allows a fast and efficient TF analysis for interference detection. The method reuses the resources already available for the acquisition stage and the analysis can be performed when the normal acquisition operations shut down or stand temporally idle.

The second part of the chapter is devoted to the design of an efficient TF excision method based on the spectrogram. This method can be implemented by exploiting the structure suggested in the first part of the chapter. Different aspects, not considered in the previous literature, are analyzed, and in particular the performances of the GNSS acquisition block with and without a mitigation unit are studied. Acquisition ROCs have been adopted as metric for establishing the effectiveness of the proposed algorithm. Comparisons with algorithms from the literature are also provided.

13.1.1 Time-Frequency representations

In this thesis two different TF representations, the spectrogram and the Wigner-Ville distribution, are considered.

The discrete time spectrogram of a discrete signal $r[n]$ is defined as [117]

$$S_w(\tau, f) = |\text{STFT}(\tau, f)|^2 \quad (13.1)$$

where $\text{STFT}(\tau, f)$ is the Short-Time Fourier Transform,

$$\text{STFT}(\tau, f) = \sum_{n=0}^{N-1} r[n]w[n-\tau] \exp \{-j2\pi n f\}, \quad (13.2)$$

where $w[n]$ is the analysis window of length L . The spectrogram has poor TF localization properties and its characteristics strictly depend on the analysis windows. However it requires a low computational load and is suitable for real-time applications. Moreover different strategies [109, 118] have been developed in order to select the analysis window that maximizes the localization of the interference on the TF plane.

The discrete time Wigner-Ville distribution is defined as [119]

$$W_{r,r}(n, f) = \sum_i r[n+i] r^*[n-i] \exp \{-j4\pi i f\} \quad (13.3)$$

and does not suffer from the time versus frequency resolution tradeoff problems of the spectrogram. This property is however paid by higher computational requirements and by the possible presence of cross-terms as highlighted in the following.

Since in practice only a finite portion of the signal $r[n]$ is available for the evaluation of the Wigner-Ville distribution, then Eq. (13.3) should be rewritten as

$$\bar{W}_{r,r}(n, f) = \sum_i r[n+i] w[n+i] r^*[n-i] w^*[n-i] \exp \{-j4\pi i f\} \quad (13.4)$$

where $w[n]$ is a window of finite duration that selects the portion of $r[n]$ available for the computation of Eq. (13.3). In Figure 13.1 an example of a spectrogram and a Wigner-Ville distribution of a signal with sinusoidal frequency modulation is presented. The Wigner-Ville distribution better localizes the signal on the TF plane, even if the presence of cross-terms due to the interaction of the different signal components is more evident.

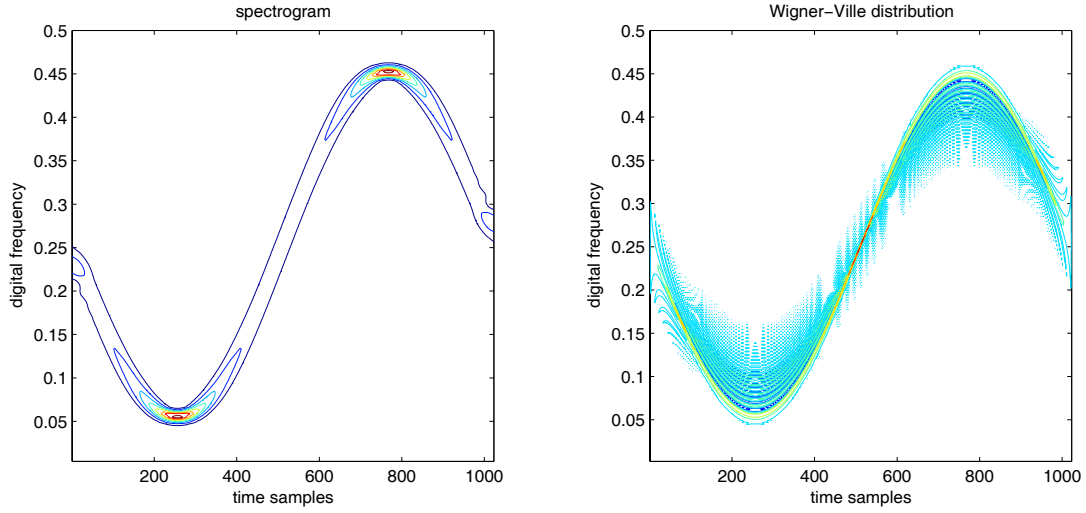


Figure 13.1. Spectrogram and Wigner-Ville distribution of a signal with sinusoidal frequency modulation. The spectrogram has been evaluated by using a Hamming window of length $L = 127$ samples.

13.2 Reconfigurable GNSS Acquisition Scheme for Time-Frequency Applications

By combining Eqs. (13.1) and (13.2) the following expression for the spectrogram is obtained:

$$S_w(\tau, f) = \left| \sum_{n=0}^{N-1} r[n]w[n-\tau] \exp\{-j2\pi n f\} \right|^2. \quad (13.5)$$

By comparing Eq. (13.5) with the complex representation of the CAF discussed in Chapter 3 and reproduced here for the sake of clarity

$$S(\tau, F_D) = \left| \frac{1}{N} \sum_{n=0}^{N-1} r[n]c[n-\tau] \exp\{-j2\pi F_D n\} \right|^2, \quad (13.6)$$

it clearly emerges that the decision variable for the acquisition block is a spectrogram scaled by the factor $1/N^2$ and with

$$w[\tau] = c[\tau], \quad (13.7)$$

that is with the analysis window adapted to the GNSS signal. Since $S(\tau, F_D)$ and $S_w(\tau, f)$ have basically the same structure, the same functional blocks used for evaluating $S(\tau, F_D)$ can be employed for determining $S_w(\tau, f)$. Thus, by replacing the local code with an appropriate analysis window and by opportunely changing the interval of Doppler frequencies under test, the acquisition block can be easily employed for TF applications.

13.2.1 Modified acquisition block

As already discussed in Chapter 3 different acquisition schemes are employed for determining a first, rough estimation of the code delay and Doppler frequency of the signal emitted by the satellite under analysis. These methods can be classified in three main classes:

- the classical serial search acquisition scheme [4,120] that evaluates the search space cell by cell, subsequently testing the different values of code delay and Doppler shift,
- the frequency domain FFT acquisition scheme [32], that exploits the FFT to evaluate all the Doppler frequencies in parallel. In this scheme an Integrate and Dump (I&D) block can be used in order to reduce the frequency points to be evaluated by the FFT. The use of the FFT implies the analysis of frequency points outside the Doppler range,
- the time domain FFT acquisition scheme [115], that uses the FFT to compute fast code circular convolution.

In this section those three acquisition schemes are adapted in order to allow TF frequency applications.

The main differences between the decision variable (13.6) and the spectrogram (13.5) are as follows:

- the set of Doppler frequencies searched for during the acquisition process is usually limited to a few kHz around the receiver intermediate frequency, whereas the spectrogram needs to be evaluated for a wider range of frequencies,
- the spectrogram and the decision variable $S(\tau, F_D)$ employ two different analysis windows.

In order to reuse the acquisition computational resources for TF applications, these two differences have to be overcome. This can be easily achieved by introducing a window generator able of producing an analysis window for the TF analysis. The window generator can be either a memory bank or a digital device producing signals used as analysis window. Different analysis windows [116] can be stored in the memory bank and different window lengths can be obtained by means of down-sampling: in the memory bank the full length version of an analysis window is stocked; when a shorter window is needed to increase the spectrogram time resolution, a new window is produced by down-sampling the original one and adding the corresponding number of zeros. The simplest digital device producing analysis windows can be a generator of the signal

$$w[n] = \begin{cases} 1 & \text{for } n = 0, 1, \dots, L - 1 \\ 0 & \text{for } n = L, \dots, N - 1 \end{cases} \quad (13.8)$$

where L and N are the window and the local code length, respectively. Notice that varying the window length, the time-frequency resolution changes and different window lengths can be suitable for different kinds of interference. The window signal $w[n]$ should have the same length of the received signal $r[n]$ and of the local code $c[n]$, since the correlation is usually evaluated by multiplying two signals of the same length and integrating the result. A selector is used to switch from the normal acquisition mode to the TF one: in this way the local code $c[n]$ is substituted by the signal $w[n]$.

The delay τ , used to progressively shift the window analysis in Eq. (13.5) can assume values that are not in the set usually used for the search space computation. The frequency

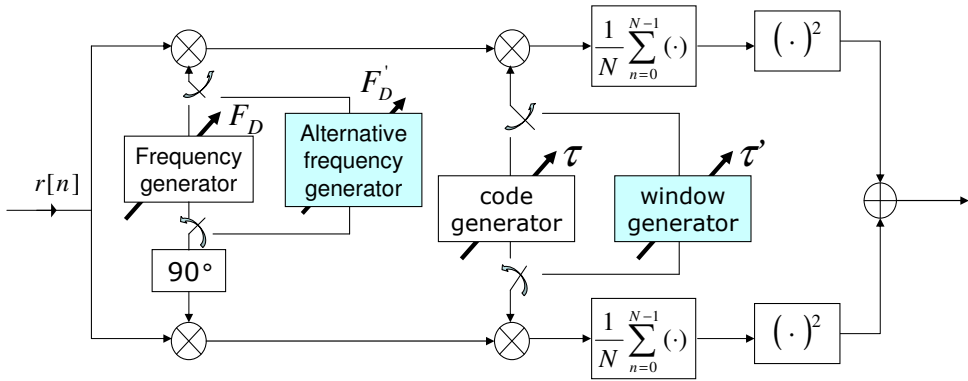


Figure 13.2. Modified serial search acquisition. The traditional serial search acquisition scheme has been modified in order to explore a wider range of Doppler frequencies and to allow the use of specific analysis windows for TF applications.

range can be extended by changing the initial frequency, the frequency step Δf and the number of frequency bins K_B . This can be achieved by adopting a frequency generator specifically designed for exploring a wider range of frequencies. The choice of increasing the number of Doppler bins results a greater computational load whereas an exceedingly large frequency step Δf can result in a spectrogram poorly represented along the frequency dimension. For this reason a compromise between frequency representation and computational load can be reached by changing both the Doppler step and the number of frequency bins. In Figures 13.2, 13.3 and 13.4 the traditional acquisition schemes have been modified, introducing a window generator and an alternative frequency generator, allowing the evaluation of the spectrogram. It is noted that the parallel acquisition scheme in the frequency domain does not require an alternative frequency generator, since the use of the FFT for exploring the Doppler dimension already allows to analyze frequency points outside the Doppler range. In this case the range of frequency under analysis depends on M , the number of points integrated by the I&D block.

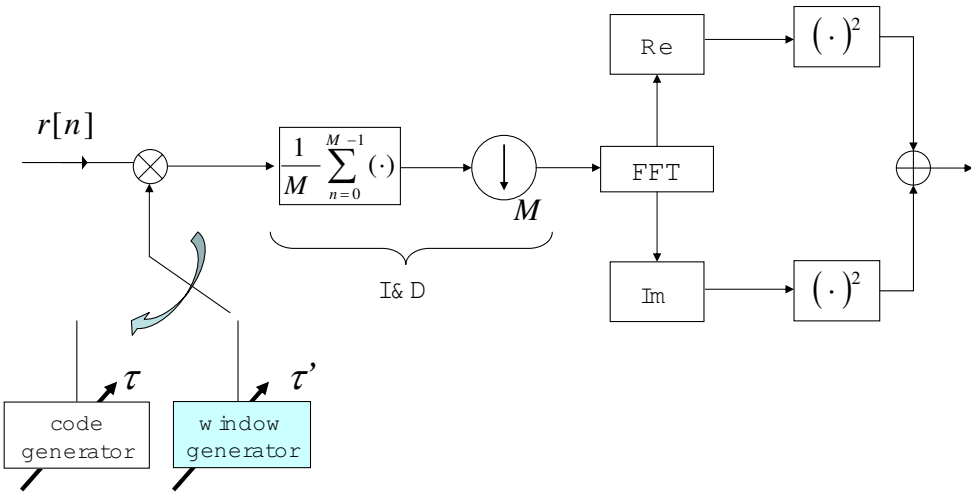


Figure 13.3. Modified parallel acquisition in the frequency domain. The parallel acquisition scheme has been modified allowing the use of specific analysis windows for TF applications.

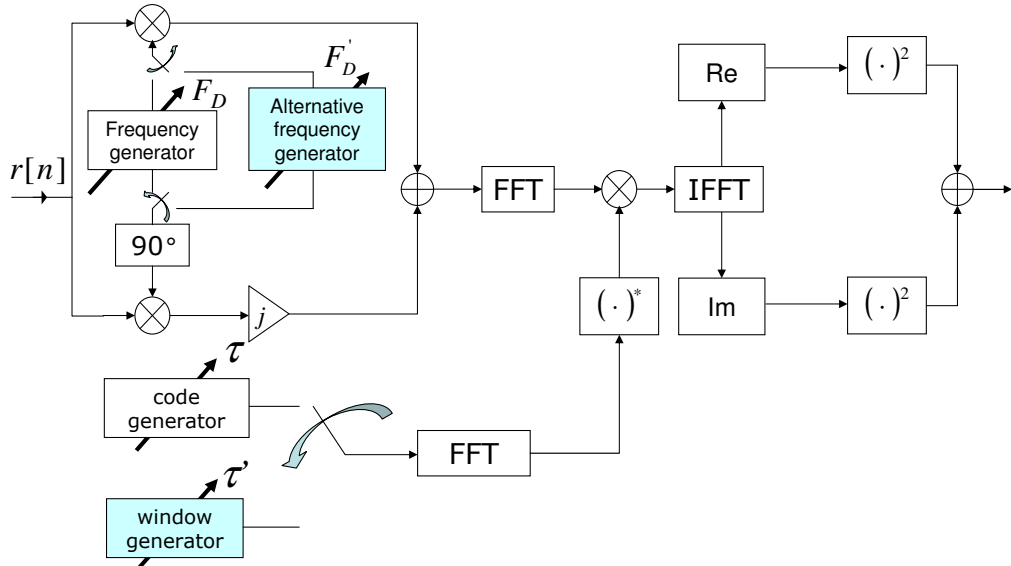


Figure 13.4. Modified parallel acquisition scheme in the time domain. The parallel acquisition scheme has been modified in order to explore a wider range of Doppler frequencies and to allow the use of specific analysis windows for TF applications.

13.2.2 Real data and simulation tests

In order to show the effectiveness of the proposed acquisition scheme some examples based on simulated and real data are reported herein.

Real data have been collected by using the NordNav-R30TM frontend [1] that is characterized by the specifications reported in Table 13.1. Data collection has been performed

Table 13.1. NordNav-R30 characteristics.

Sampling Frequency	$f_s = 16.3676 \text{ MHz}$
Intermediate Frequency	$f_{IF} = 4.1304 \text{ MHz}$
Signal quantization	4 bits
Front-end filter bandwidth	$\approx 2 \text{ MHz}$

at two different sites: the so called “colle della Maddalena” and the hill of the “Basilica di Superga”. These sites are located on two different hills in the surroundings of Torino (Italy). The first one is characterized by the presence of several antennas for the transmission of analog and digital TV signals, whereas the second one is in direct view of the colle della Maddalena antennas. Two different kinds of interference have been observed. In the proximity of the colle della Maddalena, the GPS signal was corrupted by a swept interference, whereas a strong CWI was observed on the hill of Superga.

In Figure 13.5 the spectrogram of the swept interference observed in the proximity of the colle della Maddalena is shown. This spectrogram has been evaluated by employing the modified parallel acquisition scheme in the time domain described in previous section. The input signal has first been downsampled by a factor of 4, reducing the sampling frequency to $f_s = 4.0919 \text{ MHz}$. This operation reduces the computational load without effectively degrading the signal quality since the NordNav frontend is characterized by a bandwidth of about 2 MHz. The Doppler step has been set to 10 kHz and the number of Doppler bins was $K_B = 201$. A Hamming window of duration $T_w = \frac{N}{10}$ was employed. The analysis was extended to a signal portion of 10 ms. The presence of the swept interference clearly emerges from Figure 13.5, that can be easily used for the estimation of the interference instantaneous frequency. The information extracted from the spectrogram in Figure 13.5 can then be easily used for different excision algorithms [108,111]. In Figure 13.6 the PSD of the input signal has been reported. In Figure 13.6 a) the PSD has been estimated by considering the downconverted GPS signal with a sampling frequency $f_s = 16.3676 \text{ MHz}$: in this case the interference spectral components clearly emerge, although they are spread over a band of more than 1 MHz. In Figure 13.6 b) the PSD of the signal used for the evaluation of the spectrogram in Figure 13.5 has been depicted. In this case the interference cannot be easily localized in the frequency domain, proving the effectiveness of TF detection techniques versus traditional pure frequency detection methods.

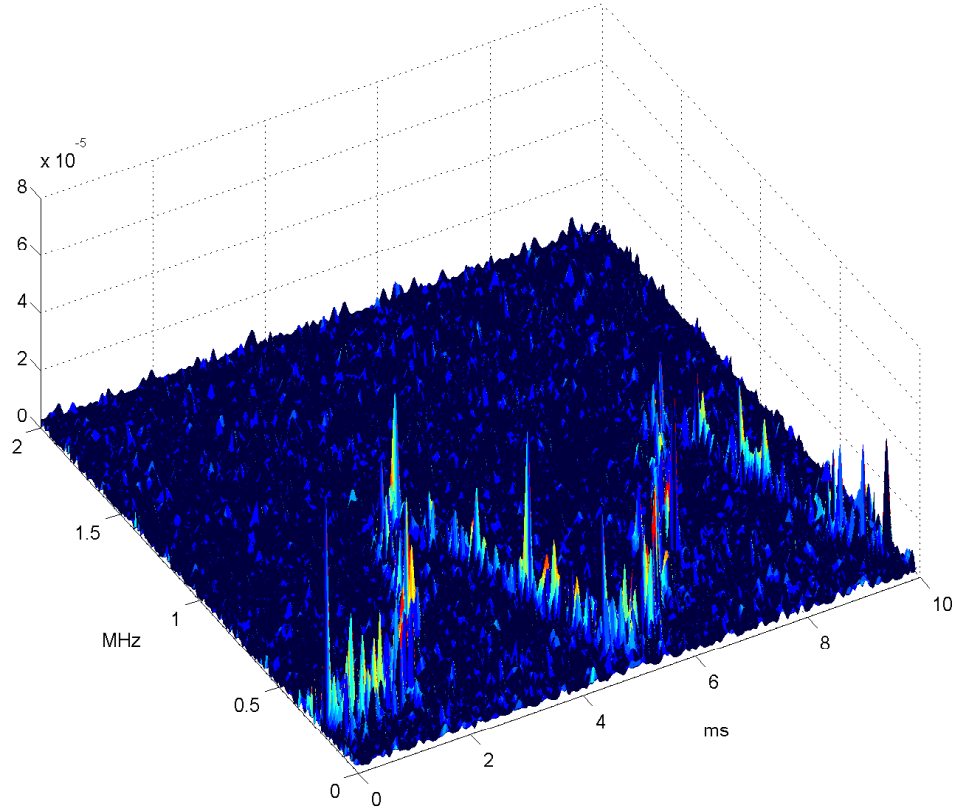


Figure 13.5. Spectrogram of a swept interference. The input signal has been collected by using the NordNav R30 frontend in the proximity of TV repeaters. The spectrogram has been evaluated by using the modified parallel acquisition scheme in the time domain.

In Figures 13.7 and 13.8 the spectrogram and the PSDs of the signal observed at the hill of Superga are depicted. In this case the CWI is well localized in both TF and frequency domains. The spectrogram has been evaluated by using the modified parallel acquisition scheme in the time domain, with a Hamming window of duration $T_w = \frac{N}{8}$. As for the first case, the Doppler step has been set to 10 kHz and the number of Doppler bins was $K_B = 201$.

In order to further test the modified acquisition scheme for TF interference detection, the case of pulsed interference has been considered. In particular GPS signals in the presence of pulsed interference have been simulated and analyzed with the modified parallel acquisition scheme in the time domain. The same sampling frequency and intermediate

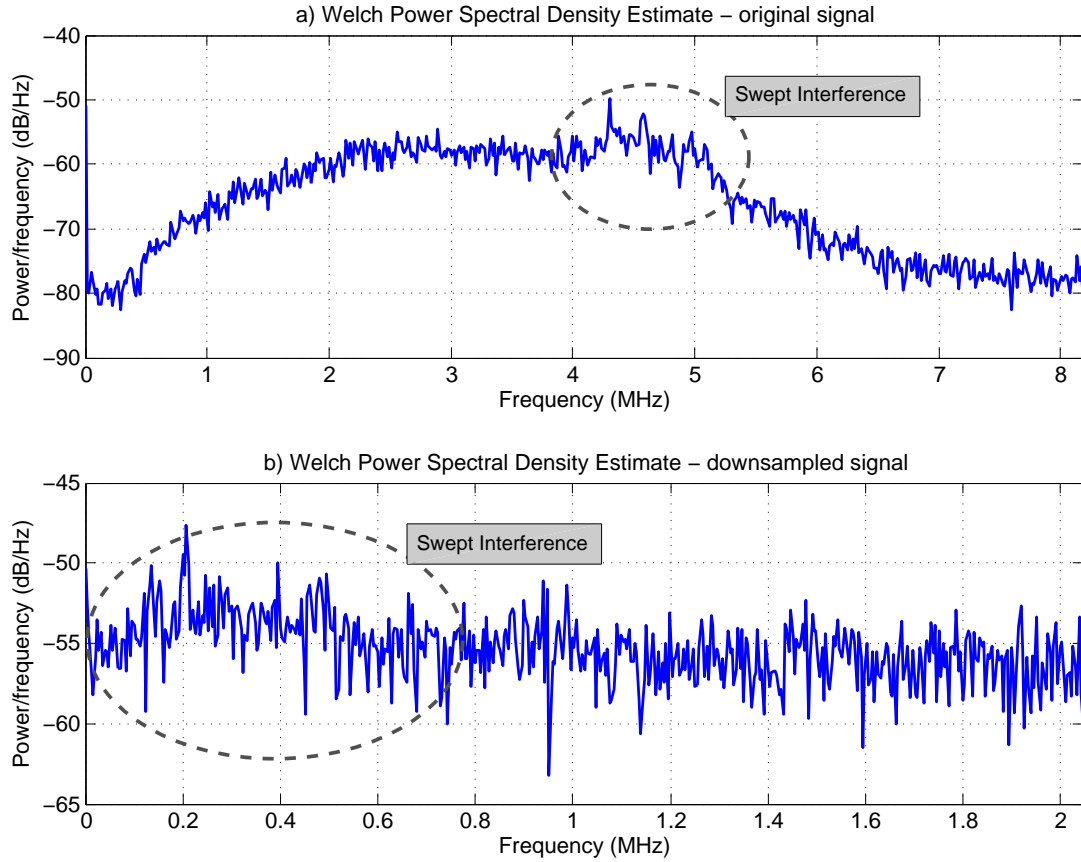


Figure 13.6. Power Spectral density estimates of the input signal used for the evaluation of the spectrogram in Figure 13.5. a) PSD of the original signal, sampling frequency $f_s = 16.3676$ MHz. b) PSD of the downsampled signal, sampling frequency $f_s = 4.0919$ MHz.

frequency of Table 13.1 have been adopted for the simulation. Pulsed interference can be generated by different sources such as Distance Measuring Equipment (DME) and Tactical Airborne Navigation (TACAN) [78] that are currently used for distance measuring and for civil and military airborne landing. The pulsed interference has been simulated as a pair of modulated Gaussian impulses [78]. The results of the test have been depicted in Figure 13.9, where the case of impulses with a peak power equal to the noise variance has been considered. In the bottom part of Figure 13.9 the time representation of the input signal is shown. The light line represents the envelope of the pulsed interference that cannot be directly identified from the time representation of the input signal. When the TF representation is considered the pulsed interference is clearly identified, allowing

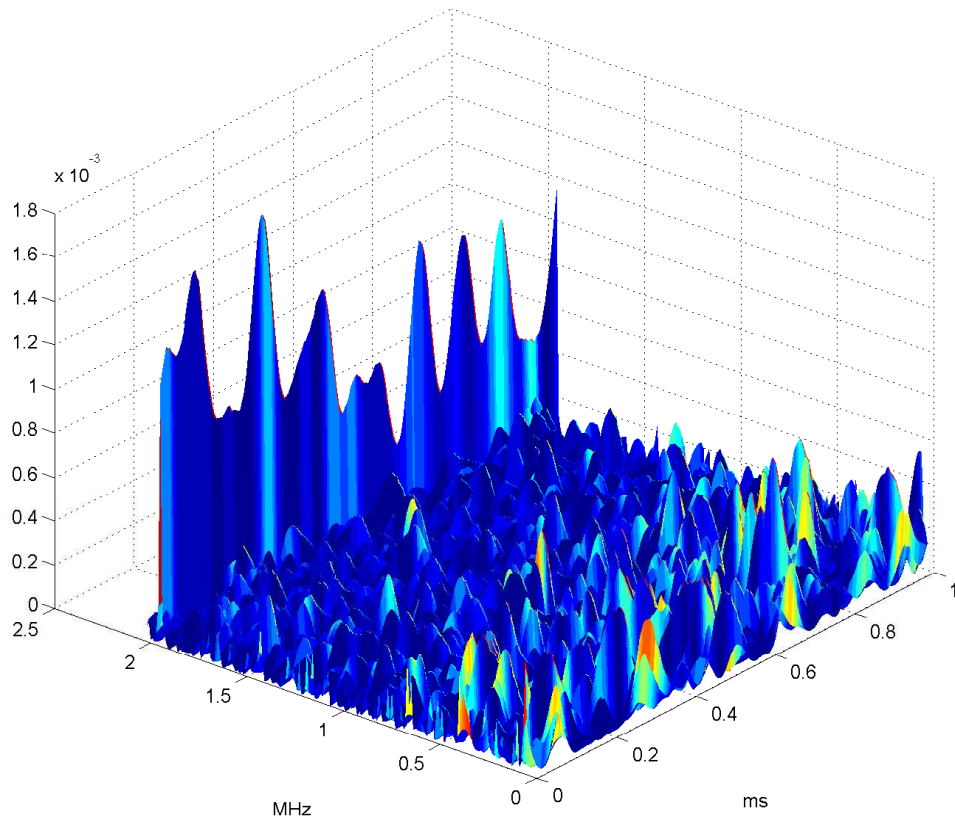


Figure 13.7. Spectrogram of a CWI. The input signal has been collected by using the NordNav R30 frontend. The spectrogram has been evaluated by using the modified parallel acquisition scheme in the time domain.

the efficient excision of the disturbing signal. The spectrogram of Figure 13.9 has been evaluated by using the modified parallel acquisition scheme in the time domain, with a Hamming window of duration $T_w = \frac{N}{64}$. The Doppler step has been set to 200 kHz and the number of Doppler bins at $K_B = 41$.

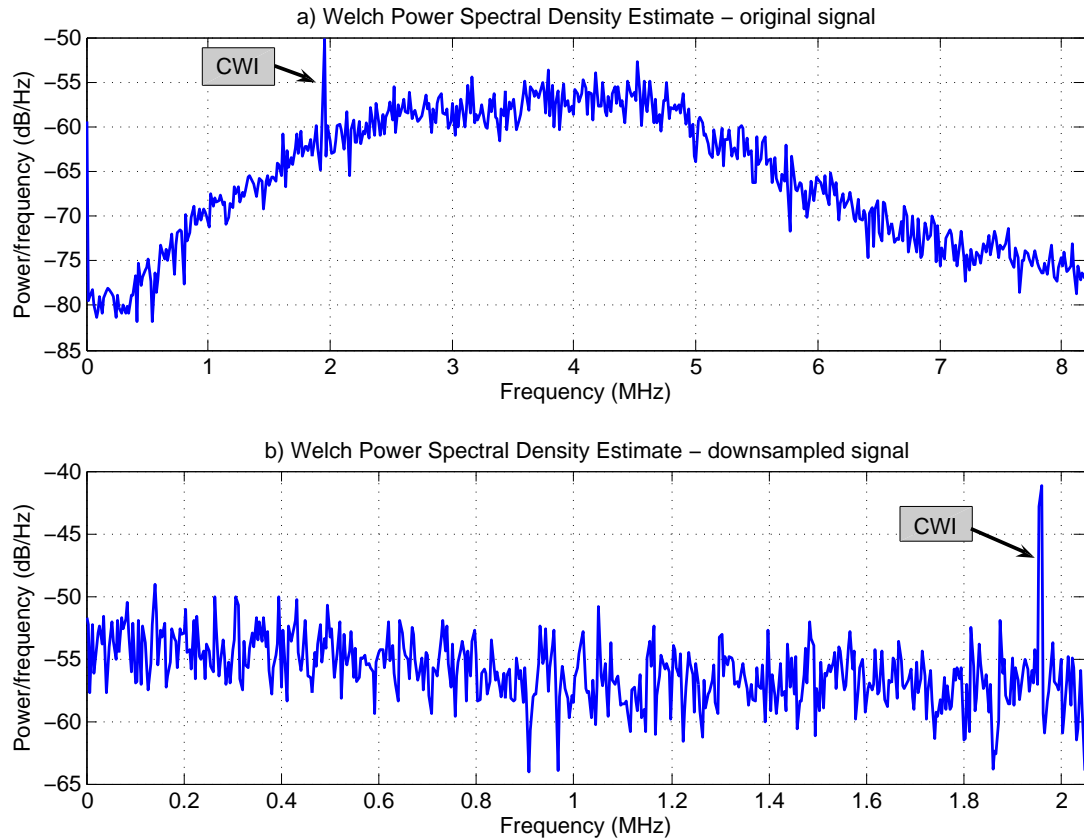


Figure 13.8. Power Spectral density estimates of the input signal used for the evaluation of the spectrogram in Figure 13.7. a) PSD of the original signal, sampling frequency $f_s = 16.3676$ MHz. b) PSD of the downsampled signal, sampling frequency $f_s = 4.0919$ MHz.

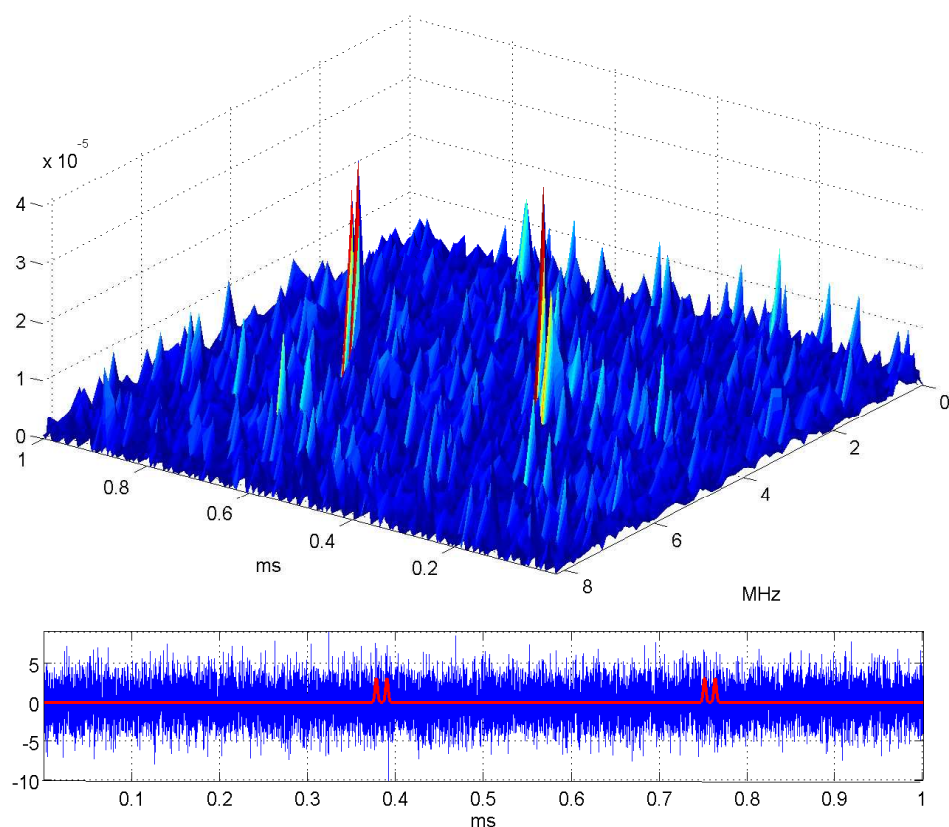


Figure 13.9. Spectrogram and time domain representation of a simulated GPS signal corrupted by pulsed interference. The spectrogram has been evaluated by using the modified parallel acquisition scheme in the time domain.

13.3 A Time-Frequency Excision Algorithm

TF excision techniques usually rely on the estimation of the interference instantaneous frequency [106]. This information is used to control the coefficients of an excision filter that adaptively removes the disturbing signal [107–109]. An alternative approach [111] consists of using the instantaneous frequency estimation to downconvert the interference around the zero frequency. A time-invariant high-pass filter is then used to remove the jammer, and the original frequency content of the received signal is restored.

In this context a TF excision algorithm that is a further development of [111] is proposed. TFRs are used for estimating the instantaneous frequency of the interference, that is excised by a notch filter. Different aspects, not considered in the previous literature, are analyzed, and in particular the performances of the acquisition block with and without mitigation are studied.

The general scheme of the proposed interference excision unit is reported in Figure 13.10.

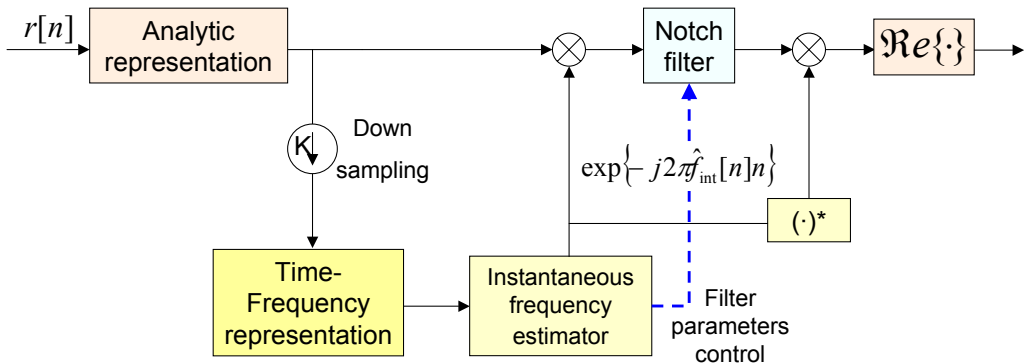


Figure 13.10. Functional scheme of the TF excision algorithm consisting of three blocks: TF representation, instantaneous frequency estimation unit and notch filter.

At first the analytic representation of the received signal is evaluated as

$$r_h[n] = r[n] + j\hat{r}[n] \quad (13.9)$$

where $\hat{r}[n]$ is the Hilbert transform of $r[n]$ [121]. The analytic signal $r_h[n]$ has components belonging only to the half plane of positive frequencies and its use is necessary for avoiding the presence of cross-terms on the TF representation. These cross-terms would be generated by the interaction between positive and negative frequency components, if the real signal $r[n]$ were employed [106].

Before entering the TF representation unit, $r_h[n]$ can be decimated by a factor K as

$$r_a[n] = r_h[Kn] \quad (13.10)$$

By decimating the signal $r_h[n]$ it is possible to reduce the computational load required by the TFR. However the decimation can introduce aliasing and distortions and thus a compromise has to be found.

The signal $r_a[n]$ enters the TF representation unit, that allows the estimation of the interference instantaneous frequency by the subsequent unit. The estimated instantaneous frequency $\hat{f}_{int}[n]$ is employed to downconvert the interference component around the zero-frequency. The jammer is then excised by a notch filter and the original frequency content is restored. At the end only the real part of the obtained signal is considered and the output signal is fed into the acquisition block.

The three functional blocks of the proposed method can be implemented by using different techniques. For example, in [111], the Wigner-Ville distribution was used as TF representation and the parameters that maximize the Hough Transform [122] of the Wigner-Ville employed for the instantaneous frequency estimation.

The TFRs adopted in this thesis for implementing the proposed methods are the spectrogram and the Wigner-Ville distributions described in Section 13.1.1.

A simple algorithm called peaks-interpolation is used for estimating the interference instantaneous frequency. This algorithm simply selects, for each time instant, the maxima of the TF representation, and interpolates them to produce an estimation of the interference frequency. This algorithm relies on the hypothesis that the interference is present and that its instantaneous frequency can be effectively approximated by a specific model. This model is then used for interpolating the maxima of the TF representation. Although this hypothesis is quite restrictive, it is usually adopted in the literature [111]. Furthermore the interference presence can be determined by monitoring the input signal power or by using other techniques spread in the GNSS context.

For instance, if the interference can be approximated by a chirp, the peaks-interpolation technique estimates the parameters that define the interference frequency as

$$\left[\hat{f}_i^0; \hat{a}_i \right] = \arg \min_{f, a} \left\| \vec{Y} - f - a \vec{X} \right\|^2 \quad (13.11)$$

where \vec{Y} and \vec{X} are the vectors of the coordinates of the TF maxima.

In [111] a simple FIR filter characterized by the transfer function

$$H_b(z) = 1 - z^{-1} \quad (13.12)$$

has been employed. However this kind of high-pass filter introduces a wide notch that results in extreme degradation of the useful signal quality.

This clearly emerges from Figure 13.11, where the transfer function of the filter defined by Eq. (13.12) is reported: all frequencies are distorted and the useful signal is compromised.

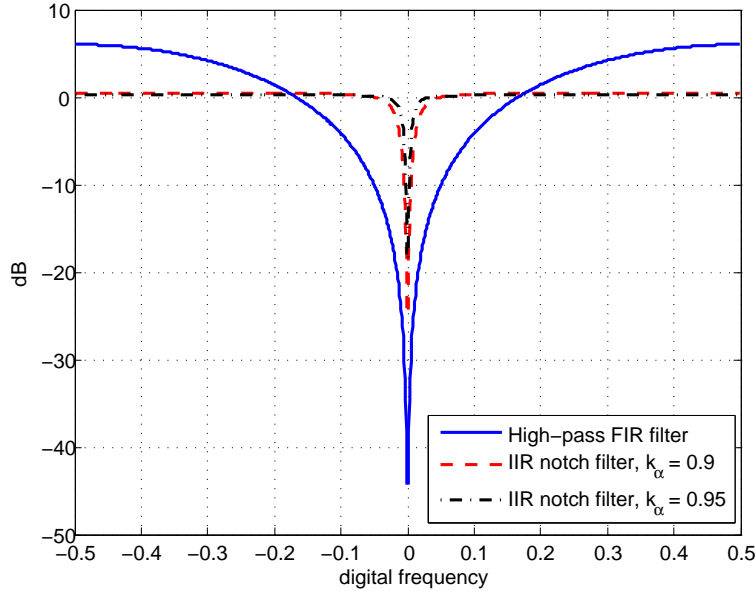


Figure 13.11. Transfer functions of the different excision filters.

In order to overcome this problem a IIR notch filter with the same structure of one-pole notch filter analyzed in Section 12.2 and defined by

$$H_n(z) = \frac{1 - z^{-1}}{1 - k_\alpha z^{-1}} \quad (13.13)$$

has been used. It is noted that the contraction factor k_α can be regulated by the information provided by the peaks-interpolation algorithm. In fact the mean square error resulting from the interpolation process indicates how much the interference samples are close to the interpolating curve. A high mean square error implies that the interference is spread around the interpolating curve and consequently a wide notch is required for effectively removing the disturbing signal.

In order to highlight the effectiveness of the notch filter (13.13), three different correlations have been reported in Figure 13.12. A linearly frequency modulated signal has been added to a BOC(1,1) signal characterized by a code of period 4092 and with a sampling rate of 4 samples per chip. The simulated signal is noise-free for better highlighting the excision filter impact on the correlation. When the mitigation unit is not present, interference makes the secondary lobes rise, potentially preventing the right detection of the correlation peak in the presence of noise. When the excision unit is active the jammer is excised and the secondary lobes are clearly reduced; however, when the simple FIR filter proposed by [111] is employed, the mean correlation peak is heavily distorted and thus the IIR notch filter is preferable. In this section the performance of the TF excision

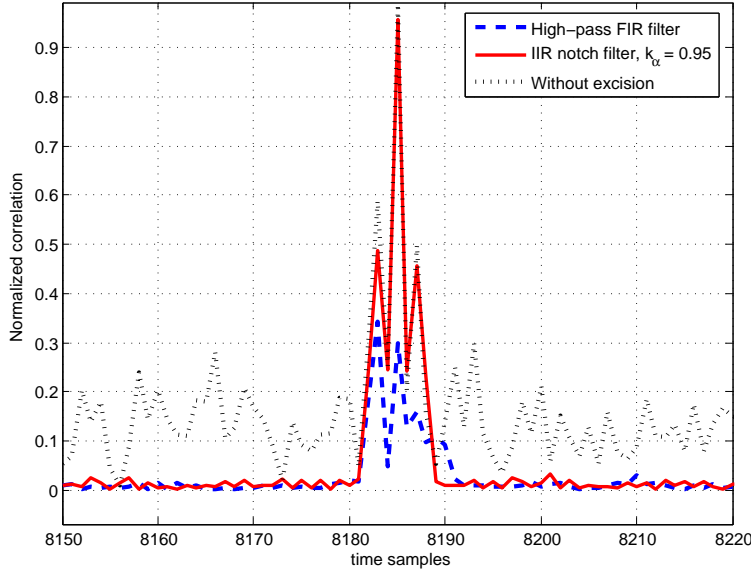


Figure 13.12. Correlations of a BOC(1,1) signal in the presence of interference only. A linearly frequency modulated signal has been added to the GNSS signal and processed with the excision algorithm. The notch filter clearly outperforms the FIR filter proposed in [111].

algorithm is analyzed. More specifically the proposed algorithm is compared with the methodology developed in [111], which is based on the Wigner-Ville distribution and on the Radon-Hough transform. Different criteria are used for assessing the performance of the TF algorithm. The quality of the IF estimation is determined through its Root Mean Squared Error (RMSE), whereas the acquisition performance is evaluated by means of ROCs. The impact of the excision algorithm is further highlighted by comparing the ambiguity functions evaluated when the anti-jamming device is sequentially on and off.

The scenario adopted for the simulation is characterized by the parameters reported in

Table 13.2. Simulation parameters.

Parameter	Value
GNSS code	GPS C/A code
Sample rate	4 samples/chip
Sampling frequency	4.092 MHz
Coherent integration time	1 ms
Intermediate frequency	38.5 kHz
Spectrogram analysis window	Hamming
Analysis window length	64 samples

Table 13.2 and consists of a GNSS signal in zero mean Gaussian noise corrupted by a constant amplitude linearly frequency modulated interference (chirp). The choice of such an interference is common in the literature [110, 111] and it has therefore been employed as test bench for the TF excision algorithm.

The instantaneous frequency of a chirp signal can be expressed as

$$f_i[n] = f_i^0 + a_i n \quad (13.14)$$

where f_i^0 is the initial interference frequency and a_i is the interference frequency drift. In Figure 13.13 the spectrogram of the signal used for simulations is depicted. The dis-

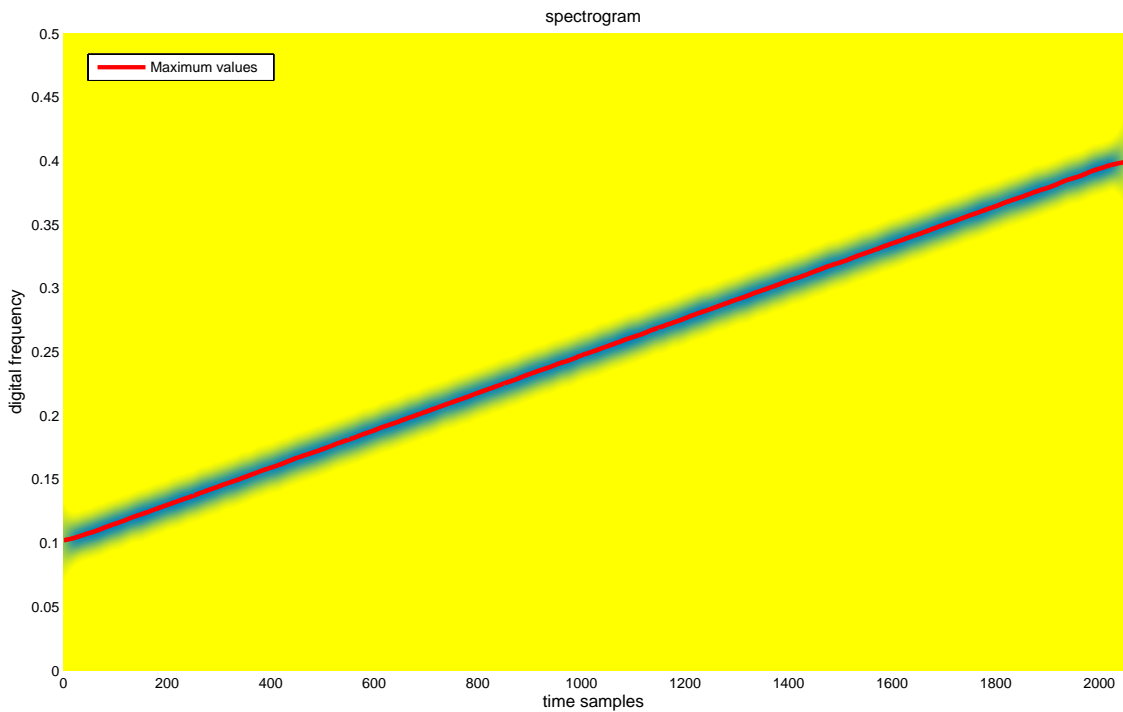


Figure 13.13. Spectrogram of simulated GPS signal in zero mean Gaussian noise and chirp interference. $C/N_0 = 36$ dB-Hz, $J/N = 10$ dB.

turbing signal clearly emerges from the TF plane and thus its instantaneous frequency can be easily estimated. In Figure 13.14 the Wigner-Ville distribution of the same signal is depicted. In order to detect the interference presence, the IF estimator is applied to the spectrogram of Figure 13.13 and to the Wigner-Ville distribution of Figure 13.14, respectively. The detection is performed taking the maximum values of the TFR.

In Figure 13.15 the RMSE of the interference frequency estimation provided by the peaks-interpolation algorithm is depicted as a function of the number of samples used for the TFR. The error is less than 6 kHz for all the used samples. This value is acceptable

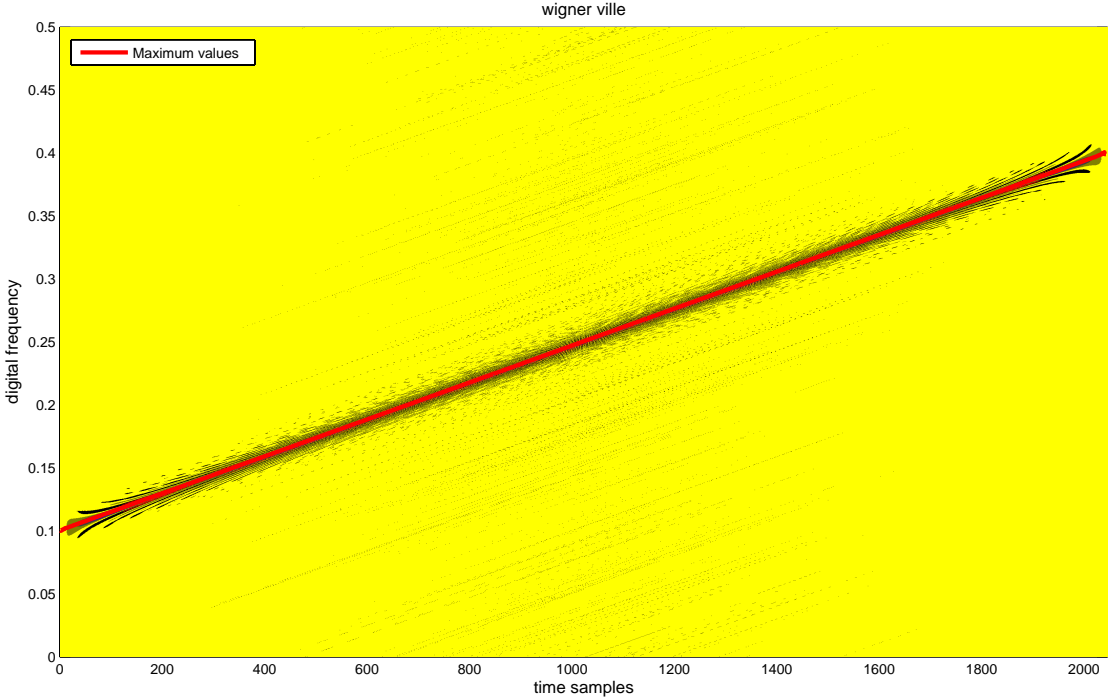


Figure 13.14. Wigner-Ville distribution of simulated GPS signal in zero mean Gaussian noise and chirp interference. $C/N_0 = 36$ dB-Hz, $J/N = 10$ dB.

since it is small enough to insure good mitigation. The Wigner-Ville distribution provides a lower error, demonstrating the degradation caused by the spectrogram on the peaks-interpolation performance. Anyhow the two curves of Figure 13.15 are comparable in terms of RMSE and this justifies the choice of the spectrogram for the rest of the analysis due to its lower computational complexity. In Figure 13.16 the RMSE for the spectrogram case is depicted as a function of the J/N . The error is less than a few kHz also for low J/N , and decreases as the J/N increases. Four different C/N_0 values have been considered, however the impact of the GNSS signal on the estimation process is only marginal and the peaks-interpolation error is almost constant with respect to the C/N_0 .
 In order to test the behavior of the excision unit, and in particular the impact of an IIR filter, ROCs under different working conditions have been evaluated by Monte Carlo simulations. In Figure 13.17 the true interference frequency has been used to downconvert the disturbing signal. As expected the presence of an excision unit extremely increases the system performance. Moreover, the higher the k_α , i.e. the more the pole-contraction factor approaches unity, the more the performance approaches to the ideal one, in absence of interference. The performance obtained by using the FIR filter proposed by [111] ($k_\alpha = 0$) results clearly worse than the one achievable by employing the IIR filter (13.13). This proves that the use of IIR notch filters very significantly increases the acquisition

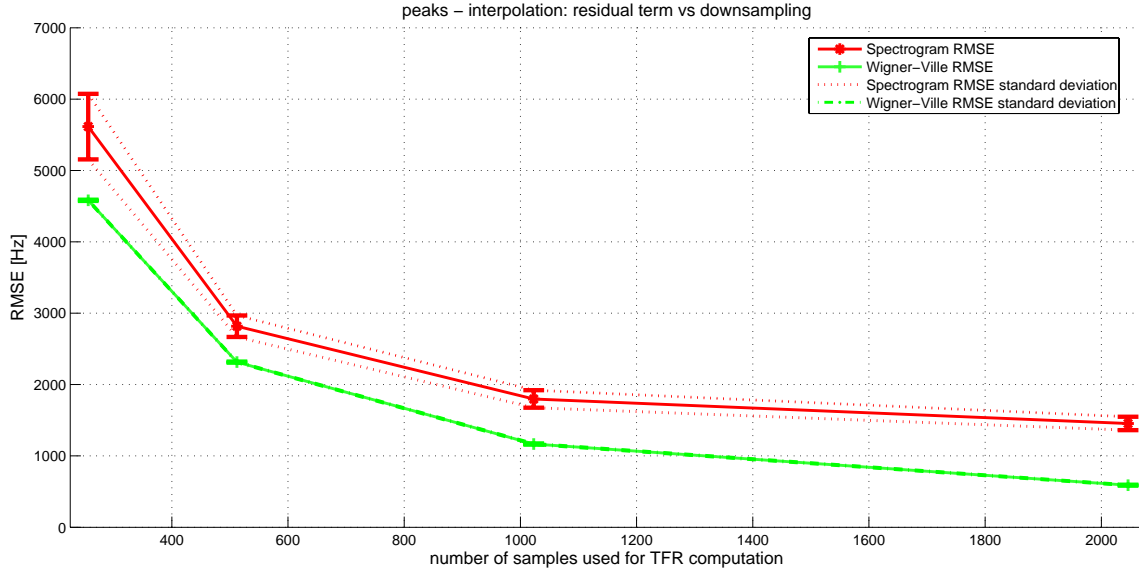


Figure 13.15. Peaks-interpolation performances in terms of RMSE vs the number of samples used for the TFR.

performance and that the GNSS signal is not essentially impacted by the correlation introduced by this kind of filters. In Figure 13.18 the interference IF has been recovered by using either the peaks-interpolation technique in conjunction with the spectrogram or the Radon transform in conjunction with the Wigner-Ville distribution [111]. Both estimation techniques cause a slight degradation of the ROCs, however, in the case analyzed in Figure 13.18, the peaks-interpolation algorithm provides a better performance. Finally, in Figures 13.19 and 13.20, the impact of the excision unit on the ambiguity function is shown. In this case, an excision filter with $k_\alpha = 0.95$ has been used and the interference frequency has been estimated by using the peaks-interpolation technique. When the excision unit is active the jammer is effectively removed and the signal peak clearly emerges from the noise floor of the ambiguity function, allowing correct signal acquisition.

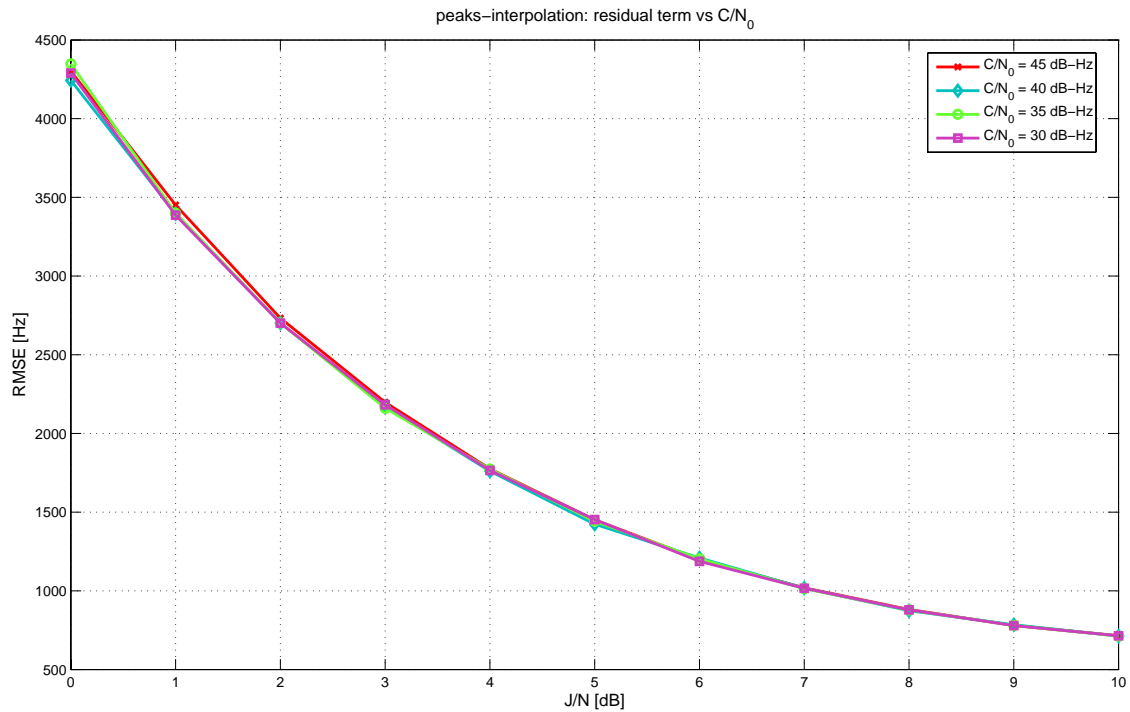


Figure 13.16. Mean squared error of the interference frequency estimation provided by the peaks-interpolation algorithm vs the J/N .

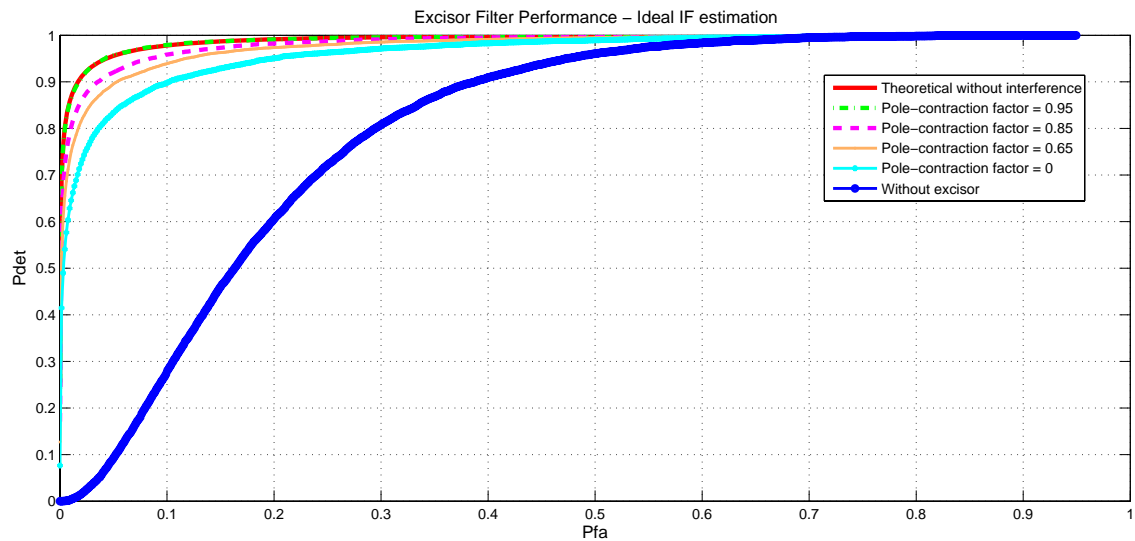


Figure 13.17. ROC curves for different pole contraction factors with an ideal IF estimation. $C/N_0 = 36 \text{ dB-Hz}$, $J/N = 10 \text{ dB}$.

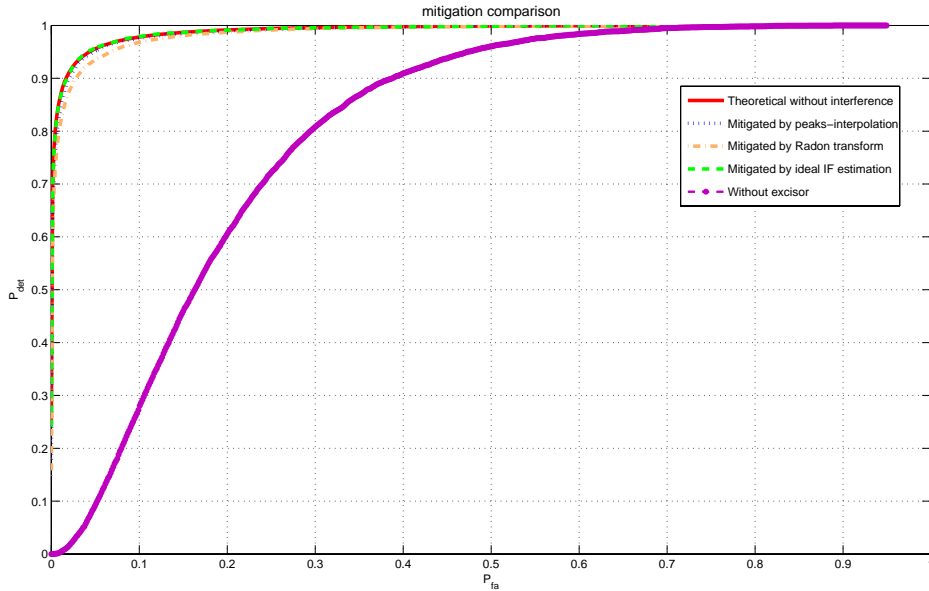


Figure 13.18. ROC curves for different IF estimation techniques. $C/N_0 = 36 \text{ dB-Hz}$, $J/N = 10 \text{ dB}$, $k_\alpha = 0.95$.

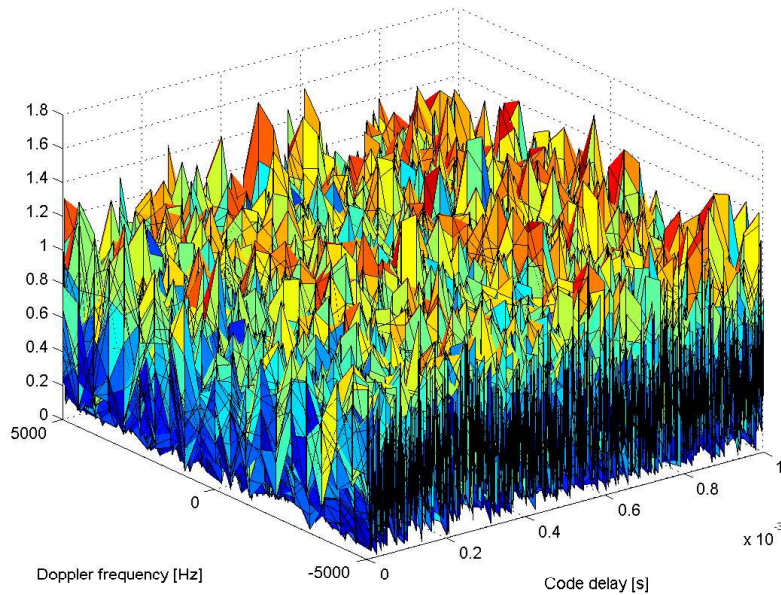


Figure 13.19. Search space of a GPS signal under interference: chirp, $J/N = 10 \text{ dB}$, $C/N_0 = 45 \text{ dB-Hz}$.

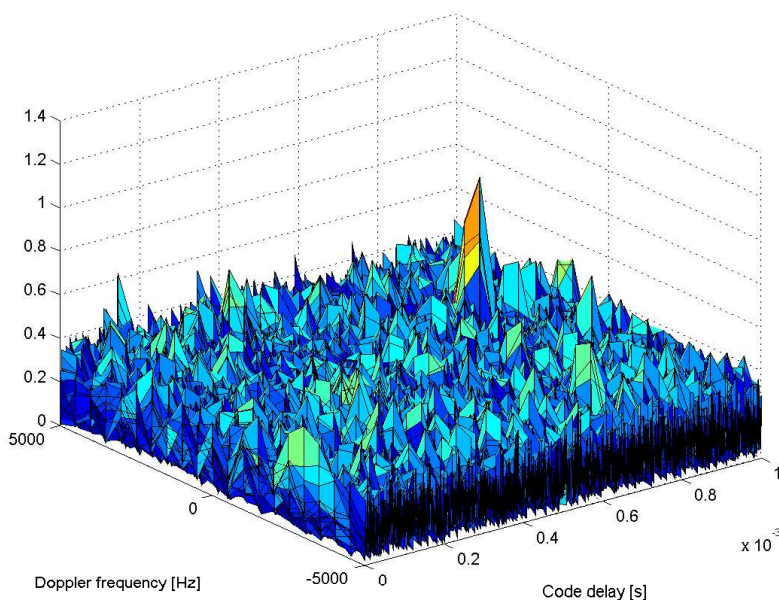


Figure 13.20. Search space of a GPS signal under interference after TF-excise: chirp, $J/N = 10 \text{ dB}$, $C/N_0 = 45 \text{ dB-Hz}$.

Chapter 14

Conclusions

This chapter concludes the second part of this thesis where signal acquisition in the presence of disturbing signals has been considered. A classification of the different interference sources has been provided and different types of interference have been discussed. Particular emphasis has been devoted to narrowband Gaussian interference and CWI.

The concept of SSC has been discussed and adapted to digital receivers. A statistical model describing the impact of CWI on the acquisition process has been developed. False alarm and detection probabilities have been analytically derived and Monte Carlo simulations have been used to support the theoretical model. The impact of the different system parameters have been analyzed by employing an equivalent representation, based on the convolution of three terms of the local signal replica. This representation has allowed isolating the role of the different parameters, giving a better insight into the interaction between the CWI and the correlation process.

Mitigation techniques have been also considered with particular attention to CWI mitigation algorithms and Time-Frequency analysis.

IIR notch filters have been considered as an effective solution for CWI removal and an innovative detection algorithm based on the convergence properties of the notch filter zero has been proposed and analyzed. The two-pole notch filter coupled with the detection unit has been used as basic element for the design of a multi-pole filter capable of efficiently removing more than one CWI. The derived results provide useful information for the design of mitigation and detection units based on adaptive notch filters that result in a computationally effective solution for CWI mitigation.

The use of TF analysis has been also considered for the design of a general mitigation algorithm able to deal with different kinds of interfering signals.

The problem of pulsed interference, such as DME and TACAN signals, has been only marginally considered. Thus their statistical characterization and the design of appropriate mitigation algorithms should be considered and further analyses should be devoted

to this kind of disturbing signals in future works.

Part III

Appendices and Bibliography

Appendix A

Acquisition analysis for Galileo BOC modulated Signals: theory and simulation

Paper presented at the European Navigation Conference (ENC)

Manchester (UK), 7-10 May 2006

Daniele Borio, Maurizio Fantino, Letizia Lo Presti, Laura Camoriano

A.1 Abstract

This paper is about the performance of a Galileo acquisition stage where the noise reduction and signal preservation is achieved by means of non-coherent summations. In fact, the presence of a secondary code, planned for many Galileo modulation and which further modulates the primary pseudo-random sequence, does not easily allow a coherent integration on more than one code period. Moreover, coherent integration is made much more complex by the longer codes employed for Galileo and by the use of the Binary Offset Carrier (BOC) modulations. In a mass-market receiver, where the complexity burdens are extremely important, these problems must be taken into account. A very easy solution is to combine the correlator outputs in a non-coherent process after the squaring operation in the acquisition block with an effective noise reduction without increasing dramatically the processing and memory capabilities of the receiver hardware. An analytical model of the acquisition block, starting from the well known statistical analysis carried out for GPS has been extended to Galileo. A complete digital acquisition system is considered and parametric expressions, depending on the number of terms coherently and non-coherently integrated, on the impact of the sampling frequency, code

time and Doppler step resolution have been derived for the threshold settings and detection probability. The derived model for the non-coherent acquisition is validated by means of Monte Carlo simulations. Finally the effects of additional impairments over the correlation function have been considered: an incomplete code delay recovery and slight mistakes in the Doppler frequency estimation, which can potentially reduce the acquisition performance, have been taken into account.

A.2 Introduction

In order to track and successfully decode the information broadcast by the satellite constellation, a GNSS receiver has to employ an acquisition strategy to first detect which satellites are in view. For each satellite, the acquisition has to supply the tracking loops with a coarse estimation of the received code delay, with an uncertainty usually of less than half a chip, and a rough estimation of the Doppler frequency shift. Sometimes an estimate of the receiver location and the time of the day are available to the receiver, so that it is possible to reduce the acquisition research among a subset of the available satellites. This solution is the so-called *warm start*. However, when such information is not available the receiver must perform a *cold start* and all the constellation satellites have to be searched for. This process is very time consuming, and to face this problem many receivers perform a parallel search for the different satellites. If the acquisition process is too slow the code delay and Doppler estimate might be out-of-date and the receiver could not be able to track the signals. Therefore the acquisition speed and complexity are very important parameters to be accounted in the GNSS receiver design. The acquisition phase is, in practice, a two-dimensional search over different values of code delay and Doppler shift for each satellite of the constellation. A two dimensional matrix, called search space, is obtained by testing a discrete set of values for these two variables. Each value of one of these two digitized variables specifies a bin in the grid, and the combination of one Doppler bin and one code bin is a cell. This search leads to a coarse estimation of the code delay and of the Doppler frequency shift affecting the GNSS signal. The resolution of the code search depends on the accuracy required by the code tracking section of the receiver and it is generally less than half a chip. The Doppler bin width depends on the maximum frequency resolution inside the pull-in range of the carrier tracking block and by the acquisition scheme properties. These parameters, and in particular the Doppler frequency steps, have to be set with great care since they are crucial for the acquisition speed. In Galileo the ranging code used for the L1F pilot channel is based on the so called tired codes. Tired codes are built by modulating a short duration primary code by a long duration secondary code. When only the primary code is used to detect the satellites, the presence of the secondary code behaves exactly as the data transition for the GPS signal and it can be the cause of sign reversals in the correlation operation

over the integration interval. In order to increase the detection probability for a given false alarm probability, a summation over more than a code period can be performed. Unfortunately the presence of the secondary code on the Galileo signal does not allow the receiver to perform the acquisition on consecutive pieces of signal, since every period of the primary code is modulated by the secondary short code, then it is not guaranteed the absence of a secondary code transition in the subsequent integration period. By the way, in order to increase the detection probability, a summation over more than one code period in a non coherent way can be applied, accepting the squaring loss due to the square operation performed prior the envelope detector. This paper analyzes the acquisition performance of a Galileo receiver, devoting particular attention to the strategy used to evaluate the search space. An analytical model is developed accounting both coherent and non-coherent integration. The analysis is provided in terms of Receiver Operating Characteristics (ROCs). The cases of an imperfect code delay recovery and of slight Doppler shift estimation errors are studied and the losses introduced by these impairments modeled. Simulations support the analytical model. The paper is organized as follows: Section A.3 introduces the GNSS signal model and presents the three main schemes used to evaluate the search space. Section A.4.2 provides the analytical model used to evaluate the system performance considering different losses that can occur during the acquisition process. In Section A.5 the model is validated by Monte Carlo simulations and in Section A.6 the effects of coherent and non-coherent integrations are compared. Finally Section A.7 concludes the paper.

A.3 Acquisition schemes

The problem of signal acquisition is commonly encountered in all CDMA applications. Many acquisition schemes for CDMA signal can be found in literature. However, many of them are not suitable for navigation purposes where the signal-to-noise ratio is very low. Moreover ([A9] [A10]), many authors do not consider the residual carrier acquisition but only the code synchronization. In the navigation context, however, the effects of the unknown residual Doppler shift cannot be neglected and the GNSS signal that enters the acquisition stage, after the down-conversion stages and the digitization, can be expressed as

$$x[n] = A_{IN}x_{IN}[n + \theta] \cos[2\pi(F_{BB} + F_D)(n + \theta) + \phi_1] + n_w[n] \quad (\text{A.1})$$

where A_{IN} is the useful signal amplitude, $x_{IN}[n]$ is the received PRN code modulated by the square sub-carrier, $n_w[n]$ is the Gaussian noise with zero mean and variance σ_n^2 , F_{BB} is the base-band frequency after the down conversions of the RF front-end, F_D is the Doppler frequency shift and finally θ is the received code delay. Notice that F_{BB} and F_D are digital frequencies, that is frequencies normalized with respect to the sampling frequency used by the ADC.

This signal $x_{IN}[n]$ is then processed by the acquisition block that can use different techniques in order to provide Doppler frequency and code delay estimations.

The most used acquisition strategies in navigation applications are the Serial Search scheme, the Parallel acquisition in time delay domain (Fast Acquisition Scheme) and Parallel acquisition in Doppler frequency domain.

A.3.1 Serial search scheme

Figure A.1 shows a basic serial search acquisition scheme, which can be found in References [A1] and [A2]. This scheme is called “serial” as it performs a serial search in time delay and Doppler frequency shift domains.

The input signal $x[n]$ is multiplied by the local replica of the PRN code plus sub-carrier $x_{LOC}[n + \hat{\theta}]$, where $\hat{\theta}$ is the local code delay. The signal is then split into two branches. The upper one is multiplied by a local cosine and the lower branch is multiplied by a local sine. The reference frequencies are the residual frequency plus the local Doppler frequency shift $F_{BB} + \hat{F}_D$. The system of Figure A.1 represents a non-coherent acqui-

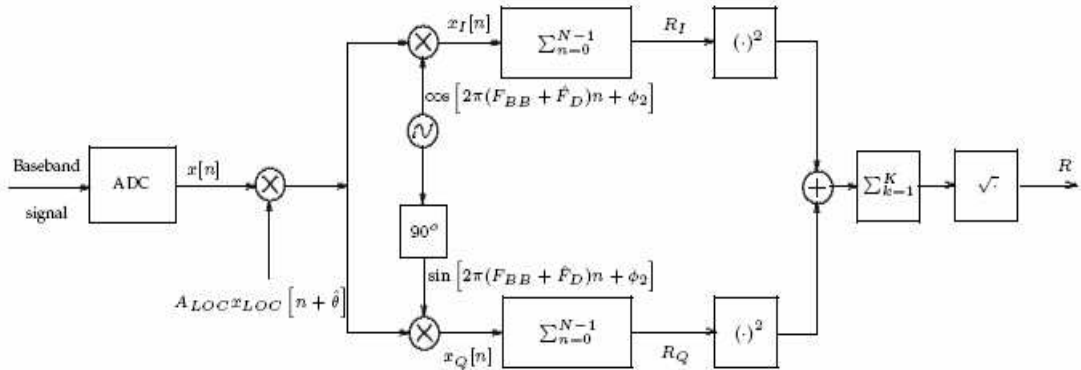


Figure A.1. Serial Search Acquisition scheme.

sition scheme, which has to be adopted because of the unknown phase ϕ_1 in Eq. (A.1). Therefore two branches are necessary in order not to lose part of the signal power. The signals on the two branches are then summed in the block called, in Figure A.1, *Average and Dump* or *Integrate and Dump* over one or more code periods to obtain a correlation value. The correlator output for the in-phase branch and for the quadrature-phase branch

can be written respectively as:

$$R_I(\theta, \hat{\theta}, F_D, \hat{F}_D) = \sum_{n=0}^{N-1} A_{IN} x_C[n + \theta] \cos[2\pi(F_{BB} + F_D)(n + \theta) + \phi_1] \\ \cdot A_{LOC} x_C[n + \hat{\theta}] \cos[2\pi(F_{BB} + \hat{F}_D)(n + \hat{\theta}) + \phi_2] \quad (\text{A.2})$$

$$R_Q(\theta, \hat{\theta}, F_D, \hat{F}_D) = \sum_{n=0}^{N-1} A_{IN} x_C[n + \theta] \cos[2\pi(F_{BB} + F_D)(n + \theta) + \phi_1] \\ \cdot A_{LOC} x_C[n + \hat{\theta}] \sin[2\pi(F_{BB} + \hat{F}_D)(n + \hat{\theta}) + \phi_2] \quad (\text{A.3})$$

where the local code is considered to be equal to the received one and it will be named $x_C[n]$ and has amplitude A_{LOC} .

The output of the envelope detector is, therefore

$$R(\theta, \hat{\theta}, F_D, \hat{F}_D) = \sqrt{R_I(\theta, \hat{\theta}, F_D, \hat{F}_D)^2 + R_Q(\theta, \hat{\theta}, F_D, \hat{F}_D)^2} \quad (\text{A.4})$$

The number of samples N depends on the sampling rate and on the so called *integration time*, which is generally an integer multiple of the code period. Increasing the integration time the acquisition speed decreases but the system becomes more robust to the additive noise. Accepting a squaring loss the robustness to the additive noise can also be obtained by means of K non-coherent integrations prior the envelope operation, as shown in Figure A.1.

A.3.2 Parallel acquisition in time delay domain

The scheme shown in Figure A.2 performs a parallel acquisition in time delay domain. This system is described in References [A3] and [A4], and is often addressed with the name of Fast Acquisition Scheme.

The input digital signal $x[n]$ is split in the in-phase and quadrature-phase branches. The resulting signals become the real part, $x_{Re}[n]$, and the imaginary part, $x_{Im}[n]$, of the FFT input. The complex samples obtained from the FFT operation are then multiplied by the complex conjugate samples of the local code $x_{LOC}[n]$ and then FFT inverse transformed.

The described operations perform a circular correlation and provides the complete correlation function over the integration period. In this way all the possible code delays are computed at once.

This acquisition system is theoretically faster than the serial search scheme, since the code delay steps are computed in parallel, but this gain is obtained only if the signal processor is fast enough to compute the FFT over all the signal samples within one dwell

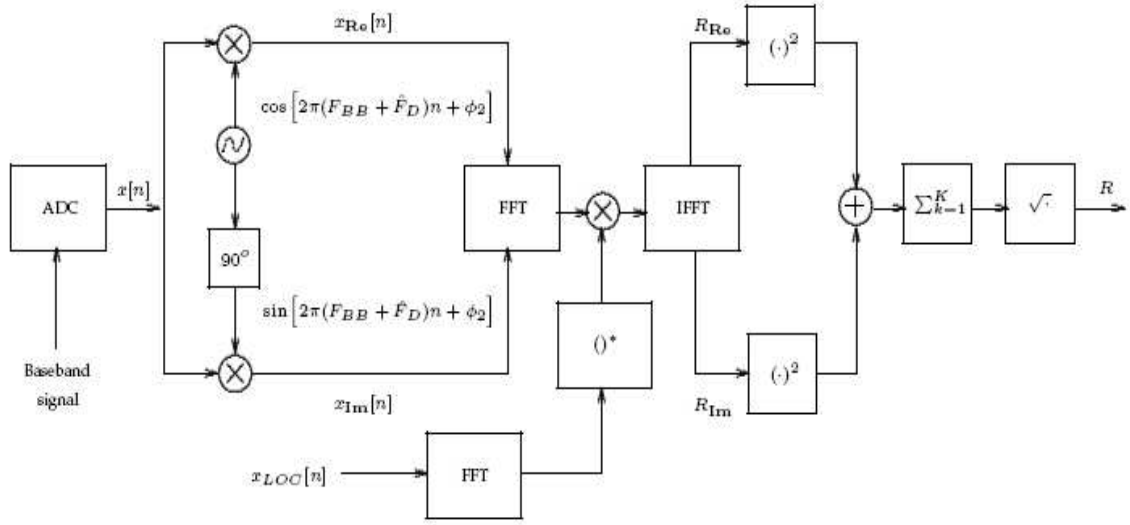


Figure A.2. Parallel Acquisition in time domain scheme.

time.

This solution can be considered an alternative implementation to the serial search scheme, that produces, in the correct frequency bin, the same results just performing the correlation by means of FFTs.

A.3.3 Parallel acquisition in Doppler frequency domain

The acquisition system shown in Figure A.3 (see Reference [A4]) performs a parallel search in the Doppler frequency domain. The digital input signal is multiplied by the local replica code shifted by the local delay estimate $\hat{\theta}$ and the FFT of the obtained burst of samples is computed. The result is passed through an envelope detector and all the desired frequency bins are then investigated in parallel.

The performed FFT operation can be shown to be identical to the operations made by the serial or fast acquisition scheme.

The number of Doppler frequency steps and FFT points are determined by the number of code periods used for the FFT calculation. If T is the temporal duration of the input samples the frequency resolution of the FFT results to be

$$\Delta \hat{f}_D = \frac{1}{T} \quad (\text{A.5})$$

This acquisition system requires, for each Doppler row of the serial search space, only one FFT calculation, but the whole time delay domain has to be scanned serially.

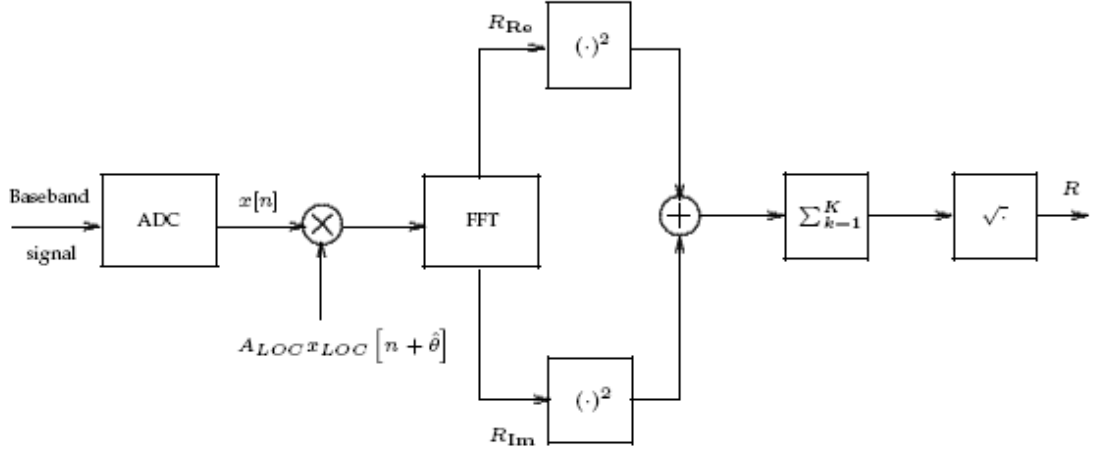


Figure A.3. Parallel Acquisition in Doppler frequency domain

A.4 Detection criteria

The acquisition system evaluates for each code delay and Doppler shift the search space matrix, as reported in Equation A.4, and a threshold is set on the basis of the required false alarm probability. The signal is then declared present when the value in a cell of the search space overcomes the threshold.

The false alarm probability is defined as the probability that the signal is declared present in a wrong cell, while the detection probability is the probability that a signal is detected under the condition of perfect code delay and Doppler shift alignment.

The false alarm probability can be easily derived considering the signal belonging to a wrong satellite or in misalignment conditions as the integral of the tail of a Rayleigh distribution (see Reference [A6]), expressed by

$$f_{na,R}(r) = \frac{r}{A_{LOC}^2 \left(\frac{N}{2}\right) \sigma_n^2} e^{-\frac{r^2}{A_{LOC}^2 N \sigma_n^2}} u(r) \quad (\text{A.6})$$

where $u(r)$ is the unitary echelon function and N is the number of samples coherently summed in the integrate and dump block or processed by the FFT operation. In order to improve the correlation performances, the detection and the decision can be taken on the summation of several samples of the squared correlator output R_I^2, R_Q^2 (non-coherent integration). In this case, according to the scheme of Figure A.1, the envelope G can be written as:

$$G = \sum_{i=1}^K R_I^2[i] + \sum_{i=1}^K R_Q^2[i] \quad (\text{A.7})$$

The summation on K independent instances of $R_I^2[i]$ and $R_Q^2[i]$ produces a mean effect that reduces the noise impact. $R_I^2[i]$ and $R_Q^2[i]$ are distributed according to a Γ distribution, which leads to a probability density function of the variable G equal to:

$$f_G^k(r) = \frac{1}{2^K(K-1)!\sigma^{2K}} r^{(K-1)} e^{-\frac{r}{2\sigma^2}} u(r) \quad (\text{A.8})$$

where, in order to keep the notation more compact, the variable $\sigma^2 = A_{LOC}^2 \sigma_n^2 N/2$ has been introduced.

The false alarm probability is then:

$$P_{fa} \left(V'_t \right) = \int_{V'_t}^{+\infty} f_G^{(K)}(x) dx \quad (\text{A.9})$$

where V'_t is the squared value of the threshold, since G is the statistic prior the squaring operation of the envelope detector. Using Equation A.8 and integrating by part $K-1$ times Equation A.9, it is possible to derive the following expression for the probability of false alarm:

$$\begin{aligned} P_{fa} \left(V'_t \right) &= \frac{1}{2^K(K-1)!\sigma^{2K}} \left[\sum_{i=1}^K (2\sigma^2)^i \frac{(K-1)!}{(K-i)!} V_t'^{K-i} e^{-\frac{V_t'}{2\sigma^2}} \right] \\ &= \frac{e^{-\frac{V_t'}{2\sigma^2}} V_t'^K}{2^K \sigma^{2K}} \sum_{i=1}^K \frac{1}{(K-i)!} \left(\frac{2\sigma^2}{V_t'} \right)^i \\ &= e^{-\frac{V_t'}{2\sigma^2}} \sum_{i=0}^{K-1} \frac{1}{i!} \left(\frac{V_t'}{2\sigma^2} \right)^i \end{aligned} \quad (\text{A.10})$$

If the signal is present, the envelope is Rice distributed (see Reference [A6]), that is its probability density function is

$$f_{a,R}(r) = \frac{r}{\sigma^2} e^{-\left(\frac{r^2+\alpha^2}{2\sigma^2}\right)} I_0 \left(\frac{r\alpha}{\sigma^2} \right) \quad (\text{A.11})$$

where $\alpha = A_{INA} A_{LOC} N/2$. As in the non-aligned case, the general expression for the probability density function, when K samples of the correlator output are summed up can be derived, giving

$$f_{a,R}^{(K)}(r) = \frac{\sqrt{k}\alpha}{\sigma^2} \left(\frac{r}{\sqrt{k}\alpha} \right)^k e^{-\frac{1}{2}\left(\frac{r^2+k\alpha^2}{\sigma^2}\right)} I_{k-1} \left(r \frac{\sqrt{k}\alpha}{\sigma^2} \right) \quad (\text{A.12})$$

The detection probability is then the integral over the tail of $f_{a,R}^{(K)}(r)$ (see reference [A7]), that is

$$\begin{aligned} P_d(V_t') &= \int_{\frac{\sqrt{V_t'}}{\sigma}}^{+\infty} f_{a,R}^K(x) dx \\ &= Q_K \left(\sqrt{K} \frac{\alpha}{\sigma}, \frac{\sqrt{V_t'}}{\sigma} \right) \end{aligned} \quad (\text{A.13})$$

A.4.1 Acquisition losses

The detection law for an acquisition system is derived supposing the system able to perfectly recover the code delay and the Doppler frequency shift. However, in real applications, these conditions are rarely verified. Neither the code delay nor the Doppler shift are exactly in the set of delays and frequencies used in the search space evaluation. This condition is the cause of additional impairments, or losses, which reduce the amplitude of the correlation peak used for the signal acquisition. The two independent effects, respectively due to Doppler and code imperfect alignment, are studied separately in this section.

Code Phase Offset loss

It is well known that the correlation function depends on the code offset positions. Figure A.4 compares the correlation samples obtained with two different code delay phase offset of the input signal and the same local generated code. Notice that, in order to perfectly reconstruct the correlation function by means of the input samples, the sampling frequency is never synchronized with the PRN code rate, as explained in [A5].

Two main effects can be seen from this comparison. The correlation is not symmetric anymore with respect to the highest peak. This can be explained by considering that a sampling frequency not synchronized to the PRN code rate, leads to different digitized sequences for different code phase offsets (see again Reference [A5]). The correlation between two sequences, which are not exactly identical, is not generally an even function. However, this aspect is not particularly meaningful for the performance of the acquisition system, due to the very low signal-to-noise ratio of the received satellite signal.

More important is the reduction of the peak amplitude, which is related to the value of the code phase offset. This introduces a system loss, with respect to the perfectly aligned case, that can be expressed as the ratio between the value of $R_{BOC}(\tau)$ and $R_{BOC}(0)$, denoting with $R_{BOC}(\tau)$ the BOC correlation function evaluated for a delay τ . Since $R_{BOC}(0) = 1$, the amplitude loss can be expressed just as

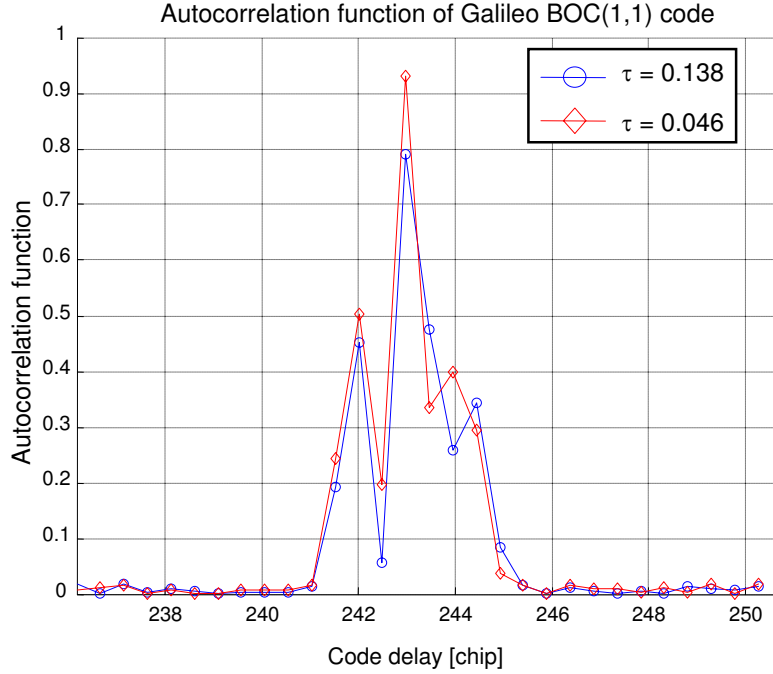


Figure A.4. Autocorrelation function of Galileo BOC(1,1) code for two different code phase alignments.

$$\alpha_{loss} = |R_{BOC}(\tau)| \quad (\text{A.14})$$

Since losses are normally in a logarithmic scale, and expressing the correlation function by means of the approximated expression for $R_{BOC}(\tau)$, it is possible to write the code loss as:

$$\begin{aligned} \alpha_{loss}|_{dB} &= 20 \log_{10} (R_{BOC}(\tau)) \\ &\approx 20 \log_{10} \left[\Lambda\left(\frac{\tau}{1/2}\right) - \frac{1}{2} \Lambda\left(\frac{\tau - 1/2}{1/2}\right) - \frac{1}{2} \Lambda\left(\frac{\tau + 1/2}{1/2}\right) \right] \end{aligned} \quad (\text{A.15})$$

where $\Lambda(\tau)$ is the triangular function defined as

$$\Lambda\left(\frac{t}{T}\right) = \begin{cases} 1 - \frac{|t|}{T} & |t| \leq T \\ 0 & |t| > T \end{cases} \quad (\text{A.16})$$

A plot of Equation (A.15) is depicted in Figure A.5:

Since the normal code resolution required for the signal identification is lower than

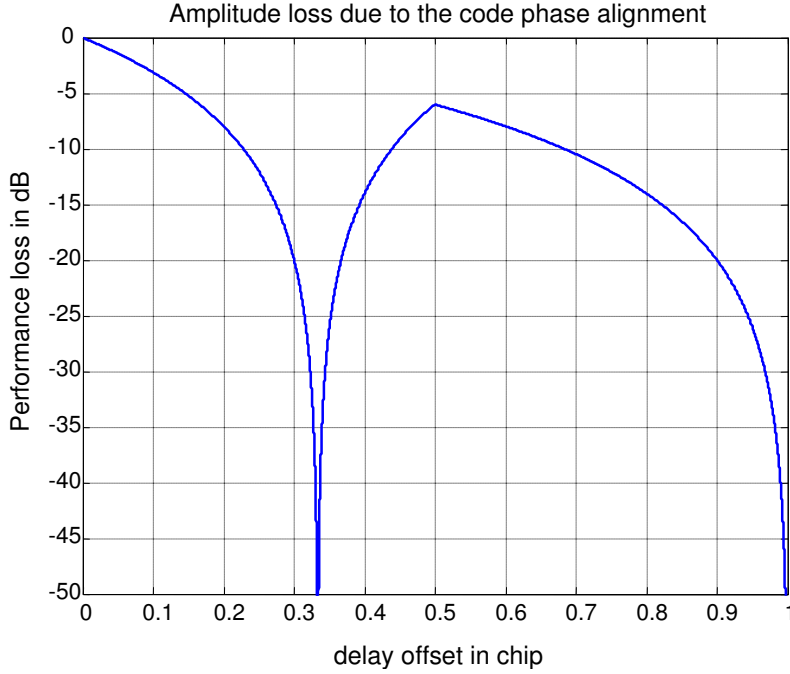


Figure A.5. Performance loss as a function of the code phase offset.

half a chip/slot¹ the reduction of correlation amplitude is always contained between 0 and about -15 dB.

Doppler Estimate Offset Error

As for the case of the correlation loss due to the code phase offset presented in Section A.4.1, the Doppler phase error encountered in the acquisition process produces a reduction of the correlation peak.

In order to analyze just the Doppler effect, it will be assumed that the local code has been aligned with the received one, in other words $\hat{\theta} = \theta$. The general expression of the In-phase correlator output becomes

$$R_I(F_D, \hat{F}_D) = A_{IN} A_{LOC} \sum_{n=0}^{N-1} x_C^2[n + \theta] \cos[2\pi F_D(n + \theta) + \phi] \cos[2\pi \hat{F}_D(n + \theta)] \quad (\text{A.17})$$

¹ Galileo code chips are further modulated by a squared sub-carrier, in this paper it is commonly referred as slot the width of the sub-carrier chip

that after some algebraic manipulation can be rewritten as

$$\begin{aligned}
R_I(F_D, \hat{F}_D) &= A_{IN} A_{LOC} \frac{N}{2} \left\{ D_N \left[\pi(F_D + \hat{F}_D) \right] \cos \left[2\pi (F_D + \hat{F}_D) \theta + \pi (F_D + \hat{F}_D) (N-1) + \phi \right] \right. \\
&\quad \left. + D_N \left[\pi(F_D - \hat{F}_D) \right] \cos \left[2\pi (F_D - \hat{F}_D) \theta + \pi (F_D - \hat{F}_D) (N-1) + \phi \right] \right\}
\end{aligned} \tag{A.18}$$

being $D_N(\omega/2) = \frac{\sin(\omega N/2)}{N \sin(\omega/2)}$ the Dirichlet function.

Equivalently, in the case of the quadrature branch

$$\begin{aligned}
R_Q(F_D, \hat{F}_D) &= A_{IN} A_{LOC} \frac{N}{2} \left\{ D_N \left[\pi(F_D + \hat{F}_D) \right] \sin \left[2\pi (F_D + \hat{F}_D) \theta + \pi (F_D + \hat{F}_D) (N-1) + \phi \right] \right. \\
&\quad \left. + D_N \left[\pi(F_D - \hat{F}_D) \right] \sin \left[2\pi (F_D - \hat{F}_D) \theta + \pi (F_D - \hat{F}_D) (N-1) + \phi \right] \right\}
\end{aligned} \tag{A.19}$$

Following the same considerations pointed out in Section A.4.1, comparing the expressions (A.18) and (A.19) with the maximum achievable value and neglecting the effect of the terms $F_D + \hat{F}_D$, which is practically negligible, the amplitude correlation loss due to the Doppler estimate offset can be modeled as:

$$\begin{aligned}
\beta_{loss} &\cong \left| D_N \left[\pi(F_D - \hat{F}_D) \right] \right| \\
\beta_{loss}|_{dB} &\cong 20 \log_{10} \left| D_N \left[\pi(F_D - \hat{F}_D) \right] \right|
\end{aligned} \tag{A.20}$$

This amplitude loss is depicted in Figure A.6, where the integration time goes from $T = 4$ ms to $T = 20$ ms with 4 ms of step (that is assuming the values 4, 8, 12, 16, 20 ms) and the Doppler search step is consequently reduced from $\Delta f_D = 250$ Hz to $\Delta f_D = 50$ Hz.

A.4.2 Detection probability in presence of losses

In the previous section it has been shown how an impairment due to code phase or Doppler shift misalignments causes a correlation loss. These two effects have to be taken into account in order to evaluate the correct detection probability of a real system. The signal level depends on two main non-idealities:

1. the code loss due to an arbitrary code phase falling in between the correlation resolution;
2. the loss due to the arbitrary Doppler frequency falling in between two frequency bins.

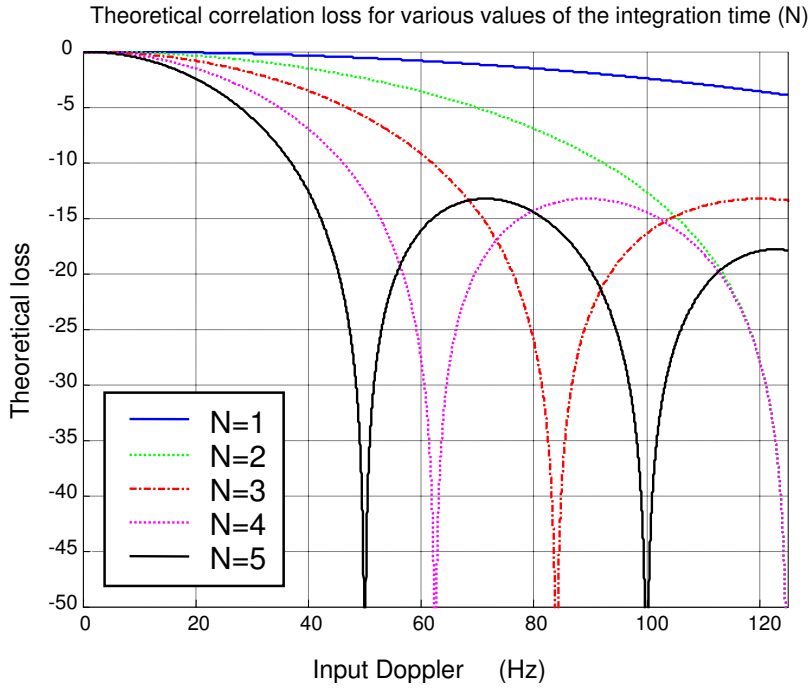


Figure A.6. Logarithmic Doppler loss.

In order to consider the different losses correctly, the probability distribution of the code phase offset and Doppler shift, considered as random variables, have to be modeled. The resolution used in the acquisition phase is usually of half a chip/slot and therefore the maximum absolute phase offset $\Delta\theta$ can be assumed uniformly distributed between $\pm\frac{1}{4}$ chip/slot; analogously the Doppler frequency Δf_D can be assumed to be uniformly distributed between zero and half the maximum absolute frequency bin width.

The combined loss due to the two independent effects is the sum of the contributions of the two losses. Thus, according to the definition of Section , the detection probability including the code phase offset and Doppler frequency shift loss effect is:

$$P_d = 2N \int_{-1/4}^{1/4} \int_{-1/2N}^{1/2N} Q_k \left(\frac{\sqrt{k}\alpha}{\sigma} D_N(\pi f) R_{BOC}(\theta), \frac{\sqrt{V'_t}}{\sigma} \right) df d\theta \quad (\text{A.21})$$

Figure A.7 reports the Receiver Operating Characteristic (ROC) which depicts the probability of detection versus the probability of false alarm. The curve has been obtained considering the integration of a single Galileo BOC(1,1) code period, an IF filter bandwidth of 4 MHz, a carrier to noise ratio $C/N_0 = 30$ dB-Hz, and a sampling frequency of about 4.21 MHz, which leads to a code ambiguity resolution of half a BOC slot. Figure A.8 is the graph that shows the detection probability versus the C/N_0 ratio for a false

alarm probability $P_{fa} = 10^{-3}$, for a Galileo BOC(1,1) signal, and with the same receiver parameters of Figure A.7. These last curves will be referred in the following as SNR curves.

Both curves have been obtained by means of the numerical solution of Equation (A.21) derived in this section, for the BOC(1,1) signal.

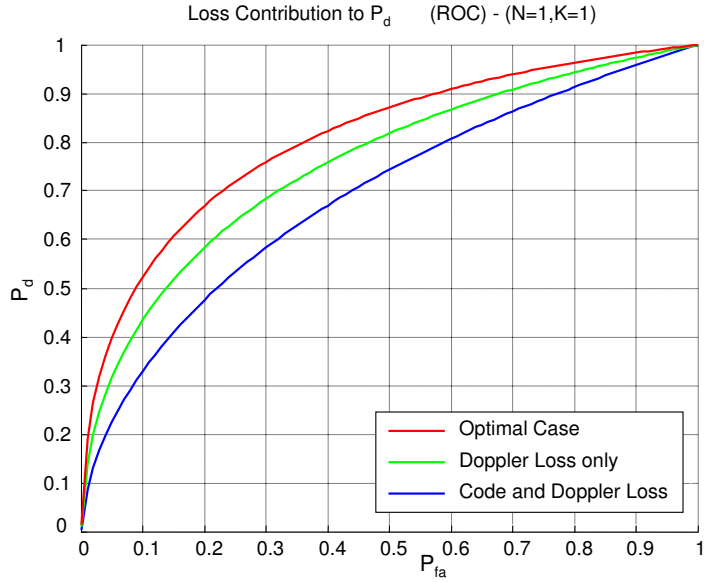


Figure A.7. Loss contribution comparison, ROC curve for the Galileo BOC(1,1) signal and $C/N_0 = 30$ dB-Hz

It is here important to remark how considerable is the loss of acquisition performance due to the Doppler and code misalignment with respect to the ideal case. Moreover it has to be considered that the curves which report the performance when both the code and Doppler loss are considered have been obtained in an average misalignment condition (both code and Doppler error uniformly distributed in the cell area), and so, they do not represent the worst case.

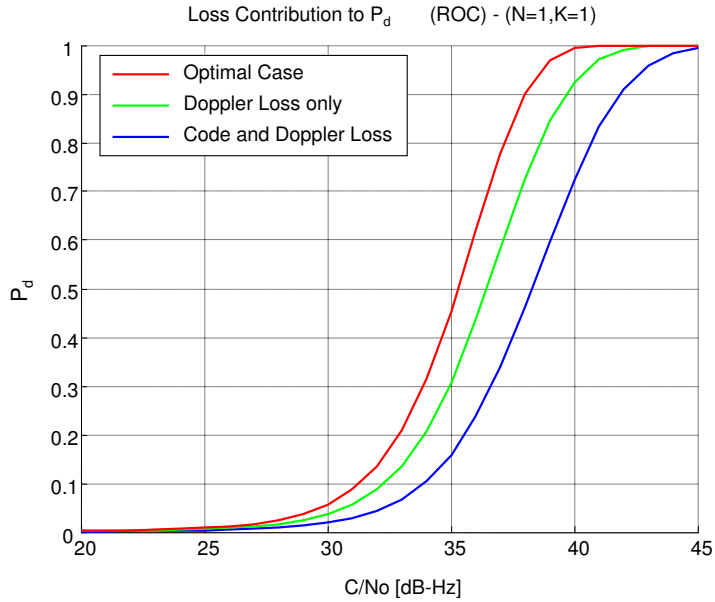


Figure A.8. Loss contribution comparison, SNR curve for the Galileo BOC(1,1) signal and desired $P_{fa} = 10^{-3}$

A.5 Acquisition Model Validation

The acquisition performance can be obtained analytically integrating Equations (A.10) and (A.21). However in order to adopt the acquisition model in the acquisition block design, it is necessary to validate the model comparing analytical and simulation results. Both the detection and false alarm probabilities are determined by means of computer simulations implementing a Monte Carlo technique or, in other words, the probabilities are obtained dividing the number of successful events by the overall number of trials.

This comparison is depicted in Figure A.9 for the ROC curve in the case of a $C/N_0 = 30$ dB-Hz and a non coherent integration from one up to five Galileo BOC(1,1) code periods. Solid lines correspond to the numerical solution of Equation (A.21) and the marked values to the Monte Carlo simulations for the Serial Search scheme of Figure A.1. The FFT in Time and in Frequency domains are not considered in this analysis, since they are equivalent in terms of performance. Therefore the results would be practically equal and indistinguishable. The validity of the model can be better appreciated by means of the graph of Figure A.10; again the solid lines refer to the model of Equation (A.21) and the marked values to the Monte Carlo simulations. As it can be seen from graphs of Figure A.9 and Figure A.10, the analytical solution of Equation (A.21) produces the same results obtained by means of the Monte Carlo simulations, which proves the validity and reliability of the acquisition model studied in this paper.

A reliable model is of extreme importance in the design phase of an acquisition block , as

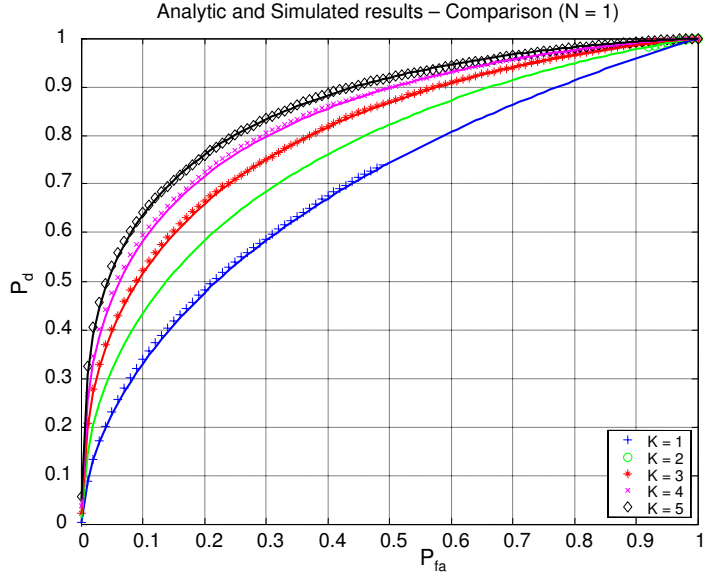


Figure A.9. ROC Comparison for the Analytic and Simulated Results for the Galileo BOC(1,1) signal for a C/N_0 of 30 dB-Hz and from one up to five non-coherent integration times.

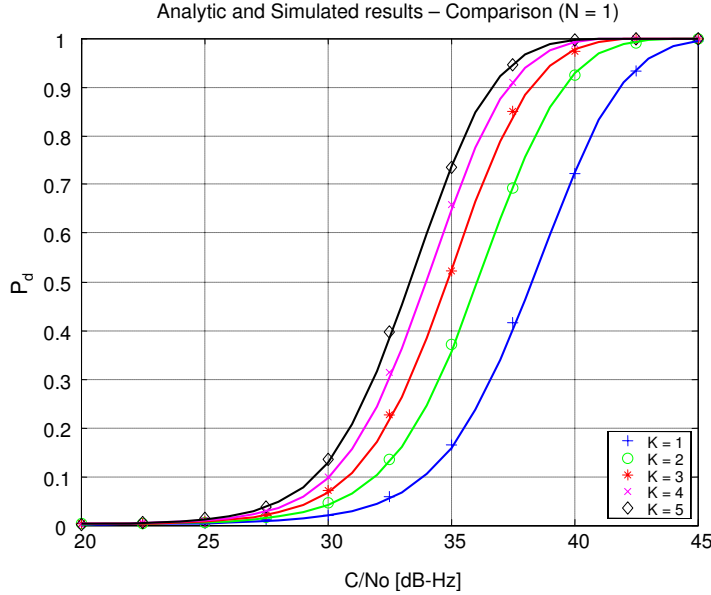


Figure A.10. SNR Comparison for the Analytic and Simulated Results for the Galileo BOC(1,1) signal for a desired $P_{fa} = 10^{-3}$ and from one up to five non-coherent integration times.

it allows the characterization of its expected performance, avoiding the use of very time consuming Monte Carlo simulations.

It is here remarked how, from the analysis of Figure A.9 and Figure A.10, both for the ROC and the SNR curve the gain in terms of Detection probability obtained increasing the non-coherent integration time tends to decrease as K becomes larger.

A.6 Coherent and non-Coherent Integration Comparison

Coherent integration over more than a single code period is a common strategy to increase the signal to noise ratio at the envelope detector input in the acquisition of GPS signals. It has been presented how the Galileo code makes the coherent approach quite difficult for the presence of the secondary codes and how the robustness in terms of signal to noise ratio can be achieved by means of non-coherent summation. In this section, however, a comparison between these two strategies for the Galileo BOC(1,1) is carried on.

For the sake of simplicity, and just with the aim to identify the loss in performance of the non-coherent strategy, the presence of the secondary code has been discarded in the analysis of the coherent integration approach.

The comparison is made both by means of the ROC and the SNR curves for the Galileo BOC(1,1) modulation. Each graph reports the comparison between the same number of code periods coherently and non-coherently integrated. The ROC curves have been determined for the usual carrier to noise ratio of 30 dB-Hz, while the SNR curves for a selected false alarm probability of 10^{-3} .

The comparison from two to five PRN code periods has been reported from Figure A.11 to Figure A.18. Once again the solid lines represent the analytical solution of Equation (A.21) while the marked values depict the results of Monte Carlo simulations.

In order to perform a fair comparison between the two different strategies the following consideration has to be highlighted: the loss due to a code misalignment is not affected by the number of integrated periods, but the case of the loss introduced by an arbitrary input Doppler frequency is different. In fact, as addressed in Section A.4.1, the Doppler loss can be approximated as stated in Equation (A.20). The Doppler loss depends mainly on two parameters, which are the number of samples coherently integrated and the difference between the input and local Doppler frequencies shift $F_D - \hat{F}_D$. From the definition of the Dirichlet function it follows that when the number of samples in the coherent integration increases, the Doppler frequency step must be reduced to maintain the same Doppler loss.

This condition is well represented in Figure A.6, where the Doppler loss is reported for different values of code periods coherently integrated as a function of the difference $F_D - \hat{F}_D$.

For such a reason, the results reported in this section have been obtained with a Doppler loss equal to the value for a single code period involved in the integration operation.

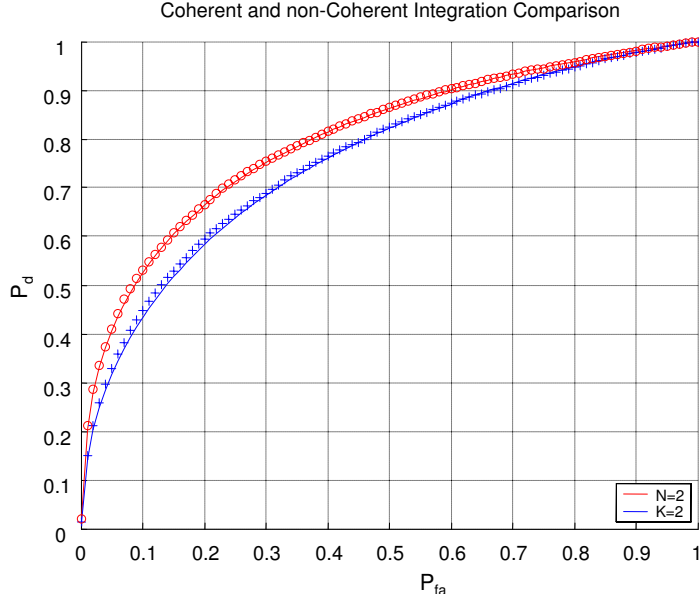


Figure A.11. Coherent and non-Coherent Integration Comparison for two Galileo BOC(1,1) Code periods, ROC curve calculated for a $C/N_0 = 30$ dB-Hz

The analysis shows how better performance can be achieved when a coherent integration strategy is adopted. The worse behavior of the non-coherent strategy can be totally attributed to the loss introduced by the square operation prior of the envelope detector. The noise samples of the autocorrelation function are less averaged by the K summations and then lower detection probabilities can be obtained under the same system conditions. The comparison can be better appreciated considering the gain in terms of C/N_0 between the coherent and non-coherent approaches required to obtain a determined detection probability for a desired false alarm probability. This is the case of the results stated in Table A.1, which reports the gain in terms of C/N_0 between the coherent and non-coherent strategies for a detection probability of 0.9 and a desired P_{fa} of 10^{-3} .

Table A.1. Coherent and non-Coherent C/N_0 gain comparison

Periods	Coherent C/N_0 [dB-Hz]	Non-Coherent C/N_0 [dB-Hz]	Gain C/N_0 [dB-Hz]
2	38.9	39.6	0.7
3	37.2	38.3	1.1
4	35.8	37.4	1.6
5	34.9	36.7	1.8

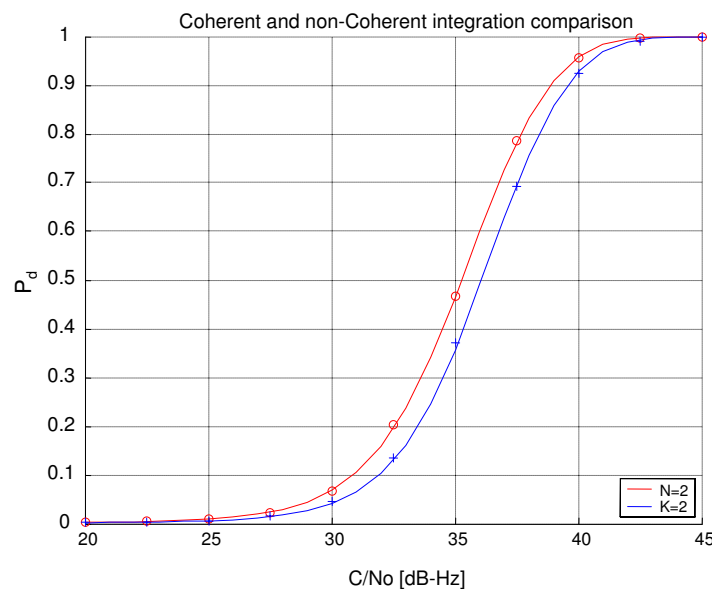


Figure A.12. Coherent and non-Coherent Integration Comparison for two Galileo BOC(1,1) Code periods, SNR curve for a desired P_{fa} of 10^{-3}

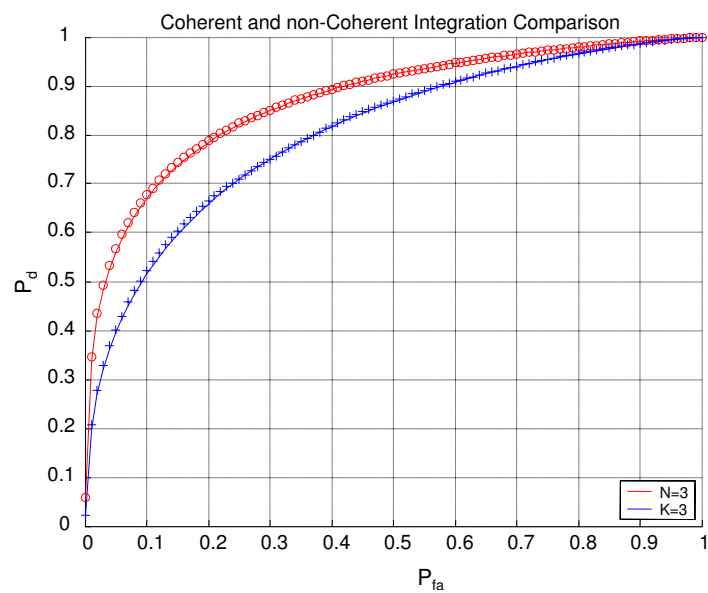


Figure A.13. Coherent and non-Coherent Integration Comparison for three Galileo BOC(1,1) Code periods, ROC curve calculated for a $C/N_0 = 30$ dB-Hz

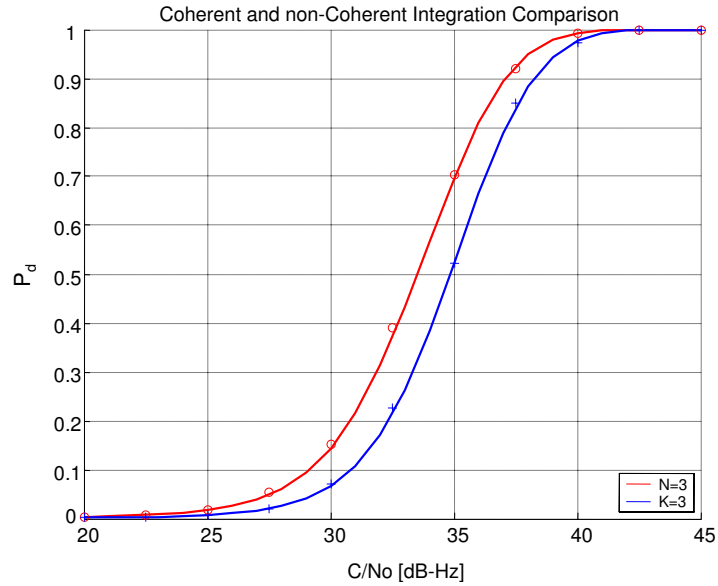


Figure A.14. Coherent and non-Coherent Integration Comparison for three Galileo BOC(1,1) Code periods, SNR curve for a desired P_{fa} of 10^{-3}

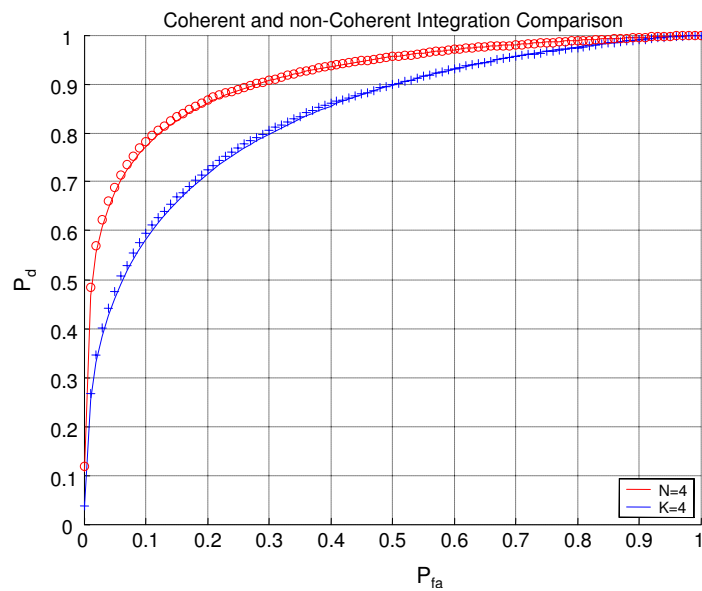


Figure A.15. Coherent and non-Coherent Integration Comparison for four Galileo BOC(1,1) Code periods, ROC curve calculated for a $C/N_0 = 30$ dB-Hz

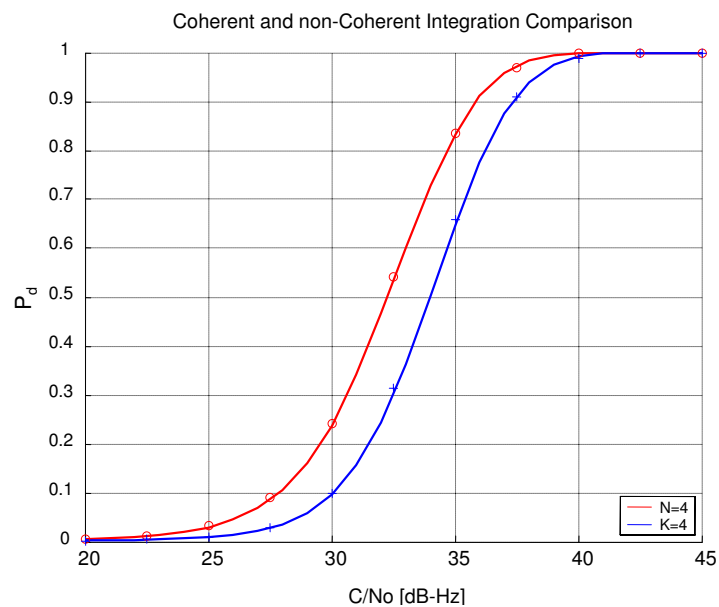


Figure A.16. Coherent and non-Coherent Integration Comparison for four Galileo BOC(1,1) Code periods, SNR curve for a desired P_{fa} of 10^{-3}

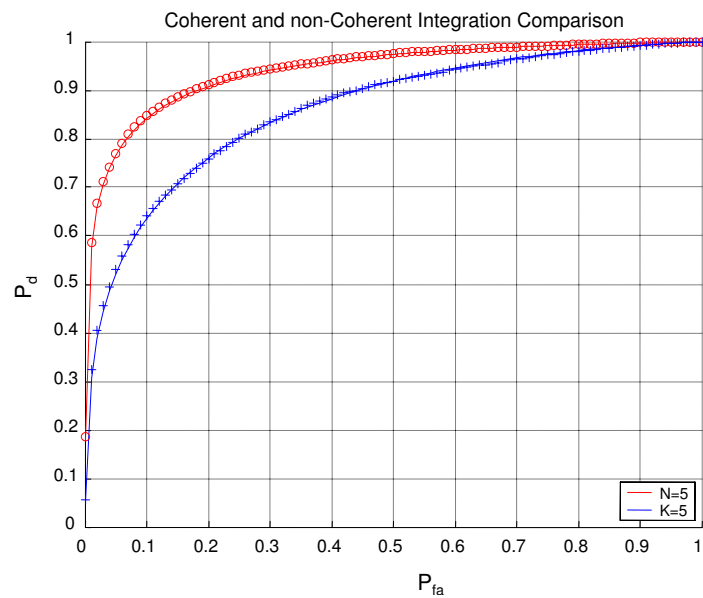


Figure A.17. Coherent and non-Coherent Integration Comparison for five Galileo BOC(1,1) Code periods, ROC curve calculated for a $C/N_0 = 30$ dB-Hz

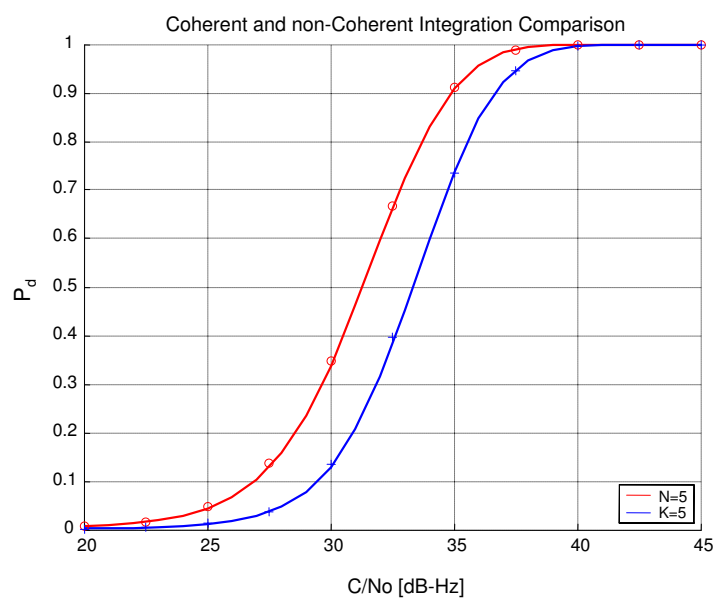


Figure A.18. Coherent and non-Coherent Integration Comparison for five Galileo BOC(1,1) Code periods, SNR curve for a desired P_{fa} of 10^{-3}

A.7 Conclusions

In this paper the conventional acquisition architectures already used for GPS have been investigated under the light of a possible employment for the acquisition of the Galileo BOC(1,1) modulation.

The acquisition blocks have been studied considering a digital implementation and considering different loss factors. The correlation level is mainly affected by two impairments due to the arbitrary code phase and Doppler frequency distribution in a cell. Considering uniform distributions for these two impairments, a model for the false alarm and detection probabilities has been derived for a digital acquisition taking into account the degradation of the performance with respect to the ideal case.

One of the main differences between GPS and Galileo is the presence of a secondary code which modulates each primary code period. This reduces the possibility of increasing the integration time in a coherent way, since a secondary code transition would lead to a sign reversal in the correlation operation. To improve the signal to noise ratio a non-coherent summation strategy can be used, both for the serial and parallel acquisition techniques, to overcome the problem of the secondary code transitions. The acquisition model has been derived considering the effect of the non-coherent strategy and subsequently validated by means of Monte Carlo simulations.

The availability of an analytic model, depending on the number of terms coherently and non-coherently integrated, simplifies the design phase of the acquisition block avoiding the use of onerous and infeasible Monte Carlo computer simulations.

A comparison between the coherent and non-coherent integration approaches is finally carried on, showing how better performance might be achieved by a coherent strategy in absence of secondary code transitions at the price of reducing the Doppler bin width and then increasing the number of cells that have to be analyzed in the acquisition search space.

The non-coherent strategy seems to be very interesting for its robustness to the sign reversal introduced by the secondary code. Therefore, without increasing the acquisition complexity and time to first fix, it is possible to achieve a good compromise between system performance and system complexity.

A.8 References

[A1] Z. Weihua and J. Tranquilla, "Modeling and analysis for the GPS pseudo-range observable," IEEE Transactions on Aerospace and Electronic Systems, vol. 31, pp. 739-751, April 1995.

[A2] E. D. Kaplan, "Understanding GPS: Principles and Applications". Norwood, MA Artech House, 1996.

- [A3] J. B.-Y. Tsui, "Fundamentals of Global Positioning System Receivers. A Software Approach", 2nd ed. New York: John Wiley and Sons, 2005.
- [A4] D. J. R. Van Nee and A. J. R. M. Coenen, "New fast GPS code-acquisition technique using FFT," Electronics Letters, vol. 27, no. 2, pp. 158-160, 17 Jan 1991.
- [A5] M. Fantino, F. Dovis, and L. Lo Presti, "Design of a reconfigurable low-complexity tracking loop for Galileo signals," International Symposium on Spread Spectrum Techniques and Applications, ISSSTA 2004, Sidney, pp. 736-740, August 2004.
- [A6] Papoulis, Probability, random variable and stochastic processes, 3rd ed. New York: McGraw Hill, 1991.
- [A7] J. I. Marcum, "A statistical theory of target detection by pulsed radar", IEEE Transaction on Information Theory, pp. 59-267, 1 December 1947.
- [A8] H. Mathis, P. Flammant, A. Thiel, "An analytic way to optimize the detector of a post-correlation FFT acquisition algorithm" ION National Technical Meeting, Portland, OR, pp. 689-699, 9-12 September 2003
- [A9] A. Polydoros and C. Weber, "A unified approach to serial search spread-spectrum code acquisition-part i: General theory", IEEE Transactions on Communications, vol. 32, no. 5, pp. 542-549, May 1984.
- [A10] A. Polydoros and C. Weber, "A unified approach to serial search spread-spectrum code acquisition-part ii: A matched-filter receiver", IEEE Transactions on Communications, vol. 32, no. 5, pp. 550-560, May 1984.

Appendix B

Independence of search space cells

In this appendix the assumption of independence of the CAF elements is justified by evaluating the cell correlation matrices.

In order to evaluate a search space $S(\tau, F_D)$, N samples of the input signal of Eq. (2.10) are collected and an input vector

$$\mathbf{r} = [r[0], r[1], \dots, r[N - 1]]^T \quad (\text{B.1})$$

is formed. This vector is then multiplied by two orthogonal sinusoids on the in-phase and quadrature ways. These two real multiplications can be modeled through a modulation by the complex sinusoid

$$\exp \{-j2\pi (f_{IF} + f_d) nT_s\} = \exp \{-j2\pi F_D n\} \quad (\text{B.2})$$

where f_{IF} is the intermediate frequency and f_d is the Doppler shift under test. Only a finite set of Doppler frequencies is tested, $f_d = f_{d,\min} + l\Delta f$ with $l = 0, 1, \dots, L - 1$, and the signals after the Doppler demodulation are given by

$$\mathbf{y}_l = \mathbf{E}_l \mathbf{r} \quad l = 0, 1, \dots, N - 1 \quad (\text{B.3})$$

where l is the Doppler frequency index and \mathbf{E}_l are diagonal matrices of the form

$$\mathbf{E}_l = \text{diag} \{-j2\pi (f_{IF} + l\Delta f) nT_s\} \quad n = 0, 1, \dots, N - 1. \quad (\text{B.4})$$

Vectors \mathbf{y}_l are then multiplied by a local replica of the code delayed of $\tau = \tau_{\min} + m\Delta\tau$ and integrated over a period of N samples.

By using the code periodicity, these multiplication and integration can be expressed as

$$\mathbf{z}_l = \mathbf{C} \mathbf{y}_l = \mathbf{C} \mathbf{E}_l \mathbf{r} \quad (\text{B.5})$$

where

$$\mathbf{C} = \begin{bmatrix} \mathbf{c} \\ \text{shift_circ}(\mathbf{c},1) \\ \text{shift_circ}(\mathbf{c},2) \\ \vdots \\ \text{shift_circ}(\mathbf{c},H-1) \end{bmatrix}$$

in which \mathbf{c} is the code, and $\text{shift_circ}(\mathbf{c},m)$ is the function that rotates it by m steps. This operation can be interpreted as a sort of transform, with a structure that is similar to the Fast Fourier Transform, where the base is no longer formed by exponentials but by rotated codes. In Eq. (B.5) the normalization factor $\frac{1}{N}$ is not considered. This normalization however does not essentially change the statistical properties of the elements of the search space that result only scaled.

At this point, it is possible to demonstrate the independence among the elements of a \mathbf{z}_l and among the different \mathbf{z}_l . To this aim it is necessary to compute

- the covariance matrix of \mathbf{z}_l ,
- the cross-covariance matrix of \mathbf{z}_l and \mathbf{z}_h , with $l \neq h$.

All kinds of search spaces are sets of random variables obtained from the elements of \mathbf{z}_l , which are normally distributed under the hypothesis of Gaussian input signals \mathbf{r} . For this reason, the proof that the \mathbf{z}_l are uncorrelated implies statistical independence.

The covariance matrix can be evaluated starting from the correlation matrix

$$\mathbf{C}_{\mathbf{z}_l} = E[\mathbf{z}_l \mathbf{z}_l^H] = E[\mathbf{C} \mathbf{E}_l \mathbf{r} \mathbf{r}^H \mathbf{E}_l^H \mathbf{C}^T] = \mathbf{C} \mathbf{E}_l E[\mathbf{r} \mathbf{r}^H] \mathbf{E}_l^H \mathbf{C}^T. \quad (\text{B.6})$$

The element $E[\mathbf{r} \mathbf{r}^H]$ contains a term due to the noise equal to σ_{IF}^2 , a cross-correlation term between the noise and the signal components of \mathbf{r} , and a term due to the signal autocorrelation. The cross-correlation term is null since the noise and signal components are uncorrelated. In the framework of the hypothesis adopted for the SIS code, the signal autocorrelation can always be considered null thanks to the orthogonal property of the codes, except in a single point of the search space. Therefore the signal only contributes with a mean value, which does not impact the covariance matrix, and that can be written as

$$\mathbf{C}_{\mathbf{z}_l} = \sigma_{IF}^2 \mathbf{C} \mathbf{E}_l \mathbf{E}_l^H \mathbf{C}^T = \sigma_{IF}^2 \mathbf{C} \mathbf{C}^T \quad (\text{B.7})$$

where $\mathbf{C} \mathbf{C}^T$ is the code correlation matrix. A portion of $\mathbf{C} \mathbf{C}^T$ is shown in Figure B.1 in the case of a BPSK signal. A GPS code with 2 samples per chip is used to form the \mathbf{C} and $\mathbf{C} \mathbf{C}^T$ matrices. The lighter colors represent high correlation values: in this case also the sub- and the super-diagonal of $\mathbf{C} \mathbf{C}^T$ are clearly different from zero, because of the code over-sampling. However, for a low over-sampling factor, due to the orthogonality

proprieties of the code, the approximation $\mathbf{C}\mathbf{C}^T \approx N\mathbf{I}$ holds, where \mathbf{I} is the identity matrix of size N and

$$E[\mathbf{z}_l \mathbf{z}_l^H] \approx \sigma_{IF}^2 N \mathbf{I} \quad (\text{B.8})$$

where \mathbf{I} is the identity matrix. This result shows the independence of the elements of \mathbf{z}_l ,

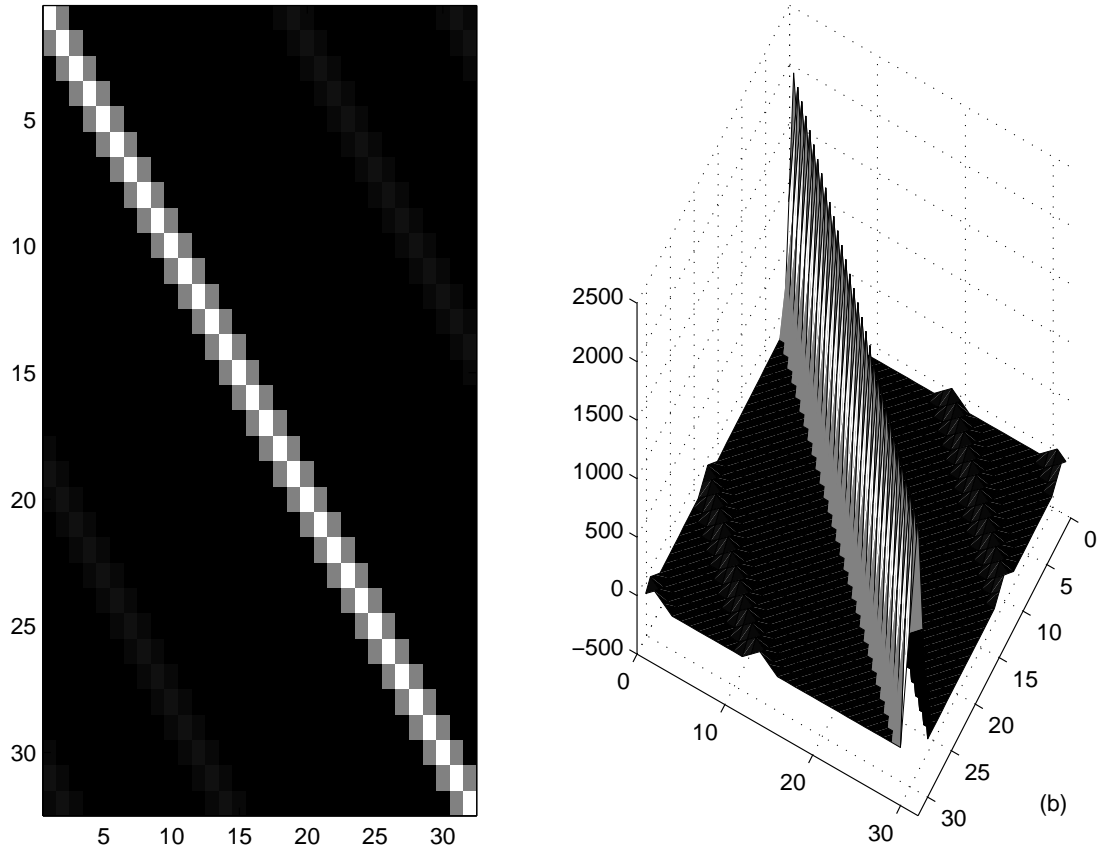


Figure B.1. Portion of the matrix $\mathbf{C}\mathbf{C}^T$ obtained with a GPS code of 1023 chips and 2 samples per chip.

since the covariance matrix elements are zero except along the diagonal: the elements are uncorrelated, Gaussian and, therefore, independent.

The cross-covariance matrix can be evaluated in the same way as that of the covariance matrix, by writing

$$E[\mathbf{z}_l \mathbf{z}_h^H] = E[\mathbf{C}\mathbf{E}_l \mathbf{r} \mathbf{r}^H \mathbf{E}_h^H \mathbf{C}^T] = \mathbf{C}\mathbf{E}_l E[\mathbf{r} \mathbf{r}^H] \mathbf{E}_h^H \mathbf{C}^T = \sigma_{IF}^2 \mathbf{C}\mathbf{E}_l \mathbf{E}_h^H \mathbf{C}^T \quad (\text{B.9})$$

with $l \neq h$. The term $\mathbf{C}\mathbf{E}_l\mathbf{E}_h^H\mathbf{C}^T$ is $\approx \mathbf{0}$ because it represents the correlation function when the delay and Doppler shift are not matched. Therefore

$$E[\mathbf{z}_l\mathbf{z}_h^H] \approx \mathbf{0} \quad (\text{B.10})$$

Appendix C

Exact computation of the polynomial $P_{K-1}(\rho_c)$

The evaluation of the polynomial

$$P_{K-1}(\rho_c) = \left(\frac{1}{2}\right)^{K-1} \sum_{i=0}^{K-1} \frac{1}{i!4^i} E\left[\left(\chi_{2K}^2\right)^i\right] = \left(\frac{1}{2}\right)^{K-1} \sum_{i=0}^{K-1} a_K^i \quad (C.1)$$

where

$$a_K^i = \frac{1}{i!4^i} E\left[\left(\chi_{2K}^2\right)^i\right]$$

can be performed by using a recursive approach based on the fact that each χ^2 random variable can be decomposed as the sum of two independent χ^2 random variables. In particular

$$\chi_{2K}^2 = \chi_m^2 + \chi_n^2$$

where m and n are two positive integers, such that $m + n = 2K$. By using this property the following relation can be derived:

$$\begin{aligned} a_K^i &= \frac{1}{i!4^i} E\left[\left(\chi_{2K}^2\right)^i\right] = \frac{1}{i!4^i} E\left[\left(\chi_m^2 + \chi_n^2\right)^i\right] = \frac{1}{i!4^i} \sum_{h=0}^i \binom{i}{h} E\left[\left(\chi_m^2\right)^h\right] E\left[\left(\chi_n^2\right)^{i-h}\right] \\ &= \frac{1}{i!4^i} \sum_{h=0}^i \frac{i!}{h!(i-h)!} E\left[\left(\chi_m^2\right)^h\right] E\left[\left(\chi_n^2\right)^{i-h}\right] = \sum_{h=0}^i \frac{1}{h!4^h} E\left[\left(\chi_m^2\right)^h\right] \frac{1}{(i-h)!4^{i-h}} E\left[\left(\chi_n^2\right)^{i-h}\right] \\ &= \sum_{h=0}^i a_m^h a_n^{i-h}. \end{aligned} \quad (C.2)$$

Thus each term a_K^i can be expressed as a convolution of coefficients deriving from χ^2 random variables with less than $2K$ degrees of freedom. Furthermore it is possible to

explicitly evaluate the coefficients $a_{0.5}^i$ as

$$a_{0.5}^i = \frac{1}{i!4^i} E \left[(\chi_1^2)^i \right] = \frac{1}{i!4^i} E \left[(Z + \mu)^{2i} \right] \quad (\text{C.3})$$

where Z is Gaussian random variable with zero mean and unitary variance and $\mu^2 = \rho_c/4$ is the non-centrality parameter of χ_1^2 from which $a_{0.5}^i$ derives. By expanding the binomial in Eq. (C.3) one finds

$$a_{0.5}^i = \frac{1}{i!4^i} \sum_{h=0}^{2i} \binom{2i}{h} E \left[Z^h \right] \mu^{2i-h}. \quad (\text{C.4})$$

Since the moments of a standard Gaussian random variable are given by

$$E \left[Z^h \right] = \begin{cases} \frac{h!}{2^{h/2}(h/2)!} & \text{for } h \text{ even} \\ 0 & \text{for } h \text{ odd.} \end{cases} \quad (\text{C.5})$$

Eq. (C.4) becomes

$$a_{0.5}^i = \frac{1}{i!4^i} \sum_{l=0}^i \binom{2i}{2l} \frac{(2l)!}{2^l l!} \mu^{2i-2l} = \frac{1}{i!4^i} \sum_{l=0}^i \frac{(2i)!}{(2i-2l)!2^l l!} \left(\frac{\rho_c}{4} \right)^{i-l}. \quad (\text{C.6})$$

In this way all the $a_{0.5}^i$ for $i = 0, \dots, K-1$ can be evaluated and used as initial values for determining a_K^i by means of Eq. (C.2).

Appendix D

$P_{K-1}(\rho_c)$ approximations

In this appendix the constant and linear terms of the polynomial $P_{K-1}(\rho_c)$ are evaluated by using Gaussian random variable properties.

From Eq. (5.40), $P_{K-1}(\rho_c)$ is given by

$$P_{K-1}(\rho_c) = \left(\frac{1}{2}\right)^{K-1} \sum_{i=0}^{K-1} \frac{1}{i!4^i} E\left[\left(\chi_{2K}^2\right)^i\right]. \quad (\text{D.1})$$

The random variable χ_{2K}^2 is obtained by summing the square of $2K$ normalized Gaussian random variables with mean μ_i as

$$\begin{aligned} \chi_{2K}^2 &= \sum_{i=1}^{2K} \left(\frac{X_i}{\sigma_i}\right)^2 = \sum_{i=1}^{2K} \left(\frac{Z_i + \mu_i}{\sigma_i}\right)^2 \\ &= \sum_{i=1}^{2K} \left(\frac{Z_i}{\sigma_i}\right)^2 + 2 \sum_{i=1}^{2K} \left(\frac{Z_i \mu_i}{\sigma_i^2}\right) + \sum_{i=1}^{2K} \left(\frac{\mu_i}{\sigma_i}\right)^2 \end{aligned} \quad (\text{D.2})$$

where $Z_i = X_i - \mu_i$ are zero mean Gaussian random variables with variance equal to σ_i^2 . Without loss of generality it is possible to assume $\sigma_i = \sigma$ and $\mu_i = \mu \forall i$ and thus Eq. (D.2) becomes

$$\begin{aligned} \chi_{2K}^2 &= \sum_{i=1}^{2K} \left(\frac{Z_i}{\sigma_i}\right)^2 + 2\frac{\mu}{\sigma} \sum_{i=1}^{2K} \left(\frac{Z_i}{\sigma}\right) + \lambda \\ &= C_{2K} + 2\sqrt{\frac{\lambda}{2K}}S + \lambda \end{aligned} \quad (\text{D.3})$$

where

- C_{2K} is a central χ^2 random variable with $2K$ degrees of freedom,
- S is the sum of the random variables Z_i normalized by σ ,

- λ is the non-centrality parameter given by

$$\lambda = 2K \left(\frac{\mu}{\sigma} \right)^2 = \frac{K}{2} \rho_c. \quad (\text{D.4})$$

By using Eq. (D.3) and the multinomial theorem it is possible to evaluate the raw moments of a non-central χ square random variable as

$$\begin{aligned} \mathbb{E} \left[(\chi_{2K}^2)^i \right] &= \mathbb{E} \left[\left(C_{2K} + 2\sqrt{\frac{\lambda}{2K}} S + \lambda \right)^i \right] \\ &= \mathbb{E} \left[\sum_{h,j} \frac{i!}{h!j!(i-h-j)!} C_{2K}^h 2^j \left(\sqrt{\frac{\lambda}{2K}} \right)^j S^j \lambda^{i-h-j} \right] \\ &= \sum_{h,j} \frac{i! 2^{j/2}}{h! j! (i-h-j)! K^{j/2}} \mathbb{E} \left[C_{2K}^h S^j \right] \lambda^{i-h-j/2} \end{aligned} \quad (\text{D.5})$$

for $0 \leq h \leq i$, $0 \leq j \leq i$, and $0 \leq i-h-j$.

Eq. (D.5) can be used for determining the first coefficients of $P_{K-1}(\rho_c)$. It is important to note that the index j in Eq. (D.5) can assume only even values. In fact when j is odd, the product $C_{2K}^h S^j$ can be decomposed into the sum of products of odd powers of independent zero mean Gaussian random variables and thus $\mathbb{E} [C_{2K}^h S^j]$ is equal to zero.

D.1 Constant term

The constant term in P_{K-1} can be found by imposing $i - h - j/2 = 0$ and evaluating the corresponding terms in Eq. (D.5). The only value of j and h that solves this condition and respects the limits

$$\begin{aligned} 0 &\leq h \leq i \\ 0 &\leq j \leq i \\ 0 &\leq i - h - j \leq i \end{aligned}$$

is

$$j = 0, h = i,$$

which leads to

$$E_0^i = \mathbb{E} [C_{2K}^i] = 2^i \frac{\Gamma(i+K)}{\Gamma(K)} = 2^i \frac{(i+K-1)!}{(K-1)!} \quad (\text{D.6})$$

where E_0^i is a constant term, with respect to λ of $\mathbb{E} \left[(\chi_{2K}^2)^i \right]$. $\Gamma(\cdot)$ is the Euler Gamma function [45].

The constant term in $P_{K-1}(\rho_c)$ is thus given by

$$\begin{aligned}
 p_0 &= \left(\frac{1}{2}\right)^{K-1} \sum_{i=0}^{K-1} \frac{1}{i!4^i} E_0^i = \left(\frac{1}{2}\right)^{K-1} \sum_{i=0}^{K-1} \frac{1}{i!4^i} 2^i \frac{(i+K-1)!}{(K-1)!} \\
 &= \left(\frac{1}{2}\right)^{K-1} \sum_{i=0}^{K-1} \frac{1}{i!2^i} \frac{(i+K-1)!}{(K-1)!} \\
 &= \left(\frac{1}{2}\right)^{K-1} \sum_{i=0}^{K-1} \frac{1}{2^i} \binom{i+K-1}{i} \\
 &= \left(\frac{1}{2}\right)^{K-1} 2^{K-1} = 1
 \end{aligned} \tag{D.7}$$

In Eq. (D.7) the binomial property [123]

$$\sum_{i=0}^N \frac{1}{2^i} \binom{i+N}{i} = 2^N$$

has been used.

Eq. (D.7) proves that the first term of $P_{K-1}(\rho_c)$ is equal to 1 independently from K .

D.2 First power coefficient

The coefficient corresponding to the first power of λ and consequently to the first power of ρ_c in $P_{K-1}(\rho_c)$ can be evaluated by proceeding in the same way as for the constant term case. The only values of h and j that lead to terms corresponding to the first power of λ in Eq. (D.5) are

I) $j = 0, h = i - 1$,

II) $j = 2, h = i - 2$.

By evaluating these two cases it is possible to show that

$$E_1^i = \frac{2^{i-1}i(i+K-1)!}{K!} \lambda = \frac{2^{i-2}i(i+K-1)!}{(K-1)!} \rho_c \tag{D.8}$$

where E_1^i is a term of degree 1 with respect to λ and ρ_c in Eq. (D.5). From the previous results it follows that

$$\begin{aligned}
 p_1 &= \frac{1}{2^{K-1}} \sum_{i=0}^{K-1} \frac{1}{i!4^i} \frac{2^{i-2}i(i+K-1)!}{(K-1)!} \\
 &= \frac{K}{4} \left[1 - \frac{1}{2^{2K-1}} \binom{2K}{K} \right].
 \end{aligned} \tag{D.9}$$

Appendix E

Independence of the random variables at the output of the data and pilot correlators

In this appendix we show that the random variables obtained by correlating the input composite GNSS signal with the local replicas of the data and pilot channels are approximatively independent.

The correlator outputs are given by the signal and noise components. In particular the noise components on the in-phase and quadrature branches are given by

$$\begin{aligned}\eta_{X,I}(\tau, F_D) &= \frac{1}{N} \sum_{n=0}^{N-1} \eta[n] e_X[n - \tau] \cos(2\pi F_D n) \\ \eta_{X,Q}(\tau, F_D) &= -\frac{1}{N} \sum_{n=0}^{N-1} \eta[n] e_X[n - \tau] \sin(2\pi F_D n)\end{aligned}\quad (\text{E.1})$$

or equivalently

$$\eta_X(\tau, F_D) = \eta_{X,I}(\tau, F_D) + j\eta_{X,Q}(\tau, F_D) = \frac{1}{N} \sum_{n=0}^{N-1} \eta[n] e_X[n - \tau] \exp\{-j2\pi F_D n\} \quad (\text{E.2})$$

where the index X can be either $X = D$ or $X = P$ denoting either the data or the pilot components. The signal $e_X[n - \tau]$ is the local code delayed by τ .

In order to prove the independence between the output of the data and pilot channels it is sufficient to prove the independence of η_D and η_P , the noise terms in the data and pilot correlations. Since both η_D and η_P are linear combinations of the samples of the Gaussian process $\eta_{IF}[n]$ they are two Gaussian random variables and thus, to prove their independence, it is sufficient to prove that $E[\eta_D \eta_P^*] = 0$.

By defining

$$M = \begin{bmatrix} \eta[0] \\ \eta[1] \\ \dots \\ \eta[N-1] \end{bmatrix}; E_x = \begin{bmatrix} 1 & 0 & \dots & 0 \\ 0 & \exp\{-j2\pi F_D\} & \dots & 0 \\ \dots & \dots & \dots & \dots \\ 0 & 0 & \dots & \exp\{-j2\pi F_D(N-1)\} \end{bmatrix};$$

$$D = \begin{bmatrix} e_D[-\tau] \\ e_D[1-\tau] \\ \dots \\ e_D[N-1-\tau] \end{bmatrix}; P = \begin{bmatrix} e_P[-\tau] \\ e_P[1-\tau] \\ \dots \\ e_P[N-1-\tau] \end{bmatrix},$$

it is possible to rewrite Eq. (E.2) for the data and pilot components in the following form:

$$\begin{aligned} \eta_D(\tau, F_D) &= \frac{1}{N} M^T E_x D \\ \eta_P(\tau, F_D) &= \frac{1}{N} M^T E_x P. \end{aligned} \tag{E.3}$$

Thus

$$\begin{aligned} \mathbb{E} [\eta_D(\tau, F_D) \eta_P^*(\tau, F_D)] &= \mathbb{E} [\eta_P^*(\tau, F_D) \eta_D(\tau, F_D)] \\ &= \mathbb{E} \left[\frac{1}{N^2} P^H E_x^H M^* M^T E_x D \right] = \frac{1}{N^2} P^H E_x^H \mathbb{E} [M^* M^T] E_x D \\ &= \frac{\sigma_{IF}^2}{N^2} P^H E_x^H E_x D = \frac{\sigma_{IF}^2}{N^2} D^H P \approx 0. \end{aligned} \tag{E.4}$$

The correlation Eq. (E.4) is almost zero for the quasi-orthogonality of the primary codes e_D and e_P . In Eq. (E.4) the fact that $E_x^H E_x = I_N$ and $\mathbb{E}\{M^* M^T\} = \sigma_{IF} I_N$ has been used. I_N is the identity matrix of size N .

From Eq. (E.4) $\eta_D(\tau, F_D)$ and $\eta_P(\tau, F_D)$ can be considered uncorrelated and thus independent.

Appendix F

Computation of the coefficients $\{a_{K,i}\}_{i=1}^K$ and $\{b_{K,i}\}_{i=1}^K$

The partial fraction expansion

$$\frac{1}{(1 - j4\sigma_n^2 t)^K (1 - j2\sigma_n^2 t)^K} = \sum_{i=1}^K \left[\frac{a_{K,i}}{(1 - j4\sigma_n^2 t)^i} - \frac{b_{K,i}}{(1 - j2\sigma_n^2 t)^i} \right]$$

can be determined by establishing a recurrence relationship between the coefficients $\{a_{K,i}, b_{K,i}\}_{i=1}^K$ and $\{a_{K-1,i}, b_{K-1,i}\}_{i=1}^{K-1}$, obtained from the partial fraction expansion of $\frac{1}{(1 - j4\sigma_n^2 t)^{K-1} (1 - j2\sigma_n^2 t)^{K-1}}$. In particular:

$$\begin{aligned} \frac{1}{(1 - j4\sigma_n^2 t)^K (1 - j2\sigma_n^2 t)^K} &= \frac{1}{(1 - j4\sigma_n^2 t)(1 - j2\sigma_n^2 t)} \frac{1}{(1 - j4\sigma_n^2 t)^{K-1} (1 - j2\sigma_n^2 t)^{K-1}} \\ &= \left[\frac{2}{(1 - j4\sigma_n^2 t)} - \frac{1}{(1 - j2\sigma_n^2 t)} \right] \sum_{i=1}^{K-1} \left[\frac{a_{K-1,i}}{(1 - j4\sigma_n^2 t)^i} - \frac{b_{K-1,i}}{(1 - j2\sigma_n^2 t)^i} \right] \\ &= \sum_{i=1}^{K-1} \frac{2a_{K-1,i}}{(1 - j4\sigma_n^2 t)^{i+1}} + \sum_{i=1}^{K-1} \frac{b_{K-1,i}}{(1 - j2\sigma_n^2 t)^{i+1}} - \sum_{i=1}^{K-1} \frac{a_{K-1,i}}{(1 - j4\sigma_n^2 t)^i (1 - j2\sigma_n^2 t)} \\ &\quad - \sum_{i=1}^{K-1} \frac{2b_{K-1,i}}{(1 - j4\sigma_n^2 t) (1 - j2\sigma_n^2 t)^i}. \end{aligned} \tag{F.1}$$

In the summations of Eq. (F.1) there is only one fraction proportional to $1/(1 - j4\sigma_n^2)^K$ and only one proportional to $1/(1 - j2\sigma_n^2)^K$, thus a first recurrence relation for $a_{K,K}$ and $b_{K,K}$ can be found

$$\begin{aligned} a_{K,K} &= 2a_{K-1,K-1} \\ b_{K,K} &= -b_{K-1,K-1}. \end{aligned} \tag{F.2}$$

For determining the other recurrence relations it is noted that $a_{K,i}$, for $i > 1$, depends only on the coefficients in the summations

$$\sum_{i=1}^{K-1} \frac{2a_{K-1,i}}{(1-j4\sigma_n^2 t)^{i+1}} - \sum_{i=1}^{K-1} \frac{a_{K-1,i}}{(1-j4\sigma_n^2 t)^i(1-j2\sigma_n^2 t)} \quad (\text{F.3})$$

and $b_{K,i}$, for $i > 1$, depends only on the coefficients in the summations

$$\sum_{i=1}^{K-1} \frac{b_{K-1,i}}{(1-j4\sigma_n^2 t)^{i+1}} - \sum_{i=1}^{K-1} \frac{2b_{K-1,i}}{(1-j4\sigma_n^2 t)(1-j2\sigma_n^2 t)^i}. \quad (\text{F.4})$$

The second summation in Eq. (F.3) can be further decomposed as:

$$\begin{aligned} - \sum_{i=1}^{K-1} \frac{a_{K-1,i}}{(1-j4\sigma_n^2 t)^i(1-j2\sigma_n^2 t)} &= - \sum_{i=1}^{K-1} \frac{a_{K-1,i}}{(1-j4\sigma_n^2 t)^{i-1}} \frac{1}{(1-j4\sigma_n^2 t)(1-j2\sigma_n^2 t)} \\ &= - \sum_{i=1}^{K-1} \frac{a_{K-1,i}}{(1-j4\sigma_n^2 t)^{i-1}} \left[\frac{2}{(1-j4\sigma_n^2 t)} - \frac{1}{(1-j2\sigma_n^2 t)} \right] \\ &= \frac{a_{K-1,1}}{(1-j2\sigma_n^2 t)} - \left[\sum_{i=1}^{K-1} \frac{2a_{K-1,i}}{(1-j4\sigma_n^2 t)^i} - \sum_{i=2}^{K-1} \frac{a_{K-1,i}}{(1-j4\sigma_n^2 t)^{i-1}(1-j2\sigma_n^2 t)} \right]. \end{aligned} \quad (\text{F.5})$$

In an analogous way, the second summation in Eq. (F.4) can be expressed as:

$$\begin{aligned} - \sum_{i=1}^{K-1} \frac{2b_{K-1,i}}{(1-j4\sigma_n^2 t)(1-j2\sigma_n^2 t)^i} &= - \sum_{i=1}^{K-1} \frac{2b_{K-1,i}}{(1-j2\sigma_n^2 t)^{i-1}} \left[\frac{2}{(1-j4\sigma_n^2 t)} - \frac{1}{(1-j2\sigma_n^2 t)} \right] \\ &= - \frac{2b_{K-1,1}}{(1-j4\sigma_n^2 t)} - 2 \left[\sum_{i=1}^{K-1} \frac{b_{K-1,i}}{(1-j2\sigma_n^2 t)^i} - \sum_{i=2}^{K-1} \frac{2b_{K-1,i}}{(1-j4\sigma_n^2 t)(1-j2\sigma_n^2 t)^{i-1}} \right]. \end{aligned} \quad (\text{F.6})$$

From Eqs. (F.3), (F.4), (F.5) and (F.6) it is possible to derive the following recurrence relationship for $a_{K,K-1}$ and $b_{K,K-1}$:

$$\begin{aligned} a_{K,K-1} &= 2a_{K-1,K-2} - 2a_{K-1,K-1} = 2a_{K-1,K-2} - a_{K,K} \\ b_{K,K-1} &= -b_{K-1,K-2} - 2b_{K-1,K-1} = -b_{K-1,K-2} + 2b_{K,K}. \end{aligned} \quad (\text{F.7})$$

The summations between square brackets in both Eqs. (F.5) and (F.6) have the same structure as those of Eqs. (F.3) and (F.4), respectively. Thus, for determining the recurrence relation for $a_{K,i}$ and $b_{K,i}$, for $i > 1$, it is sufficient to continue to expand the summations in Eqs. (F.5) and (F.6). By doing so the following recurrence relations are found:

$$\begin{aligned} a_{K,K-n} &= 2a_{K-1,K-n-1} - a_{K,K-n+1} \\ b_{K,K-n} &= -b_{K-1,K-n-1} + 2b_{K,K-n+1}. \end{aligned} \quad (\text{F.8})$$

The coefficient $a_{K,1}$ is given by two contributions, the first from Eq. (F.3) and the second from Eq. (F.4). The term from Eq. (F.3) follows the recurrence relation in Eq. (F.8), provided that $a_{K-1,0} = 0$, whereas the one from Eq. (F.4) can be easily determined by using the residues theorem. $b_{K,1}$ can be determined in the same way. Thus, the final formula for $a_{K,1}$ and $b_{K,1}$ are

$$\begin{aligned} a_{K,1} &= -a_{K,K-n+1} - \sum_{i=1}^{K-1} 2^{i+1} b_{K-1,i} \\ b_{K,1} &= 2b_{K,K-n+1} - \sum_{i=1}^{K-1} (-1)^{i+1} a_{K-1,i}. \end{aligned} \quad (\text{F.9})$$

Eqs. (F.2), (F.8) and (F.9) can be summarized in the following formula:

$$\begin{aligned} a_{K,K-n} &= 2a_{K-1,K-n-1} - a_{K,K-n+1} - B_{K-1,n} \\ b_{K,K-n} &= -b_{K-1,K-n-1} + 2b_{K,K-n+1} - A_{K-1,n} \end{aligned} \quad (\text{F.10})$$

where

- $B_{K-1,n} = \sum_{i=1}^{K-1} 2^{i+1} b_{K-1,i} \delta[n - K + 1]$
- $A_{K-1,n} = \sum_{i=1}^{K-1} (-1)^{i+1} a_{K-1,i} \delta[n - K + 1]$

and $\delta[\cdot]$ is the Kronecker delta. Using the recurrence relation (F.10) and the initial conditions

$$a_{1,1} = 2, \quad b_{1,1} = 1 \quad (\text{F.11})$$

it is finally possible to evaluate the coefficients for the partial fraction expansion of $\frac{1}{(1-j4\sigma_n^2 t)^K (1-j2\sigma_n^2 t)^K}$.

Appendix G

Equivalent probability distribution of φ_1 and φ_2

In this appendix it is shown that the random variables φ_1 and φ_2 defined by Eqs. (11.16) and (11.17) can be substituted in Eq. (11.15) by two independent random variables uniformly distributed over the range $[-\pi; \pi]$.

Firstly, the constant terms in Eqs. (11.16) and (11.17)

$$c_1 = \theta_1 + 2\pi(F_{int} - F_{D,0})\tau_0,$$

$$c_2 = \theta_2 - 2\pi(F_{int} + F_{D,0})\tau_0,$$

can be dropped. In fact φ_1 and φ_2 appear in Eq. (11.15) only as arguments of periodic functions whose values do not change if φ_1 and φ_2 are translated. In fact these random variables span a whole period of those functions even if translated. Thus the following change of variables can be considered:

$$\begin{bmatrix} \varphi_1 \\ \varphi_2 \end{bmatrix} = \begin{bmatrix} 1 & -1 \\ -1 & -1 \end{bmatrix} \begin{bmatrix} \theta_{int} \\ \phi_0 \end{bmatrix}. \quad (\text{G.1})$$

The θ_{int} and ϕ_0 independent and uniformly distributed random variables. Eq. (G.1) defines a linear transformation that rotates and expands the support of the joint probability density function of θ_{int} and ϕ_0 . The effect of this change of variables is better illustrated in Figure G.1 where the effect of Eq. (G.1) on the support of the joint distribution is reported. However only the values of φ_1 and φ_2 in the range $[-\pi, \pi]$ are of interest, since Eq. (11.15) can be expressed in terms of sines and cosines of these two variables. Thus, since trigonometric functions are 2π -periodic, the values of φ_1 and φ_2 outside $[-\pi, \pi]$ are folded into this range leading to the joint probability distribution illustrated in the last part of Figure G.1. The new joint distribution is still uniform on the new support and it can be factorized as the product of the distributions of two uniform random variables.

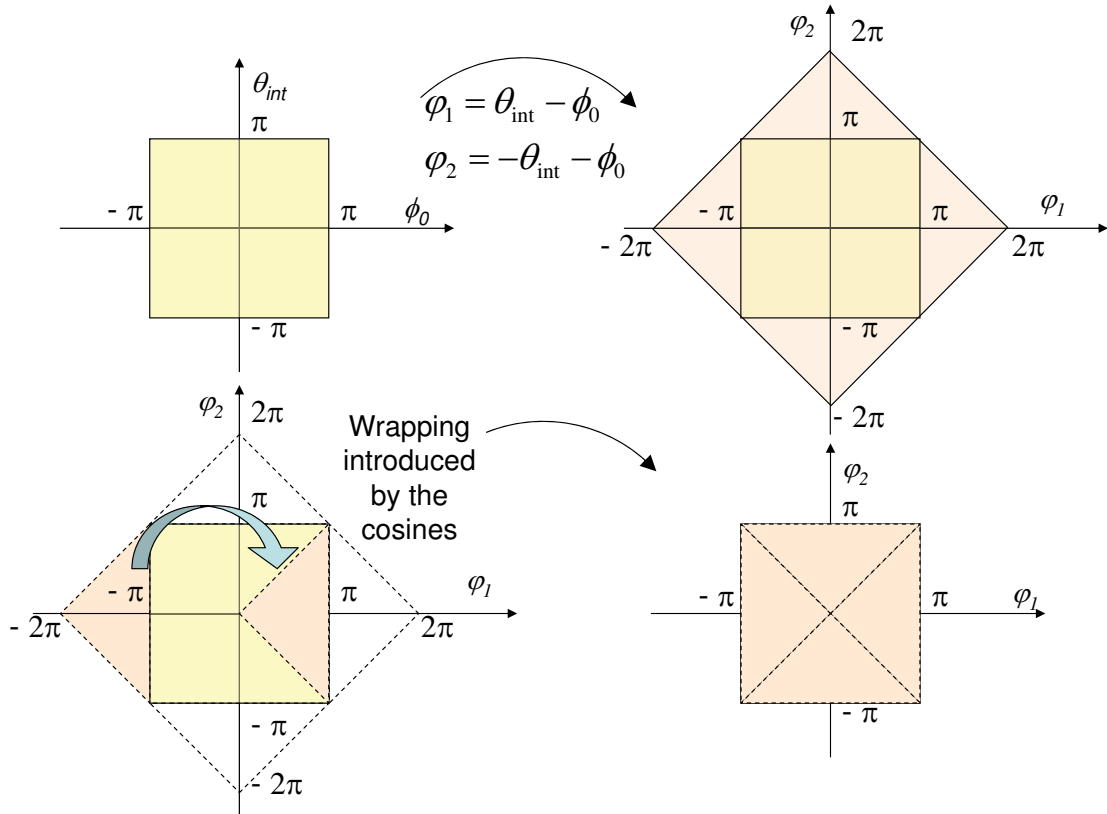


Figure G.1. Transformation from θ_{int} and ϕ_0 to φ_1 and φ_2 . Since the cosine is 2π -periodic the values of φ_1 and φ_2 outside $[-\pi; \pi]$ are folded into this range leading to two independent random variables uniformly distributed.

This proves that φ_1 and φ_2 can be considered independent and uniformly distributed on $[-\pi, \pi]$.

Appendix H

Proof of (11.20)

In this appendix the proof of Eq. (11.20) is given. Upon defining

$$p_1 = \frac{A^2}{4} + \frac{A_{INT}^2}{4}(k_1^2 + k_2^2) = \frac{C}{2} + \frac{A_{INT}^2}{4}(k_1^2 + k_2^2)$$

$$p_2 = \frac{A_{INT}}{\sqrt{2}}k_2$$

the expression (11.15) can be rewritten as

$$\begin{aligned} \alpha^2 &= p_1 + p_2\sqrt{C}\cos\varphi_2 + \frac{A_{INT}^2}{2}k_1k_2\cos(\varphi_1 - \varphi_2) + A_{INT}\sqrt{\frac{C}{2}}k_1\cos\varphi_1 \\ &= p_1 + p_2\sqrt{C}\cos\varphi_2 + \cos\varphi_1 \left[A_{INT}\sqrt{\frac{C}{2}}k_1 + \frac{A_{INT}^2}{2}k_1k_2\cos\varphi_2 \right] + \sin\varphi_1 \frac{A_{INT}^2}{2}k_1k_2\sin\varphi_2. \end{aligned} \quad (\text{H.1})$$

By defining

$$\begin{aligned} M(\varphi_2) &= \sqrt{\left(A_{INT}\sqrt{\frac{C}{2}}k_1 + \frac{A_{INT}^2}{2}k_1k_2\cos\varphi_2 \right)^2 + \left(\frac{A_{INT}^2}{2}k_1k_2\sin\varphi_2 \right)^2} \\ &= \sqrt{\left[A_{INT}^2\frac{C}{2}k_1^2 + \frac{A_{INT}^4}{4}k_1^2k_2^2 \right] + A_{INT}^3\sqrt{\frac{C}{2}}k_1^2k_2\cos\varphi_2} \\ &= \sqrt{p_3 + p_4\sqrt{C}\cos\varphi_2} \end{aligned} \quad (\text{H.2})$$

and

$$\gamma(\varphi_2) = \arctan \left[\frac{\frac{A_{INT}^2}{2}k_1k_2\sin\varphi_2}{A_{INT}\sqrt{\frac{C}{2}}k_1 + \frac{A_{INT}^2}{2}k_1k_2\cos\varphi_2} \right] \quad (\text{H.3})$$

where

$$p_3 = A_{INT}^2\frac{C}{2}k_1^2 + \frac{A_{INT}^4}{4}k_1^2k_2^2$$

$$p_4 = \frac{A_{INT}^3}{\sqrt{2}} k_1^2 k_2,$$

expression (H.1) becomes

$$\begin{aligned} \alpha^2 &= p_1 + p_2 \sqrt{C} \cos \varphi_2 + M(\varphi_2) \cos [\gamma(\varphi_2)] \cos(\varphi_1) + M(\varphi_2) \sin [\gamma(\varphi_2)] \sin(\varphi_1) \\ &= p_1 + p_2 \sqrt{C} \cos \varphi_2 + \sqrt{p_3 + p_4 \sqrt{C} \cos \varphi_2} \cos(\varphi_1 - \gamma). \end{aligned} \quad (\text{H.4})$$

The term $\cos(\varphi_1 - \gamma)$ can be substituted by $\cos \varphi_3$ where φ_3 is a new random variable statistically independent from γ , and thus from φ_2 , uniformly distributed on the range $[-\pi, \pi]$. This property can be easily proved by noticing that the probability distribution of $\cos(\varphi_1 - \gamma)$ is statistically independent from γ . In fact, for each fixed γ , φ_1 uniformly spans a period of the cosine and thus the statistical properties of $\cos(\varphi_1 - \gamma)$ do not depend on γ . This kind of argument can also be used to prove that $\cos(\varphi_1 - \varphi_2)$ behaves as $\cos \theta$ where θ is a random variable uniformly distributed over $[-\pi; \pi]$.

By using this consideration, Eq. (H.4) becomes

$$\alpha^2 = p_1 + p_2 \sqrt{C} \cos \varphi_2 + \sqrt{p_3 + p_4 \sqrt{C} \cos \varphi_2} \cos \varphi_3 \quad (\text{H.5})$$

thus proving Eq. (11.20).

Bibliography

- [1] *NordNav-R30 Package*, NordNav Technologies, www.navtechgps.com/pdf/Nordnav_R30.pdf, 2004.
- [2] E. D. Kaplan and C. Hegarty, Eds., *Understanding GPS: Principles and Applications*. Artech House Publishers, Nov. 2005.
- [3] B. W. Parkinson and J. J. Spilker, Eds., *Global Positioning System: Theory and Applications*. American Institute of Aeronautics and Ast (AIAA), Jan. 1996, vol. 1st.
- [4] P. Misra and P. Enge, *Global Positioning System: Signals, Measurements, and Performance*, 2nd ed. Ganga-Jamuna Press, 2006.
- [5] P. W. Ward, "GPS receiver search techniques," in *Proc. of IEEE Position Location and Navigation Symposium (PLANS)*, Atlanta, GA, Apr. 1996, pp. 604 – 611.
- [6] G. Corazza, C. Caini, A. Vanelli-Coralli, and A. Polydoros, "DS-CDMA code acquisition in the presence of correlated fading - part I: theoretical aspects," *IEEE Trans. Commun.*, vol. 52, no. 7, pp. 1160 – 1168, July 2004.
- [7] ——, "DS-CDMA code acquisition in the presence of correlated fading - part II: Application to cellular networks," *IEEE Trans. Commun.*, vol. 52, no. 8, pp. 1397 – 1407, Aug. 2004.
- [8] C. Yang, M. Miller, E. Blasch, and T. Nguyen, "Comparative study of coherent, non-coherent, and semi-coherent integration schemes for GNSS receivers," in *Proc. of ION 63rd Annual Meeting*, Cambridge, MA, Apr. 2007, pp. 572 – 588.
- [9] R. Pulikkoonattu and M. Antweiler, "Analysis of differential non coherent detection scheme for CDMA pseudo random (PN) code acquisition," in *Proc. of IEEE ISSSTA'04*, Aug. 2004, pp. 212 – 217.
- [10] C. O'Driscoll, "Performance analysis of the parallel acquisition of weak GPS signals," Ph.D. dissertation, National University of Ireland, Cork, Jan. 2007.
- [11] M. H. Zarabizadeh and E. S. Sousa, "A differentially coherent PN code acquisition receiver for CDMA systems," *IEEE Trans. Commun.*, vol. 45, no. 11, pp. 1456 – 1465, Nov. 1997.
- [12] J. A. Ávila Rodriguez, T. Pany, and B. Eissfeller, "A theoretical analysis of acquisition algorithms for indoor positioning," in *Proc. of the 2nd ESA Workshop on Satellite Navigation User Equipment Technologies NAVITEC*, Noordwijk, The Netherlands,

- Dec. 2004.
- [13] C. Strässle, D. Megnet, H. Mathis, and C. Bürgi, "The squaring-loss paradox," in *Proc. of ION GNSS*, Fort Worth, TX, Sept. 2007.
 - [14] J. J. Spilker, *Digital Communications by Satellite*. Prentice-Hall Information Theory Series, Feb. 1977.
 - [15] H. Chang, "Presampling filtering, sampling and quantization effects on the digital matched filter performance," in *Proc. of International Telemetering Conference*, San Diego, CA, Sept. 1982, pp. 889 – 915.
 - [16] J. W. Betz and N. R. Shnidman, "Receiver processing losses with bandlimiting and one-bit sampling," in *Proc. of ION GNSS*, Fort Worth, TX, Sept. 2007.
 - [17] F. Bastide, O. Julien, C. Macabiau, and B. Roturier, "Analisis of L5/E5 acquisition, tracking and data demodulation thresholds," in *Proc. of ION GPS/GNSS*, Portland, OR, Sept. 2002, pp. 2196 – 2207.
 - [18] C. Mongrédiens, G. Lachapelle, and M. E. Cannon, "Testing GPS L5 acquisition and tracking algorithms using a hardware simulator," in *Proc. of ION/GNSS*, Fort Worth, TX, Sept. 2006, pp. 2901 – 2913.
 - [19] C. J. Hegarty, "Optimal and near-optimal detector for acquisition of the GPS L5 signal," in *Proc. of ION NTM, National Technical Meeting*, Monterey, CA, Jan. 2006, pp. 717 – 725.
 - [20] J. W. Betz, "Effect of narrowband interference on GPS code tracking accuracy," in *Proc. of ION National Technical Meeting*, Anaheim, CA, Jan. 2000, pp. 16 – 27.
 - [21] ——, "Effect of partial-band interference on receiver estimation of C/N_0 : Theory," in *Proc. of ION National Technical Meeting*, Long Beach, CA, Jan. 2001, pp. 817 – 828.
 - [22] R. J. Landry and A. Renard, "Analysis of potential interference sources and assessment of present solutions for GPS/GNSS receivers," *4th Saint-Petersburg on INS*, May 1997.
 - [23] A. T. Balaei, A. G. Dempster, and J. Barnes, "A novel approach in detection and characterization of CW interference of GPS signal using receiver estimation of."
 - [24] R. Abimoussa and R. J. Landry, "Anti-jamming solution to narrowband CDMA interference problem," in *in Proc. of Canadian Conference on Electrical and Computer Engineering*, vol. 2, Halifax, NS, Mar. 2000, pp. 1057 – 1062.
 - [25] D. Borio, L. Camoriano, L. L. Presti, and P. Mulassano, "Analysis of the one-pole notch filter for interference mitigation: Wiener solution and loss estimations," in *in Proc. of ION/GNSS*, Fort Worth, TX, 2006.
 - [26] D. A. Shnidman, "Radar detection probabilities and their calculation," *IEEE Trans. Aerosp. Electron. Syst.*, vol. 31, no. 3, pp. 928 – 950, July 1995.
 - [27] D. Borio, L. Camoriano, and L. Lo Presti, "Impact of the acquisition searching strategy on the detection and false alarm probabilities in a CDMA receiver," in *Proc. of IEEE/ION Position, Location, And Navigation Symposium (PLANS)*, San Diego, CA, Apr. 2006, pp. 1100 – 1107.

- [28] ——, "The impact of GPS acquisition strategy on decision probabilities," *IEEE Trans. Aerosp. Electron. Syst.*, 2007, Accepted for publication.
- [29] S. Turunen, "Network assistance. What will new GNSS signals bring to it," *Inside GNSS*, vol. 2, no. 3, pp. 35 – 41, Mar. 2007.
- [30] ——, "Acquisition performance of assisted and unassisted GNSS receivers with new satellite signals," in *Proc. of ION GNSS*, Fort Worth, TX, Sept. 2007.
- [31] J. K. Holmes, *Coherent Spread Spectrum Systems*. John Wiley & Sons, Oct. 1981.
- [32] J. B.-Y. Tsui, *Fundamentals of Global Positioning System Receivers: A Software Approach*. Wiley-Interscience, 2000.
- [33] W. Z. Zhuang and J. Tranquilla, "Digital baseband processor for the GPS receiver (part I and II)," *IEEE Trans. Aerosp. Electron. Syst.*, vol. 29, no. 4, pp. 1343–1349, Oct. 1993.
- [34] H. Mathis and P. Flammant, "An analytic way to optimize the detector of a post-correlation FFT acquisition algorithm," in *Proc. ION/GNSS*, Sept. 2003.
- [35] P. S. Tong, "A suboptimum synchronization procedure for pseudo-noise communication systems," in *Proceeding of National Telecommunications Conference*, 1973.
- [36] R. N. McDonough and A. D. Whalen, *Detection of Signals in Noise*, 2nd ed. Academic Press, 1995.
- [37] J. Marcum, "A statistical theory of target detection by pulsed radar," *IEEE Trans. Inform. Theory*, vol. 6, pp. 59 – 267, Apr. 1960.
- [38] P. Swerling, "Probability of detection for fluctuating targets," *IEEE Trans. Inform. Theory*, vol. 6, no. 2, pp. 269 – 308, Apr. 1960, (Reprinted from Rand Research Memo RM-1217, Mar. 17, 1954).
- [39] D. A. Shnidman, "Radar detection in clutter," *IEEE Trans. Aerosp. Electron. Syst.*, vol. 41, no. 3, pp. 1056 – 1067, July 2005.
- [40] W. De Wilde, J.M. Sleewaegen, A. Simsky, J. Van Hees, C. Vandewiele, E. Peeters, J. Grauwen and F. Boon, "Fast signal acquisition technology for new GPS/Galileo receivers," in *Proc. of IEEE/ION PLANS'06*, San Diego, CA, USA, Apr. 2006, pp. 1074–1079.
- [41] J. W. Betz, *Systems, Signals and Receiver Signal Processing*. Navtech GPS, Sept. 2006, vol. 3.
- [42] G. Lachapelle and M. Petovello, *Weak Signal Tracking and High-Sensitivity GPS for Indoors*. Navtech GPS, Sept. 2005, vol. 3.
- [43] J. V. DiFranco and W. L. Rubin, *Radar Detection*. Dedham, MA: Artech House, Inc., 1980.
- [44] J. Proakis, *Digital Communications*, 4th ed. McGraw-Hill Science/Engineering/Math, Aug. 2000.
- [45] M. Abramowitz and I. A. Stegun, Eds., *Handbook of Mathematical Functions with Formulas, Graphs, and Mathematical Table*. Dover Publications, June 1965.

- [46] C. Helstrom, "Computing the generalized Marcum Q-function," *IEEE Trans. Inform. Theory*, vol. 38, no. 4, pp. 1422 – 1428, July 1992.
- [47] J. Iinatti, "On the threshold setting principles in code acquisition of DS-SS signals," *IEEE J. Select. Areas Commun.*, vol. 18, no. 1, pp. 62–72, Jan. 2000.
- [48] G. E. Corazza, "On the MAX/TC criterion for code acquisition and its application to DS-SSMA systems," *IEEE Trans. Commun.*, vol. 44, no. 9, pp. 1173 – 1182, Sept. 1996.
- [49] H. Park and B. Kang, "On the performance of a maximum-likelihood code-acquisition technique for preamble search in a CDMA reverse link," *IEEE Trans. Veh. Technol.*, vol. 47, no. 1, pp. 65–74, Feb. 1998.
- [50] A. Polydoros and C. Weber, "A unified approach to serial search spread-spectrum code acquisition—part I: General theory," *IEEE Trans. Commun.*, vol. 32, no. 5, pp. 542 – 549, May 1984.
- [51] ———, "A unified approach to serial search spread-spectrum code acquisition—part II: A matched-filter receiver," *IEEE Trans. Commun.*, vol. 32, no. 5, pp. 550 – 560, May 1984.
- [52] R. Stirling-Gallacher, A. Hulbert, and G. Povey, "A fast acquisition technique for a direct sequence spread spectrum signal in the presence of a large doppler shift," in *Proc. ISSSTA*, vol. 1, pp. 156 – 160, Sept. 1996.
- [53] E. Lohan, A. Lakhzouri, and M. Renfors, "Selection of the multiple-dwell hybrid-search strategy for the acquisition of Galileo signals in fading channels," in *Proc. IEEE International Symposium on Personal, Indoor and Mobile Radio Communications*, vol. 4, Barcelona, Spain, Sept. 2004, pp. 2352 – 2356.
- [54] D. Akopian, "Fast FFT based GPS satellite acquisition methods," *IEE Proc. Radar Sonar Navig.*, vol. 152, no. 4, pp. 277 – 286, Aug. 2005.
- [55] D. A. Shnidman, "The calculation of the probability of detection and the generalized Marcum Q-function," *IEEE Trans. Inform. Theory*, vol. 35, no. 2, pp. 389–400, Mar. 1989.
- [56] M. K. Simon, *Probability Distributions Involving Gaussian Random Variables: A Handbook for Engineers and Scientists*, 1st ed., ser. The International Series in Engineering and Computer Science. Springer, may 2002.
- [57] S. T. Lowe, "Voltage Signal-to-Noise ratio (SNR) nonlinearity resulting from incoherent summations," The Telecommunications and Mission Operations Progress Report, TMO PR 42-137, Tech. Rep., May 1999.
- [58] A. Papoulis and S. U. Pillai, *Probability, Random Variables and Stochastic Processes*, 4th ed. McGraw-Hill Publishing Co., Jan. 2002.
- [59] W. Feller, *An Introduction to Probability Theory and Its Applications*, 3rd ed. Wiley, 1968, vol. 1.
- [60] S. M. Kay, *Fundamentals of Statistical Signal Processing, Volume 2: Detection Theory*, 1st ed. Prentice Hall Signal Processing Series, Feb. 1998.

- [61] B. Widrow, I. KollL, and M. Liu, "Statistical theory of quantization," *IEEE Trans. Instrum. Meas.*, vol. 45, no. 2, pp. 353–361, apr 1996.
- [62] A. B. Sripad and D. L. Snyder, "A necessary and sufficient condition for quantization errors to be uniform and white," vol. 25, no. 5, pp. 442–448, oct 1977.
- [63] H. Chang, "Presampling filtering, sampling and quantization effects on the digital matched filter performance," in *International Telemetering Conference*, vol. 18, San Diego, CA, Sept. 1982, pp. 889 – 915.
- [64] D. Borio, M. Fantino, L. Lo Presti, and L. Camoriano, "Acquisition analysis for Galileo BOC modulated signals: Theory and simulation," in *Proc. of European Navigation Conference (ENC)*, Manchester, UK, May 2006.
- [65] K. Borre, "The Galileo signals with emphasis on L1 OS," in *Proc. of 12th International Power Electronics and Motion Control Conference*, Aug. 2006, pp. 2025 – 2030.
- [66] "Galileo open service signal in space interface control document," European Space Agency / Galileo Joint Undertaking, Draft GAL OS SIS ICD/D.0, May 2006.
- [67] "Navstar gps space segment/navigation user interfaces," ARINC Incorporated, Tech. Rep. IS-GPS-200 (IRN-200D-001), Mar. 2006.
- [68] P. G. Mattos, "Acquisition of the Galileo OS L1b/c signal for the mass-market receiver," in *Proc. of ION GNSS, 18th International Technical Meeting*, Long Beach, CA, Sept. 2005, pp. 1143 – 1152.
- [69] ——, "Galileo L1c - acquisition complexity: Cross correlation benefits, sensitivity discussions on the choice of pure pilot, secondary code, or something different," in *Proc. of IEEE Position Location and Navigation Symposium (PLANS/ION)*, Apr. 2006, pp. 845 – 852.
- [70] C. Hegarty, M. Tran, and A. J. Van Dierendonck, "Acquisition algorithms for the GPS L5 signal," in *Proc. of ION/GNSS*, Portland, OR, Sept. 2003, pp. 165 – 177.
- [71] C. Yang, C. Hegarty, and M. Tran, "Acquisition of the GPS L5 signal using coherent combining of I5 and Q5," in *Proc. of ION GNSS, 17th International Technical Meeting*, Long Beach, CA, Sept. 2004, pp. 2184 – 2195.
- [72] D. Borio, M. Fantino, and L. L. Presti, "The impact of the Galileo signal in space in the acquisition system," in *Proc. of — Tyrreniam Conference*, Ponza, Italy, Sept. 2006.
- [73] A. Requicha, "Direct computation of distribution functions from characteristic functions using the fast fourier transform," *Proc. IEEE*, vol. 58, no. 7, pp. 1154 – 1155, jul 1970.
- [74] "Interface specification, navstar GPS space segment / navigation L5 user interfaces," ARINC Incorporated, Tech. Rep. IS-GPS-705 (2005), Sept. 2005.
- [75] M. Hamalainen, V. Hovinen, R. Tesi, J. Iinatti, and M. Latva-aho, "On the UWB system coexistence with GSM900, UMTS/WCDMA, and GPS," *IEEE J. Select. Areas Commun.*, vol. 20, no. 9, pp. 1712 – 1721, Dec. 2002.
- [76] R. Giuliano and F. Mazzenga, "On the coexistence of power-controlled ultrawide-band systems with UMTS, GPS, DCS1800, and fixed wireless systems," *IEEE Trans.*

- Veh. Technol.*, vol. 54, no. 1, pp. 62 – 81, Jan. 2005.
- [77] D. Cummings, "Aggregate ultra wideband impact on global positioning system receivers," in *IEEE Radio and Wireless Conference RAWCON.*, Aug. 2001, pp. 101 – 104.
- [78] F. Bestide, E. Chatre, C. Macabiau, and B. Roturier, "GPS L5 and Galileo E5a/E5b signal-to-noise density ratio degradation due to DME/TACAN signals: Simulations and theoretical derivation," in *Proc. of ION/NTM*, San Diego, CA, Jan. 2004, pp. 1049 – 1062.
- [79] M. Raimondi, O. Julien, C. Macabiau, and F. Bastide, "Mitigating pulsed interference using frequency domain adaptive filtering," in *Proc. ION/GNSS 19th International Technical Meeting of the Satellite Division*, Fort Worth, TX, 2006, pp. 2252 – 2260.
- [80] "Vulnerability assessment of the transportation infrastructure relying on the global position system," John A. Volpe National Transportation Systems Center, <http://www.navcen.uscg.gov/archive/2001/Oct/FinalReport-v4.6.pdf>, Tech. Rep., Jan. 2000.
- [81] T. Buck and G. Sellick, "GPS RF interference via a TV signal," in *Proc. of ION/GPS*, Kansas City, MO, Sept. 1997, pp. 1497 – 1501.
- [82] G. R. Aiello and G. D. Rogerson, "Ultra-wideband wireless systems," *IEEE Microwave*, vol. 4, no. 2, pp. 36 – 47, June 2003.
- [83] G. R. Opshaug and P. Enge, "Integrated GPS and UWB navigation system (motivates the necessity of non-interference)," in *in Proc. of IEEE Conference on Ultra Wideband Systems and Technologies*, May 2002, pp. 123 – 127.
- [84] Y. T. Morton, M. French, Q. Zhou, J. Tsui, M. Lin, M. Miller, and D. Jennings, "A software approach to access ultra-wide band interference on GPS receivers," in *Proc. of IEEE Position Location and Navigation Symposium (PLANS)*, Apr. 2004, pp. 551 – 557.
- [85] R. M. Kalafus, "Interference to GPS receivers from mobile satellite emissions," in *Proc. of ION/GPS*, Nashville, TN, Sept. 1998, pp. 827 – 832.
- [86] J. W. Betz and B. M. Titus, "Intersystem and intrasystem interference with signal imperfections," in *Proc. of IEEE Position Location and Navigation Symposium (PLANS)*, Apr. 2004, pp. 558 – 565.
- [87] B. M. Titus, J. W. Betz, C. J. Hegarty, and R. Owen, "Intersystem and intrasystem interference analysis methodology," in *Proc. of ION/GNSS*, Portland, OR, Sept. 2003, pp. 2061 – 2069.
- [88] J. P. Cabrera Plaza and T. Burger, "Inter-system interference experiments for Galileo and GPS in L1 (1575.42 MHz)," in *Proc. of the European Navigation Conference (ENC)*, Graz, Austria, Apr. 2003.
- [89] M. Tran, T. Kim, C. J. Hegarty, and J. J. Devincentis, "Validation of the feasibility of coexistence of the new civil GPS signal (L5) with existing systems," in *MITRE Corporation technical paper*,

Bibliography

- http://www.mitre.org/work/tech_papers/tech_papers_01/tran_validation/index.html, Mar. 2001.
- [90] J. M. Silva and R. Olsen, "Use of global positioning system (GPS) receivers under power-line conductors," *IEEE Trans. Power Delivery*, vol. 17, no. 4, pp. 938 – 944, Oct. 2002.
 - [91] D. Borio, L. L. Presti, and P. Mulassano, "Spectral separation coefficients for digital GNSS receivers," in *Proc. of 14th European Signal Processing Conference (EUSIPCO)*, Florence, Italy, Sept. 2006.
 - [92] S. Pei and C. Tseng, "Complex adaptive IIR notch filter algorithm and its applications," *IEEE Trans. Circuits Syst. II*, vol. 41, no. 2, pp. 158 – 163, Feb. 1994.
 - [93] M. Ferdjallah and R. Barr, "Adaptive digital notch filter design on the unit circle for the removal of powerline noise from biomedical signals," *IEEE Trans. Biomed. Eng.*, vol. 41, no. 6, pp. 529 – 536, June 1994.
 - [94] M. A. Soderstrand, T. G. Johnson, R. H. Strandberg, H. H. J. Loomis, and K. V. Rangarao, "Suppression of multiple narrow-band interference using real-time adaptive notch filters," *IEEE Trans. Circuits Syst. II*, vol. 44, no. 3, pp. 217 – 225, Mar. 1997.
 - [95] V. Calmettes, F. Pradeilles, and M. Bousquet, "Study and comparison of interference mitigation techniques for GPS receiver," in *Proc. of ION/GPS*, Salt Lake City, UT, Sept. 2001.
 - [96] V. K. Ingle and J. G. Proakis, *Digital Signal Processing Using MATLAB*, 1st ed. Thomson-Engineering, 1999.
 - [97] R. Rifkin and J. Vaccaro, "Comparison of narrowband adaptive filter technologies for GPS," MITRE Corporation, www.mitre.org, Tech. Rep., Mar. 2000.
 - [98] J. Young and J. Lehnert, "Analysis of DFT-based frequency excision algorithms for direct-sequence spread-spectrum communications," *IEEE Trans. Commun.*, vol. 46, no. 8, pp. 1076 – 1087, Aug. 1998.
 - [99] Y. Xiao, Y. Takeshita, and K. Shida, "Steady-state analysis of a plain gradient algorithm for a second-order adaptive IIR notch filter with constrained poles and zeros," *IEEE Trans. Circuits Syst. II*, vol. 48, no. 7, pp. 733 – 740, July 2001.
 - [100] P. Stoica and A. Nehorai, "Performance analysis of an adaptive notch filter with constrained poles and zeros," *IEEE Trans. Acoust., Speech, Signal Processing*, vol. 36, no. 6, pp. 911 – 919, June 1988.
 - [101] J. W. Choi and N. I. Cho, "Narrow-band interference suppression in direct sequence spread spectrum systems using a lattice IIR notch filter," in *Proc. of IEEE International Conference on Acoustics, Speech, and Signal Processing (ICASSP '01)*, vol. 4, May 2001, pp. 2237 – 2240.
 - [102] R. J. Landry, V. Calmettes, and M. Bousquet, "Impact of interference on a generic GPS receiver and assessment of mitigation techniques," in *Proc. of IEEE 5th International Symposium on Spread Spectrum Techniques and Applications*, vol. 1, Sept. 1998, pp. 87 – 91.

- [103] A. Nehorai, "A minimal parameter adaptive notch filter with constrained poles and zeros," *IEEE Trans. Acoust., Speech, Signal Processing*, vol. 33, no. 4, pp. 983 – 996, Aug. 1985.
- [104] B. D. Rao and R. Peng, "Tracking characteristics of the constrained IIR adaptive notch filter," *IEEE Trans. Acoust., Speech, Signal Processing*, vol. 36, no. 9, pp. 1466 – 1479, Sept. 1988.
- [105] S. Haykin, *Adaptive Filter Theory*, 4th ed. Prentice Hall, Sept. 2001.
- [106] L. Cohen, *Time Frequency Analysis: Theory and Applications*. Prentice Hall PTR, Dec. 1994.
- [107] M. V. Tazebay and A. N. Akansu, "A performance analysis of interference excision techniques in direct sequence spread spectrum communications," *IEEE Trans. Signal Processing*, vol. 46, no. 9, pp. 2530 – 2535, Sept. 1998.
- [108] C. Wang and M. G. Amin, "Performance analysis of instantaneous frequency-based interference excision techniques in spread spectrum communications," *IEEE Trans. Signal Processing*, vol. 46, no. 1, pp. 70 – 82, Jan. 1998.
- [109] M. G. Amin, C. Wang, and A. R. Lindsey, "Optimum interference excision in spread spectrum communications using open-loop adaptive filters," *IEEE Trans. Signal Processing*, vol. 47, no. 7, pp. 1966 – 1976, July 1999.
- [110] X. Ouyang and M. G. Amin, "Short-time Fourier transform receiver for nonstationary interference excision in direct sequence spread spectrum communications," *IEEE Trans. Signal Processing*, vol. 49, no. 4, pp. 851 – 863, Apr. 2001.
- [111] S. Barbarossa and A. Scaglione, "Adaptive time-varying cancellation of wideband interferences in spread-spectrum communications based on time-frequency distributions," *IEEE Trans. Signal Processing*, vol. 47, no. 4, pp. 957 – 965, Apr. 1999.
- [112] S. R. Lach, M. G. Amin, and A. R. Lindsey, "Broadband interference excision for software-radio spread-spectrum communications using time-frequency distribution synthesis," *IEEE J. Select. Areas Commun.*, vol. 17, no. 4, pp. 704 – 714, Apr. 1999.
- [113] Z. Yimin, M. Amin, and A. Lindsey, "Anti-jamming GPS receivers based on bilinear signal distributions," *In Proc. of Military Communications Conference (MILCOM)*, vol. 2, pp. 1070 – 1074, Oct. 2001.
- [114] C. Yang, "Method and device for rapidly extracting time and frequency parameters from high dynamic direct sequence spread spectrum radio signals under interference," US Patent, Tech. Rep. US006407699 B1, June 2002.
- [115] D. J. R. V. Nee and A. J. R. M. Coenen, "New fast GPS code-acquisition technique using FFT," *Electronics Letters*, vol. 27, no. 2, pp. 158 – 160, Jan. 1991.
- [116] F. J. Harris, "On the use of windows for harmonic analysis with the discrete Fourier transform," *Proc. IEEE*, vol. 66, no. 1, pp. 51 – 83, Jan. 1978.
- [117] J. B. Allen and L. R. Rabiner, "A unified approach to short-time Fourier analysis and synthesis," *Proc. IEEE*, vol. 65, no. 11, pp. 1558 – 1564, Nov. 1977.

- [118] M. Amin and K. D. Feng, "Short-time fourier transforms using cascade filter structures," *IEEE Trans. Circuits Syst. II*, vol. 42, no. 10, pp. 631 – 641, Oct. 1995.
- [119] B. Boashash and P. J. Black, "An efficient real-time implementation of the wigner-ville distribution," *IEEE Trans. Acoust., Speech, Signal Processing*, vol. 35, no. 1, pp. 1611 – 1618, Nov. 1987.
- [120] Z. Weihua and J. Tranquilla, "Modeling and analysis for the GPS pseudo-range observable," *IEEE Trans. Aerosp. Electron. Syst.*, vol. 31, pp. 739 – 751, Apr. 1995.
- [121] S. L. Marple Jr., "Computing the discrete-time 'analytic' signal via FFT," *IEEE Trans. Signal Processing*, vol. 47, no. 1999, pp. 2600–2603, Sept. 9.
- [122] D. Ballard, "Generalizing the Hough transform to detect arbitrary shapes," *Pattern Recognit.*, vol. 13, no. 2, pp. 111 – 122, 1981.
- [123] R. L. Graham, D. E. Knuth, and O. Patashnik, *Concrete Mathematics: A Foundation for Computer Science*, 2nd ed. Addison-Wesley Professional, Feb. 1994.